# Infrared Spectroscopy of Molecular Solids under Extreme Conditions

By

**HIMAL BHATT**

PHYS01201004004

**Bhabha Atomic Research Centre,**

**Mumbai - 400085,**

**INDIA**

*A thesis submitted to the*
*Board of Studies in Physical Sciences*

*In partial fulfillment of requirements*
*For the Degree of*

**DOCTOR OF PHILOSOPHY**

of

**HOMI BHABHA NATIONAL INSTITUTE**

**August 2016**

# Homi Bhabha National Institute

## Recommendations of the Viva Voce Board

As members of the Viva Voce Board, we certify that we have read the dissertation prepared by Himal Bhatt entitled "Infrared spectroscopy of molecular solids under extreme conditions" and recommend that it may be accepted as fulfilling the thesis requirement for the Degree of Doctor of Philosophy.

| | | | |
|---|---|---|---|
| Chairman: | Dr. S. K. Deb | Sudip Kumar Deb | Date: 09/05/2017 |
| Convener: | for Dr. Surinder M. Sharma | | Date: 9/5/17 |
| Examiner: | Prof. Chandrabhas Narayana | Chandrabhas | Date: 09/05/2017 |
| Member: | Dr. D. K. Aswal | | Date: 9/5/17 |
| Member: | Prof. S. Wategaonkar | Wategaonkar | Date: 9/5/2017. |
| Member: | Dr. M. N. Deo | | Date: 09/05/2017 |

Final approval and acceptance of this thesis is contingent upon the candidate's submission of the final copies of the dissertation to HBNI.

I hereby certify that I have read this thesis prepared under my direction and recommend that it may be accepted as fulfilling the thesis requirement.

Date: 09/05/17

Place: Mumbai

for Guide

# CERTIFICATE

I hereby certify that I have read the thesis titled 'Infrared Spectroscopy of Molecular Solids under Extreme Conditions' by Himal Bhatt. This thesis has been prepared, compiled and completed under my supervision.

Surendra M Sharma

(S. M. Sharma)

Guide

# STATEMENT BY AUTHOR

This dissertation has been submitted in partial fulfillment of requirements for an advanced degree at Homi Bhabha National Institute (HBNI) and is deposited in the Library to be made available under rules of the HBNI.

Brief quotations from this dissertation are permissible without special permission, provided that the source is appropriately acknowledged. Requests for permissions for extended quotation from or reproduction of this manuscript in part or in whole may be granted by the Competent Authority of HBNI when in his or her judgement the proposed use of the material is in the interests of scholarship. In all other instances, however, permission must be obtained from the author.

Himal Bhatt

# DECLARATION

I hereby declare that the investigations presented in this thesis have been carried out by me. The work is original and has not been submitted earlier as a whole or in part for a degree/diploma at this or any other Institution/University.

Himal Bhatt

# List of Publications arising from the thesis

## List of Publications relevant to this thesis: 21

### Refereed Journals: 8 (6 published; 2 completed)

1. Proton transfer aiding phase transitions in oxalic acid dihydrate under pressure.
   Himal Bhatt, A. K. Mishra, Chitra Murli, Ashok K. Verma, Nandini Garg, M. N. Deo and Surinder M. Sharma; Physical Chemistry Chemical Physics, 2016, 18, 8065-8074

2. Hydrogen bond symmetrization in Glycinium oxalate under pressure.
   Himal Bhatt; Murli, Chitra; Mishra, A. K.; Verma, Ashok K.; Garg, Nandini; Deo, M. N.; Chitra, R. and Surinder M. Sharma; The Journal of Physical Chemistry B, 2016, 120 (4), 851-859

3. High pressure phase transformations in Bis(glycinium)oxalate - an infrared absorption study.
   Himal Bhatt, C. Murli, N. Garg, M. N. Deo, R. Chitra, R. R. Choudhury and Surinder. M. Sharma; Chemical Physics Letters, 2012, 532, 57

4. Effects of calcination on microscopic and mesoscopic structures in Ca- and Sr-doped nano-crystalline lanthanum chromites.
   Himal Bhatt, J. Bahadur, M.N. Deo, S. Ramanathan, K.K. Pandey, D. Sen, S. Mazumder, Surinder M. Sharma; Journal of Solid State Chemistry, 2011, 184/1, 204-213

5. Effect of deuteration: A new isotopic polymorph of Glycine silver nitrate.
   R.Chitra et al. including H. Bhatt; Journal of Molecular Structure, 2013, 1049, 27-35

6. A synchrotron infrared absorption study of pressure induced polymerization of acrylamide.

Himal Bhatt, M.N. Deo; Spectrochimica Acta Part A: Molecular and Biomolecular Spectroscopy (ICOPVS), 2017, In Press

**Completed:**

1. Optical design, installation and first results of Infrared beamline at Indus-1 synchrotron source.
2. Dielectric and low temperature properties of Bis(glycinium)oxalate.

**AIP (American Institute of Physics) Proceedings: 4**

1. A Temperature Dependent Infrared Absorption Study of Strong Hydrogen Bonds in Bis(glycinium)oxalate
   Himal Bhatt, M.N. Deo, C. Murli, S.R. Vishwakarma, R. Chitra, S.M. Sharma; AIPC 1731 (2016) 040018

2. Spectroscopic Studies of Glycinium oxalate under Pressure
   Himal Bhatt, C.Murli, N.Garg, A.K. Mishra, M.N. Deo and S.M. Sharma; AIPC 1591(2014) 230

3. Hydrogen bonds in a-Oxalic Acid Dihydrate-A Raman Spectroscopic Study
   A. K. Mishra, H. Bhatt, Chitra Murli and Surinder M. Sharma; AIPC 1591 (2014) 136

4. High Pressure Infrared Reflectivity measurements on Copper doped Ru1212
   Himal Bhatt, S.Karmakar, M.N. Deo, M.R. Gonal, N.Patel, S.M.Sharma; AIPC 1512 (2013) 854

**Conference Papers: 9**

1. Infrared spectroscopy of molecular solids under extreme conditions
   Himal Bhatt, Thesis Category, DAE Solid State Physics Symposium, 2016, Bhubaneshwar, India.

2. Proton dynamics of strong hydrogen bonds in amino acid complexes under pressure
   Himal Bhatt, M. N. Deo, ICOPVS, 2016, Lucknow, India.

3. Spectroscopy of Strong Hydrogen Bonds in Molecular Solids under Pressure - a case of glycine and oxalic acid family

   Himal Bhatt, M.N. Deo, C.Murli, A.K. Mishra, Ashok K. Verma, N.Garg, R.Chitra, S. M. Sharma; Accepted, COMPEC (Apr. 2016), Mumbai, India.

4. A new Infrared beamline at Indus-1 Synchrotron for in-situ high pressure studies

   Himal Bhatt, M.N. Deo, S.R. Vishwakarma, S.K. Deb, R.J. Kshirsagar and Surinder M. Sharma; Abstract book, Young Materials Researchers Meet, Mat. Res. Soc. India (Nov.2014), at IIT Mumbai, India.

5. Optical Conductivity studies on Copper doped Ru1212 at high pressure

   Himal Bhatt, M. N. Deo, S. Karmakar, M. R. Gonal, N. Patel and Surinder M. Sharma; Abstracts book, WIRMS 2013 (10-14 Nov.) at Lorne, Melbourne, by Australian Synchrotron

6. Short Hydrogen bond in Bis(glycinium)oxalate under pressure-an Infrared Absorption study

   Himal Bhatt, Nandini Garg, Chitra Murli, M.N. Deo, R. Chitra and Surinder M. Sharma,; Int. Conf. High Pressure Science & Techn. (AIRAPT23) Sep.2011, p180 (O44) at Mumbai, India

7. Effects of sintering temperatures on Ca- and Sr- doped Lanthanum Chromites: studied by FTIR spectroscopy

   Himal Bhatt, M. N. Deo, S. Ramanathan and Surinder M. Sharma; Proceedings of the 54th DAE Solid State Physics Symposium (2009), p.431, Vadodara, India

8. Infrared Beamline at INDUS-1 Synchrotron Radiation Source

   Himal Bhatt, S.K. Deb, R.J. Kshirsagar, M.N. Deo, S.M. Sharma, P. Dumas and V.C. Sahni; 2nd Asia-Oceania Forum for Synchrotron Radiation Research (2007); p. IV-2 at Hsinchu, Taiwan.

9. Beam Propagation Simulations for the new Infrared Beamline at INDUS-1

   Himal Bhatt, S.K. Deb, S.M. Sharma and V.C. Sahni; 52nd DAE Sol. St. Phys.

Symp.(2007)430, Mysore, India.

**Oral presentations in international conferences: 7**

1. Int. Conf. on Perspectives of Vibrational Spectroscopy, ICOPVS 2016, Lucknow, India.
2. DAE Solid State Physics Symposium, 2016, Bhubaneshwar, India.
3. Workshop on Infrared Spectroscopy and Microscopy using Accelerator based sources (WIRMS) 2013, Australian Synchrotron at Lorne, Melbourne, Australia.
4. Int. Conf. on High Pressure Science & Technology (AIRAPT23) 2011, 180 (O44), Mumbai.
5. Int. Conf. on Perspectives of Vibrational Spectroscopy, ICOPVS 2010, BHU, Varanasi, India.
6. Emerging Trends in Laser & Spectroscopy and Applications MMSETLSA-2009 Allahabad.
7. 2nd Asia-Oceania Forum for Synchr. Radiation Research (2007); at Hsinchu, Taiwan.

**Awards:**

1. Best PhD Thesis Award, DAE Solid State Physics Symposium Dec-2016 Bhubaneshwar
2. DAE - Young Applied Scientist Award, 2015, BARC, Mumbai
3. Student Award at WIRMS 2013, Australia
4. 'Outstanding Oral Presentation' award at 2nd AOFSRR, Hsinchu, Taiwan
5. Poster award at 2nd AOFSRR, Hsinchu, Taiwan

## List of publications other than the thesis work, using the facility developed: 24

1. BO and TeO speciation in bismuth tellurite and bismuth borotellurite glasses by FTIR, $^{11}$B MAS-NMR and Raman spectroscopy
   Amandeep Kaur, Atul Khanna, Himal Bhatt, Marina Gónzález-Barriuso, F. González, B. Chen,M. N. Deo; Journal of Non-Crystalline Solids, In Press (2017)

2. Effect of gamma irradiation on the ion exchange capacity of polyaniline
   P.S R. Devi, Himal Bhatt, M.N. Deo, Rakesh Verma, A.V.R. Reddy; Radiation Physics and Chemistry 96 (2014) 7-80

3. Structural and optical investigations of Fe1.03Se0.5Te0.5 under high pressure
   Pallavi S. Malavi, S. Karmakar, N. N. Patel, Himal Bhatt and Surinder M. Sharma; J. Phys.: Condens. Matter 26 (2014) 125701-8

4. High Pressure structural and vibrational properties of the spin-gap system Cu2PO4(OH)
   Pallavi S. Malavi, S. Karmakar, D. Karmakar, A. K. Mishra, Himal Bhatt, N. N. Patel, and Surinder M. Sharma; J. Phys.: Condens. Matter, 25 (2013), 045402 1-10

5. Control of Buckling in Colloidal Droplets during Evaporation-Induced Assembly of Nanoparticles
   J. Bahadur, D. Sen, S. Mazumder, B. Paul, Himal Bhatt and S. G. Singh; Langmuir 28 (2012) 1914-1923.

6. One-Step Fabrication of Thermally Stable TiO2/SiO2 Nanocomposite Microspheres by Evaporation-Induced Self-Assembly
   J. Bahadur, D. Sen, S. Mazumder, P. U. Sastry, B. Paul, Himal Bhatt, and S. G. Singh; Langmuir, 28(2012), 11343-11353

7. $\alpha-$glycine upto 4.2K - a far IR absorption study
   Naini Bajaj, Himal Bhatt, S. R. Vishwakarma, R. Chitra, C. Murli, M. N. Deo;

ICOPVS (2016), Lucknow, India.

8. Observation of a hot molecular band in difluoromethane
   C. Ashok, Himal Bhatt, S. R. Vishwakarma, M. N. Deo; ICOPVS (2016), Lucknow, India.

9. High Pressure Raman Spectroscopic Studies of Pt(II) Complex trans-PtCl2(PEt3)2
   Naini Bajaj, H.K. Poswal, Himal Bhatt, M.N. Deo, Surinder M. Sharma; AIPC 1731 (2016) 090031.

10. FT-Raman spectroscopy of structural isomers of Pt(II) complex PtCl2(PEt3)2
    Himal Bhatt, M.N. Deo, S. R. Vishwakarma, Naini Bajaj and Surinder M. Sharma; AIPC 1665 (2015) 090045(1-3).

11. Hydroxycarbonated Neodymium Sesquioxide under Pressure: An Infrared Study
    Himal Bhatt, N. Garg, M. N. Deo and K.K. Pandey; AIPC 1447 (2012) 107-108.

12. Far Infrared Absorption Study of BiFeO3 and the Effects of Cobalt Doping
    Himal Bhatt, B.P. Mandal, M.N. Deo, A.K. Tyagi and S.M. Sharma; AIPC 1349 (2011) 879-880.

13. Infrared Reflectivity Studies On Composite HfO2/SiO2 Thin Films
    Himal Bhatt, M.N.Deo, N.K.Sahoo, N.Kamble, R.B. Tokas, S.Thakur; AIPC 1313 (2010),343-345

14. High Resolution Infrared Spectroscopy of nu1 band of Difluromethane-d2 (CD2F2)
    Himal Bhatt, ParamJeet Singh, Naveen Kumar, M.N. Deo, K. Kawaguchi Book chapter in "Emerging Trends in Laser & Spectroscopy and Applications", ed. Rai, Das, Uttam, Allied Publishers Pvt. Ltd., pp. 297-301. ISBN: 978-81-8424-626-1, 297-301.

15. Effect of pressure on the metal-ligand vibrations of Pt(II)Cl2(PEt3)2 isomeric complexes - a Raman Spectroscopic study

Naini Bajaj, Himal Bhatt, H. K. Poswal, M. N. Deo and Surinder M. Sharma; accepted- Condensed Matter Physics under Extreme Conditions (COMPEC)2016, Mumbai, India

16. Measurements and Analysis of Hyperfine Structure of Atomic Iodine using High Resolution Fourier Transform Spectroscopy

    Ashok Chilukoti, S. R. Vishwakarma, Himal Bhatt, B. K. Ankush and M. N. Deo; Presented at 'Light Quanta: Modern Perspectives and Applications' (2015) - Allahabad University

17. FT-Raman spectroscopy of Pt(II) complex PtCl2(PEt3)2

    Himal Bhatt, M.N. Deo, S. R. Vishwakarma, Naini Bajaj and Surinder M. Sharma; Abstract book, DAE SSPS, held at VIT University, (Dec. 16-20, 2014) 223-224, Vellore, India

18. Composition dependent structural variations in HfO2/SiO2 composite films

    Himal Bhatt, N.K. Sahoo, M.N. Deo, N.C. Das, S.Thakur, S. Hazra, J.K. Bal and S. M. Sharma; 12th Int. Conf. Surf. X-ray and Neutron Scat.(SXNS-2012), SINP, Kolkata, India; p.127.

19. High pressure IR measurements of Ru1212

    Himal Bhatt, S. Karmakar, M.N. Deo, M.R. Gonal, N. Patel and Surinder M. Sharma; Abstracts, 57th DAE State Solid State Physics Symposium (2012) page-177 at IIT Bombay

20. Far Infrared Absorption study of BiFeO3 and the Effects of Cobalt Doping

    Himal Bhatt, B.P. Mandal, M.N. Deo, A.K. Tyagi and Surinder M. Sharma; Book of Abstracts, 55th DAE Solid State Physics Symposium, Dec.26-30 2010, 272

21. FTIR investigation of spray dried self-assembled grains of silica nanoparticles

    Himal Bhatt, M.N. Deo, J. Bahadur, D. Sen and Surinder M. Sharma; Int. Conf. on Perspectives in Vibrational Spectroscopy, ICOPVS (Feb. 21-24, 2010), p.64.

22. The $\nu_6$ band of Difluoromethane: studied by High Resolution Infrared Spectroscopy

    ParamJeet Singh, Himal Bhatt, M.N. Deo and K. Kawaguchi; Int. Conf. on Perspectives in Vibrational Spectroscopy, ICOPVS (Feb. 21-24, 2010), p.91.

23. IR Reflectivity of Composite HfO2/SiO2 Thin Films

    Himal Bhatt, M.N. Deo, N.K. Sahoo, N.M. Kamble, R.B. Tokas, S. Thakur; Abstracts book, Int. Conf. on Physics of Emerging Functional Materials, Sep. 22-24(2010), p.120

24. High Resolution Fourier Transform Infrared Spectroscopy of $\nu_1$ band of Difluoromethane

    Himal Bhatt, ParamJeet Singh, Naveen Kumar, M.N. Deo, K. Kawaguchi; Abstracts; Emerging Trends in Laser & Spectroscopy and Applications, MMSETLSA-2009 p.205

Himal Bhatt

**Dedicated**

to

**My Grandmother**

# ACKNOWLEDGEMENTS

Any joy, happiness and satisfaction that have emerged in bringing my work to some meaningful level are because of some extraordinary people around me.

At the outset, I am grateful to my supervisor Prof. Surinder M. Sharma to extract a physicist out of me. His foresight, fine understanding and sharp observations were instrumental in finding various solutions. It is also a great pleasure to thank my mentor Dr. M. N. Deo, who guided me in spectroscopy and supported in all the scientific and technical difficulties. I especially thank my doctoral committee members Prof. S. K. Deb, Prof. D. K. Aswal and Prof. Sanjay Wategaonkar not only for their scientific suggestions and guidance, but also for the personal affection and care they took to ensure that I grow in the right direction.

I owe a substantial part of the knowledge on molecular solids to Dr. Chitra Murli, who never lost patience and enthusiasm, even while we were driving on the rough roads and solutions were hiding in the dark. I thank my collaborators Dr. Nandini Garg and Dr. Ajay K. Mishra for their extensive support in experiments and analysis which helped me learn high pressure technique; Dr. R. Chitra for her help in preparing the crystals and Dr. S. Karmakar, Dr. Andrea Perucchhi for the help in IR experiments at Elettra. I am indebted to Dr. Ashok K. Verma for his great help in carrying out first principles calculations and critically reviewing my various drafts. I also wish to thank Dr. N. K. Sahoo who has been a constant motivator ever since I started my research career. I am also grateful to Dr. Paul Dumas and Dr. R. J. Kshirsagar for the help and suggestions at various times.

Next, I wish to thank my lab colleagues Nitya, Shiv, Naini, Naveen, Ashok, Shri Rajiv Sinha, Dr. D. Lahiri for maintaining a lively environment which help each of us work hard with great joy. Special thanks to Shiv for standing by me through long and tiring sessions of beamline installation, in the sleepless nights of optical alignment and experiments. I am thankful to Dr. Susy Thomas, my

close friends Lucky, Deepak Pandit, Rahul, Ravindra, Deepak Mehra, Aravind, Jitendra, Manoj, Praveen, Keshar, Kavita, Nivedita, Komila, Richa, Bhumika and my batchmates at BARC for the much needed encouragement and care.

I thank Dr. K. K. Pandey and Dr. D. Sen for their help with X-ray and neutron experiments and my colleagues and seniors for valuable inputs. I would like to especially thank Dr. V. N. Rai, Shri V. Prasad, Shri S. Chouksey, Shri Akashdeep Garg, Shri Arvind Padiyar, Shri Ashok Kumar, Shri Nilesh, Shri Rahul Singh, Shri G. Mundra and Dr. P. D. Gupta at RRCAT, Indore for their support during beamline installation. Thanks is also due to Shri Surendra Patil, staff members of Indus control room, health physics unit, Indus workshop, HP&SRPD office, transport and security sections of RRCAT and BARC.

I take this opportunity to thank my teachers, right from class X to post graduation, wherever they are, to channelize my existence to this path in life. I am blessed with a wonderful set of people in life my grandmother Smt. Jayanti Bhatt, uncle and aunty Shri K. C. Bhatt and Smt. Manorama Bhatt, siblings Devesh, Durva, Tanay, in-laws Shri N. C. Joshi, Smt. Chandra Joshi, Gaurav and Nisha; whose constant support and love always motivates me.

Heartiest congratulations to my mother, father, wife and brother for I finally finished my thesis; they were far more anxious and worried for me, my work and scientific endeavour. I am what my parents have made me and every good work that emerges from my understanding goes to their credit. I am grateful to my daughter and friend Varidhi to make life so beautiful. Thanks to the rock solid support of Shailu and Ayushi. Words have always been insufficient to express my gratitude to Himali for what she has been to me in all these years. She constantly pushed me to complete the work and helped me compile my thesis. I do take this opportunity to thank her, the soul mate, for pivoting around me, caring and giving strength for whatever I do; this is for you.

# Contents

# Synopsis

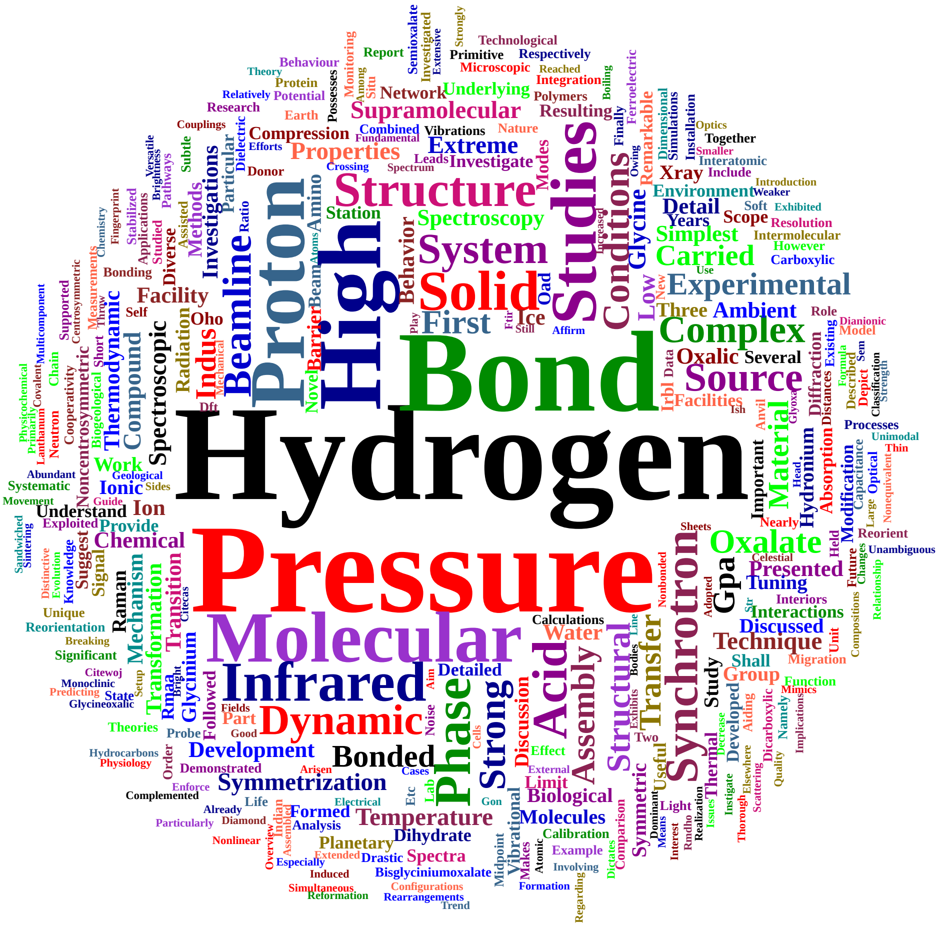

“Wordcloud” of keywords. Size of word represents number frequency.

# Synopsis

Molecular solids represent materials forming fundamental building blocks They are held together by weak intermolecular forces, viz. hydrogen bonds, which play a decisive role in their structural stabilization and hence are also referred to as soft materials. These soft molecular systems are abundant in planetary gases and ices. Thus, the underlying hydrogen bonding interactions may also be important in the assembly of organic matter under extreme thermodynamic conditions prevailing in primitive earth, planetary interiors and extra celestial bodies [1]. Despite being a much weaker bond than other chemical bonds, hydrogen bonds guide various unique physical, biological and chemical properties of molecular solids, for example unusual melting/boiling points and remarkable flexibility to form self assembled supramolecular structures - a path adopted by nature for bio-synthesis [2]. Thus, owing to their high compressibility, molecular solids provide an excellent platform for detailed investigations on the relationship between physico-chemical properties and molecular structure. In this context, compression studies using high pressure and low temperature provide a means to probe large changes in intermolecular interactions as a function of inter-atomic separations.

High pressure studies of hydrogen bonded molecular solids are also important to understand the proton dynamics across the barrier, which in turn dictates the structural relaxation mechanism; and explore new polymorphic structures through tuning of hydrogen bonds. However, the behavior of strong hydrogen bonds in the symmetrization limit ($d_{\mathrm{O{-}{-}O}} \sim 2.4$ Å in $\mathrm{O{-}H{-}{-}{-}O}$) under pressure has remained elusive. Upon compression, these bonds can reorient to enforce drastic or subtle structural transitions, induce proton migration through the potential barrier or depict a rare symmetric unimodal potential well at bond centre. For example, at high pressures, the structure of "non-molecular" phase of water ice (at $\sim$ 100 GPa) is stabilized by a symmetric hydrogen bond formed through "translational proton tunnelling" [3,4]. Though, ice, the simplest hydrogen bonded molecular solid has been investigated extensively over the years [5], the knowledge on proton dynamics of biological and geological systems in nature is still limited because of their complex structures with multiple hydrogen bonds in a diverse chemical environment.

The strong hydrogen bonded glycine (the simplest amino acid) and oxalic acid (the simplest dicarboxylic acid) complexes are model systems to understand intricate multi-component bio-geological systems [6–9] . Microstructural investigations of these systems would be very useful to look for any systematic trend which can be exploited for predicting structural properties of these compounds if the thermodynamic variables, viz. pressure, temperature or chemical compositions, are altered. Further, the study of underlying mechanism of proton dynamics may shed light on the proton transfer pathways in protein environments and molecular theories of ionic systems under extreme conditions [10–13]. The hydrogen bonded networks in these materials are also ideal to look for novel configurations like dynamic polymers [14] through hydrogen bond assisted supramolecular assembly [15] and structures with technological applications in non-linear optics, ferroelectricity etc.

However, to investigate the proton dynamics of molecular solids in the symmetrization limit, the monitoring of hydrogen positions at high pressures is very difficult using structural methods like X-ray and neutron diffraction, which makes vibrational spectroscopy, in particular infrared (IR) spectroscopy, the preferred technique to probe the hydrogen motion under pressure. Due to the distinctive spectroscopic imprints of chemical groups, vibrational couplings, electronic excitations, hydrogen bonds, combination/overtone modes and lattice vibrations, IR spectroscopy is among the most powerful techniques to study the modifications in the microscopic structure, though it makes the IR spectra of molecular solids very complex, especially in the fingerprint region. The in-situ high pressure IR studies, with specimen of the order of tens of microns sandwiched between a pair of diamond anvils, require a bright and intense source to acquire high quality spectroscopic data with good signal to noise ratio. In recent years, the importance of infrared synchrotron radiation emitted from electron storage rings has been realized which offer several orders of magnitude higher brightness than the existing sources, thus significantly enhancing the signal to noise ratio in high pressure experiments, particularly if the sample sizes are much smaller than $\sim 100\mu$m.

**Hence, the aim of this thesis is to investigate the high pressure behavior**

**of molecular solids, namely oxalic acid and glycine complexes, and development of experimental facilities, in particular an infrared beamline (IRBL) at the Indian synchrotron radiation source, Indus-1.** Both the works, i.e. high pressure studies of the above molecular systems and development of IR beamline were taken up in parallel. The diverse high pressure behaviors exhibited by this family of molecular solids have been demonstrated, which range from "hydrogen bond symmetrization" and "proton transfer" to "structural phase transition" involving dielectric anomaly and supramolecular assembly. First results from the infrared beamline facility have also been presented.

Chapter1. Introduction: In this chapter, the physics of molecular solids, their classification, technological applications, self assembly mechanisms and the role of strong hydrogen bonding in stabilizing the three dimensional network shall be discussed. A detailed literature survey on proton dynamics in strong hydrogen bonds will be presented along with its implications on the overall structure. In this line, the benchmark cases of ice, formic acid and oxalic acid dihydrate will be discussed in detail. This is followed with the discussion on diverse high pressure behaviours of amino acid, in particular glycine complexes, under high pressures showing subtle to drastic structural rearrangements. Further, in addition to the discussion on suitable techniques for these studies, the recently evolved fields of synchrotron based X-ray and infrared techniques, are also discussed. Finally the scope of the thesis is presented.

Chapter2: Experimental details, facility development and synchrotron infrared beamline: This chapter is divided into two parts, namely (i) Methods and (ii) development of a synchrotron infrared beamline at Indus-1. In the first part, sample preparation details, experimental techniques and theoretical tools used for high pressure studies shall be presented. The work carried in this thesis is primarily based on infrared studies which are well complemented by simultaneous Raman spectroscopic measurements combined with first principles DFT calculations and X-ray diffraction studies. Detailed theory of vibrational spectroscopy and instruments based on Fourier Transform interferometry are discussed. This is followed by the discussion on high pressure generation techniques and pressure calibration methods. Finally, an overview of data analysis methods is described. In the second part, comprehensive details of various experimental facilities developed for spectroscopic studies at ambient, high pressure and low temperature conditions shall be described. In all, three major facilities have been setup during the course of this work which include a versatile low resolution FTIR lab employing thermal as well as synchrotron source, a high resolution FT based integrated laboratory for ro-vibrational and atomic spectroscopy from far IR to UV and a FT-Raman facility. The design of the synchrotron IR beamline was carried out based on extensive beam extraction and beam propagation simulations. Properties of the infrared radiation as extracted from Indus-1, details of optical and mechanical assembly of the beamline, complete installation report and integration with the experimental station will be presented.

Chapter3. High pressure investigations of Oxalic Acid Dihydrate (OAD) - proton transfer aiding phase transitions: OAD, the simplest dicarboxylic acid complex and an important molecular solid in crystal chemistry, ecology and physiology, is being studied for nearly 100 years now. Its formula unit $(H_2O)((COOH)_2)(OH_2)$ is formed through two very strong hydrogen bonds (O---O $\sim$ 2.49 Å) between OA and water on both sides under ambient conditions. Most of the debated issues regarding its proton dynamics have arisen due to these unusually short hydrogen bonds. Though, several efforts have been made in the past to understand the behavior of proton across the barrier, unambiguous experimental evidences have never been reported which can affirm the thermodynamic conditions of the possible proton transfer or symmetrization of the hydrogen bond. Using combined in-situ spectroscopic studies and first-principles simulations at high pressures, we could show that the structural modification associated with this hydrogen bond is much more significant than ever assumed. Upon compression, this compound first shows proton migration along the strong hydrogen bond at very low pressures of 2 GPa. This results in the protonation of water with systematic formation of dianionic oxalate and hydronium ion motifs, thus reversing the hydrogen bond hierarchy in the high pressure phase II. The resulting hydrogen bond between hydronium ion and carboxylic group shows remarkable strengthening under pressure, even in the pure ionic phase III. Note that, due to donor as well as acceptor capabilities of water in the ambient phase, OAD exhibits alternate hydrogen bonded spiral chain structure resulting in added strength of various hydrogen bonds through the cooperativity effect. Upon proton transfer, the cooperativity effect is lost as the hydronium ion only acts as a donor of hydrogen bonds. This leads to another phase transition at $\sim$ 9 GPa to phase IV through reorientation of hydrogen bonds. It was observed that phase IV is stabilized by a strong hydrogen bond between the dominant $CO_2$ and $H_2O$ groups of oxalate and hydronium ions respectively. These findings suggest that oxalate systems may provide useful insights on proton transfer reactions and assembly of simple molecules under extreme conditions.

Chapter4. High pressure studies on glycinium oxalate - pressure induced hydrogen bond symmetrization aiding supramolecular assembly: Glycinium oxalate (GO; glycine:oxalic acid :: 1:1), the simplest amino acid- carboxylic acid complex possesses a nearly linear and strong O–H---O hydrogen bond ($d_{\text{O---O}}\sim$ 2.54 Å, $d_{\text{H---O}}\sim$ 1.6 Å and $\angle$OHO = 177°) between semioxalate molecules in a columnar arrangement along the *b*-axis. Our high pressure infrared and Raman spectroscopic investigations suggest a dynamic proton sharing along this strong hydrogen bond, which mimics the proton being at the mid-point and thus implying a symmetric state above very low pressure of 8 GPa. These observations are well supported by DFT based molecular dynamics calculations which have confirmed the movement of proton towards the bond mid-point under pressure and significant probability of crossing the barrier above 8 GPa through proton hopping. These semioxalate ($HC_2O_4$) columns hold the head to tail linked glycine ($NH_3CH_2COOH$) sheets in the *ac*-plane via other hydrogen bonds to form the three dimensional network. At pressures above 12 GPa, the glycine units systematically reorient to form hydrogen bonded supramolecular assemblies held together by the infinite symmetric hydrogen bonded oxalate chains.

Chapter5. High Pressure Phase Transformations in Bis(glycinium)oxalate: BGO (gly:oxa::2:1) also possesses a very short and strong O–H---O hydrogen bond (O–H=1.165 Å, H---O=1.3 Å and $\angle$OHO = 174.2° between glycinium and oxalate ions at ambient conditions. The distances between several non-bonded atoms in this compound are close to the steric limits. It crystallizes in a centrosymmetric monoclinic structure with space group $P2_1/n$. Our high pressure infrared absorption studies on BGO, suggest breaking and reformation of hydrogen bonds resulting in phase transformations across 1.6 and 4.5 GPa. The appearance of Raman active modes in the infrared spectra above 1.6 GPa confirms that glycine molecules become non-equivalent above this pressure leading to loss of centre of symmetry and hence a non-centrosymmetric high pressure phase is formed. The results are validated with the high pressure Raman and X-ray diffraction studies. As phase transformation to non-centrosymmetric structure may instigate ferroelectric properties, we have also investigated the dielectric behaviour of this compound. High pressure capacitance measurements were carried out using the Bridgman Anvil device and it was found that the electrical capacitance, which initially increased under pressure, reached a maximum near the phase transition beyond which it showed a monotonic decrease. The studies have been extended to investigate the low temperature behavior of structure and hydrogen bonds.

Chapter6. First results from the IRBL facility developed at Indus-1: In this chapter, we present the utility demonstration of the newly developed IRBL facility at Indus-1 by sequentially listing the first studies carried out using thermal source as well as synchrotron source on various materials in absorption, reflection and microscopy modes for microstrucutral, optical and morphological properties respectively. A thorough infrared synchrotron beam diagnostic analysis has been carried out and a comparison of synchrotron source at Indus-1 with thermal source as well as already existing beamlines elsewhere has been elucidated. During the installation of experimental station, the first studies using lab source were carried out on an inorganic system (lanthanum chromite) as it depicts a relatively simpler IR spectrum with three clear absorption bands. The compound chosen is used as an interconnect material in solid oxide fuel cells. The modifications in its microscopic structure as a function of calcination temperature were studied through internal and external molecular vibrations. These studies have revealed a novel liquid state assisted sintering mechanism of this compound at temperatures near 900°C and the results are well supported by XRD, SEM and small angle neutron scattering studies. After the integration of beamline with experimental station, the above infrared spectra were also used for comparison of signal levels using the synchrotron source and monitoring the spectral calibration. This was followed by the use of IRSR for high pressure studies inside DAC and the first of such investigations were carried out on a molecular solid Acrylamide.

Chapter7. Summary and future scope: In this chapter, we summarize the main conclusions of the thesis. It has been conclusively demonstrated that tuning of the interatomic distances in the strongly hydrogen bonded molecular solids leads to novel phase transformations, which are of interest to basic as well as applied research. The unique results of proton transfer in oxalic acid dihydrate, hydrogen bond symmetrization in glycinium oxalate and hydrogen bond reorientation in bis(glycinium)oxalate would be helpful in understanding the structural assembly of simple molecules under extreme thermodynamic conditions, which may be utilized to improve our knowledge on the evolution of life in primitive earth, planetary interiors or extra-terrestrial systems. The underlying mechanism of proton dynamics in these complexes may throw light on the proton transfer pathways in protein environments, biological processes like enzymatic catalysis and molecular theories of ionic systems under extreme conditions. Thus simple oxalate complexes, in various ionic forms, with remarkable sensitivity to pressure tuning at moderate pressures can be exploited as model systems to study proton dynamics in various bio-geological processes. Our reports of supramolecular assembly in GO and transformation to a non-centrosymmetric structure in BGO through tuning of hydrogen bonds under pressure are also of relevance to dynamic polymers with non covalent interactions and realization of new ferroelectric materials. Further, this thesis also includes the development of first infrared beamline at the Indian synchrotron radiation source, Indus-1, which would be immensely useful to study various materials including molecular solids, biological samples, thin films etc. under ambient and extreme thermodynamic conditions. This chapter is concluded by the discussion on future scope of the research works on molecular solids as well as synchrotron infrared beamline.

# References

[1] H. Bhatt, C. Murli, A. K. Mishra, et al. "Hydrogen Bond Symmetrization in Glycinium Oxalate under Pressure". *J. Phys. Chem. B*, **120(4)**, 851–859 (2016).

[2] M. Burns, S. Essafi, J. R. Bame, et al. "Assembly-line synthesis of organic molecules with tailored shapes". *Nature*, **513**, 183–188 (2014).

[3] M. Benoit, D. Marx, and M. Parrinello. "Tunnelling and zero-point motion in high-pressure ice". *Nature*, **392**, 258–261 (1998).

[4] V. V. Struzhkin, A. F. Goncharov, R. J. Hemley, et al. "Cascading Fermi Resonances and the Soft Mode in Dense Ice". *Physical Review Letters*, **78**, 4446–4449 (1997).

[5] Y. Huanga, X. Zhang, Z. Maa, et al. "Hydrogen-bond relaxation dynamics: Resolving mysteries of water ice". *Coordination Chemistry Reviews*, **285**, 109 – 165 (2015).

[6] N. Casati, P. Macchi, and A. Sironi. "Hydrogen migration in oxalic acid di-hydrate at high pressure?" *Chem. Commun.*, pp. 2679–2681 (2009).

[7] H. Bhatt, C. Murli, N. Garg, et al. "High pressure phase transformations in Bis(glycinium)oxalate - an infrared absorption study ". *Chem. Phys. Lett.*, **532**, 57–62 (2012).

[8] B. A. Zakharov and E. V. Boldyreva. "A high-pressure single-crystal to single-crystal phase transition in DL-alaninium semi-oxalate monohydrate with switching-over hydrogen bonds". *Acta Cryst. B*, **69(3)**, 271–280 (2013).

[9] A. F. Goncharov, M. R. Manaa, J. M. Zaug, et al. "Polymerization of Formic Acid under High Pressure". *Physical Review Letters*, **94**(6), 065505 (2005).

[10] M. Heyden and D. J. Tobias. "Spatial dependence of protein-water collective hydrogen-bond dynamics". *Phys. Rev. Lett.*, **111(21)**, 218101 (1–5) (2013).

[11] H. Ishikita and K. Saito. “Proton transfer reactions and hydrogen-bond networks in protein environments”. *J. Royal Soc. Interface*, **11**, 20130518 (1–17) (2014).

[12] P. A. Sigala, A. T. Fafarman, J. P. Schwans, et al. “Quantitative dissection of hydrogen bond-mediated proton transfer in the ketosteroid isomerase active site”. *Proc. Nat. Acad. Sc.*, **110**, E2552–E2561 (2013).

[13] H. Bhatt, A. K. Mishra, C. Murli, et al. “Proton transfer aiding phase transitions in oxalic acid”. *Phys. Chem. Chem. Phys.*, **18**, 8065–8074 (2016).

[14] R. J. Wojtecki, M. A. Meador, and S. J. Rowan. “Using the dynamic bond to access macroscopically responsive structurally dynamic polymers”. *Nature*, **10(1)**, 14–27 (2011).

[15] D. M. P. Mingos. *Supramolecular Assembly Via Hydrogen Bonds* (Springer-Berlin II, 2004).

# List of Figures

# List of Tables

# 1

# Introduction

## 1.1 Overview

The history of research on molecular systems can easily be extrapolated to the mankind's first rendezvous with science, when water/ice would have been first looked into with curious thoughts. The endeavour to explore new and exciting material properties, since then, has mostly rested upon tuning the fundamental parameters like pressure, temperature or chemical composition. Among these, pressure modifies the inter-atomic separations in the most significant way without the introduction of a foreign element into the structure. The emergence of diamond anvil cells to compress the materials has taken the research of molecular solids to the next level. The discovery of synchrotron radiation as a probe and advancement of research to study technological, biological and geological systems based on the fundamental understanding on systems like ice are among the milestones in the field.

Though the phase diagram of water (Figure 1.1) depicts remarkable diversity under varying thermodynamic conditions [1–3], the knowledge on other bio-geological molecular solids in nature, which are abundant in planetary gases and ices, is still limited because of their complex structures in a diverse chemical environment. For example, glycine, the fundamental building block of proteins and the simplest amino acid, can exist in different polymorphic forms and form various linkages through hydrogen bonding, as donor as well as acceptor. Even simple carboxylic acids are intriguing, as they depict diverse behaviours under extreme conditions. While Formic acid, the simplest carboxylic acid, has been reported to polymerize under pressure [4], the proton dynamics of oxalic acid dihydrate, the simplest dicarboxylic acid complex, has been debated for nearly a century in search of the proton migration phenomenon [5].

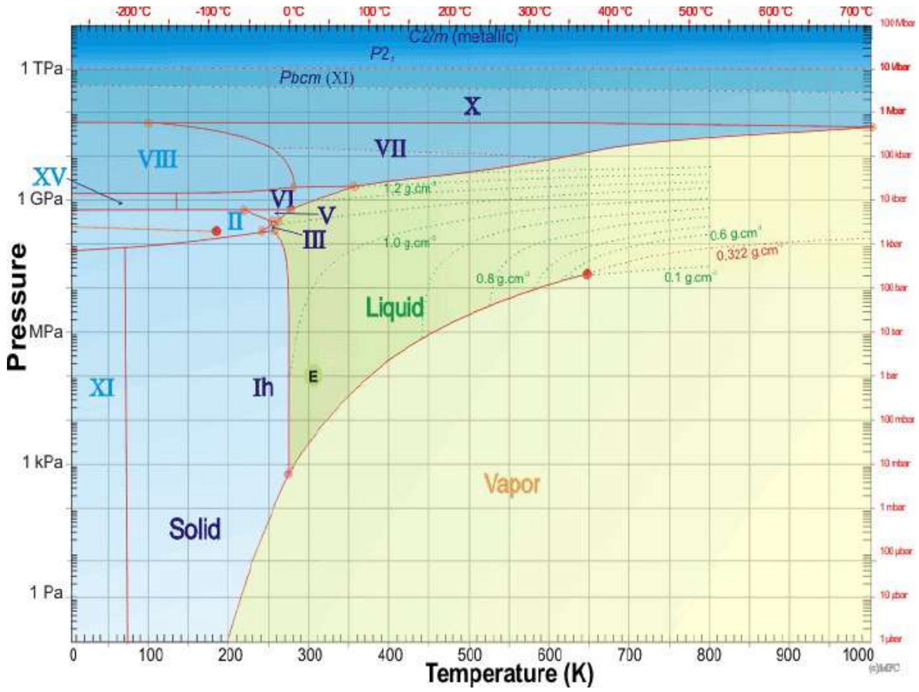

**Figure 1.1:** Phase diagram of water.
(figure taken from http://www1.lsbu.ac.uk/water/water_phase_diagram.html)

The knowledge on multi-component molecular solids is further limited by the enhanced complexities arising from inter- and intra-molecular interactions. However, simple oxalate and amino acid complexes, like oxalic acid dihydrate and glycine - oxalic acid systems have a common feature of existence of very strong hydrogen bonds even at ambient conditions. The proton dynamics of such hydrogen bonds and their influence on the three dimensional network of other hydrogen bonding interactions dictate the structural assembly and properties of molecular systems under varying thermodynamic conditions. Hence, their investigations under high pressure would be very useful to look for some systematic trend which can be exploited for predicting structural properties of large hydrogen bonded complexes under varying conditions and their influence on proton transfer processes. Due to the difficulty of structural techniques to monitor hydrogen position at very high pressures, infrared (IR) spectroscopy is the preferred technique to study proton dynamics and changes in inter/intra - molecular interactions irrespective of the crystalline form [6]. Together with the complementary techniques, viz. Raman spectroscopy, X-ray diffraction (XRD) and theory, comprehensive details of the molecular structure can be probed. The thrust areas which benefit from such research are i) technologically potential devices - ferroelectric, non-linear optic, organic semiconductors etc.; ii) synthesis of novel configurations through hydrogen bond assisted supramolecular assembly - a path adopted in nature for biosynthesis; iii) proton dynamics in complex bio-geological processes - a subject which still remains far from being well understood; and iv) exotic phases of molecular solids under extreme conditions - like metallicity, polymerization, non-molecular ices etc.

## 1.2 Strong hydrogen bonds in molecular solids

A covalent bond (X–H) is represented by an anharmonic potential. If the H atom interacts with a neighbouring atom Y through the hydrogen bond H---Y (Figure 1.2 top), the degrees of vibrational motions of proton are restricted. There are primarily three effects, i) the width of potential energy curve increases, ii) a new minima develops adjacent to this, and iii) the separation between vibrational energy levels reduces [8]. In this unsymmetrical double well potential, the two minima become more equal as the strength of the hydrogen bond increases and thus strong hydrogen bonds are depicted by a nearly symmetric double well

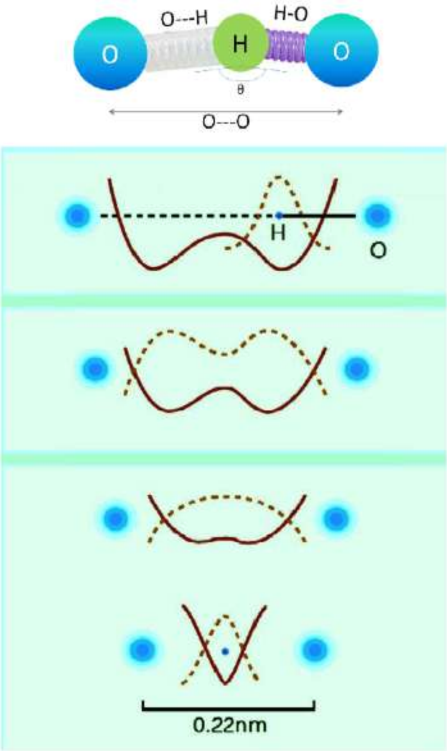

**Figure 1.2:** (Top) Spring ball model of a hydrogen bond defined by distances O-H, H---O, O---O and angle ∠OHO. (Bottom) A double well potential description of strong hydrogen bonds, dotted curves are probability [7].

potential. When the hydrogen bonds get further strengthened to approach the symmetrization limit, the height of the barrier between the two potentials and their separation get reduced and these bonds are known as low barrier hydrogen bonds (LBHB). Upon further compression, one expects hydrogen bond reorientation/ buckling/ breaking and reformation which may lead to subtle or drastic structural phase transitions. However, despite of a barrier, localized proton at the hydrogen bond centre or proton transfer through the barrier are also predicted. These are rare events and so far only in water ice at megabar pressures, the predicted unimodal potential at bond centre which depicts a symmetric hydrogen bond [9] could be experimentally probed using spectroscopy [10]. While the proton transfer can result in a reversal of hydrogen bond hierarchy, symmetric hydrogen bonds result in reduction of barrier height to negligible values, i.e. a flat potential well which from then on, tends towards a unimodal state with sharp bottom (Figure 1.2 bottom).

The potential energy of the X - H bond as a function of bond length (r) can be expanded as,

$$V(r) = V(r_{eq})+\frac{1}{1!}(\frac{\partial V}{\partial r})_{r=r_{eq}}(r-r_{eq})+\frac{1}{2!}(\frac{\partial V}{\partial r})_{r=r_{eq}}(r-r_{eq})^2+\frac{1}{3!}(\frac{\partial V}{\partial r})_{r=r_{eq}}(r-r_{eq})^3..... \tag{1.1}$$

where $r_{eq}$ is the bond length at equilibrium, the first non-zero square term represents a parabolic harmonic potential and higher order terms (from cubic) account for the anharmonicity. The most common form of the above potential is the Morse potential,

$$V(r) = D_{eq}[1 - exp(-a(r - r_{eq}))]^2 \tag{1.2}$$

where, $a$ and $D_{eq}$ describe width and depth of potential respectively. For the double minimum case, i.e. strong hydrogen bonds, a double Morse function can be used,

$$V(r) = D_{eq}exp[-2a(r - r_{eq})] - 2exp[-a(r - r_{eq})] \tag{1.3}$$

Though, several approaches have been adopted for better description of strong hydrogen bonds [11], the potential function essentially should contain the parameters of X---Y or H---Y bonds in addition to the covalent X-H bond, and can be of the following form,

$$V(r) = a_2(R)r^2 + a_3(R)r^3 + a_4(R)r^4 \tag{1.4}$$

where, $R$ and $r$ are the X----Y and X--H bond parameters respectively. $a_2$, $a_3$ and $a_4$ are coefficients which are also the functions of $R$. The first, second and third terms represent single minimum harmonic potential, asymmetry of the potential and a symmetrical double minimum potential respectively. The method usually adopted for determination of coefficients is a combined treatment of protonic potentials fitted using various bond parameters and observed vibrational stretching frequencies in conjunction with simulated broad stretching bands derived using theory. However, finding the perfect potential function which can describe all the effects and predict the molecular structure under various thermodynamic and chemical conditions is still an open problem, being of many body nature. Nonetheless, various conclusions are now available based on several investigations carried out in the past [8, 10, 11].

1. The formation of a hydrogen bond and its strengthening is reflected by the transformation of vibrational stretching mode from a sharp peak to a band and drastic red shift. Based on frequency versus bond length correlation data (Figure 1.3 ) of several hydrogen bonded species, it is observed that this red shift does not follow a linear relation with bond parameters [12,13].

2. The strengthening of hydrogen bond results in increase in anharmonicity and possible couplings of the stretching mode with other bridge vibrations (most commonly with vibrational motions related to out of plane and in plane bending) and low frequency molecular modes [10, 11, 14].

3. In the extreme case of approaching the symmetrization limit, the stretching frequency rapidly approaches zero or some minimum value where it is characterized as the soft mode, beyond which it may again increase, which may signify the onset of proton transfer state. In the symmetrization limit, the bridge vibrations are strongly damped and also interact with phonons, which may result in splitting of vibrational levels.

4. For strong hydrogen bonds, the $\angle$X-H---Y $\sim 180^\circ$, i.e. tends to be linear, which makes the X-H---Y distances a reliable measure of the hydrogen bond lengths.

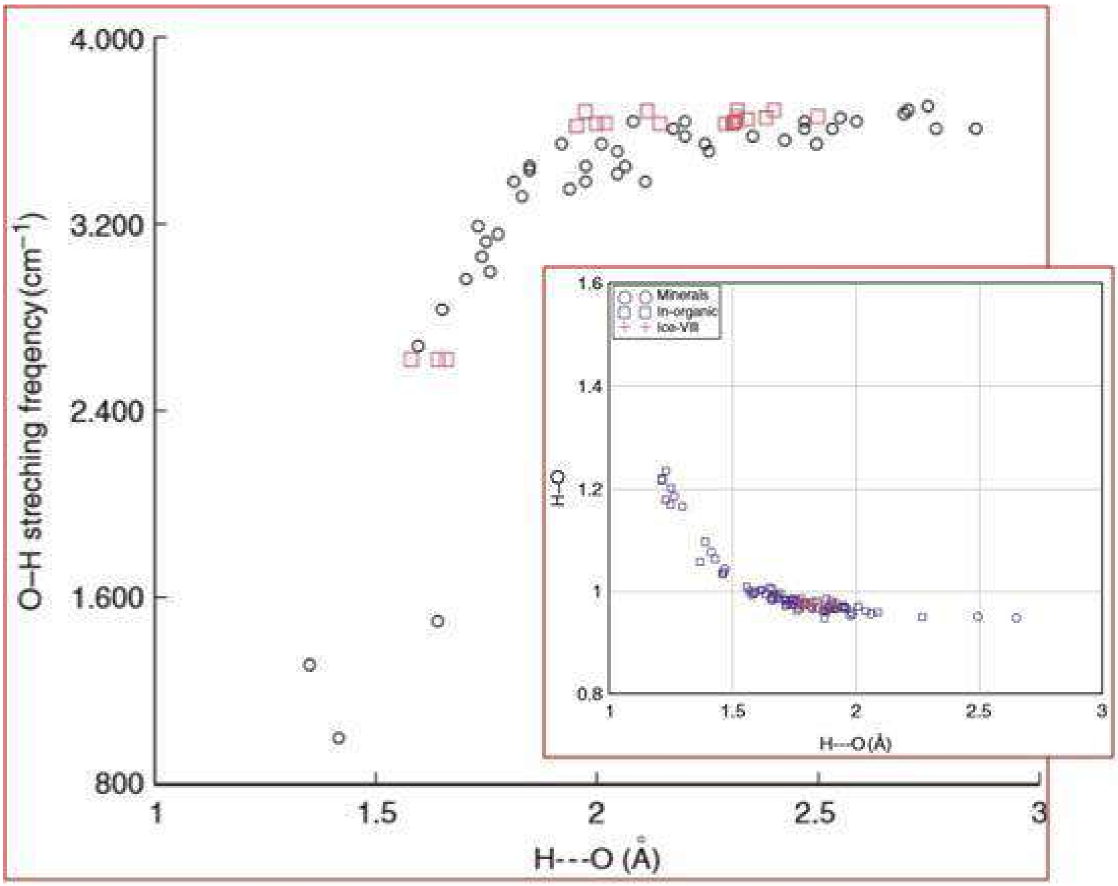

**Figure 1.3:** Covalent bond stretching frequency as a function of hydrogen bond length plotted for several hydrogen bonded materials [12], inset shows the corresponding variation in bond length.

## 1.3 High pressure effects in fundamental molecular solids

Pressure and temperature generally follow an inverse rule, i.e. an increase in pressure has the similar effects as decrease in temperature, which is the contraction of the overall system implying an increase in free energy of the system, though pressure tuning is many times as effective as temperature tuning. In physical terms,

$$P = -\frac{\partial E}{\partial V} \tag{1.5}$$

i.e., an increase in pressure leads to volume contraction and an unstable higher energy configuration. A stable structure/configuration at any given thermodynamic condition is the one which is represented by a new minimum of the Gibb's free energy G(P, T),

$$G(P,T) = H - TS = E + PV - TS \tag{1.6}$$

where $H$, $E$, $P$, $V$, $T$ and $S$ represent the system's enthalpy, internal energy, pressure, volume, temperature and entropy respectively. If under the influence of change in external pressure or temperature, the system undergoes a phase transition, the order of the phase transition is depicted by the order of the derivative of $G(P,T)$ which shows discontinuity across the transition. The process of free energy minimization, in fact, sometimes results in various unique and exciting phases of molecular solids, for example crystalline to amorphous, insulator to metal, monomer to polymer, neutral to ionic transitions and even molecular dissociation or atomization.

### 1.3.1 Homonuclear molecular solids

The hottest debates in high pressure physics begin right from the predictions of dense phases of the simplest and light homonuclear molecular solids which are bound together by weak Van der Waals forces at ambient conditions. The high pressure studies on molecular hydrogen ($H_2$) predict metallicity as well as room temperature superconductivity at very high pressures in Megabar regime [15,16]. Solid oxygen ($O_2$), on the other hand, depicts significant changes at pressures as low as 10 GPa [17–19] and the signatures of metallicity are reported at pressures just below a megabar [20–22]. In contrast, nitrogen ($N_2$), with the strongest homonuclear bond (bond energy: 945 kJ/mol), polymerizes above a megabar and 2000K [23–25]. Most recently, the reports of high temperature superconductivity in the solid hydride of sulphur at the highest temperatures so far, approaching

200 K at pressures near 150 GPa have renewed the interest in the subject [26]. Noticeably, in the relatively stronger, hydrogen bonded, molecular solids, various structural changes are observed at pressures near or even less than 1 GPa.

### 1.3.2 Vibrational energy redistribution in dense ice

Water ($H_2O$), the most fundamental hydrogen bonded molecular system, has nearly 17 known solid crystalline phases [7]. The phase diagram (Figure 1.1) shows that most of the structural variations take place in ice at pressures as low as 1 GPa or less and in the temperature range $\sim 250 - 350$ K, the conditions which are not too far from ambient. Above 2 GPa, only two phases, ice VIII and ice VII exist, of which ice VII is the room temperature high pressure structure of water. Ice VII (300 K, $P > 2$GPa) is characterized as a para-electric phase with disordered protons in the hydrogen bonded network, whereas the low temperature anti-ferroelectric ice VIII is an ordered version of VII. [27,28] Holzapfel, in 1972, used two equivalent Morse potentials to describe inter-atomic interactions in ice VII and predicted that it transforms to a symmetric hydrogen bonded state at pressures in the range 35 – 80 GPa [29]. This phase, where water becomes a non-molecular ice, is known as ice X and after the efforts of nearly 30 years, Benoit et al. could probe this phase almost precisely using molecular dynamics simulations and predicted the pressure of nearly 100 GPa for such a transition from VII $\rightarrow$ X and nearly 70 GPa from VIII $\rightarrow$ X by treating the problem quantum mechanically, i.e. introducing tunnelling effects through the potential barrier (Figure 1.4 , top) [9]. The classical treatment only increased the transition pressures. They further clarified that the phase X first exists as "proton – disordered symmetric ice", may be with a flat bottom or very small barrier, followed by the "proton – ordered symmetric ice" at higher pressures having single minimum potential with localized protons at the bond mid-point (Figure 1.4 bottom).

Experimentally, the best evidence comes from infrared spectroscopy which showed

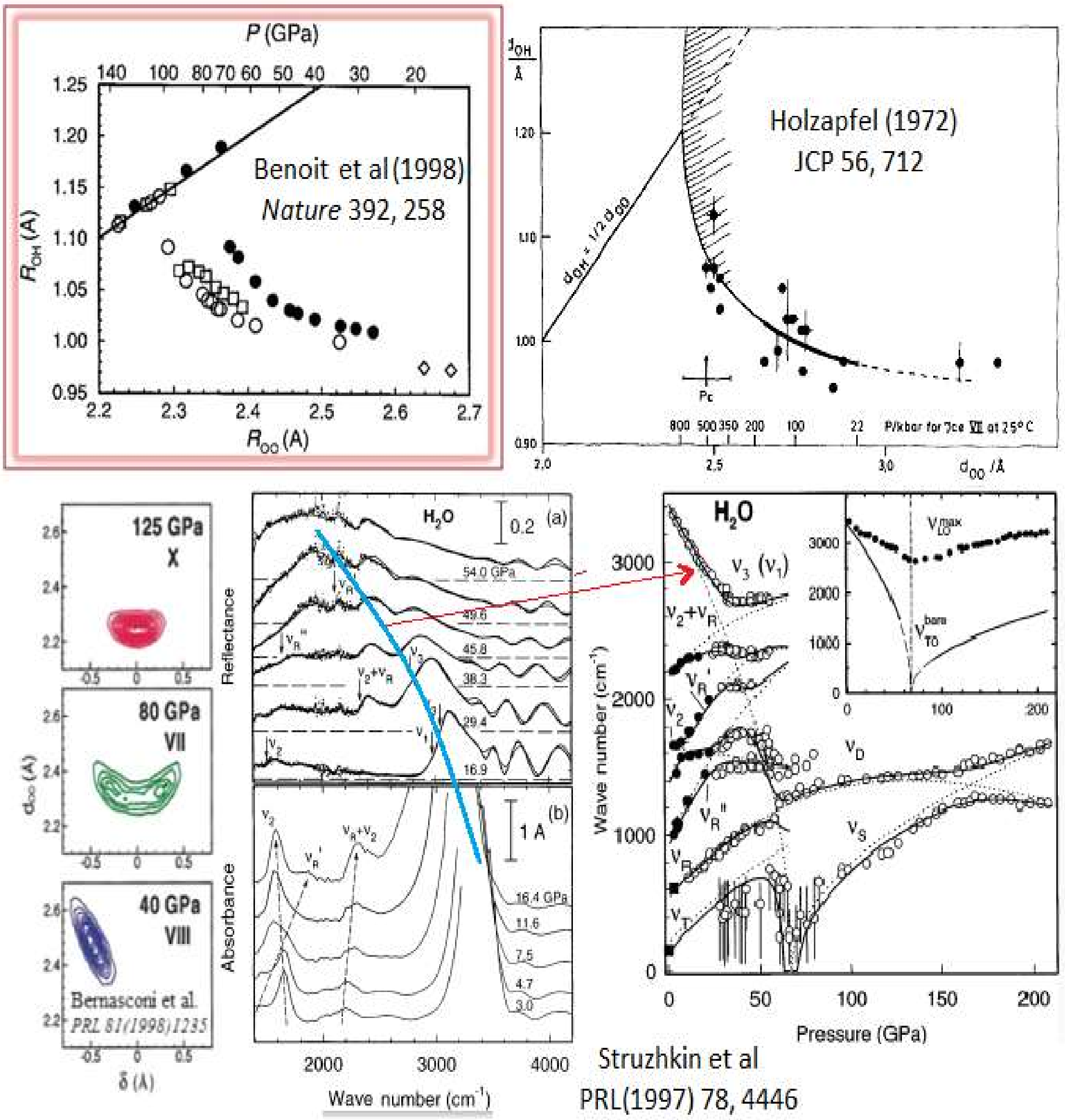

**Figure 1.4:** (Top) Calculated O–H and O---O bond parameters of ice at various pressures with quantum (open) and classical (solid) calculations [9,29]. (Bottom) High pressure behaviour of ice: (left to right) simulated evolution of proton distribution with pressure ($d_{OO}$ is O---O distance) as a function of bond mid-point; evolution of O–H stretching infrared mode; variation of various IR modes with pressure [10, 30] (reproduce with permission).

remarkable softening of the O–H stretching vibrational mode accompanied with pronounced dampening of the band (Figure 1.4 bottom). The data also showed that during the strengthening of hydrogen bond, the soft mode interacts with various vibrational levels in the infrared spectrum through Fermi resonances. However, unambiguous determination of hydrogen atom positions at very high pressures still remains an experimental challenge. Recently, Sun et al. proposed that the hidden force opposing ice compression is the columbic interaction between the lone pairs [31].

### 1.3.3 Pressure induced polymerization of HCOOH

Formic acid (HCCOH) (FA) is the simplest carboxylic acid and in the gas phase, it forms a cyclic dimer. Its presence has been reported in the interstellar medium and is anticipated to form the precursor in the formation of acetic acid and glycine [32, 33]. At low temperatures, it crystallizes in the $\mathrm{Pna2_1}$ space group forming infinite hydrogen bonded chains of cis- conformation. Under pressure, while Allan et al. proposed that the structure, different from the low temperature one, consists of alternate cis- and trans- isomers forming a pair and thus a near dimeric structure [34], Goncharov et al. found that the low temperature structure was stable at room temperature up to $\sim$ 35 GPa [4]. The latter study also indicated that the hydrogen bonds forming the chains may become symmetric at $\sim$ 20 GPa, resulting in the non-molecular phase and in the vanishing of distinction between the isomeric forms. However, the calculated bond parameters of O–H and H- - -O, which were supposed to become equivalent near 20 GPa do not show a localized state for the proton above this pressure as showed in a subsequent study (Figure 1.5) [35], suggesting a delocalized state. The dynamics of proton, thus, becomes crucial to probe such structures in the symmetrization limit.

### 1.3.4 Proton dynamics problem in oxalic acid dihydrate

Oxalic acid, the simplest dicarboxylic acid, is a benchmark system to study proton dynamics due to its rich inter- and intra- molecular hydrogen bonding networks and the possibilities of showing proton exchange and dimeric phase. In the solid

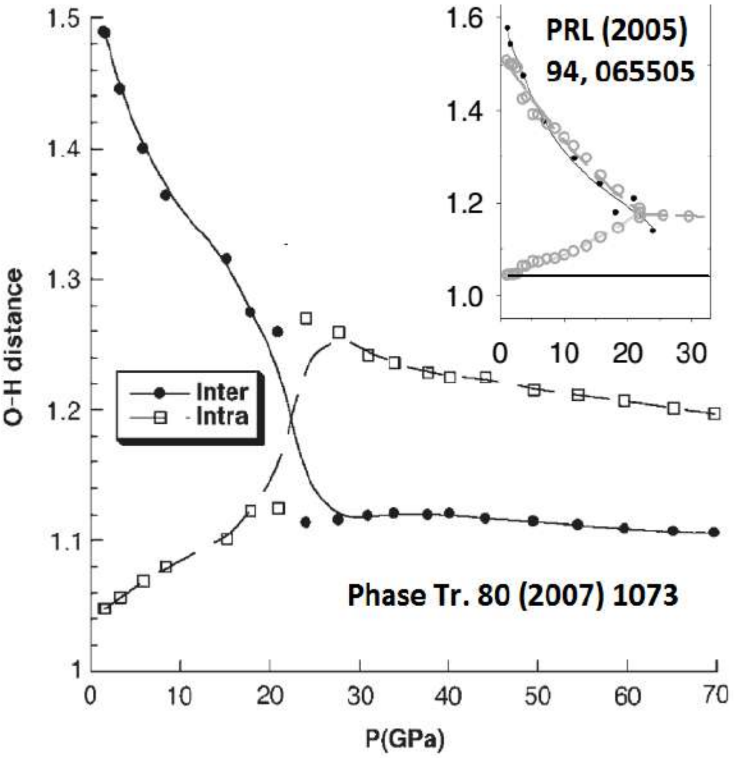

**Figure 1.5:** The O-H and H---O bond parameters with pressure in formic acid [4,36] (reproduced with permission).

state, it exists in the dihydrated form at ambient conditions. Oxalic acid dihydrate is a very important compound in crystal chemistry, ecology and physiology. The structure of this compound, formed through a network of hydrogen bonds has remained a subject of investigations for nearly 100 years. At ambient conditions, the oxalic acid molecule ($(COOH)_2$) is connected to two water molecules through the hydroxyl groups in the two ends. In this configuration, oxalic acid acts as donor and water molecules are acceptor of hydrogen bonds. This hydrogen bond is very strong at ambient conditions ($d_{O--O}\sim$ 2.49Å) and is expected to reach the symmetrization limit on compression [37]. In fact, during initial studies, the efforts were aimed at establishing the existence of neutral or charge transfer state even at ambient conditions. Later, the high pressure and low temperature studies were carried out to probe the proton migrated state in the dense phases, but no experimental results are available which can unambiguously show proton symmetrization or migration through the potential barrier under compression. The properties of this hydrogen bond have been discussed in detail in chapter 3 of the thesis.

In addition, the water molecule in oxalic acid dihydrate also acts as donor of hydrogen bond where its hydroxyl group is connected to another oxalic acid molecule through the carbonyl group [37]. Such a network of hydrogen bonds where water molecule acts as donor as well as acceptor of hydrogen bonds, forming a chain, is a peculiar case of co-operativity effect of hydrogen bonds [38]. The effect is very common in various biological species, for example polypeptide $\beta-$ sheets.

## 1.4 Hydrogen bonding in glycine complexes

Glycine is the simplest of the 20 amino acids found in proteins. It is unique due to its achiral nature, polymorphism, ability to fit to hydrophilic as well as hydrophobic environments, key precursor in many biological molecules, provides central $C_2N$ subunit of all purines, buffering agent in antacids, analgesics, cosmetics etc., used in industries like rubber- sponge products, fertilizers, metal complexes etc. and neurotransmitter in central nervous system, spinal chord, brain stem and retina. It is also of great importance in geology and astro- biology [37–46]. In 2008, glycine like molecule aminoacetonitrile was discovered in a giant gas cloud near the galactic center in the constellation sagitarius. In 2009, glycine like samples were analyzed in the comet "Wild2". In addition, the discovery of glycine compounds in hot molecular cores of star forming regions and in the planetary interiors support the theory of panspermia which claims that the seeds of life are widespread through the universe, i.e. in variable and extreme thermodynamic conditions.

### 1.4.1 Glycine polymorphs under pressure

In the solid crystalline state, three different polymorphic forms of glycine have been observed, i.e. $\alpha$, $\beta$ and $\gamma$ [47–49]. The glycine molecule exists in the zwitterionic form ($NH_3^+CH_2COO^-$) in these polymorphs. Under pressure, glycine polymorphs and complexes undergo subtle to drastic structural changes which are primarily brought about by varied high pressure behaviour of hydrogen bonding networks. While $\alpha-$ glycine, the most compressible polymorph, shows subtle transformations around 3 GPa due to changes in intralayer N-H---O hydrogen bonding interactions accompanied by weakening of interlayer hydrogen bonds [50], $\gamma-$ glycine shows drastic changes. This compound displays structural transition from hexagonal to monoclinic phase across 3 GPa, where helical hydrogen bonding network is replaced by a layered network through breaking and reformation of N-H---O hydrogen bonds [51]. $\beta-$ glycine depicts phase transition across a very low pressure of 0.8 GPa, where head to tail linked N-H---O hydrogen bonds become bifurcated [52].

Glycine provides vast opportunities of forming complexes with various other compounds due to its rich hydrogen bonding capabilities. Indeed, large number of glycine complexes, like triglycine sulphate family of crystals, diglycine nitrate, glycine phosphate and glycine silver nitrate (GSN) are ferroelectric in nature.

### 1.4.2 High pressure behaviour of important glycine complexes

Triglycine sulphate (TGS) forms the most famous room temperature mid-infrared detector. It shows a ferro - paraelectric phase transition at 318 K due to conformational change in one of the three glycine molecules, which was found to be order- disorder type [53, 54]. In contrast, the pressure induced transition was found to be displacive in nature [55]. In the high temperature paraelectric phase, the $NH_3^+$ group of the glycine molecule which is responsible for ferroelectricity, is in dynamic equilibrium with equal occupancy at two sites, making time averaged spontaneous polarization zero. In the high pressure phase, the additional energy supplied by pressure makes the glycine molecule planar by bending hydrogen bonds and stabilizes the position of $NH_3^+$ group resulting in the vanishing of ferroelectricity.

Glycine lithium sulphate, a semi-organic complex of glycine, depicts formation of an intramolecular hydrogen bond with pressure and phase transition at 9 GPa [56]. Above 14 GPa, glycine conformation transforms from zwitterionic to neutral and above 18 GPa, the compound depicts hydrogen bond assisted polymerization.

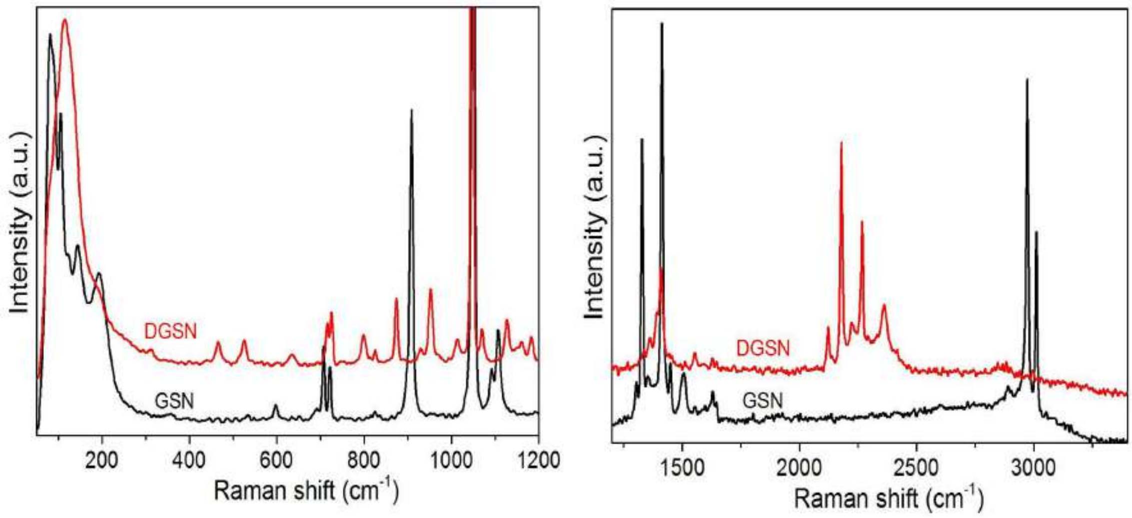

**Figure 1.6:** FT-Raman spectra of GSN (glycine silver nitrate) and DGSN (Deuterated GSN).

Glycine silver nitrate (GSN) was the first organometallic crystal with silver or nitrate ion in which ferroeclectricity was observed [57]. The unique characteristic of GSN undergoing displacive phase transition makes it interesting. Infrared, proton magnetic resonance and structural studies of GSN have indicated that ferroelectricity in GSN is due to the motion of the silver ions (Ag+) [58–60]. Generally it is believed that isotopic substitution does not perturb the crystal structure, but may bring about change in the geometry of molecular structure. In an attempt to study the structure in different isomeric forms, during the course of this thesis, we investigated deuterated glycine silver nitrate at ambient conditions using FT-Raman spectroscopy (Figure 1.6) which supported the neutron diffraction results [61]. It was found that the crystallization of the completely deuterated glycine silver nitrate (DGSN) from $D_2O$ gave a new polymorph with the crystal structure significantly differing from that of the nondeuterated form (GSN): space group P21/c with polymeric two-dimensional layers parallel to the *ab*-plane. In DGSN, the silver ions are mono-nuclear, whereas in GSN Ag-Ag dimers are present. In contrast to GSN, DGSN does not undergo any phase transitions on cooling at least till 100 K.

### 1.4.3 Glycine and oxalic acid complexes

Recently, Losev et al investigated the effect of carboxylic acids on glycine polymorphism, salt and co-crystal formations. It was found that among the acids used, only oxalic acid yielded crystallized salts in different stoichiometries from either slow evaporation or other techniques [62]. Interestingly, glycine and oxalic acid complexes form a special class as these compounds contain very strong hydrogen bonds which are in the limit of symmetrization even at ambient conditions [62–66]. While in glycinium oxalate (gly:oxa :: 1:1), the oxalic acid molecules exist as semioxalate i.e. in a singly ionized state with the strong hydrogen bond forming between semioxalate chains, in bis(glycinium)oxalate (gly:oxa :: 2:1), oxalic acid molecule exists in doubly ionized state and the strong hydrogen bond is formed between oxalic acid and two glycine molecules on its two ends.

## 1.5 High pressure infrared spectroscopy: the emergence of diamond anvil cell and synchrotron sources

Since the Nobel prize winning invention of Bridgman anvil apparatus in 1946 for the generation of high pressures, high pressure science and technology has matured into a sophisticated field and diamond anvil cells (DAC) are now routinely used for studies in gigapascal as well as megabar regimes. Diamond is the hardest material available and it also serves as a transparent window in substantial part of electromagnetic spectrum covering from far infrared to $\gamma-$ rays. However, for high pressure infrared studies, the diamond anvils used are type IIa impurity (nitrogen) free stones. This technique became more common only in nearly last two to three decades. In fact, the advent of Michelson interferometer based spectrometers over the earlier used grating based instruments played the key role in the emergence of infrared spectroscopy as a versatile technique in condensed matter physics. However, the problem of interfacing a DAC with interferometer still persists as the gasket hole ($\sim 300\mu$m) in DAC acts like a diaphragm for the infrared beam of a large diameter (few mm) and most of the incident beam is stopped. The use of infrared microscope comprising of on-axis cassegrain type beam condensers overcomes this limitation to certain extent. These condensers do not contain lenses and are free from refractive index dispersion. However, the dimension of DAC is to be modified to fit into the sample stage. It is noteworthy that the design of anvils and DAC are closely related to the ultimate pressure achievable. Further, the field stops used in IR microscopes also cut substantial part of beam which emphasizes the need for a highly brilliant source which can be focussed to a tight spot of size in tens or hundreds of microns. Understandably, synchrotron sources are ideal for infrared microspectroscopic studies of specimens of the order of tens of microns, as the SR is emitted as a directed “fan” from relativistic electrons in a storage ring. In addition, high pressure infrared spectroscopy, particularly in far IR regions, is diffraction limited technique as the wavelength matches with the focussed spot size and therefore anvils of large culet sizes are required for high pressure far-IR studies.

**Table 1.1:** A few oxalate complexes forming strong hydrogen bond with the corresoponding O---O distances. Highlighted compounds are studied in the thesis.

| Compound | O---O distances |
|---|---|
| $H_2C_2O_4.2H_2O$ | **2.49** |
| $N_2H_5HC_2O_4$ | 2.44 |
| $NH_4HC_2O_4.H_2C_2O_4.2H_2O$ | 2.50 |
| $(NH_3CH_2COOH)_2C_2O_4$ | **2.461** |
| $(NH_3CH_2COOH)HC_2O_4$ | **2.54** |
| $NaHC_2O_4.H_2O$ | 2.57 |
| $LiHC_2O_4.H_2O$ | 2.49 |
| $\mathrm{Pyridine}-2,3-\mathrm{dicarboxylicacid}$ | 2.4 |

## 1.6 Scope of thesis

If one does a survey of very strong hydrogen bonded molecular solids, it can be found that carboxylates, in particular oxalate complexes are capable of forming such bonds in various networks. Table 1.1 shows a few of such compounds. In this thesis, we have investigated three compounds in the class of hydrogen bonded molecular solids. The first being one of the fundamental and benchmark system for hydrogen bonding, oxalic acid dihydrate (OAD) and other two are the complexes of oxalic acid with the simplest amino acid glycine, i.e. glycinium oxalate (GO) and bis(glycinium)oxalate (BGO). In OAD, GO and BGO, the oxalic acid molecules exist in neutral, anionic and dianionic states respectively. While in GO, the strongest hydrogen bond is formed between semioxalate molecules, in OAD and BGO, the strongest one is between oxalic acid and water; and oxalic acid and glycine respectively at ambient conditions.

In addition, because of the advantages of synchrotron source over thermal source for IR microspectroscopic studies, such as under high pressure, the development of an infrared beamline at the Indus-1 synchrotron radiation source at RRCAT, Indore, India was carried out in parallel, during the course of this thesis. The infrared beamline development work and research methods including sample preparation, spectroscopic characterization and details of instruments and complementary techniques are described in chapter 2. It also includes the development of other facilities like a high resolution IR lab, FT-Raman facility, in-situ high pressure and in-situ low temperature facilities.

In chapter 3, the details of hydrogen bonds in oxalic acid dihydrate and enhancement of their strength due to a co-operative network are described. The first experimental observations of the proton transfer process under pressure and its influence on the three dimensional hydrogen bonded framework in this benchmark system are presented. Chapter 4 deals with the high pressure effects in the first glycine-oxalic acid complex, glycinium oxalate in which a symmetric hydrogen bonded state has been observed in the infinite semioxalate chains along the crystal *b*-axis. In chapter 5, the pressure induced phase transformation in Bis(glycinium)oxalate (gly: oxa :: 2:1) is shown. Here the oxalic acid molecule exists as dianionic, i.e. devoid of any hydrogen and is sandwiched between two glycine molecules formic a centrosymmetric structure. In chapter 6, we have presented the first results from the infrared beamline (using lab source after the commissioning of instrument and using SR after the integration of beamline) and some representative studies were carried out to demonstrate its utility in condensed matter spectroscopy. This also includes the results on high pressure effects on the dimeric structure of an amide based molecular solid, Acrylamide, high pressure reflectivity measurements on a superconductor to deduce its optical properties and effects of calcinations temperatures on the molecular structure of a SOFC (solid oxide fuel cell) interconnect material.

# 2

# Facility Development - Synchrotron Infrared Beamline at Indus-1 and Experimental Methods

## 2.1 Theory of Vibrational Spectroscopy

### 2.1.1 Infrared Spectroscopy

Vibrational spectroscopy is often used to study local molecular structures by probing various bond and functional group vibrational frequencies using infrared absorption and Raman scattering techniques [67–70]. The total number of vibrations in any polyatomic molecule having N atoms is 3N-6 (3N-5 for linear molecules), which are classified as normal modes. Even in the crystalline state, these free molecular modes may not be severely modified. Thus, for n molecules per unit cell, there will be n(3N-6) "internal" frequencies. This number may be reduced due to degeneracies. However, there are 3n translational and 3n rotational degrees of freedom and 3 of these are responsible for acoustic modes leaving

6n-3 maximum numbers of optical "external" modes. Therefore, useful information on lattice dynamics can also be obtained by studying the phonons (quanta of lattice vibrations) in the long wavelength regions of IR spectra or closer to the excitation frequency in Raman spectra.

The equilibrium molecular configuration at any given thermodynamic condition is determined by the minimization of the vibrational potential energy of the system, which can be described using a Taylor series expansion, as in equation1.1 (Chapter1). In the limit of small oscillations and under the harmonic approximation, only the quadratic term (the third term) contributes significantly to the potential energy, so that,

$$V = \frac{1}{2} f x^2, or \left( \frac{1}{2} \sum_{j,j'}^{3N-6} f S_j S_{j'} \right) \quad (S_j{}'\text{s are the normal coordinates}). \tag{2.1}$$

Here $x$ is displacement and $f = \frac{\partial^2 V}{\partial x^2}$, or $\left( \frac{\partial^2 V}{\partial S_j \partial S_{J'}} \right)_0$ defines the force constant, which provides insight into the nature of the bond, semi-quantitatively is a measure of the bond length, dissociation energy etc. For each normal mode of vibration, the quantized vibrational energy levels are defined as,

$$E_v = h\nu \left( v + \frac{1}{2} \right) \tag{2.2}$$

where $v$=0,1,2,..... is the vibrational quantum number and $\nu$ is the frequency. In addition, some information on electronic transitions and optical properties can be obtained from reflectivity spectra by employing Drude-Lorentz formalism to exploit the Kramer-Kronig transformation between real and imaginary parts [71]. This is discussed in Chapter 6.

During an absorption experiment, the electric vector of the incident IR light couples with the electric dipole moment $\mu$ of the molecule, which is also related to the geometrical symmetry, i.e. "symmetry species", of the molecule. A given transition, say from vibrational state n→m, is allowed or forbidden depends on

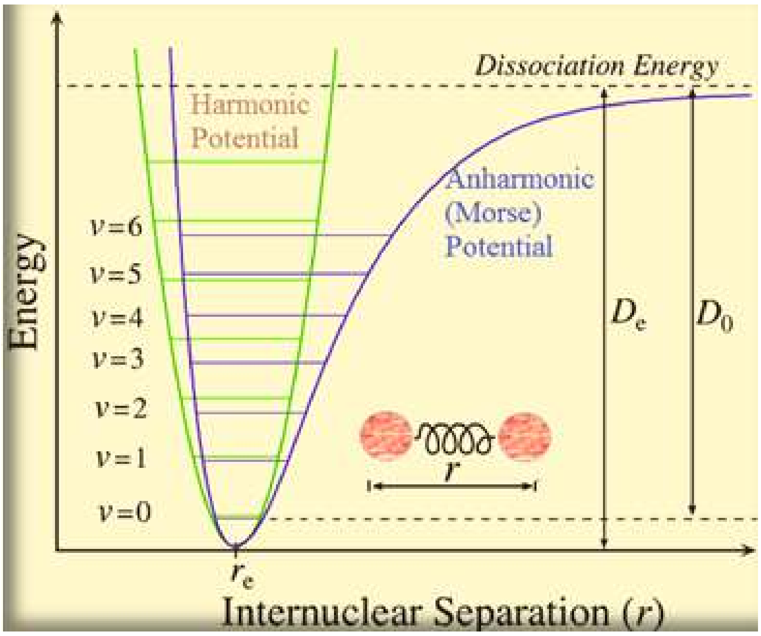

**Figure 2.1:** Modifications in energy levels and potential well for harmonic and anharmonic approximations.

whether the transition dipole moment,

$$(\mu)_{mn} = \langle m|\mu_z|n\rangle = \int \psi_m^* \mu_z \psi_n d\tau \tag{2.3}$$

is non-zero or vanishes. The intensity of an infrared absorption band is proportional to the square of the change in dipole moment,

$$I_{IR} \propto \left(\frac{\partial\mu}{\partial S}\right)_0^2 \tag{2.4}$$

where $S$ is the normal coordinate. By solving the quantum equations, one can readily find that the dipole moment must change during a vibration and also obtain the vibrational selection rules $\Delta v = \pm 1$ under the harmonic approximation. When anharmonicity is introduced, cubic and higher order terms must also be considered in the Taylor expansion of potential energy (equation1.1) which modifies the regular spacing of energy levels and relaxes the selection rule to $\Delta v = \pm 1, \pm 2, \pm 3....$ so that overtones and combinations also become allowed as shown in Figure2.1 (more details in Appendix A). However, as most of the molecules are in vibrational ground state at ambient temperatures, the most important absorption features are due to the transitions $v$=0→ $v$=1, i.e. fundamentals. Anharmonicity always plays some role in molecular vibrations and becomes extremely important in some peculiar cases like proton dynamics in very strong hydrogen bond bridges. From symmetry considerations, if the symmetry species of a given normal coordinate matches with any component of the dipole moment, the fundamental transition corresponding to that coordinate will be active in IR spectrum. For combinations, the direct product of symmetry species of initial and final states should be in the same species as a component of the dipole moment. Finally, mode couplings (e.g. Fermi resonance) between various vibrational energy levels may further enhance complexities in the spectra (Appendix A).

### 2.1.2 Raman Spectroscopy

Similar analogy can be derived for the Raman effect, where the electric field of the exciting radiation induces a dipole moment in the system which modifies the charge distribution.

$$\mu_{induced} = \alpha \mathbf{E} \tag{2.5}$$

Here **E** is electric vector and $\alpha$ is the polarizability tensor of rank 2.
Raman effect, in principle, is described as the inelastic scattering of photons by atomic vibrations or phonons. Thus, during a vibration, it is the change in polarizability of the medium which modifies atomic configuration, giving rise to the Raman signal. Again, for small oscillatory approximation, a Taylor series expansion of $\alpha$ can be done in terms of the normal coordinate S, which gives,

$$\mu_{ind}(t) = \alpha_0 E_0 cos\omega t + \frac{1}{2}\left(\frac{\partial\alpha}{\partial S}\right)_0 S_0 E_0[cos(\omega-\omega_0)t + cos(\omega+\omega_0)t] + .... \quad (2.6)$$

where $\alpha_0$ is molecular polarizability in the equilibrium configuration, $\omega_0$ is the molecular vibrational frequency and the scattered intensity from the oscillating dipole is proportional to the square of induced dipole moment. Thus, the first term (where intensity $\sim \alpha_0^2$) is the Rayleigh or elastic scattering contribution, whereas the inelastic Raman scattering is associated with the terms involving change in polarizability. In the second term, there are two components and thus two lines corresponding to $(\omega - \omega_0)$ and $(\omega + \omega_0)$ which are known as Stokes and antistokes lines respectively. These shifts determine the vibrational frequencies of the molecule.

The most important requirement for IR as well as Raman experiments is the availability of appropriate source of electromagnetic radiation. Although the Raman signal is proportional to the source frequency (laser) but fluorescence effects in some cases may compel the use of a lower frequency as in FT- Raman instruments, whereas for infrared spectroscopy, intense and bright sources with good emission characteristics in a broad spectral range are required for the studies in different spectral regions. The brightest source, for microscopic applications, in infrared spectroscopy in a wide spectral range available today is the synchrotron radiation emitted by relativistic electrons in a storage ring.

## 2.2 Development of infrared beamline at Indus-1 synchrotron radiation source

The synchrotron light, with brightness (photon flux emitted per unit source area and solid angle) several orders of magnitude more than the existing sources, is a unique source of infrared (IR) radiation [72] which can be used for spectroscopic studies in the fields of material science to biology, geology, forensics, environmental sciences and cultural heritage. The high brightness in the infrared region as compared to the thermal sources comes from the very small size of the source and the directional property of the emitted radiation (narrow emission angles) [73]. Unlike in the VUV/X-ray regions, no dispersive elements are required in the design of an infrared beamline due to the advent of modern high performance Michelson interferometer based spectrometers which accept broad band radiation. The spectrum of a bending magnet radiation is uniform in the horizontal plane of emission. But in the vertical plane, it is strongly wavelength dependent and the cross section of the "fan" emitted is systematically filled with higher wavelength contributions as one moves away from centre [74]. Hence an optimization of the acceptance angle becomes crucial to extract the high wavelength infrared components from the storage rings. The design and installation of a new, and the first in India, infrared beamline at Indus-1 synchrotron radiation source at RRCAT, Indore is described here. The performance and first results are presented in chapter 6.

## 2.2.1 Beam extraction and optical design for transportation

### 2.2.1.1 Infrared radiation at Indus-1 source

Indus-1 (Figure 2.2) commissioned in 1999, operates at 100 mA beam current with beam lifetime of ∼1.8 hours [75–77]. The infrared beamline is installed at the 10° port of the bending magnet (DP-4) and the first mirror can be conveniently placed close to the beamport so that the radiation can be collected over a large vertical and horizontal emission angle, which makes it possible to obtain both horizontal and vertically polarized IR radiation from the source, which is very difficult to obtain from a conventional IR source.

For different regions of the electromagnetic spectrum, the divergence of SR can

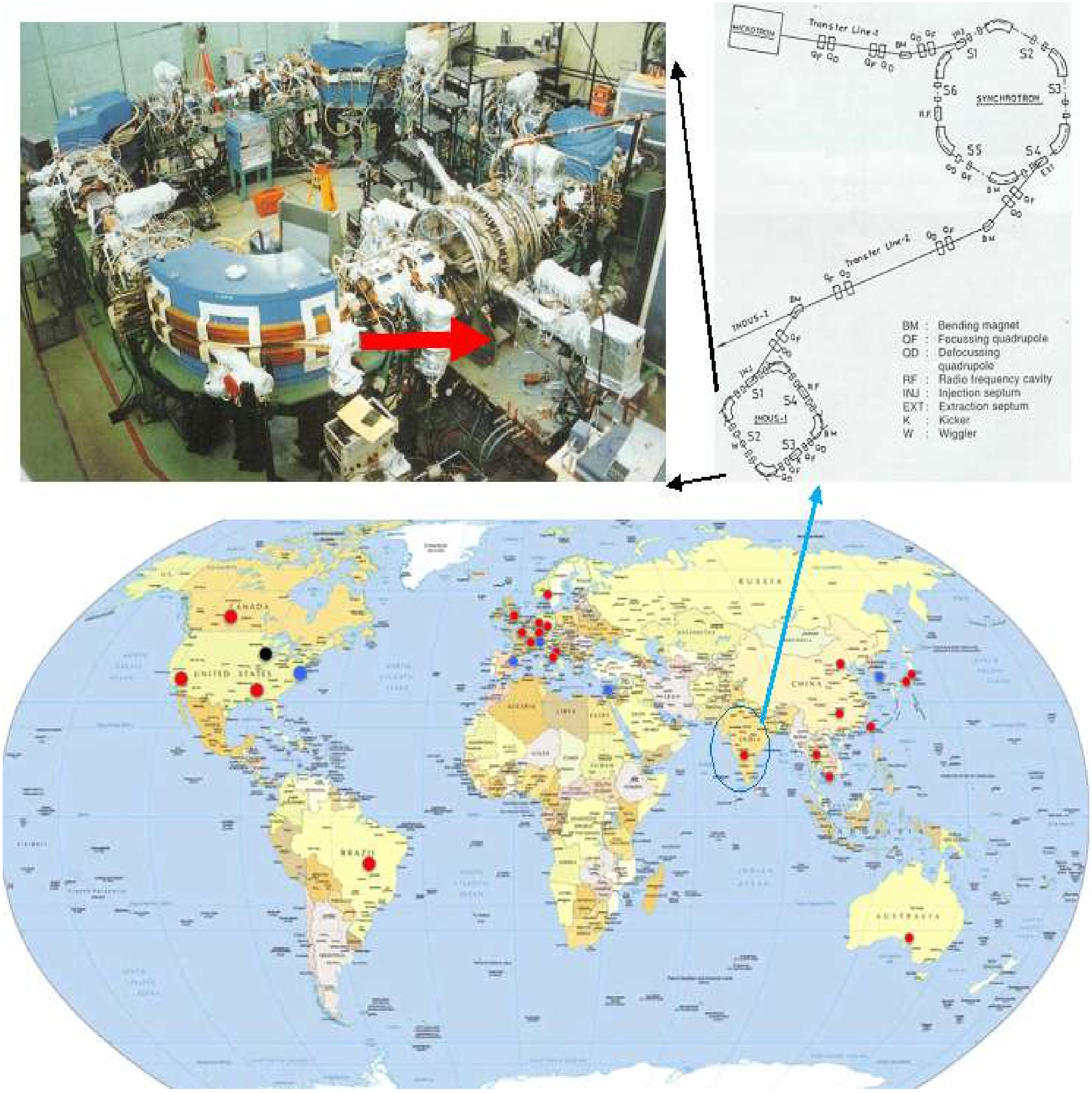

**Figure 2.2:** (anticlockwise from bottom) A world map of infrared synchrotron radiation facilities (dots), which have grown from ∼13 in the year 2000 to ∼29 in 2015 (Courtsey: Prof. P. Dumas, SR IR spectroscopy, European Hercules SR school 2016); the Indus-1 source at RRCAT, India showing electron beam injection from Microtron to the storage ring via a Booster synchrotron; photograph of Indus-1, red arrow pointing away from dipole shows the direction of extraction of IR energies.

be estimated using the following relations.

For horizontal direction,

$$\theta = \frac{7}{12} \frac{0.608}{\gamma} \tag{2.7}$$

For vertical direction,

$$\theta = \frac{E_0}{E} \left( \frac{\lambda}{\lambda_c} \right)^{1/3} \qquad for \lambda >> \lambda_c; \lambda > 507\lambda_c \tag{2.8}$$

$$\theta = 0.565 \frac{E_0}{E} \left( \frac{\lambda}{\lambda_c} \right)^{0.425} \qquad for \lambda > 0.750\lambda_c \tag{2.9}$$

$$\theta = \frac{E_0}{E} \left( \frac{\lambda}{3\lambda_c} \right)^{1/2} \qquad for \lambda < 0.750\lambda_c \tag{2.10}$$

For long wavelengths, $\lambda >> \lambda_c$ (critical wavelength, $\lambda_c$= 61Å, i.e. $\sim$ 202 eV for Indus-1), the single electron emission for *s*- and *p*- polarization is approximated as [74]:

$$S(\theta) \propto \{(\theta/\theta_\nu)^2 K_{2/3}[(\theta/\theta_\nu)^{3/2}]\}^2 \text{and} P(\theta) \propto \{(\theta/\theta_\nu)^2 K_{1/3}[(\theta/\theta_\nu)^{3/2}]\}^2 \text{respectively,} \tag{2.11}$$

where the characteristic angle $\theta_\nu \propto (1/\rho\omega)^{1/3}$ , i.e. depends on wavenumber ($\omega$) of the radiation emitted ($\rho$ is the radius of curvature of electron trajectory). Further, the smaller the electron energy of the facility, the wider is the emitted wavelength distribution along vertical plane in SR cross-section (Figure 2.3).

With the acceptance angle of 35 mrad, vertical collection of radiation covering the complete mid infrared region became possible at Indus-1, as shown in Figure 2.4. In the design of an IRSR beamline, the foremost requirement is to block the high energy components (hard X-rays) and collect the maximum power emitted using appropriate optics. The challenges imposed by heat load on optical components

**Figure 2.3:** The spread of 10 $\mu$m wavelength away from central line in the SR cross section at Spring-8 Japan (8 GeV), Australian Synchrotron (3 GeV) and Indus-1(0.45 GeV) with 20 × 20 mrad$^2$ beamport opening. (Courtsey: presentation by Prof. P. Dumas, SR IR spectroscopy, European Hercules SR school 2016).

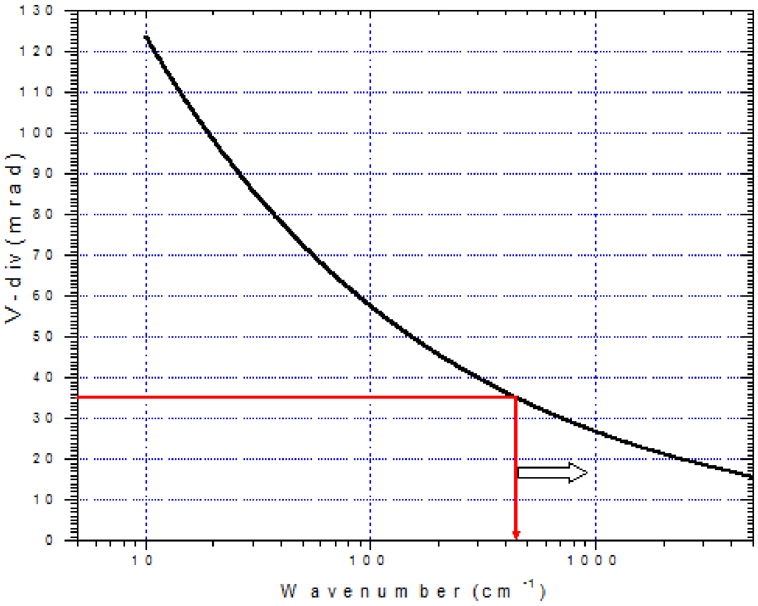

**Figure 2.4:** Vertical collection angle as a function of minimum frequency which can be extracted at Indus-1.

and focusing of beam emitted from large emission lengths of bending magnet can be minimized in relatively lower electron energy storage rings like Indus-1 (0.45 GeV), which are devoid of high frequency X-ray components. The absence of any elaborate shielding wall also provides access to the front end of the beamline making the alignment easier. Such rings if used at high currents and large apertures can also provide significant flux for IR microscopy studies.

#### 2.2.1.2 Beam propagation simulations

In order to transport the beam from Indus-1 storage ring to the experimental hall, it was necessary to divert the direction of the beamline away from the direction of SR emission, due to the presence of other beamlines/injection line in close vicinity and the existing site constraints. In the optimized design, the beamline is uplifted and then back folded by 180° from where the beam pipes start, the schematic is shown in Figure 2.5. For final specifications of the optical and mechanical components, the beam propagation simulations were carried out using SRW (Synchrotron Radiation Workshop) package [78], a popular program in IR beamline simulations developed at NSLS, USA, for various wavelengths in the infrared region. Starting with the parameters of Indus-1 source, SRW generates the beam profile at the beamport and then simulates the propagation of the wavefront, instead of using geometrical optics, from one optical element to the next till the focused point. This takes care of the diffraction effects arising due to large wavelength of the radiation.

The diverging IR radiation from the beamport is reflected vertically up by a flat mirror M1, located at a distance of nearly 1500 mm from the tangent point, where it is collimated employing a focusing-defocusing geometry. The beam from M1 is focused by the off axis concave mirror M2. The distance from the source to M2 is $\sim$ 2337 mm and the radius of M2 is 1011.9 mm (diameter 85 mm, thickness 30 mm, off axis- half angle= 3.48°). The downward converging beam is then intercepted by a convex mirror M3 (diameter 22 mm, radius 331.43 mm, thickness 10mm, off axis - half angle = 7.9°). Angle between axis and M2-M3 is 6.96° and the distance between M2 and M3 is 480 mm. The image formed by M2 is at the focus of M3 which acts as the virtual object for M3 and hence the reflected beam is collimated right after M3. The collimated beam is diverted towards the experimental hall using a plane mirror (M4). For further calculations, we used another plane mirror M5 at a distance of $\sim$ 6 m from M4 which deflects the beam down to be intercepted and focused horizontally by an off-axis parabolloidal mirror of focal length 1 m. Results for beam propagation simulations for $\lambda$= 20 $\mu$m are shown in Figures 2.6, 2.7 and 2.8. Figure 2.6 shows the initial wavefront from the beamport in which the maximum and minimum intensities are shown by yellow and black colours respectively. Beam sizes at M1, M2 and M3 are 36×40 mm$^2$, 54×60 mm$^2$ and 16×18 mm$^2$ respectively ( Figure 2.7). After M3 the beam is almost collimated and the final focused spot size was less than 500 $\mu$m ( Figure 2.8). Similar calculations were carried out for a range of wavelengths in the complete infrared region and typical results for $\lambda$= 50 $\mu$m and 10 $\mu$m are shown in Figures 2.9 and 2.10 respectively, with the focal spots significantly less than 1 mm$^2$ in all the cases.

### 2.2.2 Installation of the beamline

#### 2.2.2.1 Extraction and collimation

In the optimized alignment condition for extraction of a nearly collimated beam, the front end, of length nearly 1485 mm from the source point, consists of UHV gate valve and fast closing shutter apart from a vacuum port. Two vacuum pumps (sputter ion pumps) operate continuously to maintain an ultra high vacuum (nearly $10^{-10}$ mbar) up to the spherical mirror chamber, above which a rough vacuum of the order of $10^{-4}$ mbar is maintained in the rest of the beamline using Turbo molecular pumps. The initial optics including the collimating assembly is housed in separate and rigid vacuum chambers supported by adjustable kine-

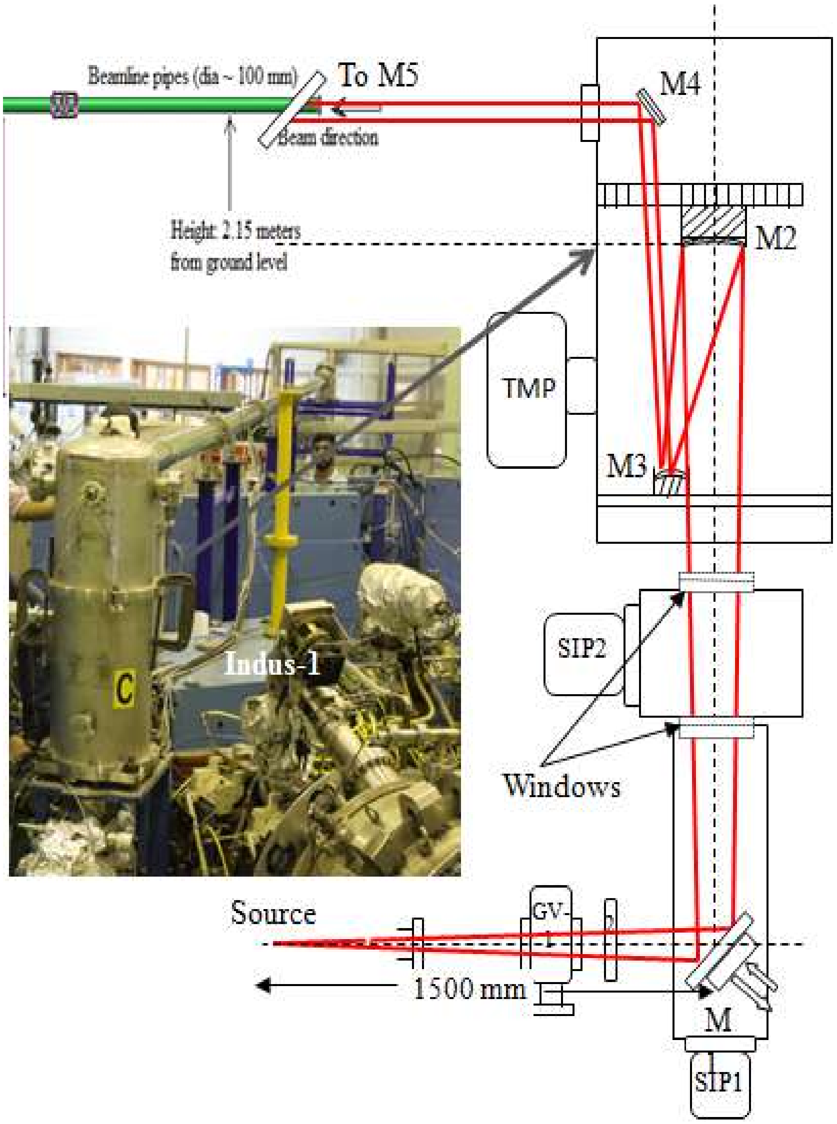

**Figure 2.5:** Photograph of the mirror chamber assembly connected to the front end and schematic showing synchrotron beam collection and transportation towards the experimental hall. GV-1 and 2 are vacuum gate valve and fast closing shutter respectively, TMP - Turbo molecular pump, SIP - Sputter ion pump.

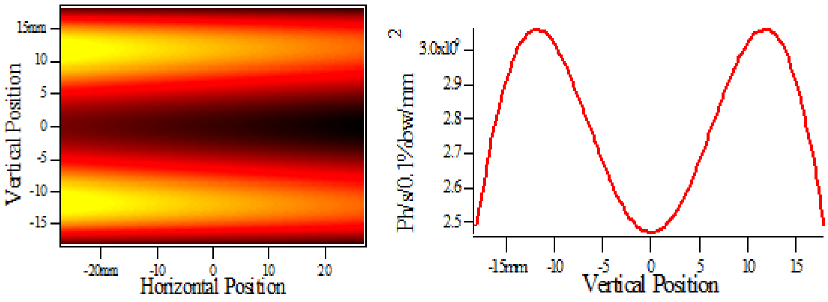

**Figure 2.6:** Calculated beam profile ($\lambda$= 20 $\mu$m) as extracted from the Indus-1 source.

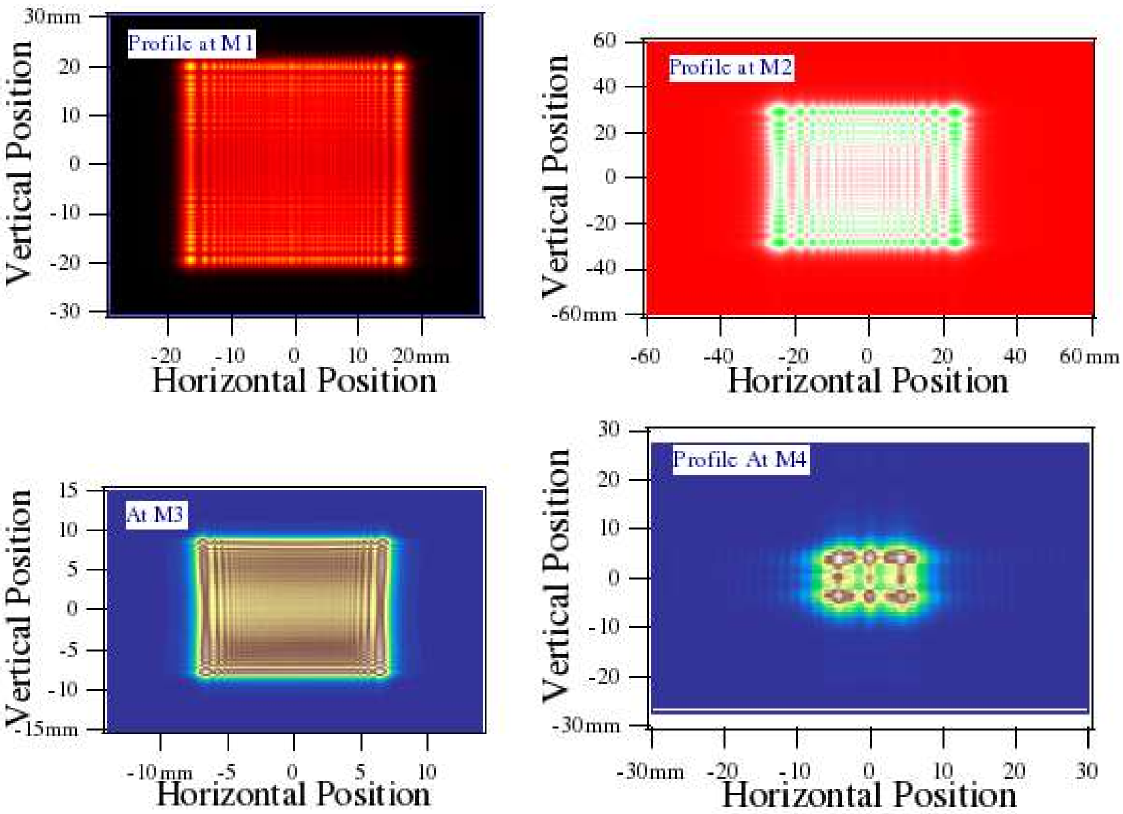

**Figure 2.7:** Beam Propagation results at various optical components of the Beamline for $\lambda$= 20 $\mu$m using SRW code.

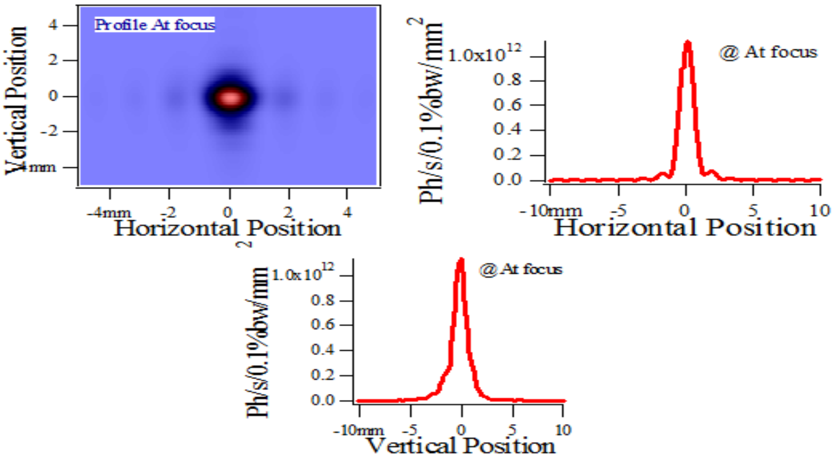

**Figure 2.8:** The focused spot (using a parabolodial mirror, f = 1 m) as calculated for $\lambda$= 20 $\mu$m.

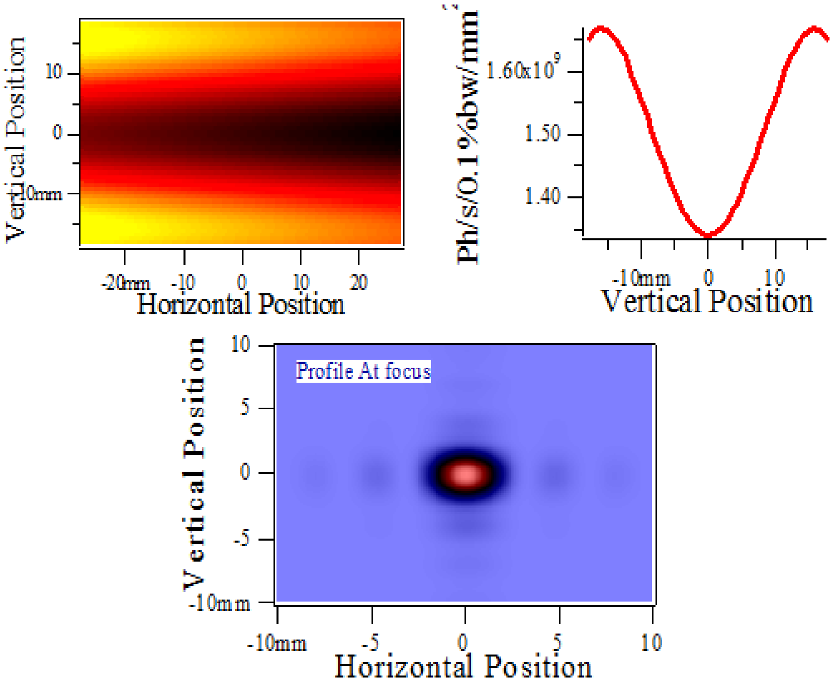

**Figure 2.9:** Extracted beam profile and final focused spot for $\lambda$= 50 $\mu$m.

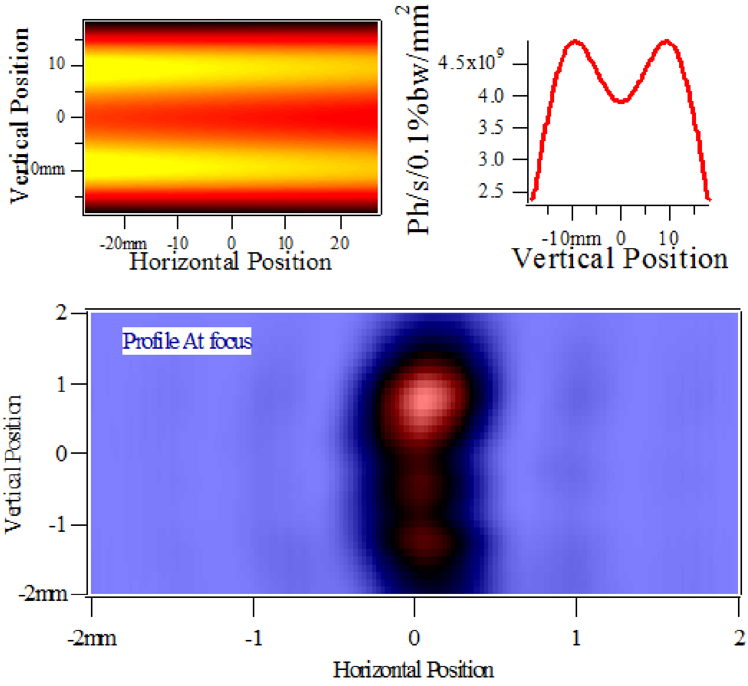

**Figure 2.10:** Extracted beam profile and final focused spot for $\lambda$= 10 $\mu$m.

matic bearings on the base plate of the chambers. The initial beam manipulation design is similar, but at variance with the beamline direction with respect to emission direction, in the IR microscopy beamline (MIRAGE) installed on the SA5 - SuperACO (0.75 GeV - LURE, France). As this facility has been decommissioned, the mirror chamber consisting of two spherical mirrors, connected to the first mirror chamber was requested and shipped to our facility. As its optics was developed considering the diffraction point spread function correlation with the IR microscopy set up and the diffraction limited source size of the low energy ring [79], it could be accommodated at Indus-1, but with major mechanical modifications in optical alignment, mirror orientations and connecting bellows. Based on the optical design and simulations, the diverging IR radiation from the beamport is reflected upstream by the flat mirror M1 and the beam collimation is carried out in the vertical plane. All the mirrors are high quality Aluminium coated mirrors except M1, which is a gold coated mirror. The lower chamber

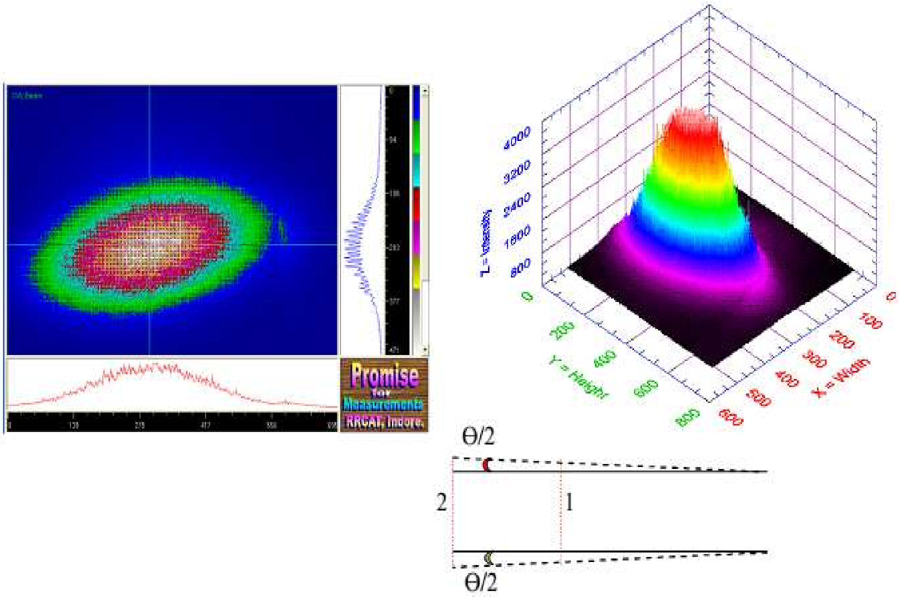

**Figure 2.11:** The Collimated SR beam travelling across the shielding wall: (clockwise from top left) the captured beam profile of the collimated SR beam; spot profile as a function of CCD pixel numbers; calculation of beam divergence ($\theta$) for horizontal as well as vertical cross sections of the beam.

has been designed so as to provide a provision for water or air cooling of M1 if required. Above the mirror M1, a pair of ZnSe windows are used to isolate the UHV of storage ring with the rough vacuum in rest of the beamline.

Figure 2.11 shows the picture of the collimated SR beam travelling across the shielding wall towards the experimental station. For beam profile measurements, the SR beam was obstructed on a metallic plate (40 mm × 40 mm) with fine laser graded lines along the horizontal as well as vertical axes with a spacing of 500 $\mu$m. A CCD camera, PCO PixelFly CCD, facing the plate at a distance of 30 cm and placed slightly off in the beam direction, captured the obstructed beam. “Promise” software, developed at RRCAT, was used for spectral profile measurements and the background stray light was used for calibration of image in the graded plate with CCD pixels [80]. The image of the beam was captured at several locations in the beam transport section for the analysis of vertical and horizontal divergence of the beam using simple mathematical formulation, pictorially shown in Figure 2.11 (bottom). The average vertical and horizontal divergences were found to be $\sim 0.10^\circ$ and $0.13^\circ$ respectively.

#### 2.2.2.2 Beam Transport and Integration with Experimental Station

Subsequent to the plane mirror M4, the collimated beam travels horizontally in vacuum without any obstruction to a distance of nearly 10 meters. The mechanical assembly of the beam transport system of the beamline up to the experimental station has been shown in Figure 2.12 (top). The beam is deflected 90° downwards in to another mirror chamber through a plane mirror M5 as shown in Figure 2.12 (bottom). This mirror chamber is designed to facilitate the flexibility of desired beam manipulation in terms of shape, size and direction. It also serves as a vacuum station for the beamline. In the present configuration, the size of the collimated beam is reduced using a pair of gold coated off-axis (right angle) parabolloidal mirrors (M7 and M8) having different focal lengths. M7 focusses the collimated beam to a larger focal length from where the diverging beam is intercepted by M8 having a lower focal length, which again collimates the beam. Thus, using two parabolloids of focal lengths 40 and 10 cm respectively and with an initial beam size of $\sim$ (36 $\times$ 24) mm$^2$, we get the final collimated beam size of $\sim$ (9 $\times$ 6) mm$^2$. The optics ($f$ - number) is matched with the spectrometer (Bruker Vertex 80V) optics. Further, we use plane Aluminium mirrors to tune and direct the beam towards the experimental station and finally inside the FTIR microspectroscopy set up.

The final focussed spot size, using the paraboloidal mirror M7, of the SR beam was approximately 300 $\mu$m in diameter as viewed in the measuring scale and after further focusing on to the aperture wheel inside the FTIR instrument, which is close to the source size as estimated using the beam diagnostics beamline at Indus-1 (Figure 2.13).

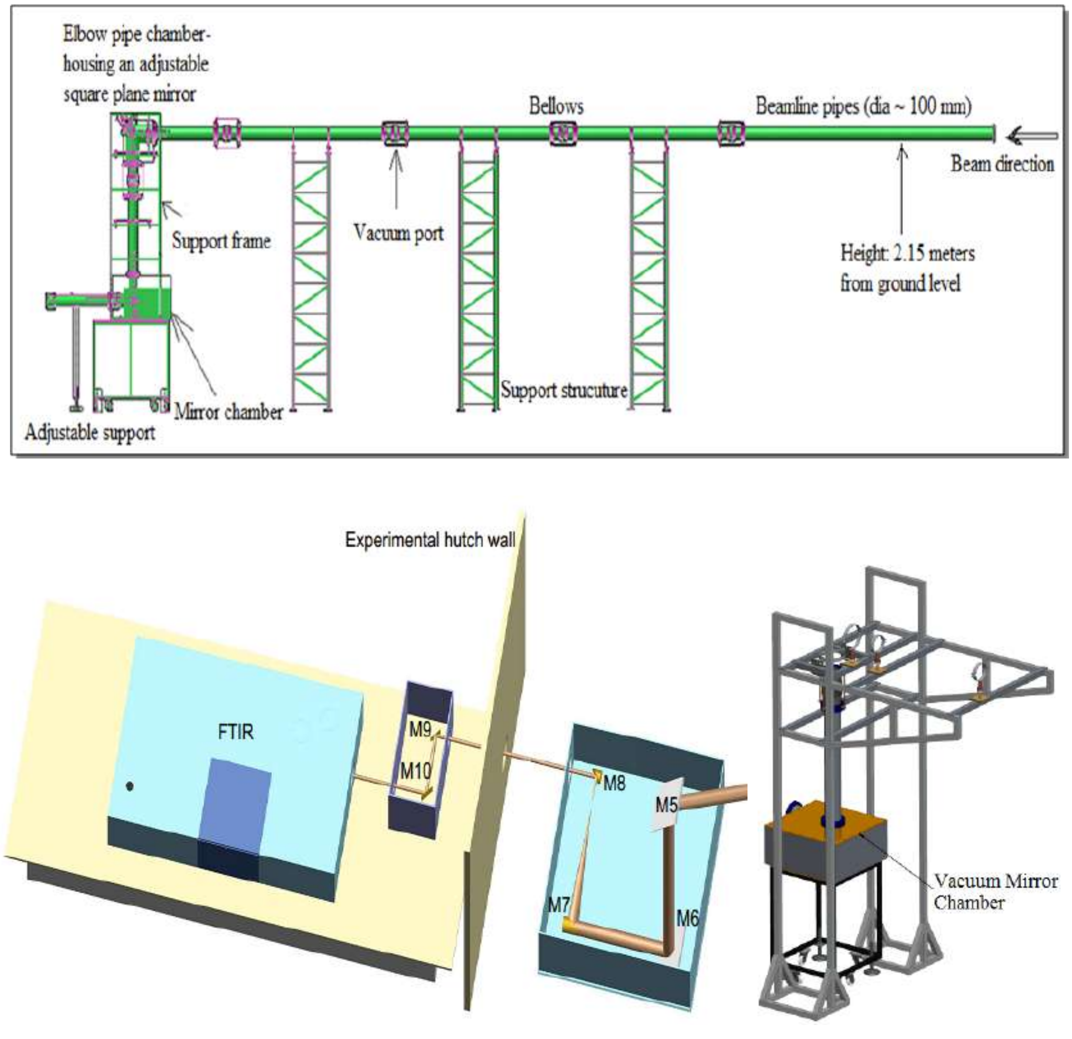

**Figure 2.12:** (top) Mechanical assembly of the beamline across and after the shielding wall. A specially designed elbow pipe chamber houses the plane mirror M5 along with the micrometer controlled adjustable mount, which deflects the beam 90° downwards towards another mirror chamber. (Bottom: right to left) Mechanical assembly of the mirror chamber and beamline with support structure housing the plane mirror M6 and the paraboloidal mirrors M7 and M8; also shown the schematic of beam propagation through M5, M6, M7, M8 (top view) outside the experimental station and M9, M10 inside the hutch which integrate the beamline with the spectrometer (FTIR).

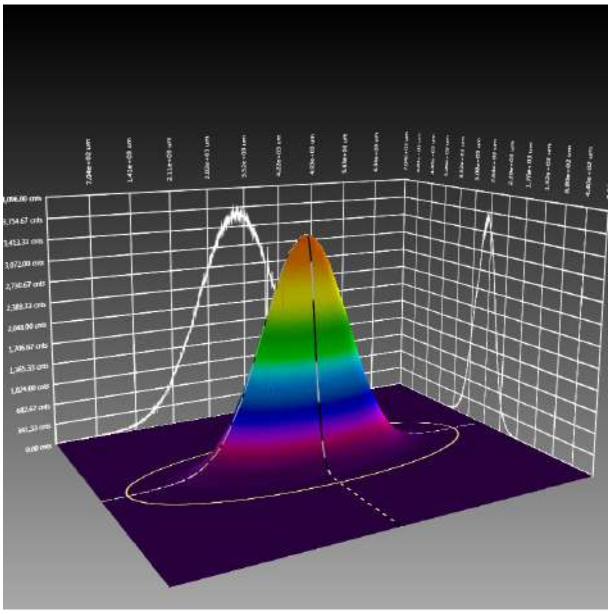

**Figure 2.13:** Focused synchrotron beam size (visible part), $4\sigma$ values in horizontal and vertical directions, measured using the Beam diagnostics beamline at Indus-1 employing a 1:1 optics, which gives an estimate of the source, i.e. electron beam size (rms values) to be approximately 520 (H) × 250 (V) $\mu$m$^2$

## 2.3 Infrared Spectroscopy setup - the experimental station at IR beamline

Infrared spectrometer used in this dissertation is based on Michelson interferometer [81,82]. The interferometer was first used by Michelson in 1880 in the famous test experiment for the existence of "ether", when many interferograms (intensity vs. path difference) were measured manually. This technique became important in spectroscopy only after the era of computers emerged and the algorithms of fast fourier transform (Cooley Tukey algorithm) were developed [83]. Figure 2.14 shows the optical layout of a modern interferometer based Fourier Transform Infrared Spectrometer (FTIR), in which two interfering waves are generated from the same wave so that phase relationship is maintained. The waves are sent to a beam-splitter and then to two plane reflecting mirrors. One of these mirrors moves back and forth to generate the path difference between the two waves

(Figure 2.15a) and the interfered beam (interferogram) travels to the sample and finally to detector, where it is fourier transformed to obtain the spectrum (intensity vs. wavenumber). For zero path difference (ZPD) condition, all the wavelengths interfere constructively. The beamsplitter (Figure 2.15) is designed to reflect and transmit 50% each of the beam.

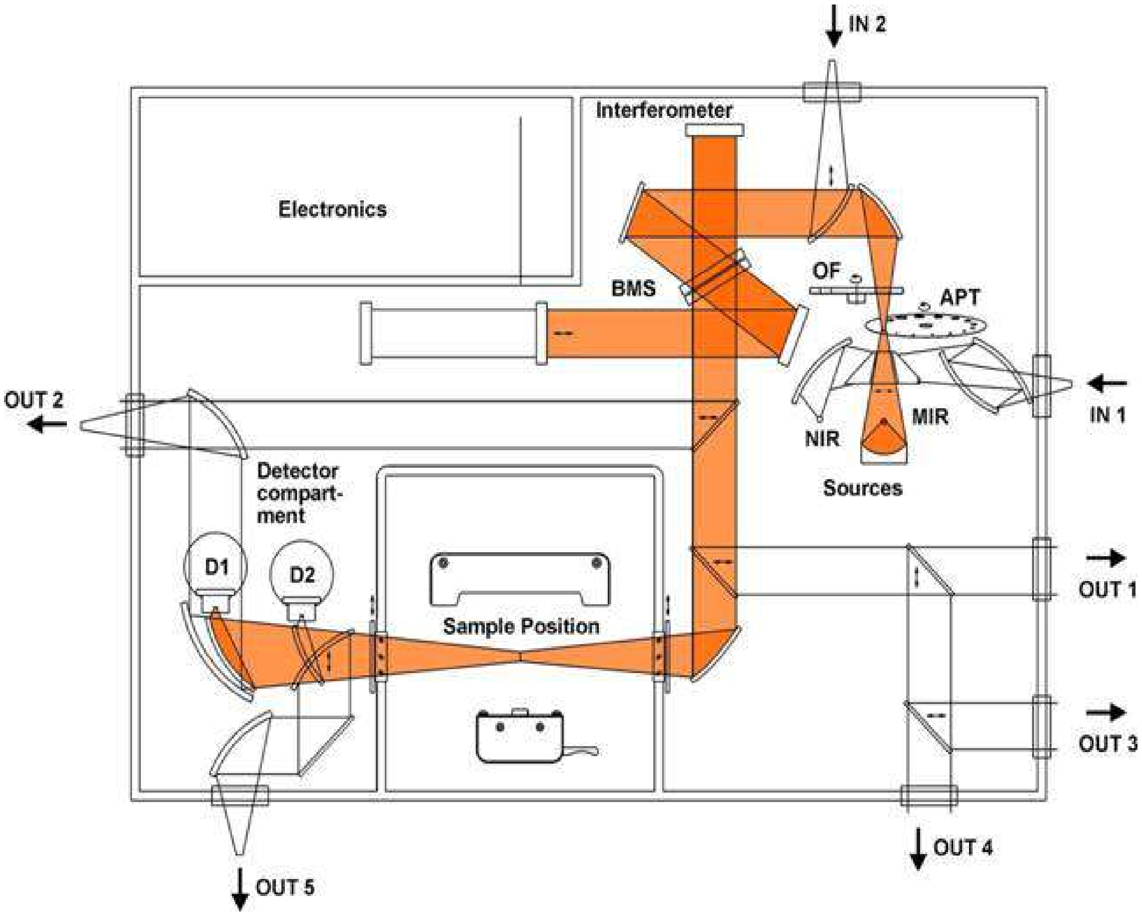

**Figure 2.14:** Optical layout of a commercial FTIR spectrometer. Red shaded region - beam path, BMS- Beamsplitter, APT- aperture, D- detector, IN- provision for external source like synchrotron radiation, OUT- provision to take interfered beam out, for example to an infrared microscope.

A plane monochromatic wave at a point $z$ and time zero can be described as,

$$y(z,\sigma) = a(\sigma)cos(kz) = a(\sigma)cos(2\pi\sigma z) \tag{2.12}$$

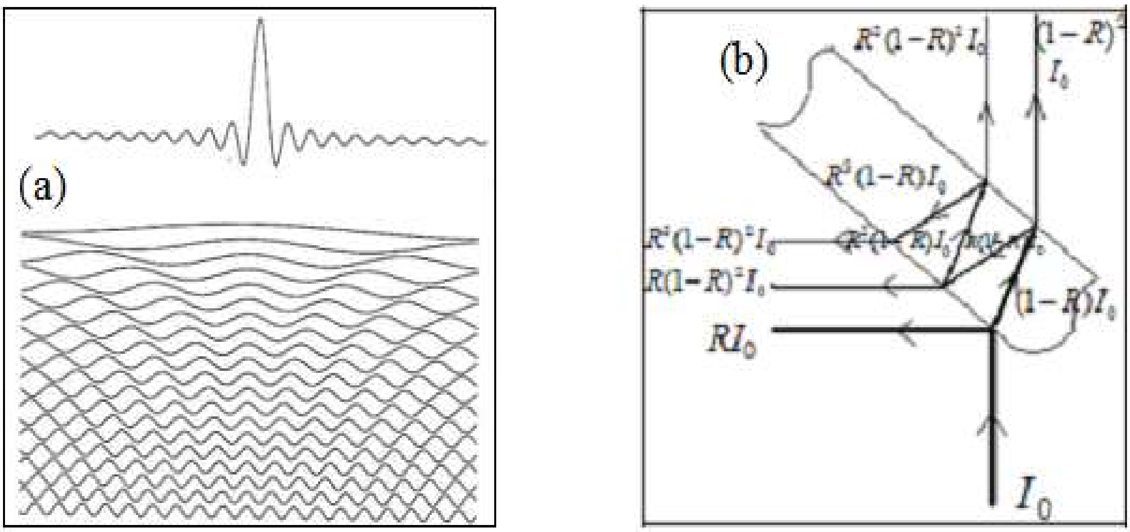

**Figure 2.15:** (a) Generation of interferogram at the beamsplitter by the superposition of many interfered beams of different wavelengths, (b) Reflection and transmittance of the beam through a beamsplitter. Generally primary transmitted and primary + secondary reflected beams are important.

where $k$ is wavevector and $\sigma$ is frequency. For many waves, the amplitude in the wavetrain is

$$\begin{aligned} y(z) &= (1/\bar{\sigma}) \int_0^{\infty} a(\sigma)\ cos(2\pi\sigma z)\ \mathrm{d}\sigma \\ &= \int_0^{\infty} b(\sigma)\ cos(2\pi\sigma z)\ \mathrm{d}\sigma = \frac{1}{2}\int_{-\infty}^{\infty} b(\sigma)\ e^{(i2\pi\sigma z)}\ \mathrm{d}\sigma \end{aligned} \tag{2.13}$$

where, $b(\sigma) = a(\sigma)/\bar{\sigma}$ is real and let $\frac{1}{2}b(\sigma) = \in(\sigma)$ = field amplitude of wavenumber $\sigma$

Therefore,

$$\begin{aligned} y(z) &= \int_{-\infty}^{\infty} \in(\sigma)\ e^{i2\pi\sigma z}\mathrm{d}\sigma \equiv f\{\in(\sigma)\} \\ \in(\sigma) &= \int_{-\infty}^{\infty} y(z)\ e^{-i2\pi\sigma z}\mathrm{d}\sigma \equiv f^{-1}\{y(z)\} \end{aligned} \tag{2.14}$$

For two arms of the interferometer,

$$\begin{aligned} y(z) &= y_1(z) + y_2(z) \\ &= \int_{-\infty}^{\infty} \in(\sigma)\, e^{i2\pi\sigma z}\mathrm{d}\sigma + \int_{-\infty}^{\infty} \in(\sigma)\, e^{i2\pi\sigma(z-\delta)}\mathrm{d}\sigma \\ &= \int_{-\infty}^{\infty} \in_R(\delta,\sigma) e^{i2\pi\sigma z}\mathrm{d}\sigma \end{aligned} \tag{2.15}$$

where, $\in_{\mathrm{R}} = \in(\sigma)[1+\mathrm{e}^{-\mathrm{i}2\pi\sigma\delta}]$ is the net amplitude and $\delta$ is the path difference. Various steps in the calculations to obtain the spectrum are combining waves from two arms of the interferometer, finding the resultant amplitude, computing the flux density, solving the equations to find the flux vs. wavenumber [82]. The final result is,

$$B(\sigma) = (const.)\int_{0}^{\infty} I(\delta) cos(2\pi\sigma\delta)\mathrm{d}\delta \tag{2.16}$$

where, I($\delta$) is interferogram and B($\sigma$) is spectrum.

The resolution is defined by the Rayleigh criteria. For higher resolutions, more data points are required in a given spectral range for which the mirror should move a longer distance, i.e. R $\propto$ ($1/\delta$), where R is resolution and $\delta$ is path difference and equals two times mirror displacement. To resolve two features separated by $\Delta\sigma$, length of the scan distance is given by L = $1/2\Delta\sigma$. Further, in the interferometer, the detector sees a modulated beam and the frequency of detection is given by $f = 2v_m\sigma$, where $v_m$= mirror velocity and $\sigma$ is wavenumber. The advantages of these interferometers over grating instruments are:

1. Throughput/ Jacquinot advantage - no slits used, full source power reaches the detector.

2. Multiplexing/ Fellgett advantage - No monochromator is used, i.e. all the wavelengths are simultaneously sent to the sample.

3. Rapid data collection.

These advantages imply that many scans can be co-added to achieve a very high signal to noise ratio. In addition, it also offers other advantages like:

4. Resolution - depends on length of mirror scan, can be very high.
5. Conne's advantage - Single frequency He-Ne laser is used for mirror movement control, which is very precise and several repetitive scans can be co-added to give better S/N ratio.
6. Highly precise frequency calibration possible with He-Ne laser.

The limitations of FT- infrared spectroscopy technique are:

1. Fourier transform limits go to infinity on either side and infinite path difference is not possible in practice. This introduces side lobes into the transformed spectra because of finite optical path difference and one has to use correction factor called "Apodization function", ("*apod*" means "*having no feet*") to reduce these spurious features. Moreover due to phase shift introduced from beam splitter, interferogram is not symmetric. So an extra phase shift is introduced, deviating from the ideal case of symmetric about ZPD.
2. FTS is a doppler limited technique, thus sample temperature plays a role in high resolution studies.
3. Water is strong absorber in IR region and can dissolve various IR transparent materials, which introduces several constraints in instrumentation and data analysis.
4. FTS is a single beam technique. Background spectrum ($I_0$) & sample spectrum (I) are measured at different times.

Table 2.1 summarizes various important components used in different regions of the infrared part of electromagnetic spectrum.

Table 2.1: Various components used in different regions of infrared spectra.

| | **Spectral range ($cm^{-1}$)** | **Source** | **Beamsplitter** | **Detector** |
|---|---|---|---|---|
| **Far infrared** | 10–600 | Hg lamp | Mylar (Polyethylene terepthalate;$n$=1.8) | LHe - Bolometer<br>DTGS - polythelene |
| **Mid infrared** | 300–8000 | Globar(SiC) | KBr | $LN_2$ -HgCdTe, DTGS |
| **Near infrared** | 6000–15000 | Tungsten lamp | $CaF_2$, Quartz | $LN_2$ -InSb, Si diode |
| | | Synchrotron radiation far-IR to UV | | |

## 2.4 High pressure infrared spectroscopy

### 2.4.1 Infrared microspectroscopy

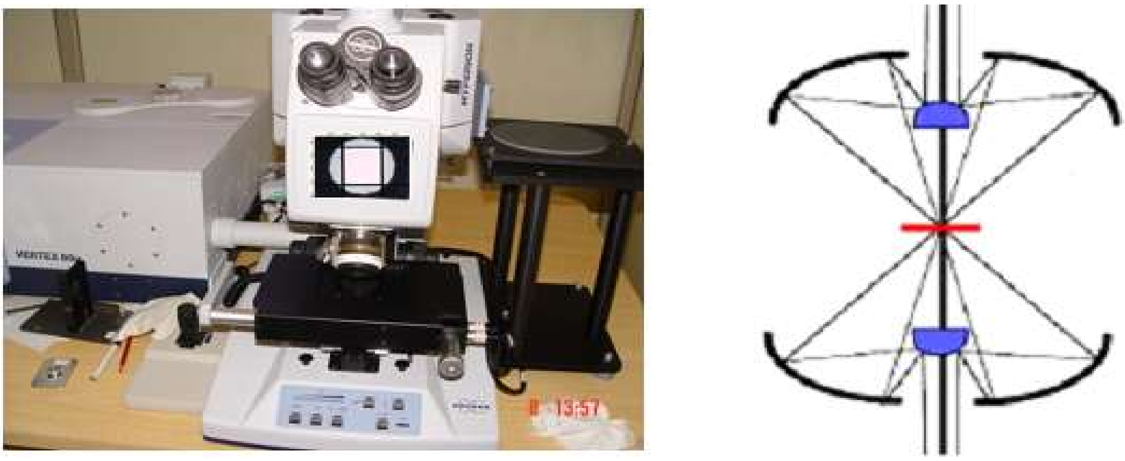

Figure 2.16: Photograph of the IR microscope coupled to the interferometer and the objectives employed in the microscope showing focussing and defocusing of beam at the sample.

In order to investigate samples of spatial dimensions in tens or few hundreds of microns, special focusing systems are required to achieve the desired spot size (Figure 2.16). The beam from the interferometer is focused by the Cassegrain condenser onto the sample and the transmitted beam, collected by another short focal length objective, is sent to the detector. A flip mirror can be used to see

**Table 2.2:** Details of various objectives used with Hyperion 2000 IR microscope.

| Objective | Objective magnification | Visible magnification | Numerical Aperture | Working distance (mm) | Distance between |
|---|---|---|---|---|---|
| 4× viewing | 4× | 57× | 0.1 | 21 | Sample-objective |
| 15× IR | 15× | 215× | 0.4 | 24 | Sample-objective |
| 36× IR | 36× | 515× | 0.5 | 10 | Sample-objective |
| ATR | 20× | 286× | 0.6 | 6 | Sample-crystal crystal |

the sample visually or capture image/video. The spatial resolution depends on the wavelength of the incident radiation, which becomes a matter of concern for longer wavelengths (far-IR) due to diffraction limit. With the coupling of an infrared spectrometer to a microscope, it becomes possible to study samples with a spatial resolution limited by the near diffraction limit of IR radiation (up to $\sim$ 3 - 10 $\mu$m for mid-IR). Synchrotron source particularly benefits such studies by offering reasonable signal to noise ratios at small spot sizes. Numerically, spatial resolution for confocal microscopes is,

$$1.22\lambda/(NA_{Objective} + NA_{Condenser}) \tag{2.17}$$

where $\lambda$ is wavelength and $NA$ is numerical aperture. This implies, for very long wavelengths (far-IR), the spatially resolved spot sizes are too large and thus sample sizes need to be increased which imposes constraints in high pressure experiments. The specifications and details of the objectives used with the present microscope are described in Table 2.2. Thus, for example, while doing reflectance studies using a 15x objective having numerical aperture of 0.4, the theoretical limit of diffraction limit can be estimated to be around 152 $\mu$m, 76 $\mu$m and 30 $\mu$m for 100, 200 and 500 cm$^{-1}$ respectively.

However in high pressure studies, due to the shortening of the wavelength, as the beam enters inside the diamond anvils with a higher refractive index ($\sim 2.38$ in far-IR), it may become possible to obtain some signal in the far-IR regions even if the wavelengths are greater than the diameter of gasket hole. Further, a wide-aperture miniature cell is preferable due to the limited space in the microscope. The measurements, in the microscopy setup, can be performed in transmission, reflection, diffuse reflection, reflection-absorption, grazing incidence and attenuated total reflection (ATR) modes and one can also conduct polarization dependent experiments. There are three objectives available for magnifications of 4×, 15× and 36×. However, for higher magnifications, working distances are smaller. For high pressure studies, a 15× objective was used.

### 2.4.2 High Pressure technique

Pressure is defined as force per unit area. When we apply external pressure on a deformable body, for example of cubic shape, stress is generated, which is a measure of the activated internal forces. The stress tensor has nine components, 3 orthogonal normal stresses - normal to surfaces and 6 orthogonal shear stresses - parallel to surfaces. Thus on each of the six faces, there are three components acting, i.e. one direct/normal stress and two shear stresses. In the matrix describing the tensor, the off diagonal terms, i.e. shear stresses are equal in the case of static equilibrium. Further, the matrix can well be described as a combination of two other matrices, one of which is the quasi-hydrostatic case (diagonal matrix with off-diagonal terms zero) and the other containing rest of the elements. In the pure hydrostatic case, this second matrix should be equal to zero with the first having all the diagonal elements equal to the average of the three normal stress components along $x$, $y$ and $z$ directions. In practice, although the pressure is applied uniaxially, the hydrostatic condition can be approached by using pressure transmitting medium (PTM) (generally a fluid or soft material) which

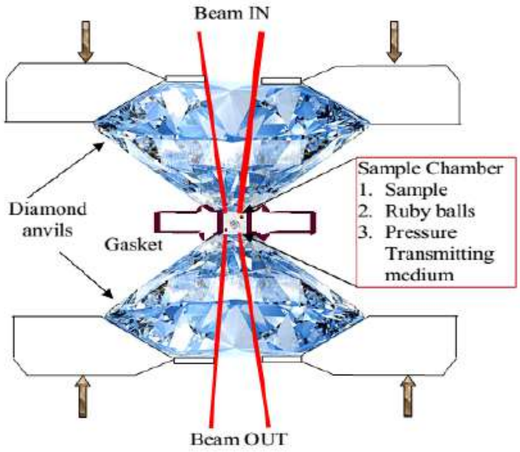

**Figure 2.17:** A Diamond Anvil Cell (DAC) consisting of two diamonds, a sample chamber between two culets, gasket and rockers used for in-situ high pressure measurements.

ensures that the material is compressed homogenously and the load is transmitted slowly. Thus, we prepare a sample chamber filled with PTM, pressure marker and the sample, which can be compressed using appropriate static high pressure generating devices like piston-cylinder or opposed-anvil type (Figure 2.17).

The opposed anvil devices have smaller sample volume implying higher pressure capabilities. The high pressure generating capabilities also depend upon the strength of the anvil material. Diamond offers the best solution, which has the highest strength with bulk modulus of $\sim$ 440 GPa and at the same time transmits nearly full electromagnetic spectrum. It is also a good thermal conductor and a wide band gap insulator. The tip of the diamonds, "culets", are fine polished to generate flat surfaces of size $\sim$300 $\mu$m. A metallic gasket of thickness $\sim$ 50 - 100 $\mu$m, with a drilled hole of diameter $\sim$200 $\mu$m, is used to prepare sample chamber between the two culets. For very high pressures, for example in Mbar region, the sample as well as gasket hole sizes need to be further reduced.

The most common PTMs are liquids (methanol-ethanol, silicone oil etc.) and soft solids (eg. alkali halides - NaCl, KBr, CsI, KCl etc.) which provide reasonably good quasihydrostatic conditions for high pressure experiments. Condensed gasses (He, Ne, $N_2$, Ar etc.) are best mediums for room and low temperature,

but it is difficult to load them in DAC without gas loading or cryogenic devices. For pressure monitoring, the most commonly used methods are equation of state of elemental metals like Au, Pt, Cu, Ag etc and Ruby fluorescence method. Ruby is $Cr^{3+}$ (0.05 wt%) doped $\alpha$-$Al_2O_3$ and it does not show phase transition upto Mbar pressures [84–86]. Upon laser excitation, it de-excites first to the metastable states ($E_{1/2}$ and $E_{3/2}$) through non radiative decay and then to the ground state giving two intense luminescence lines [87]:
R1:($E_{1/2} \rightarrow {}^4A_2$) at 694.2 nm (14402 $cm^{-1}$)
R2:($E_{3/2} \rightarrow {}^4A_2$) at 692.82 nm (14432 $cm^{-1}$)

By measuring the shift (see Figure 2.18) in the ruby luminescence lines upon compression, the pressure value can be calibrated (nearly up to 30 GPa) using the linear relation :

$$P(kbar) = 2.746\Delta\lambda(\mathring{A}) \tag{2.18}$$

This pressure scale has also been extended for higher pressures and upto Mbar regions where it does not follow a linear relation, for quasi- as well as non-hydrostatic conditions [88]. For a perfect hydrostatic compression, the difference between the Ruby lines, R1-R2, also remains constant and thus, one can also anticipate the deviations from hydrostatic nature during the experiments [89]. The deviations result from two effects, first is the line broadening due to inhomogeneous stress distribution and second, more sensitivity of the R1 line compared to R2 for non- hydrostatic compression.
Though, DACs (Figure 2.19) are ideal for high pressure experiments in various fields, for infrared studies, there are certain limitations. As mentioned previously, the experiments are conducted using an infrared microscope employing Shwarzchild objectives which offer small working distance. Thus,

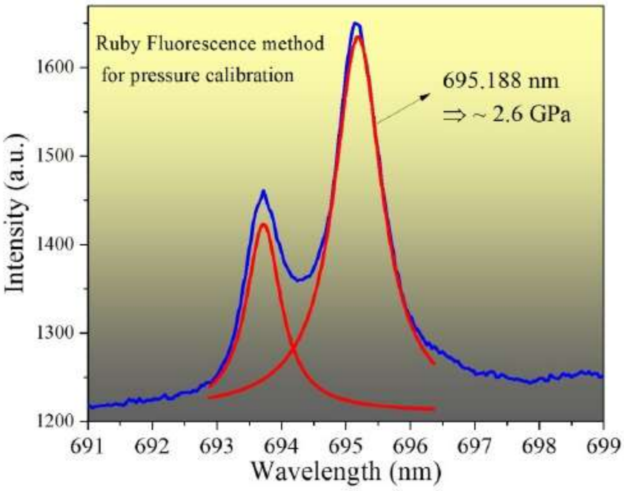

**Figure 2.18:** Increase in fluorescence wavelength of Ruby R lines under compression used to monitor the change in pressure.

1. Working distance should be more than twice the cell length (DAC height).
2. The optical aperture on both sides of DAC must be $\geq$ cassegrain mirror.
3. Cell design should ensure the parallelism of anvils to the highest pressures.
4. Owing to their IR absorption, as shown in Figure 2.20, normal diamonds can't be used and type IIa impurity free diamonds are required which are not commonly available. These diamonds, however, also show IR absorption in the region 1800–2600 cm$^{-1}$ (two-phonon spectrum).

Thus, although, a conventional piston-cylinder type Mao-Bell DAC could be used for Raman and X-ray diffraction measurements, special small DACs were used for IR studies by compensating the above requirements (Figure 2.19 ).

For infrared absorption studies, an indigenously developed clamp type symmetric DAC (Figure 2.19 top left) was mounted on the sample stage of Hyperion-2000 IR microscope coupled to the Bruker Vertex 80 V FTIR equipped with various sources and beamsplitters, installed at the experimental station of IR beamline

**Figure 2.19:** (Top) Diamond anvil cells used for IR spectroscopy: an in-house made symmetric DAC and a Bohler type DAC; (bottom) Mao-Bell cell which was used for Raman and XRD measurements.

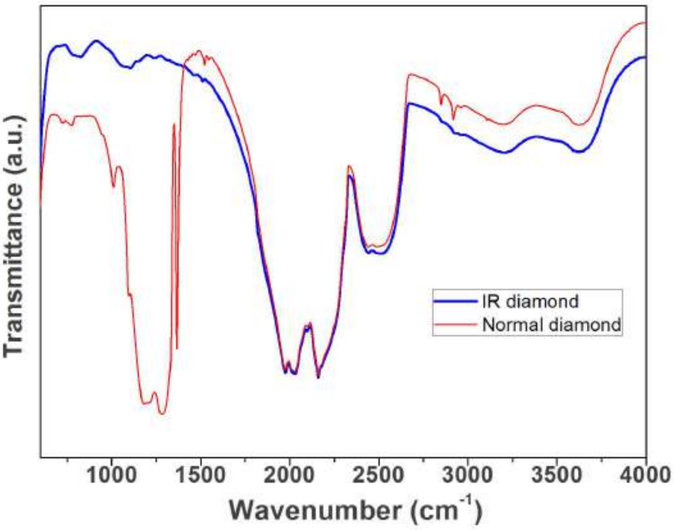

**Figure 2.20:** Mid- infrared absorption spectra of normal diamond and type IIa IR diamond, recorded using Bruker IFS125 instrument.

at Indus-1 synchrotron source facility in India. A liquid nitrogen-cooled MCT detector was used for the complete mid-infrared range. Polycrystalline sample in CsI matrix along with a ruby ball was loaded in a 150 $\mu$m hole of a tungsten gasket preindented to a thickness of $\sim$60 $\mu$m for absorption studies. Ruby balls were kept both near the center and at the periphery of the diamond anvil cell. Pressure calibration was done using ruby fluorescence method. Empty cell spectra and that of CsI loaded in the DAC were used to deduce the sample transmittance. For clear identification of all the spectral features in the 600-4000 cm$^{-1}$ spectral range, the spectra were recorded at 2 cm$^{-1}$ resolution. To check the reproducibility of the observed features, the measurements were repeated at resolution of 2 as well as 4 cm$^{-1}$. The ambient pressure spectra of various molecular solids, which were characterized using thermal as well as synchrotron source, were also recorded using Bruker IFS125 HR FT-spectrometer and all the peak positions recorded from the two spectrometers showed excellent agreement. The measurements on glycinium oxalate were also repeated to probe the far infrared response at the SISSI beamline of Elettra synchrotron source, Italy (electron beam current 300 mA, energy 2.0 GeV) using a liquid Helium cooled Bolometer detector to cover the spectral range from 100-700 cm$^{-1}$.

## 2.5 Low temperature Infrared spectroscopy

The facility for in-situ low temperature studies has also been setup at the beamline (Figure 2.21). A continuous flow cryostat (Oxford make, Optisat CF-V) is mounted in the sample compartment of the instrument, which is connected to a liquid Helium Dewar through a transfer line. Helium vapour recovery lines, from cryostat, dewar, transfer line and dewar safety adapters, have been installed in the experimental hutch which are connected to the main line of the Cryogenic facility to ensure zero leakage of the expensive Helium gas from any of the components. Further, the dewar is routinely evacuated to minimize the He evap-

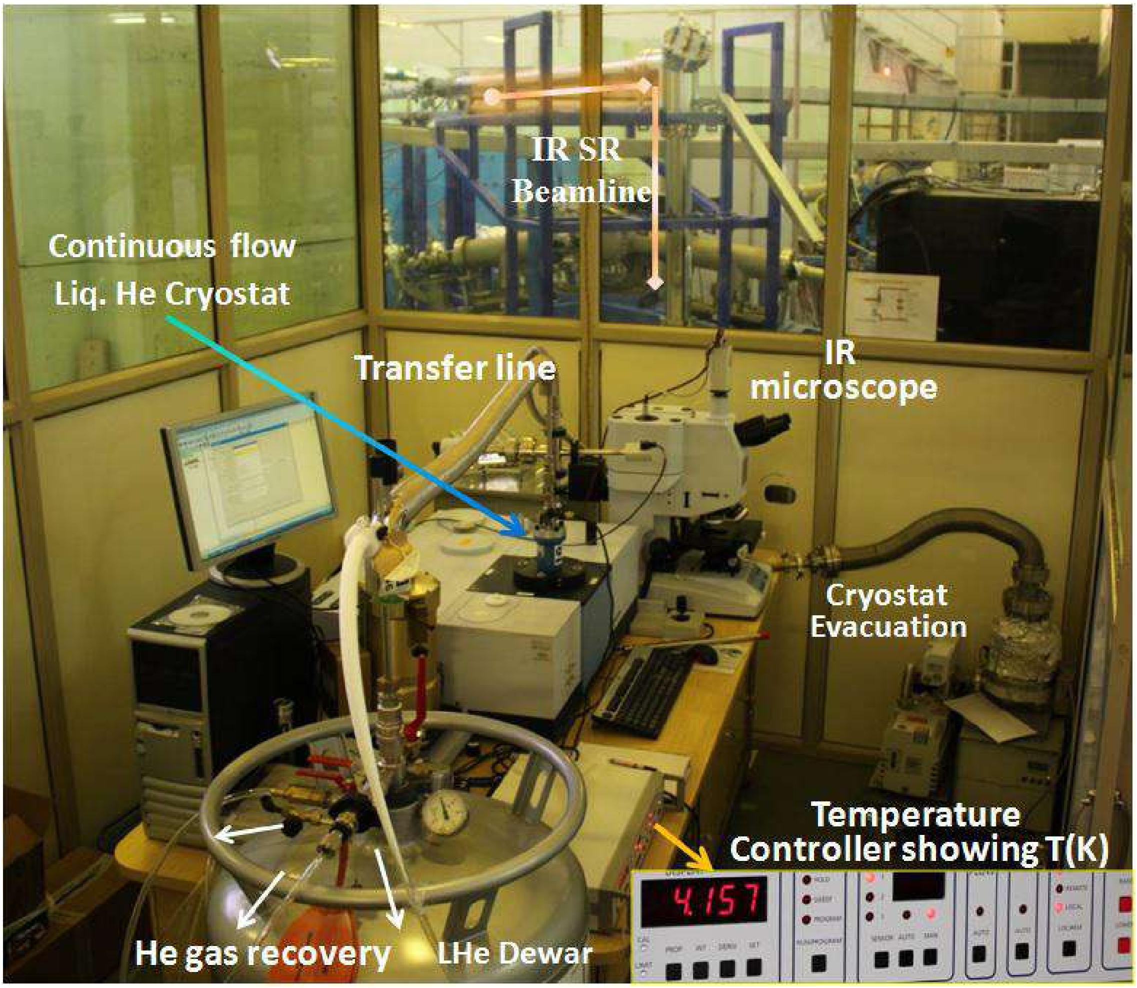

**Figure 2.21:** Photograph of the experimental station of the IR beamline at Indus-1, with IR microscopy setup for high pressure, low temperature setup showing minimum temperature achieved (~4.2 K) and far-IR measurements using liquid He cooled Bolometer detector.

oration rate. Helium flow is monitored using a gas flow controller calibrated for He vapours. Flow rate is controlled using the gas flow controller, an oil free pump and mechanical valves at the transfer line and liquid He dewar. Measurements can be done at fine temperature steps of less than 1 K which can be controlled using a temperature controller having a temperature sensor as well as heater. A minimum temperature of $\sim$ 4.2 K has been achieved. The same system can be used to record the spectra at high temperatures also, up to 500 K. Further, for applications up to 77 K, liquid nitrogen can also be used as the cryogen along with a nitrogen flow meter. However, the transfer line has to be flushed and evacuated thoroughly while switching the cryogen. Highly thermal conducting sample mounting blocks of varying sizes, surfaces and shapes have been designed to study various kinds of samples, like small single crystals, using this set up.

## 2.6 Other facilities setup

In addition to the above facilities, a versatile lab based facility has also been setup which consists of a high resolution (0.0012 cm$^{-1}$) FTS system (Bruker IFS 125HR, spectral range far-IR to UV), a FT-Raman (Bruker MultiRam) system, an indigenously developed long optical path length (max. 60 m) gas absorption cell and various other auxiliary systems for high resolution absorption and emission spectroscopy (Figure 2.22). These IR and Raman systems were utilized for ambient characterization of all the samples studied in the present thesis. With FT-Raman technique, one can get rid of the possible fluorescence background and it is possible to record high quality spectra, particularly for organic samples, in the complete frequency range (60-3800 cm$^{-1}$) in a single scan.

In addition, there are various accessories available for versatile use of all the facilities that have been setup. For example, the accessories used for specular reflection (to study plane- smooth surfaces) at near normal incidence as well as at variable angle of incidences from 13° to 89°, DRIFT (Diffuse reflectance) to

**Figure 2.22:** (first row) (left to right) A high resolution FTS system, also shown is a long path length gas absorption cell optially coupled with the FTS; FT-Raman system employing a NIR 1064 nm Nd:YAG laser for excitation, liquid nitrogen cooled Ge detetector and a Michelson interferometer. (second row) the optical set up/ internal view of the high resolution FTS system. (third row) (left to right) schematic showing working principles of specular, DRIFT and ATR reflection techniques.

study reflectance data of powders by collecting scattered light from various directions and ATR (Attenuated Total internal Reflection) used to study polymers, liquids, thin films, surface enhanced spectroscopic studies etc., which works on the principle of total internal reflection inside a crystal surface and the interaction of evanescent wave with the sample, have been shown in Figure 2.22 third panel.

## 2.7 Raman scattering system used for high pressure studies

High pressure Raman spectroscopic studies were carried out using an already existing facility, which is based on an indigenously developed confocal micro Raman setup in back scattering geometry, configured around Jobin Yuon (HR 460) spectrograph (Figure 2.23). This is a dispersive type spectrograph and is equipped with a liquid nitrogen cooled CCD detector. There are two pre-aligned gratings with 1200 and 2400 groves per mm at 500 and 250 nm respectively, which give a resolution of 0.015 and 0.03 nm respectively. There are two lasers which can be used for excitation, a diode pumped solid state Nd:YAG laser (532 nm) or an Ar-ion laser (457 nm). A notch filter is used to block the Rayleigh scattered signal.

The spectra at each pressure were calibrated using standard neon lines [90, 91]. Polycrystalline sample along with $\sim$10 $\mu$m ruby ball was loaded in the preindented tungsten gasket of thickness $\sim$70 $\mu$m with a hole of diameter $\sim$100 $\mu$m in a modified Mao-Bell type of DAC (Figure 2.19). In the repeat measurements, ruby balls were kept at the center as well as at the peripheries for accurate pressure determination. The ambient pressure spectra were also recorded using the Bruker MultiRAM FT-Raman spectrometer, and all the peak positions in ambient pressure spectra recorded from the two spectrometers were in excellent agreement. The experimental details of other complementary techniques used

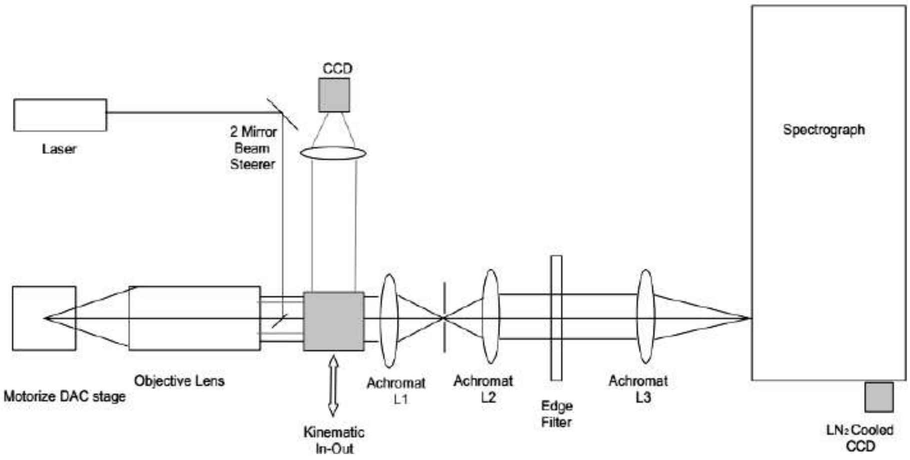

**Figure 2.23:** Layout of the confocal micro-Raman setup used for high pressure studies. The shaded beamsplitter, used with a kinematic mount is used to divert the beam to a viewing arrangement.

for the investigations, like X-ray diffraction and first principles simulations are described in the respective chapters.

## 2.8 Sample preparation

### Glycine and oxalic acid complexes

Colourless single crystals of bis(glycinium) oxalate were grown by slow evaporation from an aqueous solution containing glycine and oxalic acid in a 2:1 molar ratio. The melting points of crystalline samples were determined using differential scanning calorimetry (Mettler Toledeo DSC 821E). The samples were heated at a rate of 10K min$^{-1}$ from 123 K up to the melting point. The samples were were characterized using single-crystal X-ray diffraction, neutron diffraction, Raman spectroscopy as well as infrared absorption studies. Similar procedure was adopted for glycinium oxalate (glycine: oxalaic acid :: 1:1). In each case, clear crystals of approximately 2×2×1 mm$^3$ were selected and used for the measurements. Polycrystalline samples of oxalic acid dihydrate and acrylamide were purchased commercially from Thomas Baker and Sigma Aldrich. The purity of the samples was better than 99.99%.

**Doped lanthanum chromite samples**

An aqueous solution of nitrates of lanthanum, chromium, calcium or strontium corresponding to the composition $La_{0.7}Ca_{0.3}CrO_3$ (LCC) and $La_{0.8}Sr_{0.2}CrO_3$ (LSC) was obtained from stock solutions of individual metal nitrates. Stoichiometric amount of citric acid required for combustion was dissolved in the mixed solution. The solution was evaporated overnight to form into a dried gel at 80°C in air oven. The oven dried gel was subjected to smooth combustion on a laboratory heater to form into a porous powder mass.The resulting powder was dried and wet ground in a planetary mill to a fine mass and has been denoted as "As prepared" specimen in the forthcoming text. Powder samples were calcined at varying temperatures in the range of 600°C to 1200°C in a programmable laboratory kanthal furnace for 1 hour to tailor their pore structure. As prepared as well as powders calcined at 600°C, 900°C and 1200°C of LCC and LSC have been taken for infrared absorption, X-ray diffraction, small angle neutron scattering and scanning electron microscopy experiments.

**$RuSr_2GdCu_2O_8$(Ru1212)**

Stoichiometric ratios of spectroscopic grade $RuO_2$, $SrCO_3$, $Gd_2O_3$ and CuO powders were mixed. The mixture was subjected to a series of calcination steps after ball milling at around 1000°C. Pelletized powder was sintered at 1060°C in air followed by in excess oxygen for 96 hours to attain a high purity sample. Phase formation was confirmed by XRD.

# 3

# High pressure investigations of Oxalic Acid Dihydrate - proton transfer aiding phase transitions

## 3.1 Introduction

Oxalic acid dihydrate $(COOH)_2.2H_2O$ (OAD) is the simplest dicarboxylic acid complex. In the crystal structure, one oxalic acid molecule is connected to two water molecules on both sides through a strong hydrogen bond and the three dimensional network is framed by other hydrogen bonds. OAD, though an extensively studied system for past several decades, has continued to show many new surprises, especially in the solid state.

### 3.1.1 OAD - a model system

A detailed survey of prior studies on OAD and some of its applications have recently been reported by Stare and Hadzì [92]. The compound is being studied for nearly a century and has been investigated by a number of techniques like X-ray diffraction [93–97], neutron diffraction [98–101], isotopic substitution [102] and electronic density studies [103–105] using experiments as well as theory [92, 106–109], which have established it as a benchmark crystallographic system for neutron diffractometers [110] and also a benchmark hydrogen bonding system, as it is a simple complex offering rich hydrogen bonding network comprising of a very strong and two moderately strong hydrogen bonds governing its structure and properties. The strong hydrogen bond in OAD is a very short $O_1$-$H_t$---$O_w$ bond ($d_{O1---Ow} \sim 2.49$ Å, $\angle O_1HO_w \sim 177°$) between oxalic acid and water, which makes it an ideal system to study proton dynamics [35]. This hydrogen bond falls on the very short side of the values collected for a number of carboxylic acid monohydrates, dihydrates, pyrazine di-, tri- and tetra- acid hydrates where the average value for $d_{O---O}$ lies around $\sim 2.59$ Å [101, 111, 112].

The proton dynamics of such hydrogen bonds, which still remains intriguing, is vital in the context of determining the properties of several hydrogen bonded species where the hydrogen is placed close to the symmetrised position. Recently, it has been shown that the hidden force responsible for anomalous proton dynamics in O-H---O hydrogen bonds in ice close to symmetrisation is the coulombic interaction between a covalently shared electron pair and a virtually bonded lone pair [31]. Such interactions are enhanced in the cooperative network of several hydrogen bonds in series which eventually increases their strength.

### 3.1.2 Cooperativity of hydrogen bonds

In $O_1$-$H_t$---$O_w$, the acceptor $O_w$ (oxygen atom of water) also acts as a donor for the carbonyl group of subsequent OA molecule, forming a chain,

--C-$O_1$-$H_t$---$O_w - H_w$---$O_2 = $ C-, as shown in Figure 3.1. The C = O group is an acceptor of the two moderately strong hydrogen bonds from water. The alternate hydrogen bonded chain causes small polarization in the associated bonds, including the covalent single as well as double bonds, thus leading to a net decrease in O---O through the well known cooperativity effect of hydrogen

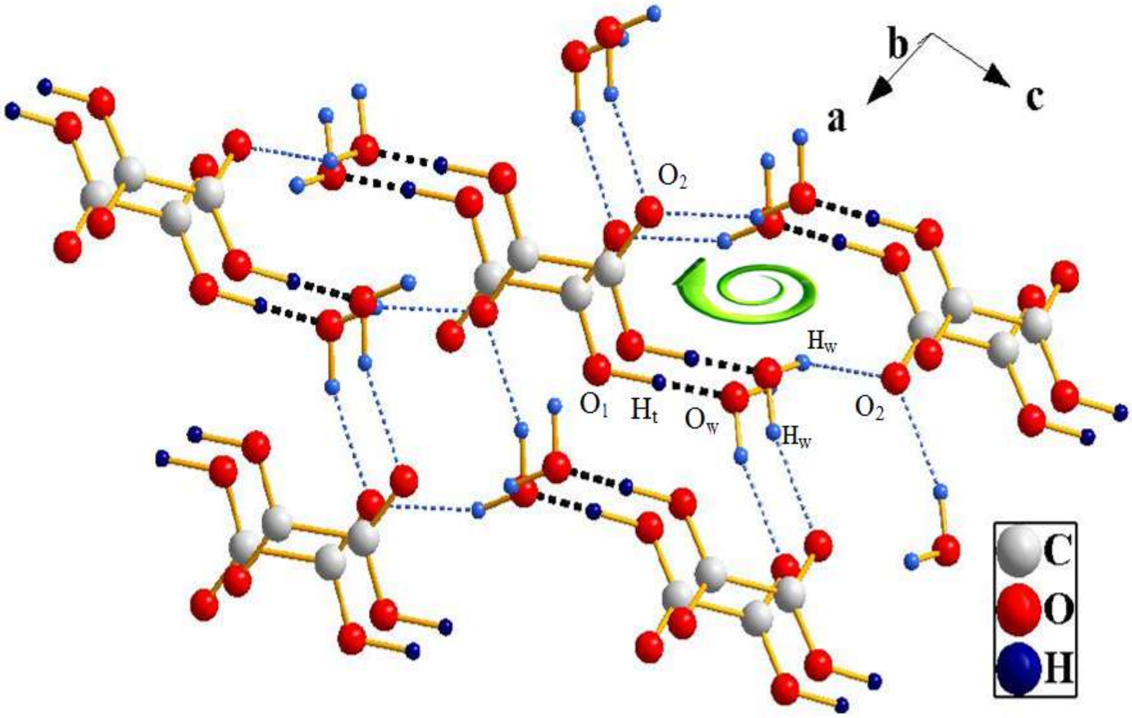

**Figure 3.1:** In the three dimensional network in OAD, cooperativity effect among the hydrogen bonds in series runs through spiral motifs along the screw axis to enhance structural stabilization and strengthening of $O_1$-$H_t$---$O_w$ hydrogen bond ($O_1$ and $O_2$ are single and double bonded oxygen atoms respectively, $O_w$ - water oxygen, $H_t$ - acid hydrogen and $H_w$ - water hydrogen). Here, blue balls and lines (dashed) are hydrogen atoms and bonds respectively and dark blue shows the proton transfer pathway (where water is acceptor).

bonds [8,92,113–115]. The nature of this cooperative effect has also been a subject of study through model calculations as well as experiments. Various structural assemblies like dimeric, trimeric, linear, circular and quasi circular chains have been analyzed to establish and understand the quasi-circular motifs of acid molecules in OAD which are connected by the strong hydrogen bonds ($O_1$-$H_t$---$O_w$) with water molecules nearly in the same plane [92, 95, 111, 112]. The relatively longer hydrogen bonds ($H_w$---$O_2 = C$) connect these planes, thus forming a spiral network approximately in the direction of the crystal *b*-axis. Note that the cooperativity effect in hydrogen bonded chains in acids, fluorides, cyanides, formamide, polyglutamine, water clusters etc. has been used to model this effect in biological systems and proton dynamics in biological processes [116–119].

### 3.1.3 Towards strengthening of the short hydrogen bond in OAD

When the hydrogen atom ($H_t$) moves further towards the bond centre, interesting proton dynamics resulting in increase in anharmonicity and proton migration in the hydrogen bonded network leading to doubly ionized oxalates are expected. However, the initial beliefs, which date back to 1930s, of observing a proton transfer state of oxalic acid dihydrate at ambient conditions [93–96, 120] were ruled out by a number of X-ray and neutron diffraction and electron density studies which established the presence of neutral oxalic acid with single as well as double C−O bonds [97–100, 103–105, 121]. Also, at low temperatures only a sustained strengthening of the hydrogen bond was noted [122–125]. The first high pressure powder neutron diffraction experiments up to 0.5 GPa did not show any significant movement in proton [126]. Subsequent studies were primarily focussed on the shortness of this hydrogen bond, where the O---O distance was found to be less than the average carboxylic acid monohydrates as well as the hetero-trimer (with two water molecules) acids [92, 101, 111, 112].

The recent DFT calculations by Casati et al. predicted that a proton migrated state may become possible only at pressures as high as 5.3 GPa with the geometry posing a symmetric disposition of hydrogen bond up to this pressure [5]. Their X-ray diffraction studies showed significant changes in molecular geometries, specially the C−O bond lengths, but unambiguous determination of hydrogen atom positions was not possible. The neutron diffraction experiments, carried out on deuterated samples, did not show the proton migrated state up to 6 GPa, though the accompanied theoretical treatment on neutral and charge transfer configurations provided useful information on this phenomenon [127]. It is the idea, as indicated by theory [5], of the double minimum on the potential energy surface, with more stable neutral state above 4 GPa, constantly evolving towards the symmetric character up to $\sim$ 5 GPa, that prompted us to look for the possible experimental signatures of hydrogen bond close to the symmetrization limit. Such an event at further higher pressures may bring about equivalence between the constantly competing lone pair and shared bond pair, thereby distorting the cooperativity in hydrogen bonded three dimensional network. Thus, a concerted treatment of the hydrogen bond dynamics and the surrounding cooperative local structure is essential to understand its high pressure behaviour. In this context, spectroscopic studies are the ideal tools as they provide the necessary insights with regard to proton dynamics under pressure [5].

## 3.2 Methods

Our experimental investigations using infrared spectroscopy well complemented by Raman spectroscopy (details in chapter 2), provide unambiguous evidence of proton transfer at much lower pressures of 2 GPa in OAD. This is followed by the formation of a novel structure as a result of phase transition at further higher pressures.

### 3.2.1 Vibrational assignments

$\alpha$-oxalic acid dihydrate is an extensively studied system and its vibrational spectra are well characterized at ambient conditions. The mode assignments in the ambient infrared and Raman spectra have been carried out on the basis of theoretical and experimentally observed modes of OAD [35, 128], oxalic acid [129, 130] and various oxalate complexes [66,130–138] which have also been theoretically verified. To differentiate between various ionic forms of oxalic acid, vibrational studies on neutral-, semi- and dianionic- oxalic acid complexes; and ambient and high pressure infrared and Raman studies on Bis(glycinium)oxalate, and glycinium oxalate were utilized [66, 131, 132, 136–138]. This is supported by simultaneously probing the trend of the high pressure behaviour of IR and Raman active modes of OAD in the present study. Additional information could be retrieved based on the well

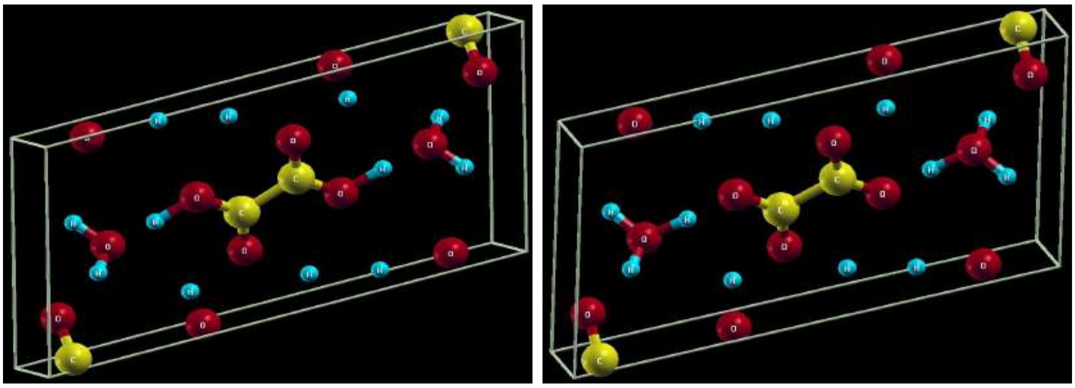

**Figure 3.2:** Simulated crystal structure of $\alpha$-OAD (monoclinic, $P2_1/n$) at (left) 0.1 MPa, (right) 1.5 GPa. Thermal ellipsoids are shown at the 50% probability level; yellow, red and cyan balls denote C, O and H atoms respectively.

known vibrational frequencies of hydronium ion [139–144]. For OH stretching modes, the correlation curves for stretching frequencies as a function of hydrogen bond strength, i.e. bond parameters have also been used [13, 145].

### 3.2.2 First Principles DFT calculations

The first-principles structural relaxations, as a function of volume, were carried out using Vienna ab-initio Simulation Package (VASP computer code) in order to corroborate our experimental results on proton transfer [146–149]. The initial structure model was constructed on the basis of reported experimental data [5, 150]. The exchange-correlation functional was treated with the generalized gradient corrected scheme of Perdew-Burke-Ernzerhof (PBE) [151]. The interactions between valence electrons and core were treated within the frozen-core all electron projector-augmented-wave (PAW) approach. Plane wave basis set was constructed using 600 eV energy cut off and the full Brillouin zone was sampled using a uniform 6×12×4 Monkhorst-Pack k point mesh [152]. The Cell shape and ions positions were optimized as a function of cell volume. Figure 3.2 displays the calculated crystal structures of OAD at ambient pressure and 1.5 GPa. As the crystal structures of the high pressure phases subsequent to proton transfer (above 2 GPa) were not known, the computational treatment has not been extended to higher pressures.

## 3.3 Pressure induced proton transfer

The hydrogen bonds connecting the acid groups of oxalic acid to the two water molecules on both sides are close to the symmetrization limit in OAD. In such strong O-H---O hydrogen bonds, the proton is relatively delocalized and the virtual bond has small covalent character [31]. The delocalization of proton results in interactions of the $\nu$OH (stretching) mode with other bridge vibrations and crystal modes [153, 154]. This leads to a broad absorption band, resembling a continuum, in the infrared spectrum [14, 155–158]. The centre of this band has been reported at nearly 2100 cm$^{-1}$ for oxalic acid dihydrate [35, 92]. If the hydrogen bond further strengthens under pressure and progresses towards a symmetric state, as predicted by theory [5], the $\nu$OH mode is expected to show softening accompanied with dampening. This would lead to an increase in system anharmonicity resulting in cascading interactions between vibrational energy levels [10]. However, depending upon the barrier height of the double well potential, any external stimuli may also result in the reorientation of hydrogen bond or immediate crossing over of the potential barrier. In the latter case of proton migration along $\mathrm{O_1}$-$\mathrm{H_t}$---$\mathrm{O_w}$, one would expect protonation of water thus forming hydronium ion. The present work provides key spectroscopic evidences of this phenomenon as described below.

In Figure 3.3, the vibrational stretching region (3250 – 3600 cm$^{-1}$) corresponding to the water $\mathrm{O_w} - \mathrm{H_w}$ bonds has been shown which depicts two clear bands in the ambient phase. At high pressures, above 2 GPa, we note the emergence of the characteristic $\nu_1$ ($\mathrm{O_w} - \mathrm{H_w}$) IR mode at $\sim$ 3100 cm$^{-1}$ which confirms the formation of hydronium ion ($\mathrm{H_3O^+}$) [143, 144], thus implying protonation of water molecules across 2 GPa in oxalic acid dihydrate. In the corresponding pressure

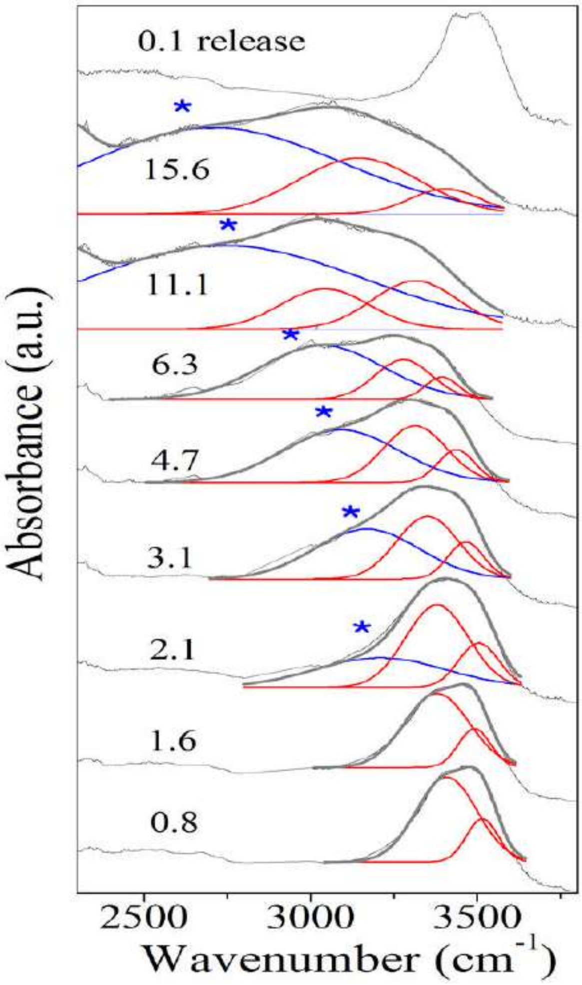

**Figure 3.3:** High pressure infrared spectra of OAD in the region 2300 – 3800 cm$^{-1}$ which shows evolution of the water stretching region with pressure; here asterisks ($*$) show the emergence of $H_3O^+$ stretching band (blue) with pressure and the spectra are normalized with respect to instrumental and environmental effects. Numbers denote pressure values in GPa.

range, proton migration from oxalic acid molecules is also revealed by an abrupt non-discernibility of the spectral signatures of oxalate $O_1$-$H_t$ (Figure 3.4), i.e. the broad stretching band, deformation modes as well as the features due to $\nu$OH mode couplings like the Evans transmission window (a relatively sharper negative dip near 1800 $cm^{-1}$, denoted by ⧫) [35]. These observations are well supported by the theoretical calculations that the proton transfer along $O_1$-$H_t$---$O_w$ takes place at quite low pressures (Figure 3.2), which is indicated by a reversal in the bond parameters of $O_1 - H_t$ ($d_{OH}$: ambient - 1.161 Å, 1.5 GPa - 1.30 Å) and $H_t$-$O_w$ ($d_{HO}$: ambient -1.267 Å, 1.5 GPa - 1.14 Å) bonds above 1.5 GPa. Different results in an earlier computational study may be due to a different computational methodology [5].

While the emergence of hydronium $\nu_1$ mode indicates protonation of water, its width indicates formation of another hydrogen bond suggesting reversal of hydrogen bond hierarchy, as depicted in Figure 3.5. The position of this mode, i.e. a relatively higher frequency, indicates asymmetrization of the resulting hydrogen bond, as also predicted by the calculated bond parameters $d_{\text{O-H}}$ and $d_{\text{H---O}}$. The stiffening of the $\nu O_1$---$O_w$ Raman mode ($\sim$ 280 $cm^{-1}$) [7,35] up to 2 GPa (Figure 3.6c) and softening thereafter up to 5 GPa provides experimental evidence of the elongation of $\nu O_1$---$O_w$ upon proton transfer (see also Table 3.1). In the subsequent sections, we discuss the molecular structure, mechanism of this proton transfer and the resulting hydrogen bonded network through the study of vibrational modes corresponding to COOH and OH groups of oxalate and water motifs respectively.

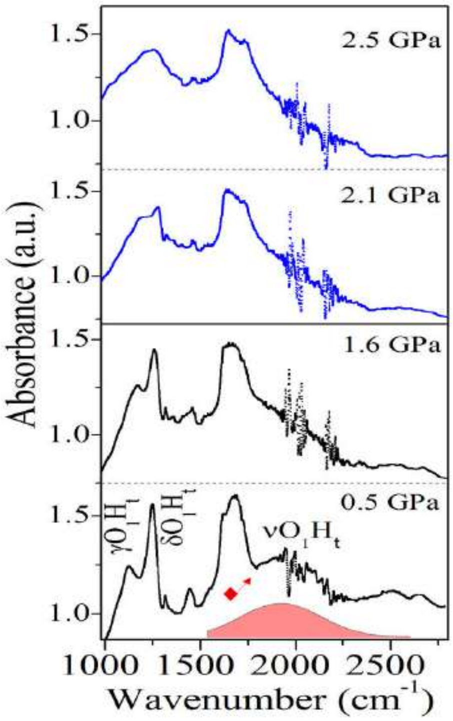

**Figure 3.4:** Mid-IR spectra of OAD in 1000-2800 cm$^{-1}$ region up to 2.5 GPa, before (black) and after (blue) proton transfer. The shaded band (pink) marks the presence of a broad $\nu$OH mode , small fluctuations near 2000 cm$^{-1}$ are due to second order diamond absorption and "♦" (in red) denotes the reported Evans transmission dip for OAD.

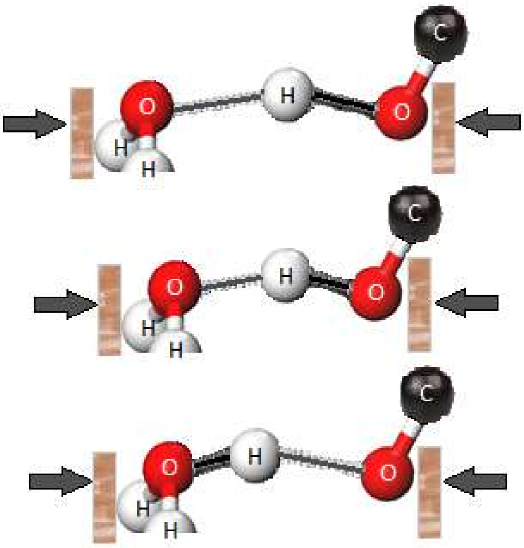

**Figure 3.5:** Pressure induced changes in the $O_1$-$H_t$---$O_w$ hydrogen bond.

**Table 3.1:** A summary of changes observed in the vibrational modes in various high pressure phases. A negative slope indicates pressure induced softening.

| Vibrational Mode | Value 0.1 MPa | Slope ($d\nu/dP$) $cm^{-1}/GPa$ Atm– 2GPa | 2–5 GPa | 5–9 GPa | >9 GPa | Remarks |
|---|---|---|---|---|---|---|
| **Raman** | | | | | | |
| $\nu O_1$---$O_w$ | 282 | 22.2 | -3.05 | 4.71 | 4.49 | |
| lib. $H_2O$ | 480 | 14.22 | 12.16 | 16.1 | 0.43 | Discontinuous shift across 9 GPa |
| $\nu CC$ | 846 | 1.14 | 0.5 | 0.06 | -0.76 | |
| $\nu CO_2$ | 1493 | 15.03 | 1.5 | 4.9 | 3.6 | Intensity increases above 5 and 9 GPa |
| $\delta H_2O$ coupled mode | 1630 | 1.4 | | | | Vanishes above 2 GPa |
| $\nu C = O$ | 1740 | -5.05 | weak | | | Vanishes above 2 GPa |
| $\nu CO + \nu C = O + \delta OH$ | 1694 | 3.4 | weak | weak | weak | |
| **IR** | | | | | | |
| $\nu C = O$ | 1680 | -5.3 | -2.3 | 0.05 | 2.8 | Merge into a band above 5 GPa |
| $\nu CO + \nu C = O + \delta OH$ | 1621 | 5.6 | 4.9 | | | |
| $\nu C$–O | | | 1.04 | 2.4 | 1.25 | |
| $\delta OH + \nu C$–O | 1255 | 15.4 | 5.9 | | | Vanishes above 5 GPa |
| $\gamma OH$ | 1145 | 27.5 | 10.5 | | | Vanishes above 5 GPa |
| $\nu OH$water | 3540 | -52.1 | -4.5 | -14.5 | 22.4 | Discontinuous shift across 9 GPa |
| | 3448 | -36.2 | -8.3 | -34.5 | 16.15 | |
| $\nu_1 H_3O^+$ | | | -45.9 | -60.4 | -7.5 | |
| $\nu_2 H_3O^+$ | | | 10 | 2.3 | 1.3 | |
| $\nu_4 H_3O^+$ | | | 1.43 | 3.0 | 1.32 | |
| $\delta(CO_2 + H_2O)$ | 725 | 6.05 | 11.5 | 10.9 | 3.2 | Discontinuous shift |

### 3.3.1 Proton migration - change in ionic state of OA

In oxalic acid, the migration of proton ($H_t$) is revealed by the systematic vanishing of the intense $O_1H_t$ deformation IR modes i.e. out of plane ($\gamma O_1H_t$ ~1145 cm$^{-1}$) and in-plane ($\delta O_1H_t$ coupled to $\nu$C–O ~1255 cm$^{-1}$) bending modes, with pressure as pointed in Figure 3.4) with detailed evolution showed in Figure 3.7. The transition to ionic state above 2 GPa due to loss of proton is indicated by the emergence of a new, relatively sharper, $\nu$C–O IR mode near 1318 cm$^{-1}$ which is a characteristic mode of dianionic form of oxalate (devoid of any hydrogen) and its relative intensity increases with pressure (Figure 3.7) [132, 136]. It is noteworthy that the neutral state of oxalic acid in OAD is characterized by strong coupling between various modes [35]. For example, the C–O ($\nu_{\mathrm{asy}}$: 1621 cm$^{-1}$) and C=O (~1680 cm$^{-1}$) bond stretching vibrational energy levels are strongly coupled, which has been attributed to Fermi resonance (Appendix A) [128, 129]. This coupling results in a complex spectral profile near 1700 cm$^{-1}$ and is expected to push the vibrational energy levels apart at ambient conditions. Under compression, systematic vanishing of this coupling is revealed by the large stiffening and softening in the $\nu_{\mathrm{asy}}$C–O and $\nu$C=O IR modes respectively which brings the two modes closer, as shown in Figure 3.8. Eventually, the disappearance of the C=O signature is complete and only a single broad band, resembling the $CO_2$ asymmetric stretching mode of dianionic oxalate is observed (Figure 3.7) in the ionic phase III above $\sim$ 5 GPa [132]. The vanishing of $\nu$C=O features in the 1700 cm$^{-1}$ region, as also clearly evident in the Raman spectra beyond 2 GPa (Figure 3.6b) is a definite signature of loss in the double bond character and emergence of anionic form of oxalate on both the carboxyl sides. This implies an equivalence of the two CO bonds in the acid group. The bond parameters obtained from first principles calculations have also shown that C–O (1.284 Å -at 0.1 MPa, 1.269 Å -at 1.5 GPa) and C=O (1.251 Å -at 0.1 MPa, 1.261 Å -at 1.5 GPa) bond lengths in OA approach each other upon proton migration. Thus, as the proton is transferred from oxalate carboxyl group to water at $\sim$ 2 GPa, all the C–O bonds in the COOH groups, in high pressure phase II, systematically become equivalent up to nearly 5 GPa, above which they are essentially indistinguishable in phase III (Table 3.1). The above spectroscopic observations also qualitatively explain the geometrical modifications in the C–O bonds measured earlier using X-ray diffraction [5].

The changes observed in the $CO_2$ deformation region (600 – 800 cm$^{-1}$) in high pressure IR spectra (Figure 3.7) upon proton ($H_t$) transfer are also consistent with the above observations. While the $\delta CCOOH_t$ mode ($\sim$ 620 cm$^{-1}$ ) [136], which weakens under pressure, merges with a new mode appeared near 715 cm$^{-1}$ at 2.1 GPa and systematically transform in to the $\delta CO_2$ band of dianionic oxalate [132], the ($\delta CO_2$ + $\delta OH_w$) coupled mode [35] near 725 cm$^{-1}$ shows a discontinuous jump across 2 GPa (Figure 3.8b) suggesting an abrupt change in the electronic environment of acid $COOH_t$ and water $OH_w$ groups across 2 GPa.

## 3.3.2 The hydronium ion strucutre

The structural arrangement in hydronium ion, and other similar structures like ammonia, is distinguished by their characteristic deformation modes. The weak shoulder in $\delta H_2O$ IR mode coupled with $\nu C = O$ ($\sim$ 1726 cm$^{-1}$) also shows a discontinuous increase in position and width above 2 GPa due to simultaneous change in the C=O and $H_2O$ electronic environment upon proton transfer and the mode observed beyond 2 GPa is therefore attributed to the $\nu_4$ mode of $H_3O^+$ (Figures 3.7 and 3.8a). Note that the $\nu_4$ mode of $H_3O^+$ (found in the range 1670 – 1750 cm$^{-1}$) is observed at a higher frequency than the $\nu_2$ mode of $H_2O$ (1596 – 1700 cm$^{-1}$) [143]. For the hydronium ion, $\nu_2$ deformation mode, based on the umbrella inversion motion, is expected in the range 1000 - 1200 cm$^{-1}$ [139–143]. We distinctly see the evolution of this mode in the IR spectra (shown by a star in Figure 3.7) around 1020 cm$^{-1}$ across 2 GPa, beyond which it systematically gains

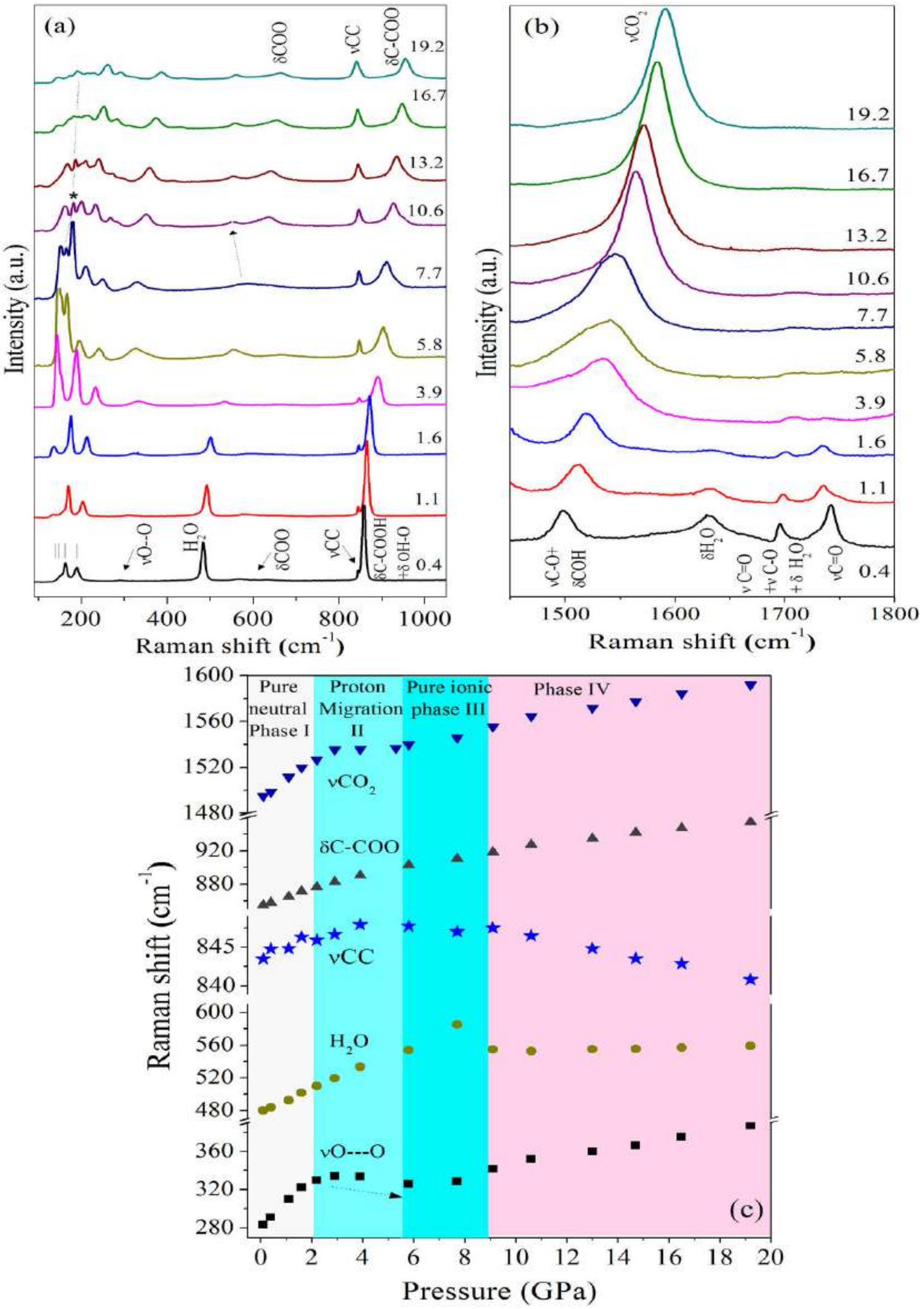

**Figure 3.6:** High Pressure Raman spectra at some representative pressures in the spectral region (a) 90 – 1050 cm$^{-1}$ and (b) 1450 – 1800 cm$^{-1}$. All the spectra, plotted in the same intensity scale, have been offset for clarity in both the regions; numbers are pressure values in GPa (c) Variation of some important Raman modes with pressure.

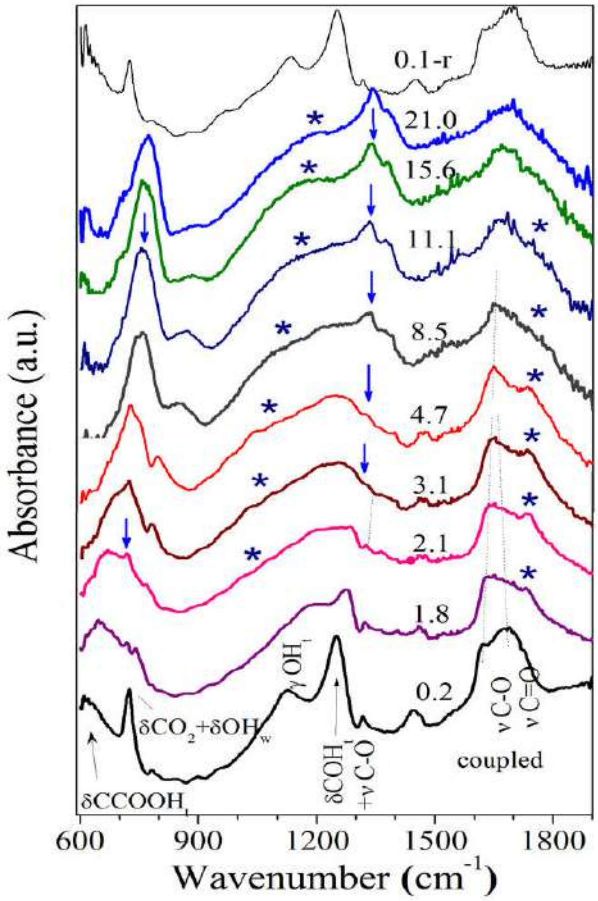

**Figure 3.7:** High pressure infrared spectra of OAD in the range 600 – 1850 cm$^{-1}$. Here asterisks ($*$) show $H_3O^+$ features and blue down arrows show dianionic oxalate features emerging with pressure and “r” denotes data on release. Numbers denote pressure values in GPa.

intensity and stiffens with pressure (Figure 3.8b). The first-principles calculations also indicate that ∠HOH, around 105.8° at ambient conditions, shows an increase at 1.5 GPa and the three angles in the protonated phase become 107°, 112° and 115°, in reasonable accordance with the hydronium structure [159]. The above spectroscopic and theoretical observations are also accompanied with vanishing of the $\delta H_2O$ coupled Raman mode ($\sim$ 1630cm$^{-1}$) at 2 GPa (Figure 3.6b).

Noticeably, the O–H$_w$ bonds of water get elongated under compression as indicated by the softening behaviour of $\nu$O–H$_w$ IR modes with pressure (Figure 3.8a). This behavior is well supported by the calculated bond parameters, i.e. the two

$d_{\mathrm{O\text{-}H}}$ distances of water (0.996 Å and 0.997 Å) which show an increase at 1.5 GPa (1.009 Å and 1.014 Å) and become comparable with the $\mathrm{O_w - H_t}$ distance (1.14 Å, bond formed after the proton transfer) under pressure. Indeed, the cooperative mechanism favors such an elongation and strengthening of the corresponding hydrogen bonds. However, we observe continued softening of all the three $\nu$OH modes in the hydronium structure even after the proton transfer indicating strengthening of all the O-H---O interactions. The most interesting feature of the incipient (phase II, above 2 GPa) and pure ionic phase (III, above 5 GPa) is the remarkable pressure induced broadening (Figure 3.3) accompanied by a large rate of softening ($> 50$ cm$^{-1}$/GPa) (Figure 3.8a and Table 3.1) of the newly emerged $\nu\mathrm{O_w - H_t}$ hydronium mode ($\nu_1$ mode of $\mathrm{H_3O^+}$) indicating increase in anharmonicity. We also notice that the $\nu\mathrm{O_1\text{--}O_w}$ Raman mode shows stiffening above 5 GPa (Figure 3.6c and Table 3.1). Therefore it is anticipated that this hydrogen bond, between $-\mathrm{CO_2^-}$ and $\mathrm{H_3O^+}$ groups may be strengthened to the symmetrization limit at very high pressures. The pressure induced behavior of the $\nu\mathrm{O_w - H_t}$ hydronium mode shown in Figure 3.8a, in the range 2 to 9 GPa, could be well approximated by the formula $\nu = [\mathrm{A(P_c - P)}]^{1/2}$, which predicts $\mathrm{P_c} \sim 36$ GPa as the pressure corresponding to $\nu$OH mode instability [4]. However, the rate of $\nu\mathrm{OH_t}$ softening, depicting the power law behaviour analogous to the soft mode, reduces above 9 GPa, indicating another structural modification across this pressure.

## 3.4 Proton transfer aided phase transition

In OAD (monoclinic structure, space group $P2_1/n$), a layered spiral structure of oxalic acid and water molecules is formed along the screw axis due to excess stabilization of hydrogen bonds resulting from their cooperative behaviour (Figure 3.1). Subsequent to proton transfer, the hydronium oxygen is no more a hydrogen bond acceptor (Figure 3.9). But, the sustained strengthening of all the

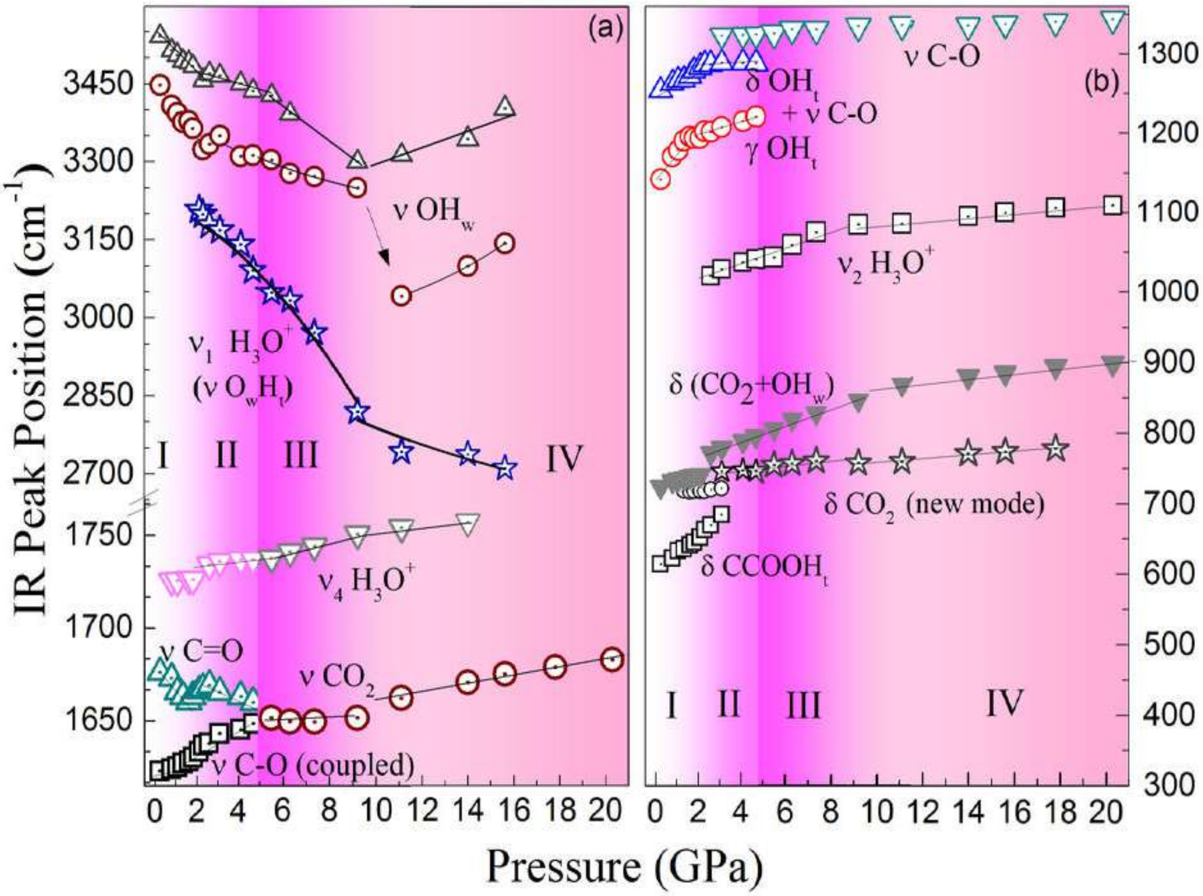

**Figure 3.8:** Pressure induced variation of infrared active modes ((a) 1600 – 3600 cm$^{-1}$, (b) 600 - 1350 cm$^{-1}$) of OAD in the ambient phase I, proton transfer phase II, ionic phase III and the high pressure phase IV above 9 GPa.

O-1H---O interactions, as discussed above, may imply continued elongation of hydronium O-H bond lengths. It is only across 9 GPa that the $\nu$OH$_w$ frequency variations show discontinuous behaviour and they start stiffening thereafter (Figure 3.8a), suggesting loss of cooperativity. Across 9 GPa, we also observe the emergence of new Raman modes in the lattice region (Figure 3.6a) and slope change in the frequency versus pressure plots of many IR and Raman modes (Table 3.1).

These results point towards a phase transition in OAD at 9 GPa. Across the transition, the water libration Raman mode ($\sim$ 480 cm$^{-1}$), [35] which showed

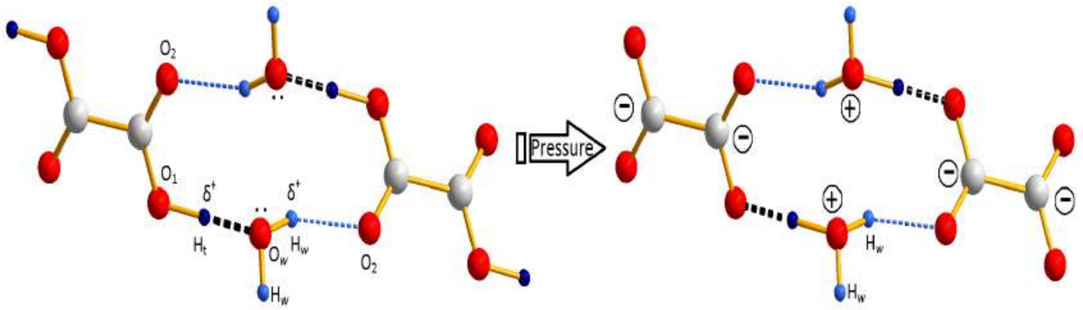

**Figure 3.9:** Two dimensional view of the spiral motif. Pressure induced proton transfer restricts the water oxygen to be an acceptor of hydrogen bond and ionizes the local structural moieties. The higher pressure structure is only tentative.

monotonous stiffening and broadening upon proton transfer (Figure 3.6c), also displays a discontinuous jump and slope change. Therefore, the abrupt shift of the $\nu O_w - H_w$ mode across 9 GPa (Figure 3.8a) can also be linked to breaking and reformation of the relatively weaker $O_w$-$H_w$---$O_2$ hydrogen bonds. On the other hand, the $\nu O_w - H_t$ mode continues to soften in the high pressure phase IV above 9 GPa, though at a lesser rate, with increase in width up to the highest pressure measured, i.e. 21 GPa . This is also accompanied with monotonous stiffening of the $\nu O_1$---$O_w$ Raman mode (corresponding to $O_1$---$H_t$-$O_w$) as observed from Figure 3.6c, which indicates sustained strengthening of this hydrogen bond in phase IV above 9 GPa.

Such a hydrogen bond strengthening may however pull the oxalate motif from both sides thus squeezing the spiral motif (Figure 3.1), which gets support from the repulsion between the resonating electronic densities in the two $COO^-$ ends of oxalate ion due to loss of proton (schematically depicted in Figure 3.10). But this squeezing is limited by the stiff C-C backbone of oxalate molecule. We observe that in the new phase above 9 GPa, the $\nu CC$ Raman mode is found to soften with pressure up to the highest pressure recorded in this study, i.e. 20 GPa, and the rate of this softening ($\sim$ 0.8 $cm^{-1}$/GPa) is significant in view of the strength of this bond (Figure 3.6c), thus weakening the backbone. The $\nu CO_2$ Raman mode

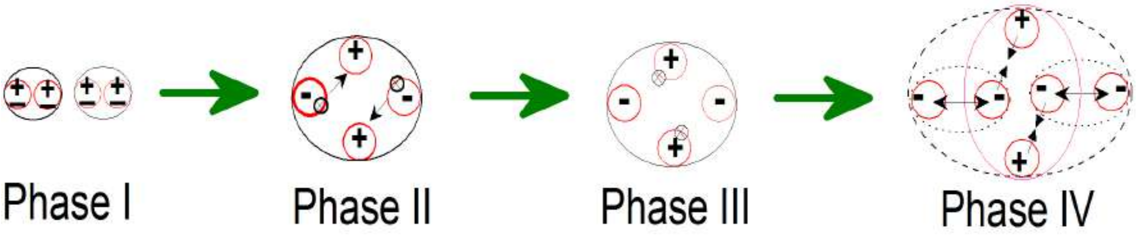

**Figure 3.10:** Changes in hydrogen bonding and electrostatic interactions in different high pressure phases in oxalic acid dihydrate. Phase I consists of neutral acid and water molecules.

near 1500 cm$^{-1}$ also shows pronounced stiffening accompanied with steep rise in the relative intensity (Figure 3.6b).

Therefore, one may expect that the $O_1$---$H_t$-$O_w$ hydrogen bond, between the dominant $CO_2$ and $H_3O^+$ groups gains significant strength at high pressures, and, if it continues to strengthen at further higher pressures, would lead to a structure with the two fundamental entities, $CO_2$ and $H_2O$ hinging through a proton. It would be interesting to look for the resulting structural arrangement and hydrogen position at very high pressures above 20 GPa. These results would be helpful in understanding the structural assembly of simple molecules under extreme thermodynamic conditions prevailing in primitive earth, planetary interiors or extra-terrestrial systems.

## 3.5 Conclusions

Our Infrared (IR) spectroscopic measurements well supported by Raman spectroscopy and first-principles simulations on OAD have provided the first unambiguous experimental evidences of proton migration resulting in a complete transfer of proton from oxalic acid to water at very low pressures ($\sim$ 2 GPa), thus settling a long standing debate. Subsequent to proton transfer, due to the loss of cooperativity of hydrogen bonds, novel high pressure phases, with significant local structure rearrangements, are formed at pressures above 5 GPa in which the new hydrogen bond formed with reversed hierarchy due to proton transfer again starts strengthening. This hydrogen bond has depicted a sustained strengthening above the phase transformation across 9 GPa, when other hydrogen bonds show pressure induced weakening.

# 4

# High pressure studies on Glycinium oxalate

## 4.1 Introduction

Amino acid- oxalic acid complexes, with strong hydrogen bonded networks, provide unique opportunity to study proton dynamics near the symmetrization limit, in multi-component bio-geological materals, due to their extreme sensitivity to hydrogen bond tunability under pressure [62, 63, 127, 132, 160–163]. Glycinium oxalate (GO), the simplest amino acid- carboxylic acid complex crystallizes in monoclinic structure with space group $P2_1/c$ and four formula units per unit cell (Z=4) [65]. It possesses a nearly linear and strong `O3-H7---O6` hydrogen bond ($d_{\text{O---O}} \sim 2.54$ Å, $d_{\text{H---O}} \sim 1.65$ Å and $\angle \text{OHO} = 177°$) between semioxalate molecules in a columnar arrangement along the *b*-axis (Figure 4.1 bottom, Table 4.1). These semioxalate ($HC_2O_4$) columns hold the head to tail linked glycine ($NH_3CH_2COOH$) sheets in the *ac*-plane via other hydrogen bonds to form the three dimensional network (Figure 4.1 top, Table 4.1 ). We have studied the proton dynamics of this strong `O3-H7---O6` hydrogen bond under pressure, beyond the symmetrization limit up to $\sim$ 20 GPa. Our high pressure Raman and infrared

(IR) spectroscopic investigations suggest a dynamic proton sharing between the semioxalate units, which mimics the proton being at the mid-point and thus implying a symmetric state above 8 GPa and these results are well supported by the density functional theory (DFT) based first principles molecular dynamics (MD) calculations.

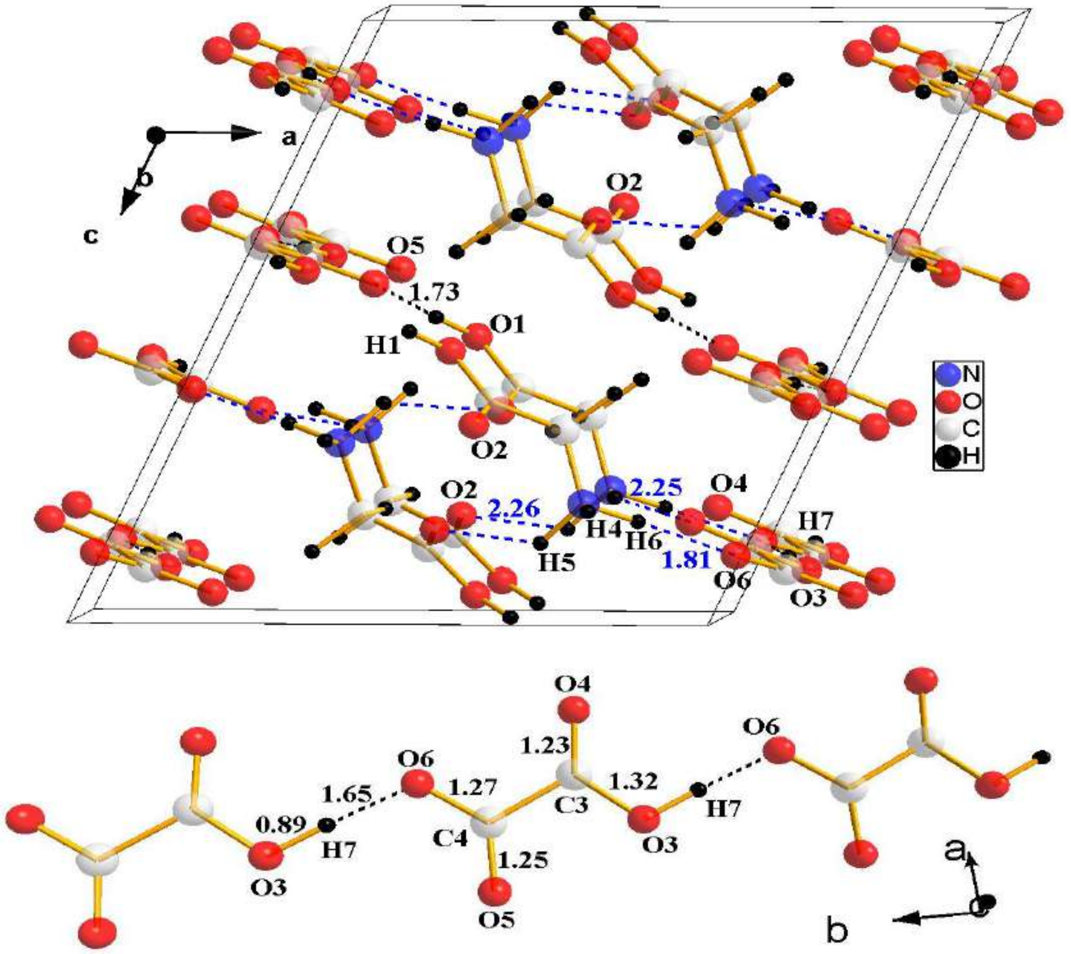

**Figure 4.1:** Top: Unit cell of GO with dashed lines for strong hydrogen bonds (blue: NH---O, black: OH---O, numbers are in Å units). Two glycine molecules are linked from head to tail via N1-H5---O2 in the *ac* plane forming bilayers. Two semioxalate columns along *b*-axis, linked through inversion symmetry connect two glycine columns also along *b*-axis through strong O1-H1---O5 (H---O = 1.63Å), N1-H6---O6 (H---O = 1.81 Å) and N1-H4---O4 (H---O = 2.25 Å) hydrogen bonds. Bottom: One semioxalate column along *b*-axis bridged through strong O3-H7---O6 hydrogen bond.

**Table 4.1:** Various hydrogen bond parameters in glycinium oxalate [65].

| X-H---Y | X-H | H---Y | X---Y | ∠X-H-Y |
|---|---|---|---|---|
| O1-H1---O5 | 0.86 | 1.73 | 2.593 | 174 |
| N1-H4---O4 | 0.91 | 2.25 | 3.082 | 152 |
| N1-H5---O2 | 0.90 | 2.26 | 2.949 | 133 |
| N1-H5---O5 | 0.90 | 2.51 | 3.172 | 130 |
| N1-H6---O6 | 0.94 | 1.81 | 2.698 | 156 |
| O3-H7---O6 | 0.89 | 1.65 | 2.540 | 177 |
| C2-H2---O5 | 0.96 | 2.53 | 3.314 | 139 |

## 4.2 Methods

For experimental studies of proton movement, vibrational energy levels and pressure induced changes in ionic states and glycine confirmation, we have primarily used infrared spectroscopy well supported by Raman scattering (details in chapter 2).

### 4.2.1 Vibrational mode assignments

Mode assignments of glycinium oxalate (GO) have been carried out based on earlier IR, Raman and theoretical studies of GO [66], bis(glycinium)oxalate (BGO) [138], triglycine sulphate (TGS) [54], $\alpha$-glycine [50] and oxalic acid dihydrate [35, 56, 128, 130, 136]. The assignments were also checked using reported values under ambient conditions for various other glycine and oxalate complexes [51, 56, 63, 132, 135, 162–167] and the high pressure behavior of IR and Raman active modes in GO (present study), BGO [132, 138] and oxalic acid dihydrate (OAD) [56]. The mode assignments for oxalic acid have further been verified based on the extensive works by Novak and coworkers on various oxalate and semioxalate compounds possessing hydrogen bonds of varying strengths at ambient conditions [129, 130, 133, 134, 168]. For OH and NH stretching IR modes, the correlation curves reported for stretching frequencies as a function of hydrogen bond strength, i.e. bond parameters have been used [13, 145]. The modes assignments were finally verified using our first-principles calculations which are also in agreement with the reported values.

### 4.2.2 Theoretical simulations to monitor proton position

All the simulations were performed using the Vienna Ab Initio Simulation Package (VASP) [146–148]. The interactions between core and valence electrons were treated with projector plane wave (PAW) method with $s^1$ (H), $s^2p^2$ (C), $s^2p^3$ (N) and $s^2p^4$ (O) valence configurations. The exchange-correlation energy was treated with PBE version of GGA and an energy cut-off of 600 eV was used for plane wave basis construction [151].

In the case of structural optimization, Brillouin zone was sampled by 4×6×4 Monkhorst-Pack mesh whereas Γ-point was used for molecular dynamics (MD) simulations [152]. The MD simulations were performed for a 1×2×1 (144 atoms) supercell in the canonical (NVT) ensemble and the temperature was controlled using the Nosè thermostat. The MD time-step was taken equal to 1 femto-second. All simulations run for 15 ps. Initial 3 ps data were not used in the analysis.

The vibrational properties were studied using density functional perturbation theory as implemented in the Quantum-Espresso computer code [169]. For these calculations, we have used the local density approximation for exchange-correlation [170] as the code does not allow the Raman and infrared intensities calculation for GGA exchange-correlation. An energy cutoff of 160 Ry was used for plane wave expansion. The Brillouin zone was sampled using same Monkhorst-Pack k-point grid as in structural relaxations. The crystal structures were fully optimized before these calculations.

### 4.2.3 High pressure ADXRD studies

Angular Dispersive X-ray Diffraction (ADXRD) studies were carried out at the 5.2R (XRD1) beamline of Elettra synchrotron source with monochromatized X-rays ($\lambda$ ~0.6888Å). For these experiments, the polycrystalline sample of glycinium oxalate along with few particles of Cu, was loaded in a ~120 $\mu$m diameter hole drilled in a pre-indented tungsten gasket of a Mao-Bell type of DAC and no pressure transmitting medium was used. Pressure was calculated using Birch-Murnaghan equation of state of Cu [91]. The diffraction patterns were recorded using a MAR345 imaging plate detector kept at a distance of ~ 20 cm from the sample. The diffraction profiles were obtained by the radial integration of the two dimensional diffraction rings using the FIT2D software [171].

### 4.2.4 Structural investigations

The observed X-ray diffraction (XRD) patterns (Figure 4.2) match with the Bragg reflections corresponding to the monoclinic structure with space group $P2_1/c$ and four formula units per unit cell (Z=4). The ambient pressure lattice parameters obtained using Rietveld refinement [172] are: a = 10.614 (4) Å, b = 5.649 (3) Å, c = 12.096 (5) Å, $\alpha = \gamma = 90°$ and $\beta = 113.769°$ (3), which are in close agreement with the earlier published values [65]. At high pressure, experimental lattice parameters were determined using Le'Bail refinement incorporated into GSAS (Figure 4.3) up to 4 GPa, above which the intensities of diffraction peaks were weak. The unit cell volumes at different pressures, determined from X-ray diffraction experiments and theoretical calculations agree reasonably well up to 4 GPa with no indication of any structural transition. The linear compressibilities ($-(1/l) \times (dl/dp)$) (Table 4.2) show anisotropic compression with *b*-direction showing least compressibility (Figure 4.3). This is in good qualitative agreement with the theoretically calculated values. The full width at half maximum (FWHM) of X-ray diffraction peaks slightly increases with pressure. As nearly

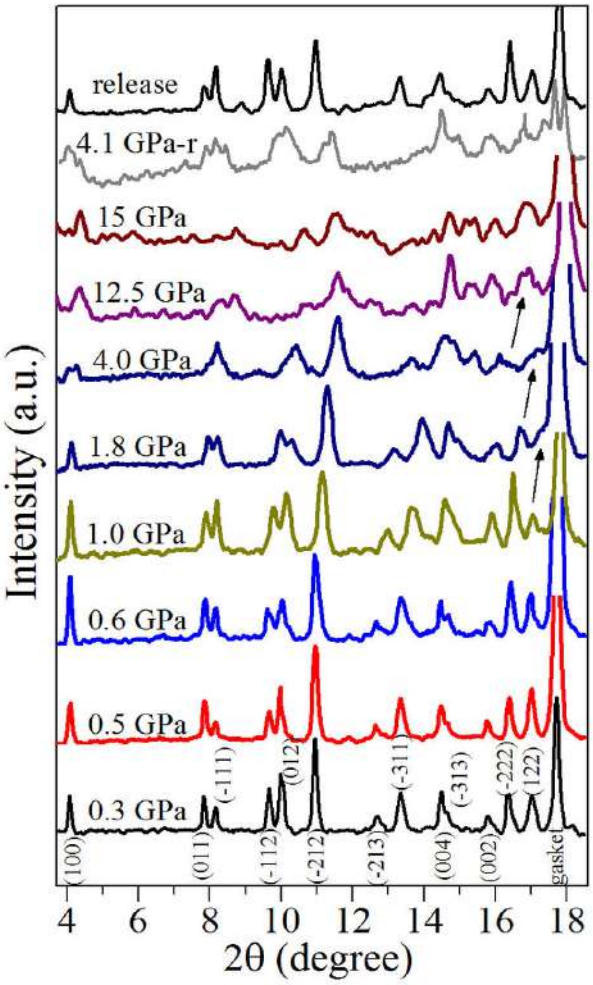

**Figure 4.2:** High pressure X-ray diffraction patterns of glycinium oxalate stacked at a few representative pressures. The XRD peaks from sample are indexed with the respective (hkl);"r" indicates the XRD pattern corresponding to released run.

all the prominent diffraction peaks could be followed up to the highest pressure, no drastic structural transition is indicated up to 15 GPa. However, at pressures above 12 GPa, the peaks are relatively broadened and we also notice a broad hump emerging in the background above 13°, which may due to the emergence of a supramolecular phase above this pressure. The diffraction patterns above 18° contain several very intense peaks due to gasket and pressure marker (Cu), hence the features could not be followed at higher angles. Ambient structure could be retrieved on release of pressure.

**Table 4.2:** Linear compressibilities of glycinium oxalate crystal.

| Linear Compressibility | Synchrotron XRD experiments up to 4 GPa | Theory |
|---|---|---|
| *a*-axis | $2.6 \times 10^{-2}$ /GPa | $2.4 \times 10^{-2}$ /GPa |
| *b*-axis | $0.92 \times 10^{-2}$ /GPa | $0.9 \times 10^{-2}$ /GPa |
| *c*-axis | $5.5 \times 10^{-2}$ /GPa | $5.3 \times 10^{-2}$ /GPa |

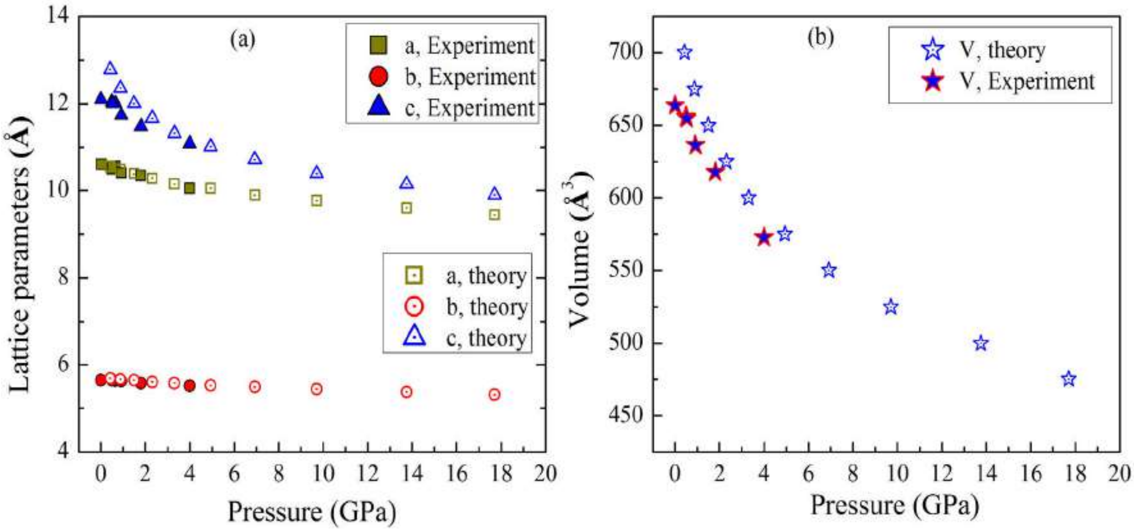

**Figure 4.3:** Variation of lattice parameters (a) and unit cell volume (b) with pressure. Filled and open symbols correspond to experiment and theory. The *a* and *c* parameters approach each other with pressure (this is accompanied with reduction in $\beta$ angle, ($\sim 113°$ at ambient)).

## 4.3 Hydrogen bond strengthening under pressure

Under compression when the proton moves close to the mid-point of a very strong hydrogen bond O−H---O, the system becomes highly anharmonic leading to OH instability and resulting in remarkable dampening of $\nu$OH (stretching) mode [10, 153, 154]. In glycinium oxalate, as the $\nu$O−H IR mode ($\sim$ 2360 cm$^{-1}$) [13, 145] corresponding to O3-H7---O6 (between adjacent semioxalate molecules along *b*-axis) lies in the second order diamond absorption region, a first-hand information on its high pressure behaviour was obtained by phonon calculations using quantum espresso code as shown in Figure 4.4a (observed IR spectra are shown in Figures 4.4b and 4.5b). A large red shift of $\sim 250$ cm$^{-1}$ up to 2.5 GPa in $\nu$OH infrared mode (See Figure 4.4a) and a substantial reduction in the O3---O6 distance ($d_{\mathrm{O3--O6}} < 2.5$Å, see Figure 4.7d of next section) implies that this hydrogen bond is strengthened under pressure and is on the verge of approaching symmetrization limit. We also note a relative increase in the background of the observed IR band profile above 2 GPa [164,168] (See Figures 4.4b). Such broad envelopes, resembling a continuum arise due to large $\nu$OH dampening and are used as prime evidence of strengthening of hydrogen bond in the low barrier hydrogen bonded systems close to symmetrization [10,154,164,168], based on experiments and anharmonic calculations on various systems [14,154–158]. The significant stiffening of the out of plane bending ($\gamma$OH $\sim 1018$ cm$^{-1}$) and in-plane bending ($\delta$OH $\sim 1232$ cm$^{-1}$) modes (Figure 4.5a) also support strengthening of this hydrogen bond under pressure [35,164,173].

The pressure induced softening of the bare $\nu$O-H mode corresponding to O3-H7---O6, as obtained from Lorentz oscillator fit of ambient reflectance and phonon calculations up to 2.5 GPa (Figure 4.4a), fitted by the formula $\nu = [\mathrm{A}(\mathrm{P_c} - \mathrm{P})]^{\mathrm{m}}$, gives A $\sim 6.9 \times 10^5$ , m $\sim 0.50$ and P$_\mathrm{c}$ $\sim 8.1$ GPa (Figure 4.5c). The anomaly in the pressure variation of $\delta$OH mode near 5 GPa due to the intersection with bare $\nu$O-H mode (shown by vertical down arrow in Figure 4.5a and 4.5c) and narrow transmission dips above 8 GPa resembling Evans hole (marked as ! in Figure 4.4b) are some of the spectral features arising due to the $\nu$OH mode couplings [10], similar to the case of ice and other low barrier systems [35,154,164,174]. In the Raman spectra, the emergence and pressure induced stiffening of $\nu$OHO hydrogen bond stretching vibrational mode near 200 cm$^{-1}$ (shown by $*$ in Figure 4.6) across 2 GPa also suggests the possible low barrier hydrogen bond formation [7,35,128].

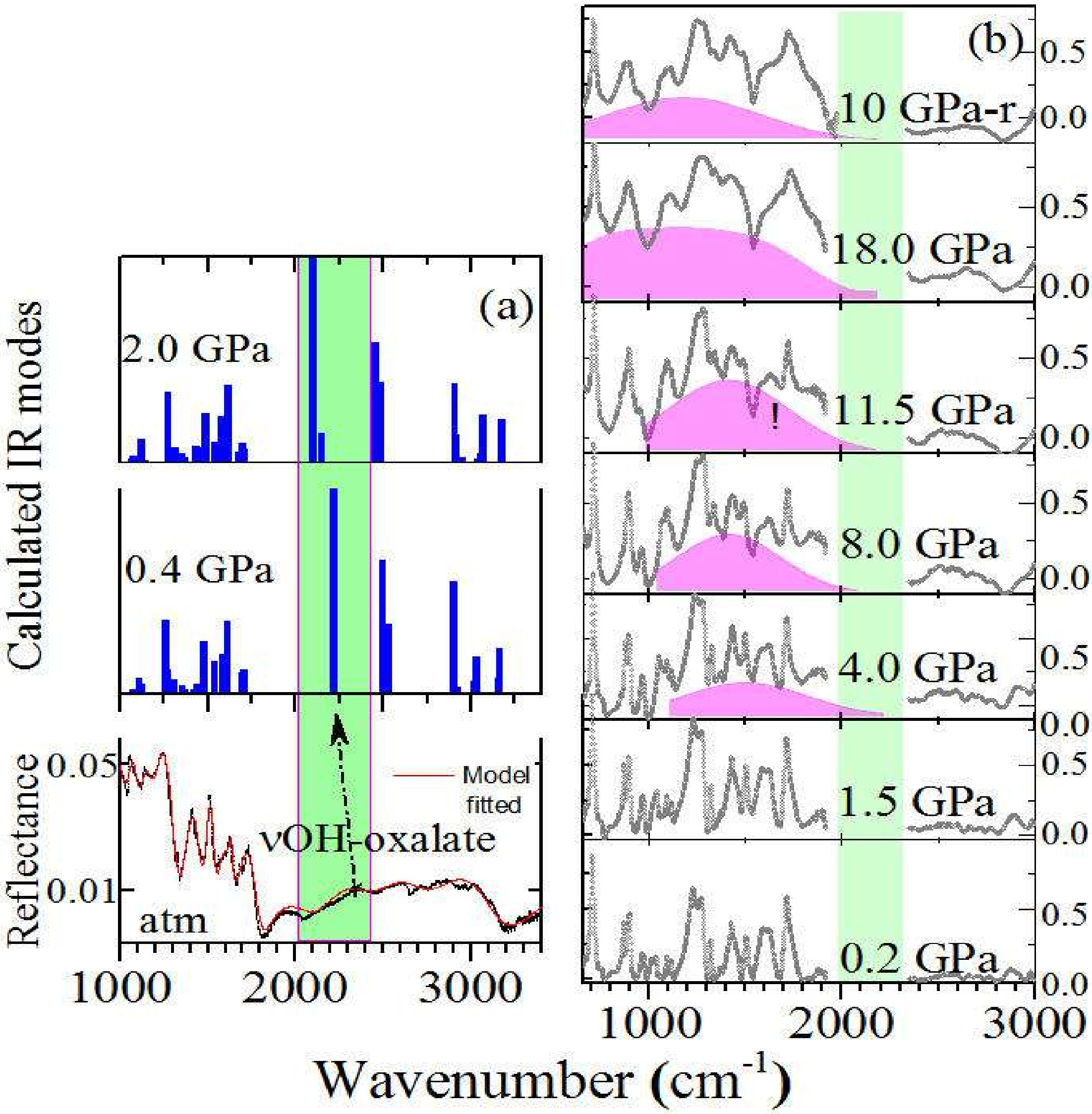

**Figure 4.4:** (a) Ambient (observed) and calculated IR phonon modes show large red shift in bare $\nu$O3-H7 oxalate mode with pressure. (b) Observed mid IR spectra of GO at various pressures in 650 – 3000 $\mathrm{cm}^{-1}$ region. The highlighted hump (arbitrary) emerging above 2.5 GPa, due to $\nu$OH mode, and showing softening/broadening above 8 GPa is guide to the eye . Narrow transmission dips (for example shown by ! near 1600 $\mathrm{cm}^{-1}$ in 11.5 GPa plot) resembling Evans hole arise due to $\nu$OH mode coupling. “r” denotes release pressure data and green shaded bar is second order diamond absorption region.

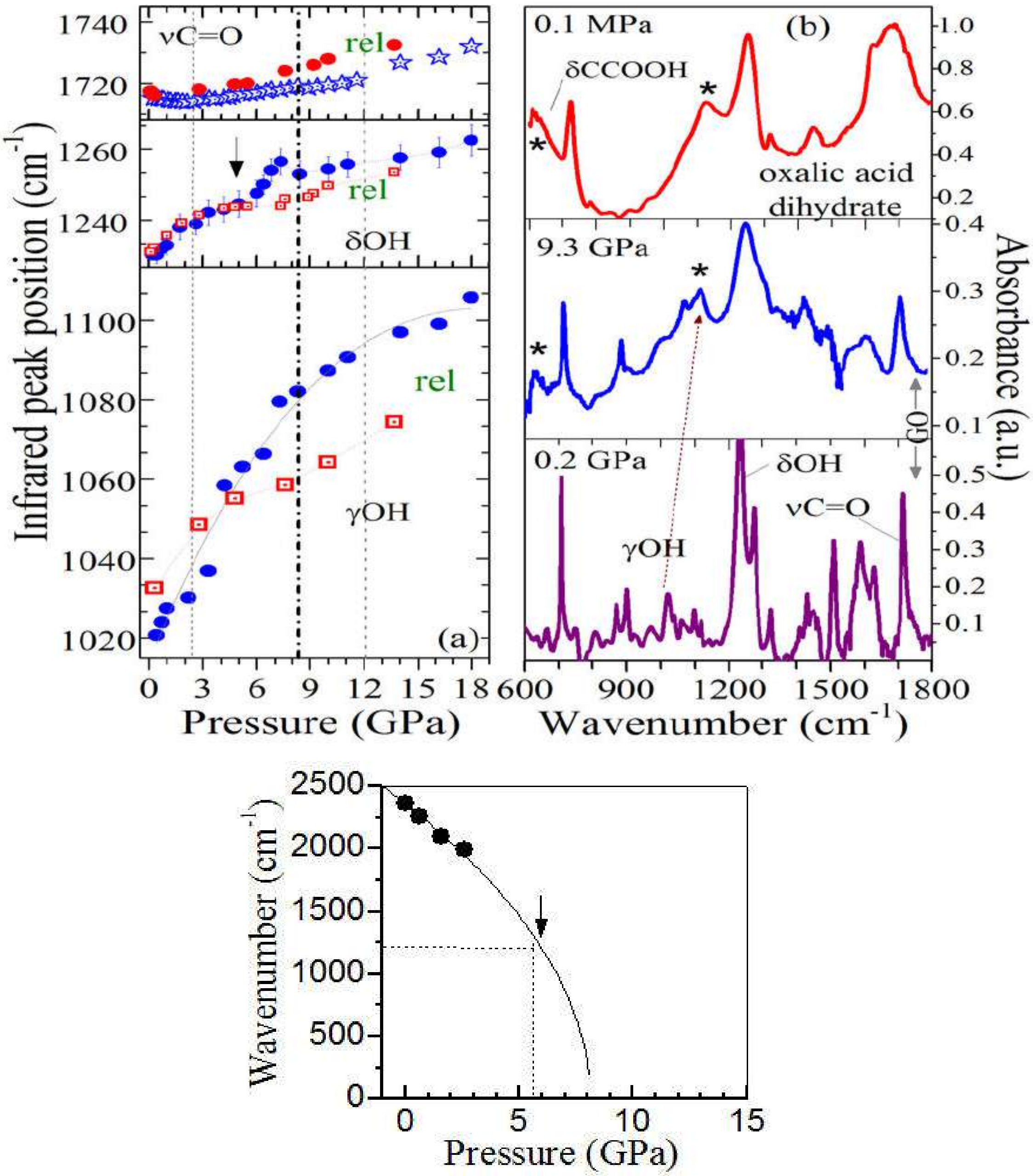

**Figure 4.5:** (a) Variation of selected observed IR modes with pressure (blue- compression, red- decompression data; “rel”- release). Vertical dotted lines: onset of low barrier hydrogen bond formation above 2 GPa, symmetrized hydrogen bond above 8 GPa and emergence of supramolecular phase above 12 GPa. (b) lower two panels: Expanded view of the mid IR spectra of GO before and after symmetrization; top panel shows the spectrum of a neutral oxalic acid complex, oxalic acid dihydrate (OAD) [35] at ambient pressure and “*” denotes spectral resemblance of high pressure phase of GO with OAD. The spectra of GO in Figure 4.4b and Figure 4.5b are from different experiments and all the features show good repeatability. (c) A power law fit to the bare $\nu$OH (O3–H7) mode up to 2.5 GPa.

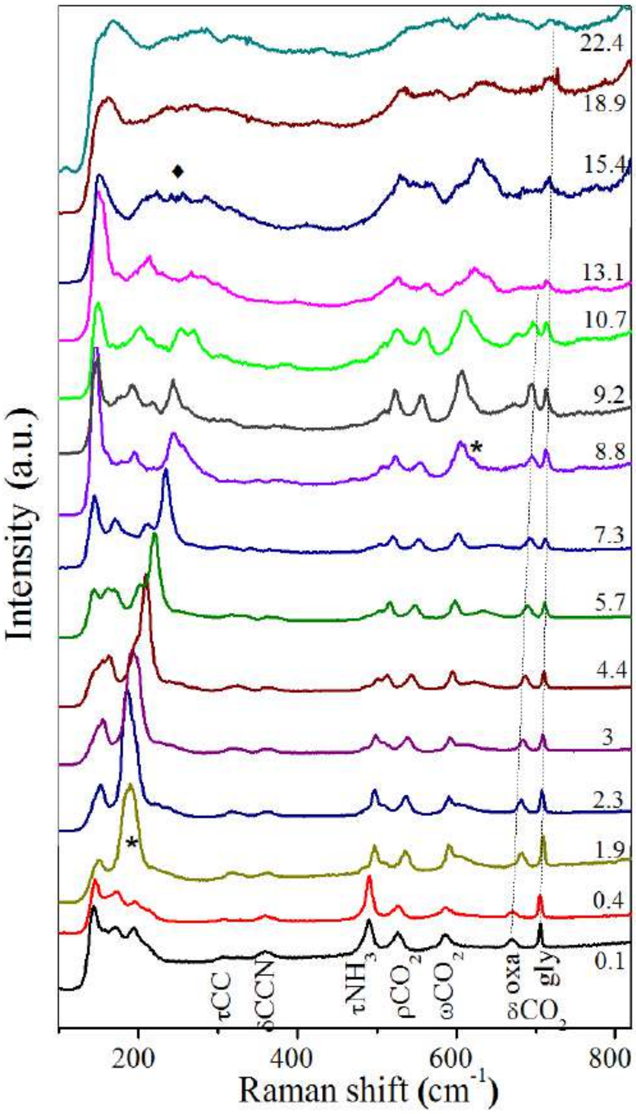

**Figure 4.6:** High pressure Raman spectra of GO at various pressures in the region 100 – 800 $cm^{-1}$. ($\delta$-bending, $\omega$-waggging, $\tau$- torsional, $\rho$-rocking). Numbers are pressure values in GPa.

## 4.4 Pressure induced hydrogen bond symmetrization

The strengthening of hydrogen bond up to the symmetrization limit results in dynamic proton sharing which can be investigated in two steps, i.e finding the proton position from the structure and probing the experimental evidences which come from spectroscopy. This is discussed in the following subsections.

### 4.4.1 Proton distribution calculated from molecular dynamics

The strengthening of the O3-H7---O6 hydrogen bond under pressure to the symmetrization limit is further evident from the bond parameters obtained from MD calculations (Figure 4.7). A total of 12000 equilibrated configurations, in 1 femtosecond time steps, were used at each pressure to generate the dynamical picture. It shows that the spread of the proton distribution reduces with pressure and shifts towards the bond mid-point (i.e., $\delta = 0$). The large pressure induced softening of infrared $\nu$OH mode ($> 250\text{cm}^{-1}$ up to 2.5 GPa, Figure 4.4a), as approximated by a power law fit ($\nu \sim [\mathrm{A}(\mathrm{P_c} - \mathrm{P})]^{0.5}$ ) for the soft mode (Figure 4.5c), gives $\mathrm{P_c} \sim 8.15$ GPa as the pressure corresponding to $\nu$OH mode instability [4]. Figure 4.7d shows that at pressures close to 10 GPa, the distance between oxygen atoms, $d_{\text{O3---O6}}$ continuously reduces to $\sim 2.4$ Å. This variation is also accompanied by an increase in the covalent bond length ($d_{\text{O3-H7}}$), decrease in the hydrogen bond length ($d_{\text{H7---O6}}$). However, $\angle$OHO remains close to $\sim 180°$ (Figure 4.7c inset). One can also see from the Figure 4.7d that the probability of crossing the mid-point through proton hopping increases with pressure and is already significant at $\sim$ 10 GPa. This implies proton sharing between the closely overlapped potential minima in which the proton hops between the two sites. It is of interest to note that a nearly linear geometry of the hydrogen bond O3-H7---O6 in this compound at ambient as well as at higher pressures, i.e. $\angle$OHO $\sim 180°$ favors this mechanism.

### 4.4.2 Experimental evidence of proton hopping

#### 4.4.2.1 Raman spectrosocpic signatures of proton sharing

The dynamic proton hopping along the O3-H7---O6 hydrogen bond, which mimics the proton being at the mid point, and consequent proton sharing be-

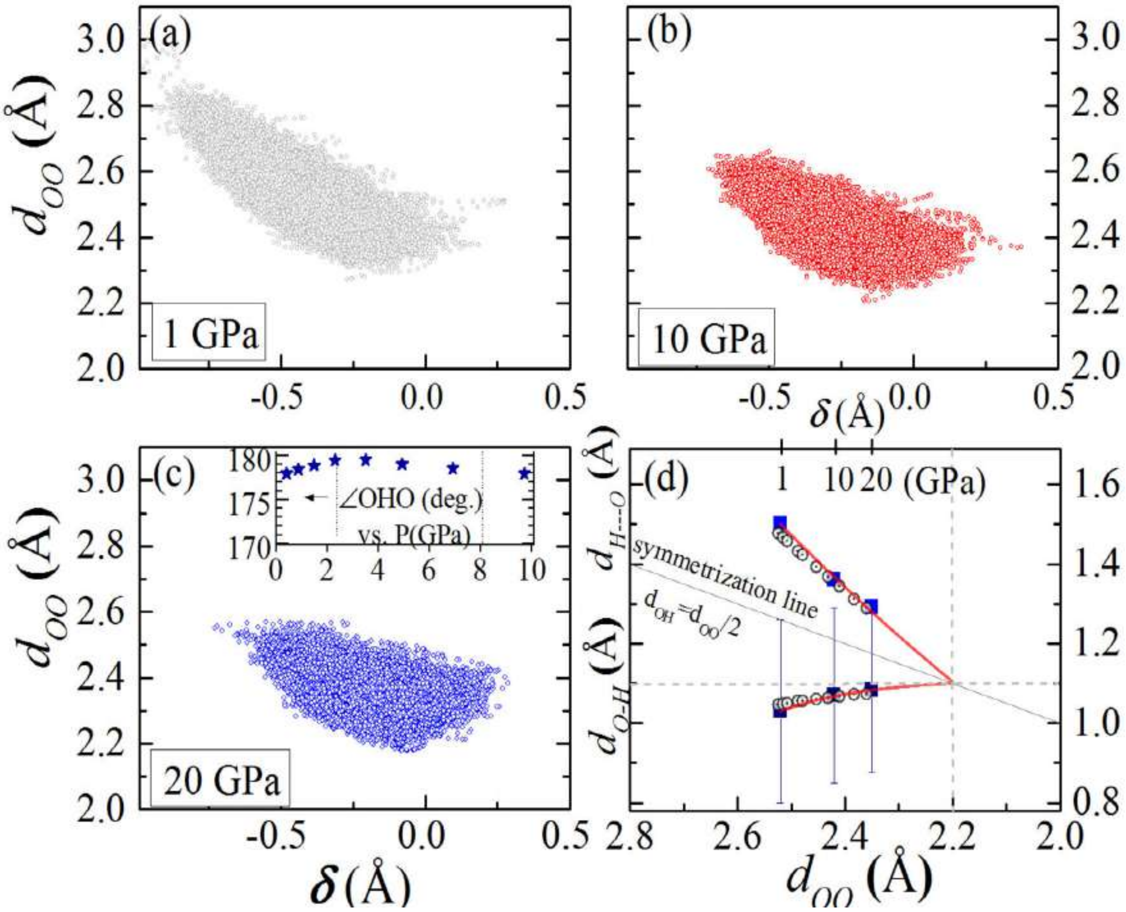

**Figure 4.7:** (a-c) Evolution of dynamic spread in proton distribution function with pressure towards the bond midpoint ($\delta = d_{\text{O-H}} - d_{\text{H---O}}$). Inset in (c) shows variation of ∠O3-H7-O6 with pressure (d) Bond parameters of O3–H7---O6 (open circles-0K DFT; filled squares-300K first-principles MD); vertical bars represent spread in the $d_{\text{O-H}}$ values, this is linked to the probability of crossing the potential barrier for the classical proton. The fitted curves meet near 60 GPa if the initial phase persists. Proton quantum tunnelling may however reduce this pressure [9].

tween the two semioxalate units would result in the emergence of neutral oxalic acid like spectral features, which can be inferred from the Raman and infrared measurements [4]. Above 8 GPa, we indeed observed new characteristic modes of neutral oxalic acid in the Raman spectra (See Figure 4.8a). A comparison with the ambient spectrum of a well studied neutral oxalic acid compound (oxalic acid dihydrate) shows that the new Raman modes at $\sim 1500$ cm$^{-1}$ and $\sim 1700$ cm$^{-1}$ correspond to the characteristic coupled modes ($\delta\mathrm{COH} + \nu\mathrm{C-O}$) and ($\nu\mathrm{C=O} + \nu\mathrm{C-O}$) respectively of neutral oxalic acid (Figure 4.8b) [35, 128].

In addition, abrupt increase in the relative intensity of $\delta\text{C} - \text{COOH}$ oxalate modes ($\sim 860$ cm$^{-1}$) across 8 GPa (Figure 4.8a), large blue shift ($\sim$ 20 cm$^{-1}$ up to 8 GPa) of $\nu\text{C} = \text{O}$ oxalate mode ($\sim$ 1709 cm$^{-1}$, Figures 4.8b and c), emergence of new mode (shoulder peak) in the $\delta\text{CO}_2$ region above 8 GPa (near 620 cm$^{-1}$, shown by $*$ in Figure 4.6) also correspond to neutral oxalic acid like features [35, 128, 133, 134, 173]. The semioxalate $\delta\text{CO}_2$ mode (669 cm$^{-1}$ at ambient pressure) becomes indiscernible above 10 GPa. Raman spectroscopic signatures in glycinium oxalate above 8 GPa thus provide an important experimental evidence of proton sharing due to hydrogen bond symmetrization between semioxalate molecules.

#### 4.4.2.2 Infrared signatures of the soft mode

In the infrared absorption spectra, above 8 GPa, OH instability due to proton hopping results in further increase in the width of the $\nu$OH absorption band, which rides over the background of various other fundamentals (Figure 4.4b). Its centroid shifts to lower frequencies (up to $\sim$ 1000 cm$^{-1}$ at 18 GPa), at an increased rate above 8 GPa and the extent of this band crosses the lowest 600 cm$^{-1}$ mark to enter even in the far IR regions at higher pressures. Thus, in order to probe the signatures of this band in the far infrared regions, we have carried out high pressure measurements at the bright far-IR source of Elettra synchrotron, Italy, to cover the spectral region below 600 cm$^{-1}$, as shown in Figure 4.9. The distinct rise in the band profile of the spectra at pressures higher than 15 GPa indeed confirm the observations inferred from mid infrared measurements. The relative intensity of the band increases with pressure with continued softening up to the highest pressure measured, i.e. 24 GPa.

A remarkable stiffening of the $\gamma$OH mode of semioxalate (nearly 65 cm$^{-1}$ up to 8 GPa, Figure 4.5a) and drastic reduction in the separation between $\gamma$OH and $\delta$OH modes indicate the emergence of spectral signatures resembling neutral oxalic acid (see also Figure 4.5b). Beyond 8 GPa, these two modes depict a similar

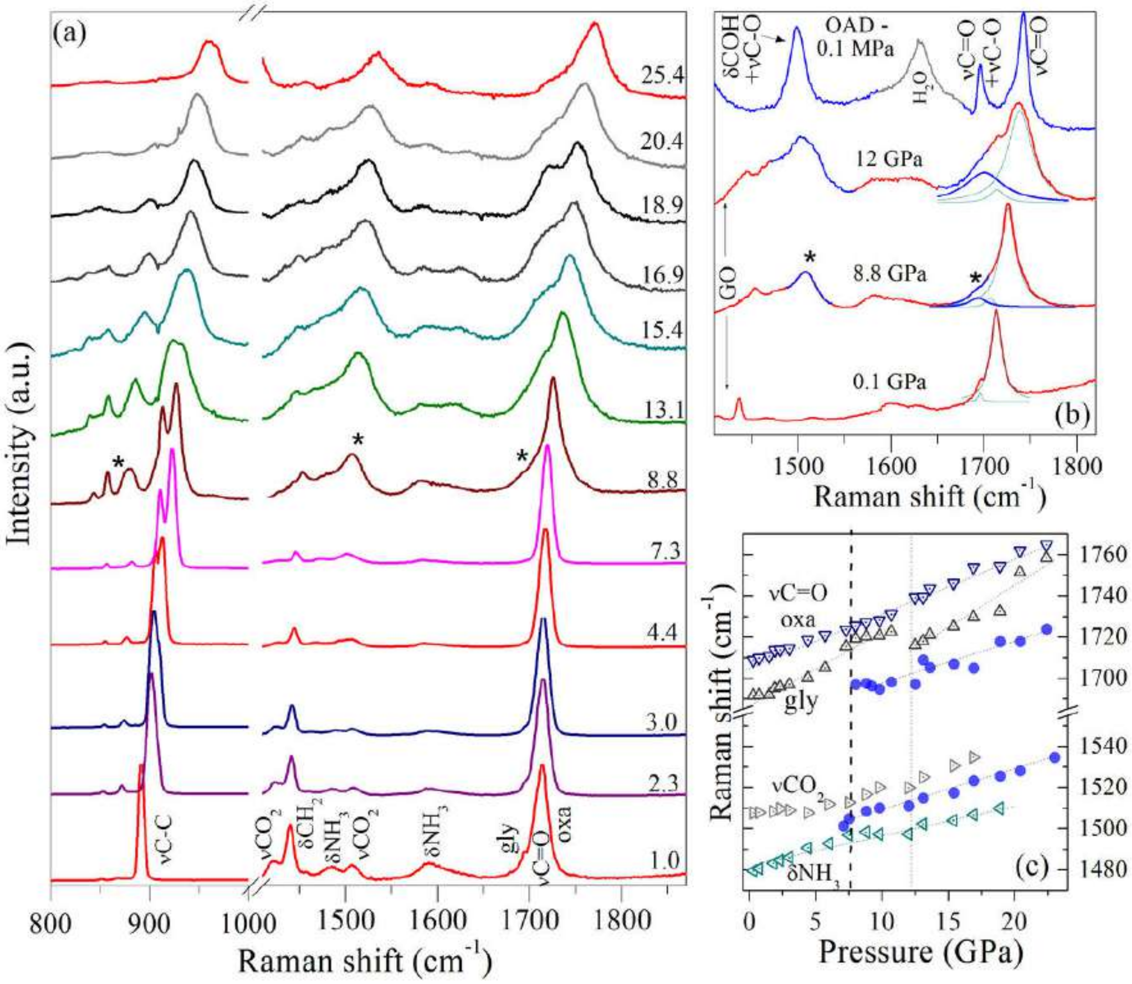

**Figure 4.8:** (a) High Pressure Raman spectra of GO in the range 800 – 1000 cm$^{-1}$ and 1410 – 1860 cm$^{-1}$ before (ambient to 8 GPa) and after symmetrization (above 8 GPa) of hydrogen bond between semioxalate molecules. Numbers denote pressure values in GPa. (b) A comparison of internal modes of GO in the high pressure symmetrized phase with OAD, where new modes appeared (in blue, marked with "$*$") are highlighted to show resemblance with neutral oxalic acid and light grey mode in OAD is due to water [35, 128]. (c) Pressure induced variation of some Raman modes of glycinium oxalate: "gly" denotes glycine and "oxa" denotes oxalate, blue solid circles are new modes appeared across 8 GPa.

stiffening behavior. Discontinuous reduction ($\sim$7 cm$^{-1}$) in the $\delta$OH mode across 8 GPa (Figure 4.5a) [136] and appearance of $\delta$CCOOH like features near 650 cm$^{-1}$ (Figure 4.5b) are also consistent with the neutral oxalic acid like features [35]. Figure 4.5b also shows the infrared spectrum of a neutral oxalic acid complex at ambient conditions for comparison, however the infrared spectra of GO are broad and much more populated and complex compared to OAD due to large number of fundamentals.

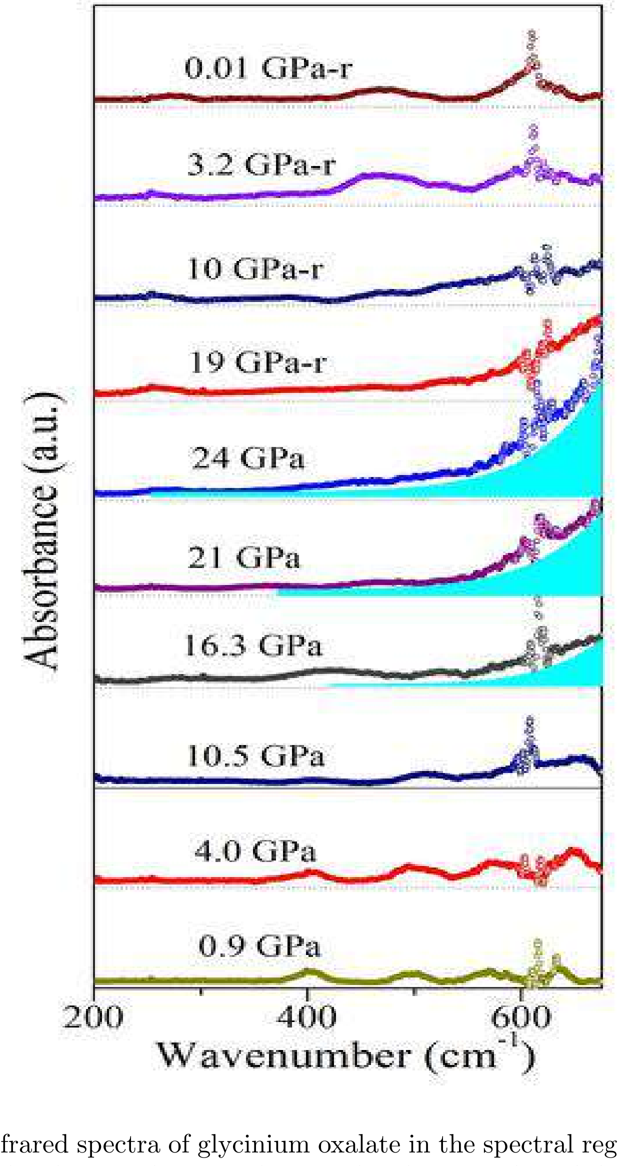

**Figure 4.9:** Far infrared spectra of glycinium oxalate in the spectral region 200 – 660 cm$^{-1}$ at high pressures. All the plots are drawn with same absorbance scale and the zero line (dotted) has been shown with the corresponding spectra. "r" denotes release pressure data. The fluctuations near 600 cm$^{-1}$ are due to a sharp dip in detector response in this region.

Thus, our high pressure Raman and infrared spectroscopic investigations combined with molecular dynamics calculations suggest the formation of a symmetric hydrogen bonded state above 8 GPa (see Figure 4.9). In addition, our X-ray diffraction measurements suggest that hydrogen bond symmetrization in this compound may occur without any drastic change in the structure [4]. This is inferred from the persistence of all the observed X-ray diffraction peaks of the ambient phase up to 15 GPa. All the experimental observations in glycinium oxalate are reproducible and reversible on complete release of pressure. However, the spectral signatures of the high pressure phase above 8 GPa are well preserved up to ∼ 3 GPa on release (See Figures 4.4b, 4.5a, 4.9 and 4.11), thus showing a hysteresis behavior. As such a behavior has been attributed to the covalent like O3-H7---O6 interactions between the semi-oxalate units in the high pressure phase [4], it further confirms our proposition of hydrogen bond symmetrization in this compound above 8 GPa.

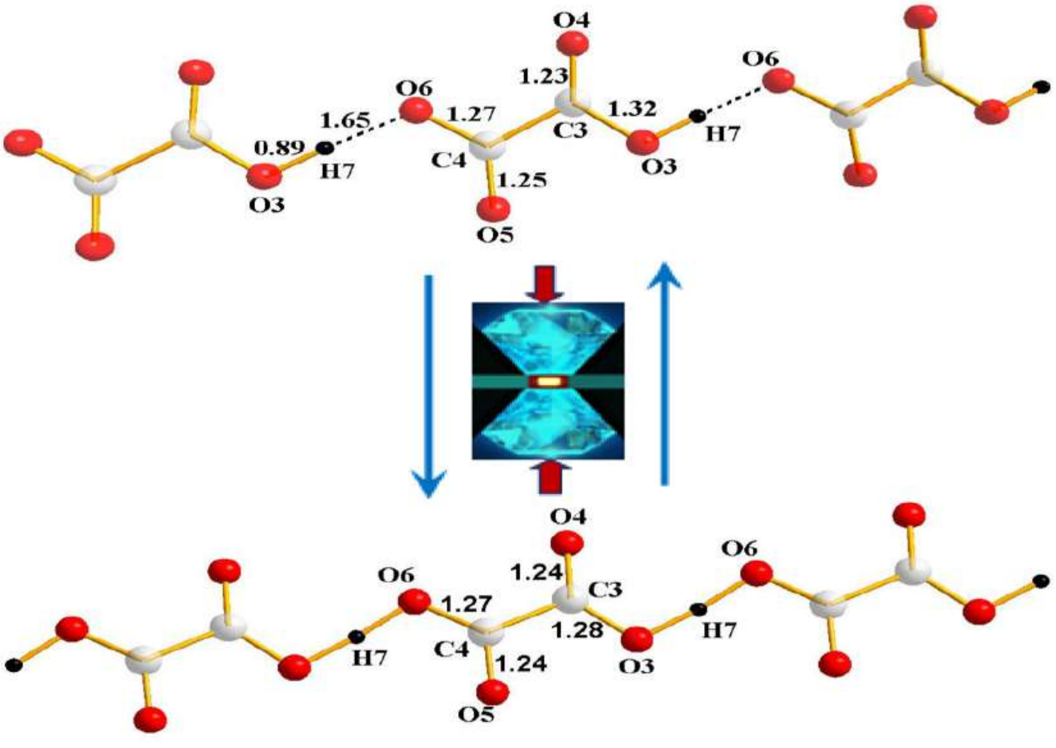

**Figure 4.10:** One semioxalate column along *b*-axis bridged through strong O3-H7---O6 hydrogen bond (top) with bond parameters at ambient condition and (bottom) snapshot of simulated chain at 20 GPa (from MD) after pressure induced hydrogen bond symmetrization (reversible) with average C-O/C=O distances.

Further, in O3-H7---O6, the proton (H7) sharing between two $COO^-$ groups (C3O4O3H7 and O6O5C4) would change the electronic structure of C4-O5 bond resulting in a double bond like character (C4=O5) (see Figure 4.1 bottom). It is

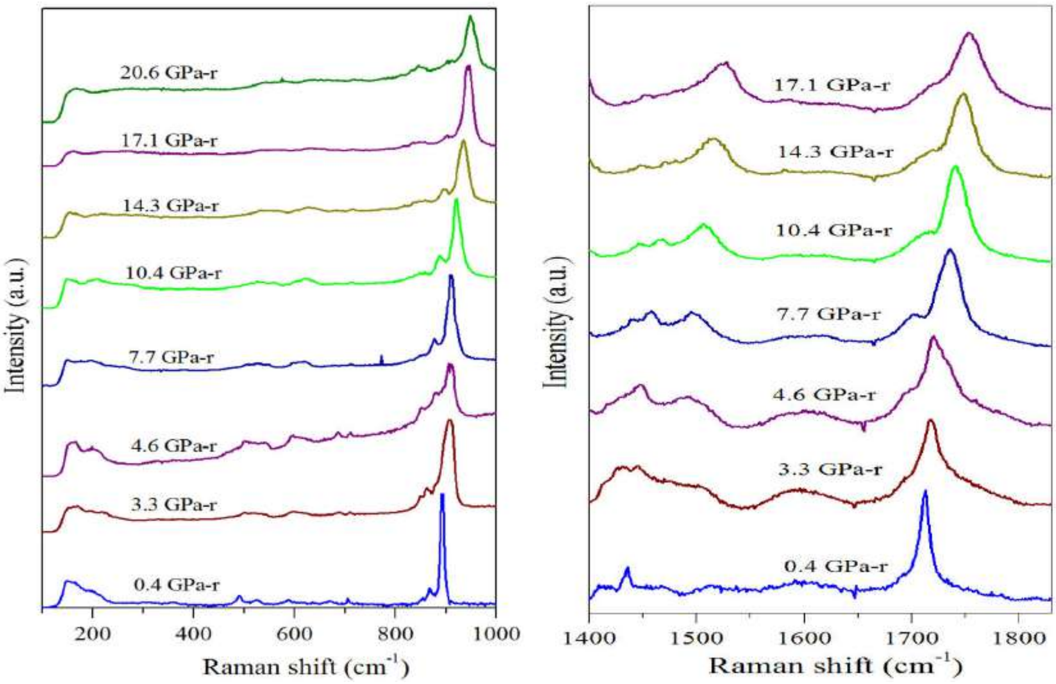

**Figure 4.11:** Raman spectra of GO during pressure release (r) in the region (left) 100 – 1000 cm$^{-1}$ and (right) 1400 – 1830 cm$^{-1}$.

of interest to note that, in the symmetrtized phase, the calculated C–O (C4–O6; C3–O3) and C=O (C4=O5; C3=O4) bond parameters of oxalate units approach values as expected for the neutral oxalic acid (Figure 4.10). Also note that the resulting anti-planar motif is an energetically favorable conformation [175]. Thus, in the high pressure phase, hydrogen bond symmetrization results in infinite oxalate ($HC_2O_4$) chains along the *b*-axis (Figure 4.10). In the three dimensional framework, these chains hold the glycine sheets in the *ac*-plane through strong O1–H1---O5 and N–H---O hydrogen bonds (Figure 4.1 top).

## 4.5 Hydrogen bond symmetrization aided supramolecular assembly

The structural implications of O3–H7---O6 hydrogen bond symmetrization in this compound and the influences of other hydrogen bonds at pressures above 12

GPa are discussed below. Glycine molecule is connected to the C3=O4 unit of carboxyl group of an oxalate chain through N1-H4---O4 hydrogen bonds. While the $\nu$N1-H5 and $\nu$N1-H6 IR bands show stiffening under pressure, $\nu$N1-H4 IR band remains nearly constant and shows small softening and discontinuous broadening at higher pressures (Figure 4.12a). The increase in the calculated N1-H4 bond length and reduction in $d_{\mathrm{H4---O4}}$ at pressures above 12 GPa (Figure 4.12b) shows that N1-H4---O4=C3 hydrogen bond becomes stronger at higher pressures as compared to the other N-H---O hydrogen bonds. The reduction in the relative intensity of $\nu$C=O oxalate mode (corresponding to C3=O4 near 1700 cm$^{-1}$) (Figure 4.8a) indicates onset of loss of $\pi$ bond character of C3=O4 and the formation of N1-H4---O4-C3 chain.

### 4.5.1 Bent to planar conformation of glycine

The formation of a supramolecular assembly (Figure 4.13) above 12 GPa through strengthening of N1-H4---O4 interactions is also indicated by the observed changes in glycine conformation with pressure. In the *ac*-plane, two adjacent glycine molecules are connected in a head to tail configuration (through N1-H5---O2), which are described here as bilayers (Figure 4.1). At high pressures, the inter-bilayer O2(gly)---O2(gly) distance (more than 4 Å at ambient pressure) consistently decreases (Figure 4.14b -inset), and reaches the limiting value ∼ 3 Å above ∼ 2.5 GPa, ∼2.9 Å at 8 GPa and 2.8 Å (extreme limit) above 12 GPa. Under compression, to overcome the steric repulsion in the *ac*-plane, molecular reorientations would be necessitated. Note that the inter-bilayer separation becomes less than the intra-bilayer separation above 2.5 GPa. The N1-H5---O2 hydrogen bond also weakens with pressure, as indicated by bond parameters and the variation of IR stretching mode with pressure (Figures 4.12a, b and 4.14b). In the observed IR and Raman spectra, the pressure induced reduction in the separation between the $\nu_{\mathrm{sym}}$ and $\nu_{\mathrm{asy}}$ CH$_2$ IR and Raman modes (∼60 to 40 cm$^{-1}$

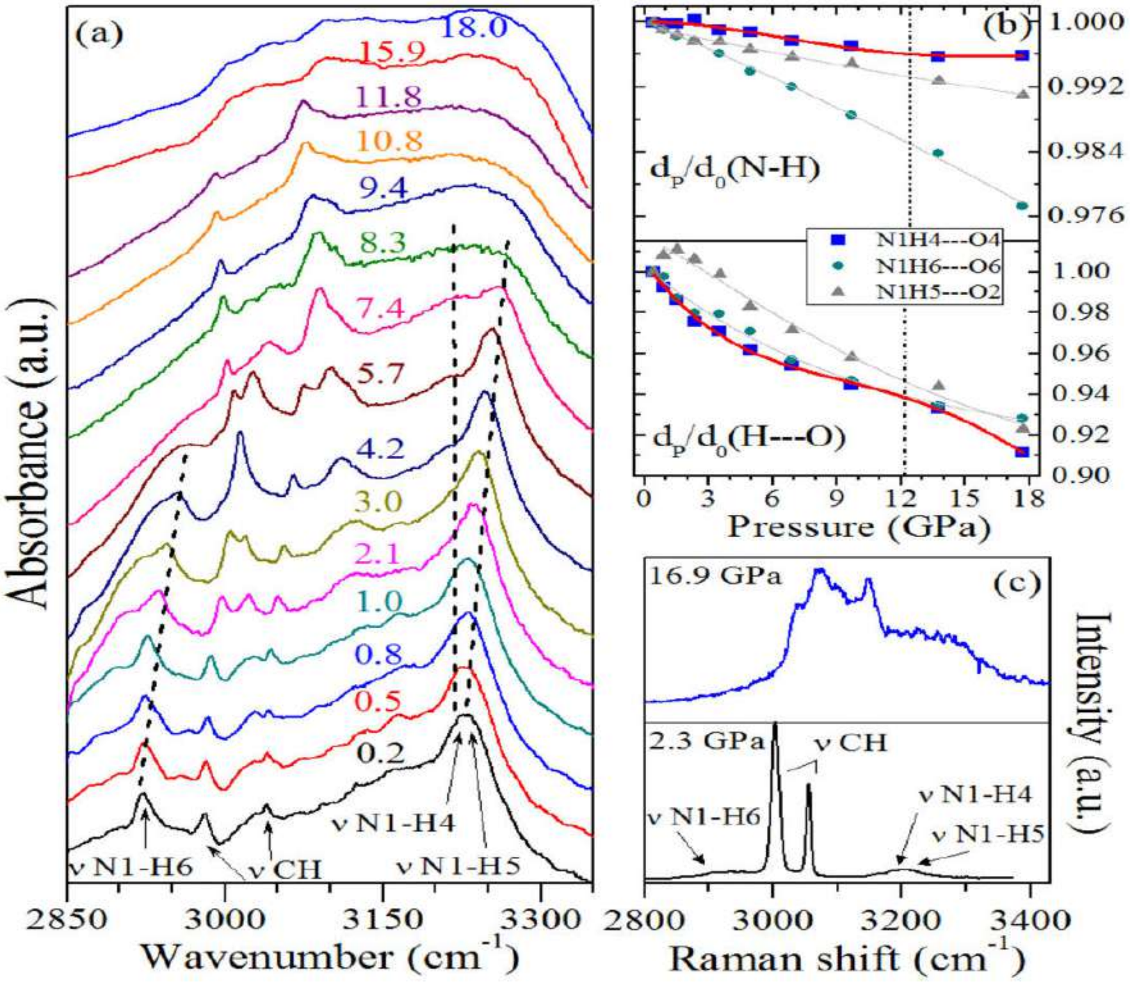

**Figure 4.12:** (a) High pressure IR spectra in CH/NH stretching region (2850–3350 cm$^{-1}$ ) with various fundamental and combination/overtone modes. Dotted lines in $\nu$NH modes are guide to eye. (b) Variation of normalized N-H and H---O distances (calculated) for various N-H---O hydrogen bonds with pressure. (c) Corresponding Raman spectra in NH stretching region also shows broad band emerging above 12 GPa due to formation of a supramolecular assembly in GO through N1-H4---O4 interactions.

up to 8 GPa) (Figure 4.14a) and the corresponding C-H bond distances (Figure 4.14b indeed indicate systematic changes in the conformation of glycine from bent to planar [56, 176]. The planar conformation of glycine implies reduction in the separation between glycine molecule (in *ac*-plane) and symmetrized oxalate chains (*b*-axis) on its two ends (see Figures 4.1 and 4.13), where the interactions between glycine and oxalates are through N1-H4---O4 and O1-H1---O5 hydrogen bonds. This is also evident from the simulated structure at higher pressures

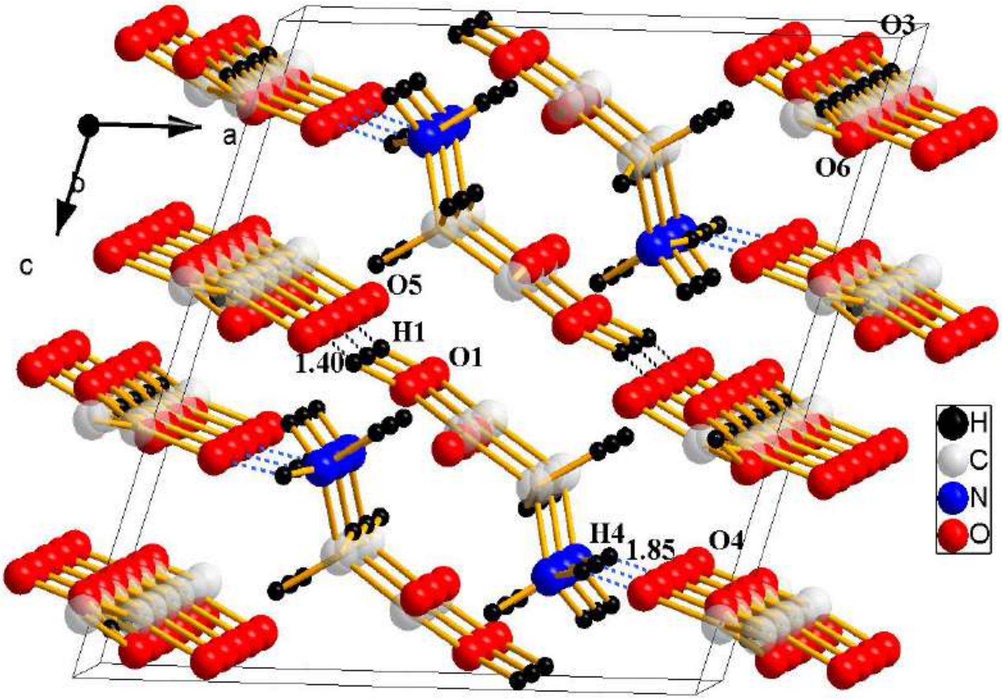

**Figure 4.13:** Structure of GO at 20 GPa (from MD) showing supramolecular assembly of glycinium oxalate in the high pressure phase where glycine is connected to two symmetrized oxalate chains through N1-H4---O4 and O1-H1---O5 hydrogen bonds. Pressure induced transformation of glycine units from bent (see Figure 4.1) to planar structure supports the formation of supramolecular chains.

(Figure 4.13). The splitting of the modes observed in the $\nu$CH region of IR and Raman spectra at higher pressures (Figure 4.12) [56,176] and $\nu$CC glycine Raman mode [54] (Figure 4.8a) may be due to systematic change in glycine conformation. Thus, the formation of a planar conformation of glycine suggested by the first principles calculations and spectral features corresponding to the glycine molecular units further support the above mentioned proposition. The evolution of broad envelopes in the lattice and $\nu$N-H regions in both IR (Figure 4.12a) and Raman spectra (Figure 4.12c) indeed suggest possible emergence of a supramolecular phase assisted by strong N1-H4---O4=C3 interactions at high pressures where glycine hammocks (in *ac*-plane) are tied to the infinite oxalate poles (*b*-axis) as shown in Figure 4.13.

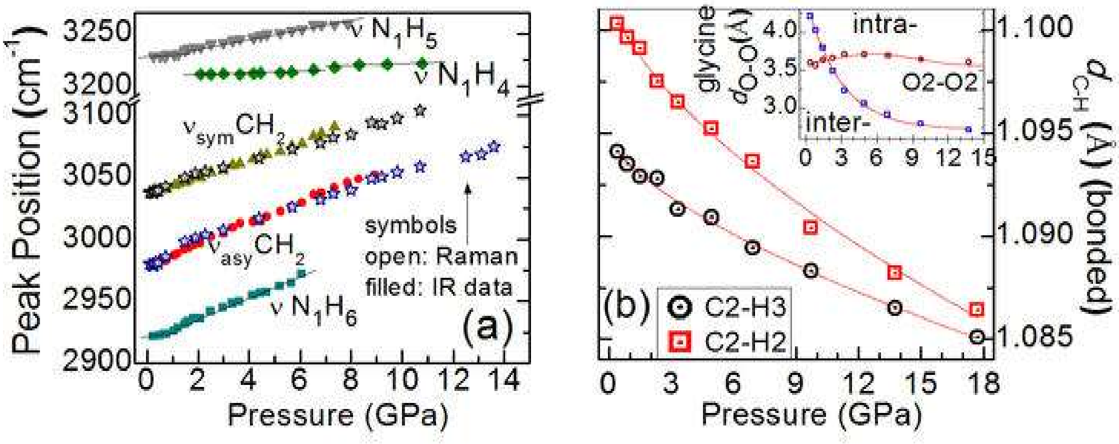

**Figure 4.14:** (a): Pressure dependence of νCH and νNH modes in GO. (b): Variation of bonded glycine CH distances; inset: non-bonded glycine O2–O2 distances (inter and intra bilayer described in Figure 4.1 of main text) with pressure.

## 4.6 Conclusions

To summarize, we have reported hydrogen bond symmetrization in glycinium oxalate, the simplest amino acid-carboxylic acid molecular system at moderate pressures of 8 GPa. The large softening accompanied by pronounced broadening of the O–H stretching vibrations of semioxalate units and emergence of spectral features corresponding to neutral like oxalic acid suggest a delocalized proton which is dynamically shared between two carboxylic groups, thus forming an infinite chain along the crystal *b*-axis. These observations are well supported by DFT based molecular dynamics calculations which have confirmed the movement of proton towards the bond mid-point under pressure and significant probability of crossing the barrier above 8 GPa. At pressures above 12 GPa, the glycine units systematically reorient with pressure to form hydrogen bonded supramolecular assemblies held together by these chains.

# 5

# Phase transformations in Bis(glycinium)oxalate- high pressure and low temperature studies

## 5.1 Introduction

Bis(glycinium) oxalate (BGO - $C_2H_6NO_2.0.5C_2O_4$), another organic complex of glycine and oxalic acid family (glycine: oxalic acid :: 2:1) has a very short and strong O-H---O hydrogen bond (O-H=1.165 Å, H---O=1.3 Å, O---O=2.461 Å and ∠ O-H---O=174.2°) between glycinium ($NH_3CH_2COOH^+$) and oxalate ions ($C_2O_4^{2-}$) [64]. In addition there are various moderately strong N-H---O and weak C-H---O hydrogen bonds (Table 5.1). As the distances between several non-bonded atoms in this compound are close to the steric limits [138, 145] and the bond parameters of the strong O-H---O hydrogen bond (non-linear) are close to the symmetrization limit, the compression of BGO can significantly alter the intermolecular interactions leading to new structures, which may be of technological interest. It is noteworthy that many complexes of glycine such as triglycine sulphate, diglycine nitrate etc. are also found to display ferroelectric properties which have possible applications in electronic devices [177–182]. In fact, Tri glycine sulphate forms the most famous room temperature infrared detector. The ferroelectric transitions in such compounds are reported to be significantly influenced by the hydrogen bonding networks [60].

At ambient conditions Bis(glycinium) oxalate crystallizes in a centrosymmetric monoclinic structure with space group $P2_1/n$ and 4 formula units per unit cell as shown in Figure 5.1 [64]. One cationic glycine molecule (with a positively charged amino group and an uncharged carboxylic acid group) and half of doubly ionized oxalic acid form the asymmetric unit. The oxalate anion lies across the inversion centre in the crystal. Two hydrogen atoms H1 and H2 of the amino group form bifurcated, i.e. three-centered hydrogen bonds. If the inversion symmetry in the crystal is lost at higher pressures, a non centrosymmetric phase would be obtained which may exhibit pyroelectric properties. It may also show ferroelectricity as reported for many non-centrosymmetric complexes of glycine if appropriate polarization conditions are met.

Recent high pressure Raman and X-ray diffraction investigations of Bis(glycinium) oxalate indicate a structural transformation above $\sim$ 1.7 GPa [138]. Across the transition pressure, new modes were observed to be emerging in the Raman spectra [138], where the N-H---O hydrogen bonds show significant changes. However, so far no information is available about the high pressure or low temperature behaviour of the strong O-H---O hydrogen bond. As O-H stretching mode corresponding to this strong O-H---O hydrogen bond of Bis(glycinium) oxalate can be observed only in the infrared spectrum, we have studied the high pressure behaviour of the OH infrared active mode and the nature of the possible phase transformations in this compound. Dielectric measurements under high pressure capacitance have also been carried out to shed light on the nature of the phase transformation. In addition, low temperature infrared and X-ray diffraction studies have been presented which show remarkable stability of the hydrogen bonding network.

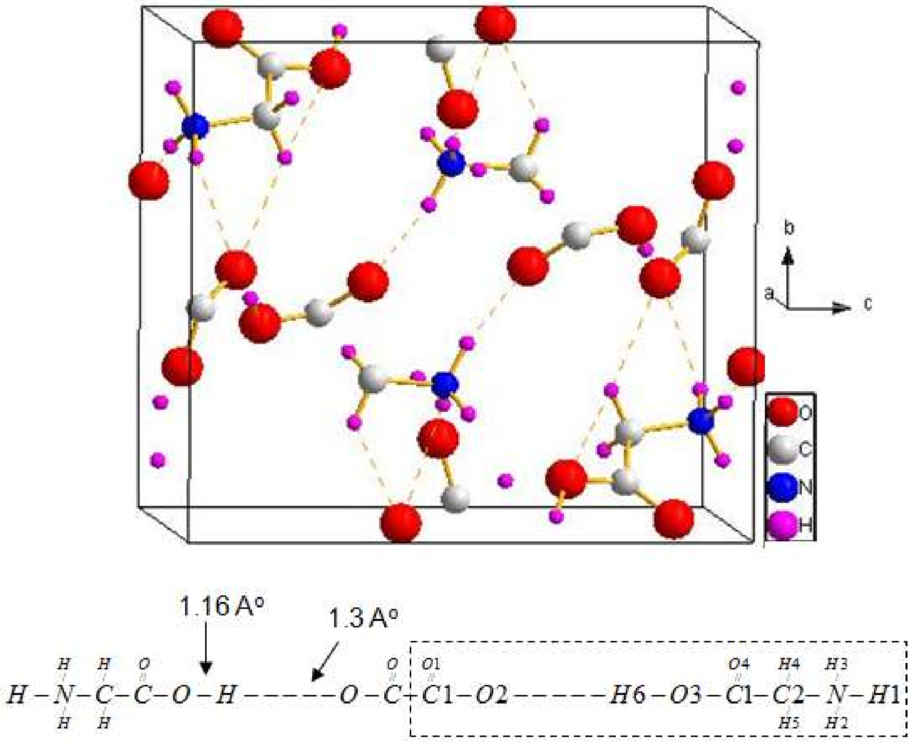

**Figure 5.1:** (top) The strucuture of Bis(glycinium) oxalate; (bottom) shematic showing strong O-H---O hydrogen bond formation between glycinium and oxalate ions; dashed block is one asymmetric unit.

## 5.2 High pressure studies - Internal modes in the fingerprint region

Infrared (IR) spectrum of Bis(glycinium) oxalate has been recorded in the spectral region 600 - 4000 cm$^{-1}$ at different pressures. However, the analysis of IR spectra of BGO, particularly in the spectral region above 2000 cm$^{-1}$, is relatively complex as the spectrum is populated with large number of fundamentals, overtones and combination bands (Figure 5.2). As complete assignment of infrared active modes of this compound is not available in the literature, we have assigned the modes in

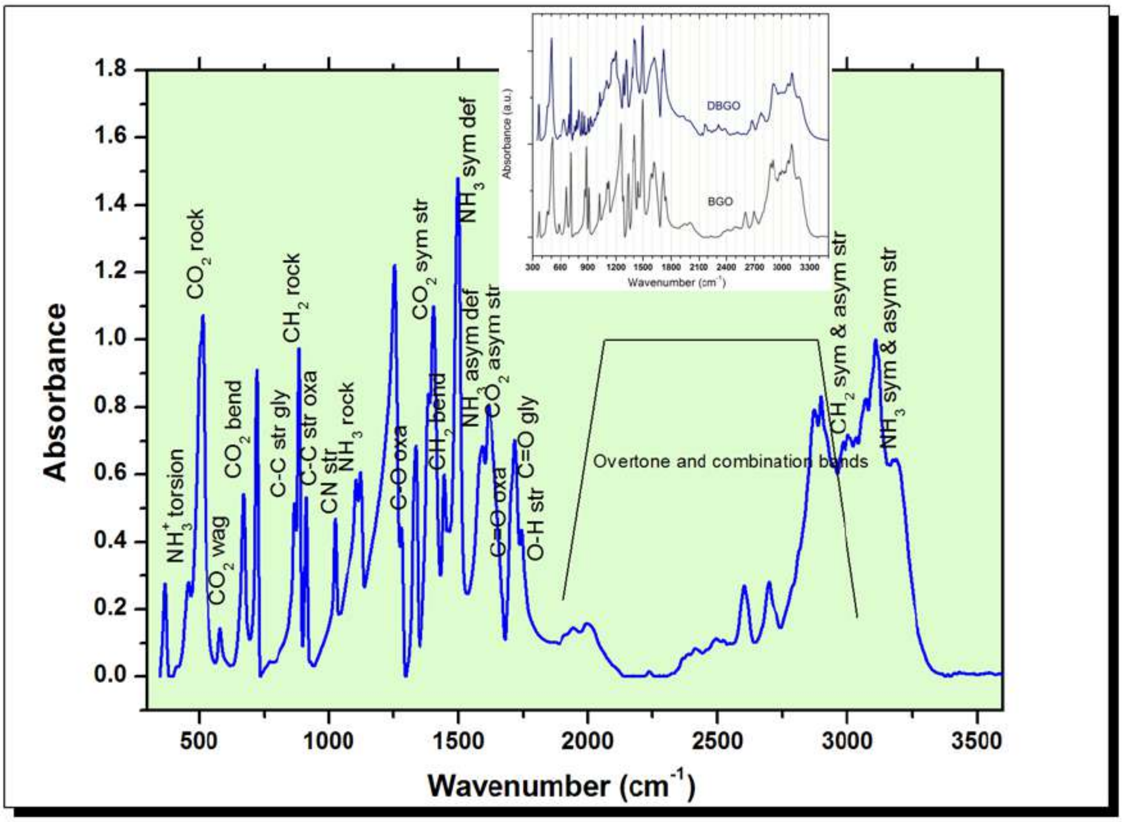

**Figure 5.2:** Infrared spectrum of Bis(glycinium) oxalate; inset: comparison of IR spectra of BGO and its deuterated analogue.

the spectral region 600-2000 cm$^{-1}$ and above 3000 cm$^{-1}$ at ambient conditions as well as at higher pressures based on the individual Raman and IR active modes of glycine, oxalic acid and glycinium oxalate as well as the Raman active modes of Bis(glycinium) oxalate [54, 64, 66, 128, 138, 183–185]; also a comparison of IR modes of BGO and its deuterated analogue was used to confirm the assignments (Figure 5.2). For identifying the vibrational modes of cationic glycine we have used the assignments given for triglycine sulphate [54, 183]. We have catalogued all the observed spectral changes in the region 600-1650 cm$^{-1}$ in sub-sections 5.2.1 and 5.2.2 and their structural implications are discussed in §5.3. The spectral changes in the region 1650 - 1800 cm$^{-1}$ and near 3200 cm$^{-1}$ region are reported and discussed in the context of changes in the O-H---O and N-H---O hydrogen

**Table 5.1:** Various hydrogen bond parameters in Bis(glycinium) oxalate at ambient conditions.

| X-H---Y | X-H (Å) | H---Y (Å) | X---Y (Å) | ∠XHY (°) |
|---|---|---|---|---|
| N2-H1---O1 | 1.025 | 1.937 | 2.910 | 157.3 |
| N1-H1---O3 | 1.025 | 2.556 | 3.062 | 110.0 |
| N1-H2---O1 | 1.040 | 1.810 | 2.848 | 175.1 |
| N1-H2---O2 | 1.040 | 2.445 | 2.925 | 107.1 |
| N1-H3---O4 | 1.009 | 1.885 | 2.874 | 166.3 |
| O3-H6---O2 | 1.165 | 1.300 | 2.461 | 174.2 |
| O3-H6---O1 | 1.165 | 2.531 | 3.203 | 115.0 |
| C3-H4---O2 | 1.075 | 2.566 | 3.460 | 140.2 |
| C3-H5---O2 | 1.056 | 2.392 | 3.099 | 123.1 |

bonds in §5.4.

### 5.2.1 The skeletal region

Figure 5.3 displays the high pressure infrared spectra in the region 650-1200 cm$^{-1}$ and Figure 5.4 gives variation of the peak positions of these IR modes with pressure. Particular attention has been paid to understand the high pressure behavior of skeletal modes, which form the backbone of glycine and oxalic acid molecules and have shown significant changes in the high pressure Raman spectra [138]. These C-C and C-N stretching modes are expected in the spectral region 800-1050 cm$^{-1}$.

As shown in Figure 5.3, three modes are observed between 850 and 920 cm$^{-1}$. They are at 869 cm$^{-1}$ (C-C stretch of glycine), 888 cm$^{-1}$ (CH$_2$ rock of glycine) and 912 cm$^{-1}$ (C-C stretch of oxalate). All these modes are found to display very small stiffening with pressure (Figure 5.4). However, beyond 1.6 GPa, the frequency of the peak at 912 cm$^{-1}$ does not increase much with pressure and in fact shows a tendency to decrease at further higher pressures. The peak at 888 cm$^{-1}$ also remains nearly constant up to 4 GPa. The peak at 869 cm$^{-1}$ continues to stiffen up to 4.5 GPa and at 1.6 GPa, this mode is observed at 874 cm$^{-1}$. A new mode emerges at ∼894 cm$^{-1}$ at pressures above 1.6 GPa, which also stiffens with pressure. The intensity of this new mode is found to increase at higher pressures. We find that this mode corresponds to the C-C stretching Raman mode of glycine at ambient conditions [54, 138]. It may be noted here that a new mode was also reported at 874 $cm^{-1}$ in the high pressure Raman spectrum above 1.7 GPa and its position as well as intensity increased at higher pressures [138]. As revealed from the frequency and intensity variations in the present IR spectra, the new mode in the Raman spectra can be assigned as the C-C stretching mode of glycine.

It is of interest to note that the mode at 912 $cm^{-1}$, which we have assigned as C-C stretching mode of oxalate shows a slight softening at pressures above 4 GPa. This high pressure behaviour is consistent with the Raman active C-C stretching mode (857 $cm^{-1}$) of oxalate which shows softening in the similar pressure range. These observations suggest that our assignment for this mode is appropriate. The large variation in the positions of infrared and Raman active mode has also been reported for some materials in the literature [186]. The softening of the C-C stretch of oxalate and stiffening of the new C-C stretch glycine and $CH_2$ rock modes result in a single broad band, comprising of these three peaks, after 5 GPa.

The $CO_2$ bending mode, which is very weak in the Raman spectrum [138], appears with prominent intensity at 672 $cm^{-1}$ in the infrared spectrum as shown in Figure 5.3. This mode shows pressure induced stiffening in both infrared and Raman spectra. At 1.6 and 4.5 GPa, the peak position increases to 675 $cm^{-1}$ and 682 $cm^{-1}$ respectively as shown in Figure 5.4. Interestingly, the peak becomes broad at higher pressures and a new shoulder emerges at nearly 670 $cm^{-1}$ after 4.5 GPa, but it is not well resolved in the current pressure range. It should be noted here that the $CO_2$ bending mode appears at 669 $cm^{-1}$ in the Raman spectrum.

The C-N stretch (1025 $cm^{-1}$) and $NH_3$ rock (1124 $cm^{-1}$) modes, as shown in Figure 5.4, show stiffening at higher pressures. In the case of Raman spectra,

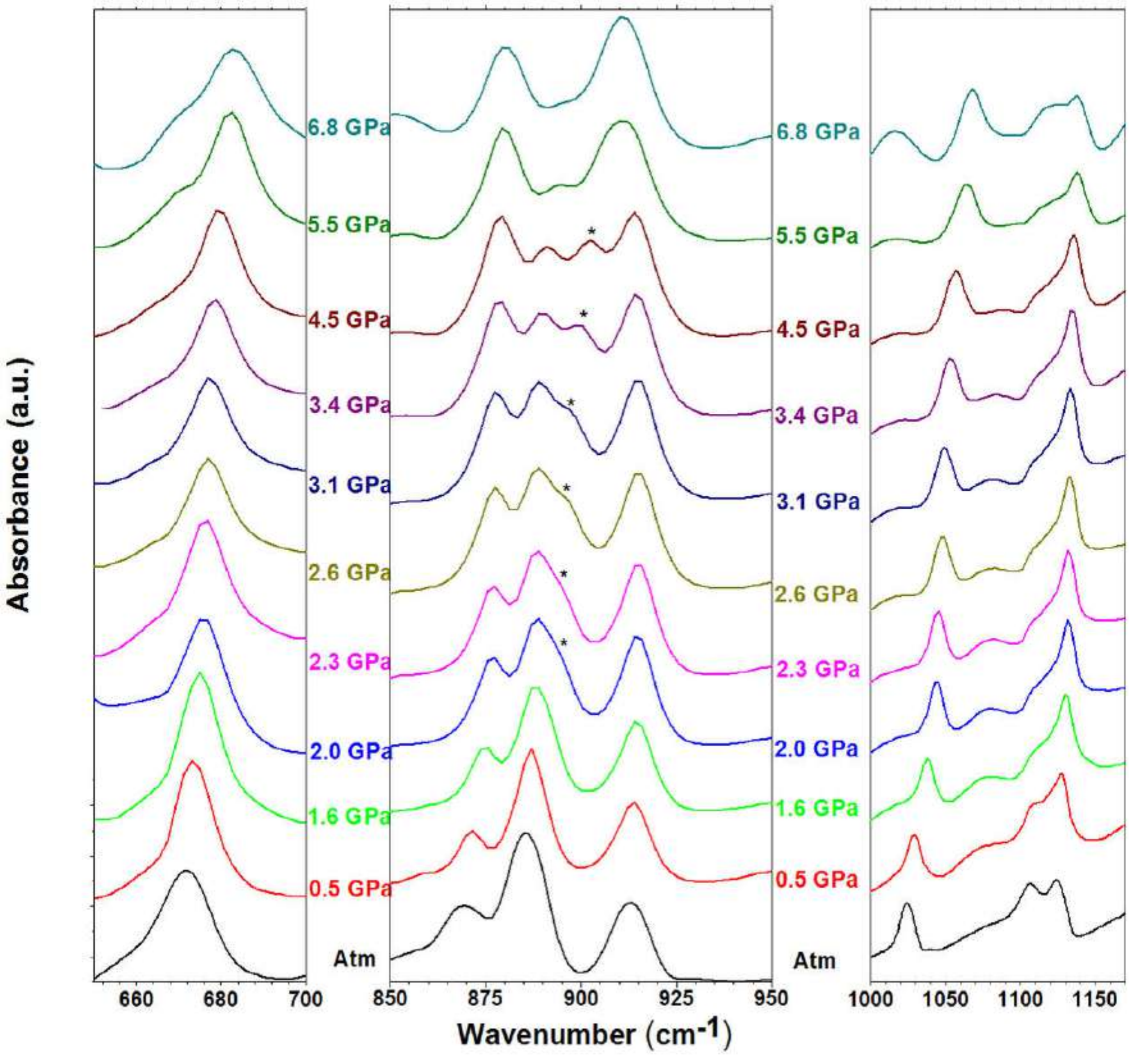

**Figure 5.3:** High pressure infrared spectra of Bis(glycinium) oxalate showing $CO_2$ bend, C-C stretch, $CH_2$ rock, C-N stretch and $NH_3$ rock modes in the 600-1200 $cm^{-1}$ region. New peaks emerged at higher pressures have been marked with asterisk.

across the transition C-N stretch mode showed a discontinuous jump to a higher value and a new mode appeared at a lower value [138]. In the present infrared spectra, above the transition pressure, the C-N stretching mode shows broadening (in FWHM) which increases with pressure, as shown in the inset of Figure 5.4. Moreover its intensity also increases with pressure (Figure 5.3).

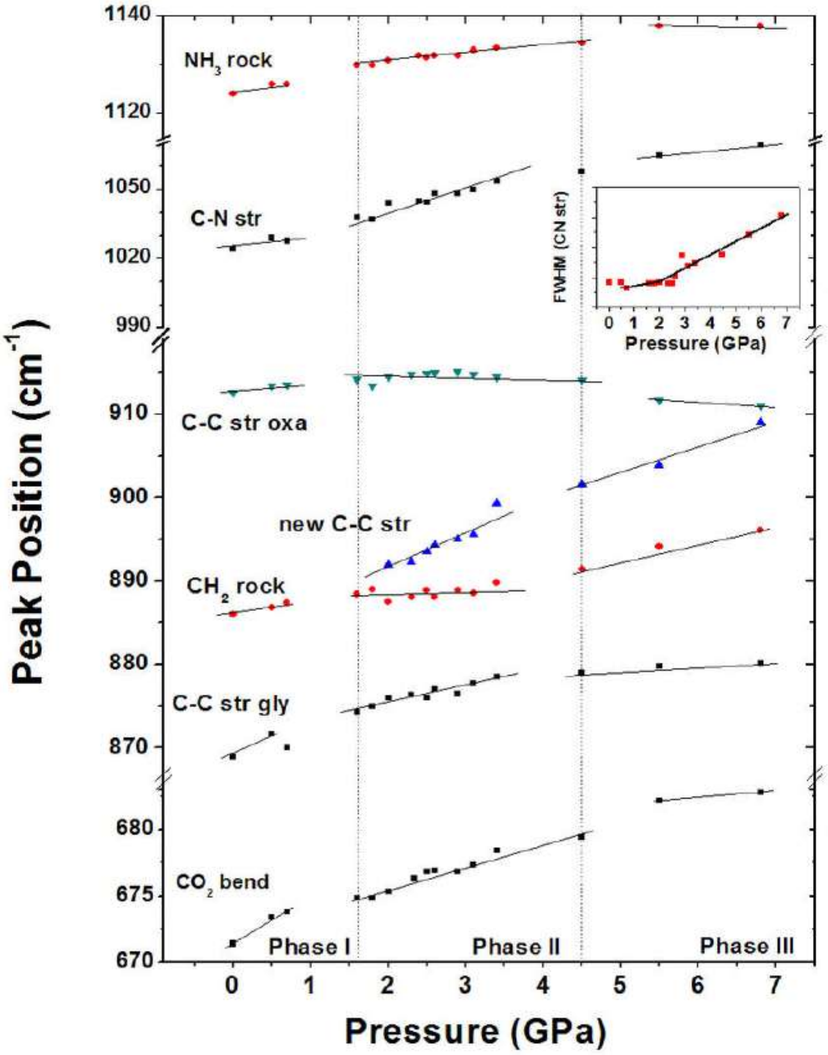

**Figure 5.4:** High pressure infrared spectra of BGO in the spectral region 650-1150 cm$^{-1}$. Inset shows the variation in FWHM of CN stretch mode with pressure.

### 5.2.2 The bending region

High pressure infrared spectra in the region 1300 - 1700 cm$^{-1}$ have been plotted in Figures 5.5(a) and (b) and the pressure induced variations of the corresponding infrared modes have been plotted in Figure 5.6. The CH$_2$ twist and wagging modes appear in the 1300 cm$^{-1}$ region. Note that in high pressure Raman spectroscopy, it is difficult to study vibrational modes in the 1300 cm$^{-1}$ region as they get buried under strong diamond peak from DAC. In the ambient infrared spectrum, the $CH_2$ twist and wagging modes are merged as one broad band and have been deconvoluted with peak positions at 1327 $cm^{-1}$ and 1337 $cm^{-1}$ respectively. These peaks are well split at higher pressures. Initially these modes depict opposite high pressure behavior, though the rate of change of peak positions is small, as shown in Figure 5.6, with $CH_2$ twist mode showing stiffening and $CH_2$ wag showing softening. However, beyond 1.6 GPa both the modes stiffen with pressure. In addition, across 1.6 GPa, the $CH_2$ twist and wagging modes discontinuously jump towards lower and higher values respectively and after 4.5 GPa, both of these modes show pressure induced softening.

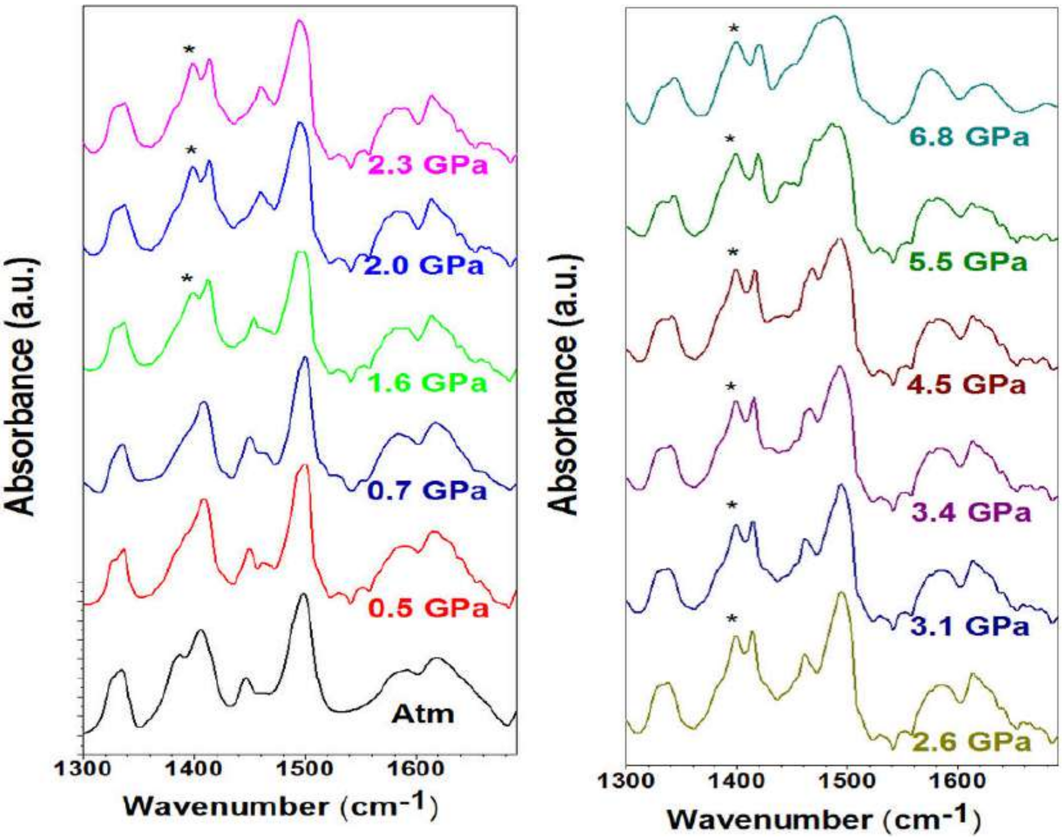

**Figure 5.5:** High pressure infrared spectra of BGO in the spectral region 1300-1700 $cm^{-1}$ (a) 0.1 MPa to 2.3 GPa, (b) 2.6 to 6.8 GPa. The new peaks emerged at higher pressures have been marked with asterisk.

The two $CO_2$ symmetric stretching modes observed at 1382 $cm^{-1}$ and 1406 $cm^{-1}$ at ambient pressure, show stiffening at different rates with pressure as shown in

Figure 5.6. The intensity of the first mode reduces sharply with pressure and it tends to get buried under the second mode, thus is observed as a shoulder peak, as can be seen in Figures 5.5(a). After the phase transition at 1.6 GPa, a new mode appears near 1400 $cm^{-1}$. The first peak remains as weak shoulder in all the spectra in the new phase. Although, the peak positions of the new mode and the strong second peak do not vary much (Figures 5.5b), their separation increases at further higher pressures. Interestingly, the intensity of the new mode consistently increases with pressure.

$CH_2$ bending and scissoring modes appear at 1460 $cm^{-1}$ and 1446 $cm^{-1}$ respectively, whereas the $NH_3$ symmetric deformation mode appears at nearly 1496 $cm^{-1}$. The $CH_2$ bending mode in BGO shows relatively weak absorption in the infrared spectrum as compared to $CH_2$ scissoring mode, whereas the $NH_3$ symmetric deformation mode is relatively strong as shown in Figures 5.5(a). Across the phase transition at 1.6 GPa, $CH_2$ scissoring mode discontinuously shifts towards a higher value (see Figure 5.6). In contrast, the $NH_3$ deformation mode shows pressure induced softening in the high pressure phase and across 4.5 GPa, undergoes a discontinuous jump to a higher value beyond which it further softens but with relatively lesser rate. The broad $NH_3$ asymmetric deformation and $CO_2$ asymmetric stretching modes appear as a doublet near 1600 $cm^{-1}$. The $CO_2$ asymmetric stretching mode at 1590 $cm^{-1}$ is weaker than $NH_3$ asymmetric deformation mode at 1617 $cm^{-1}$ at ambient pressure. But, its intensity consistently increases with pressure.

## 5.3 Phase transition to a non-centrosymmetric structure

Based on the experimental results discussed above, it can be summarized that the pressure induced spectral changes in the region 650-1650 $cm^{-1}$ are indicative of a

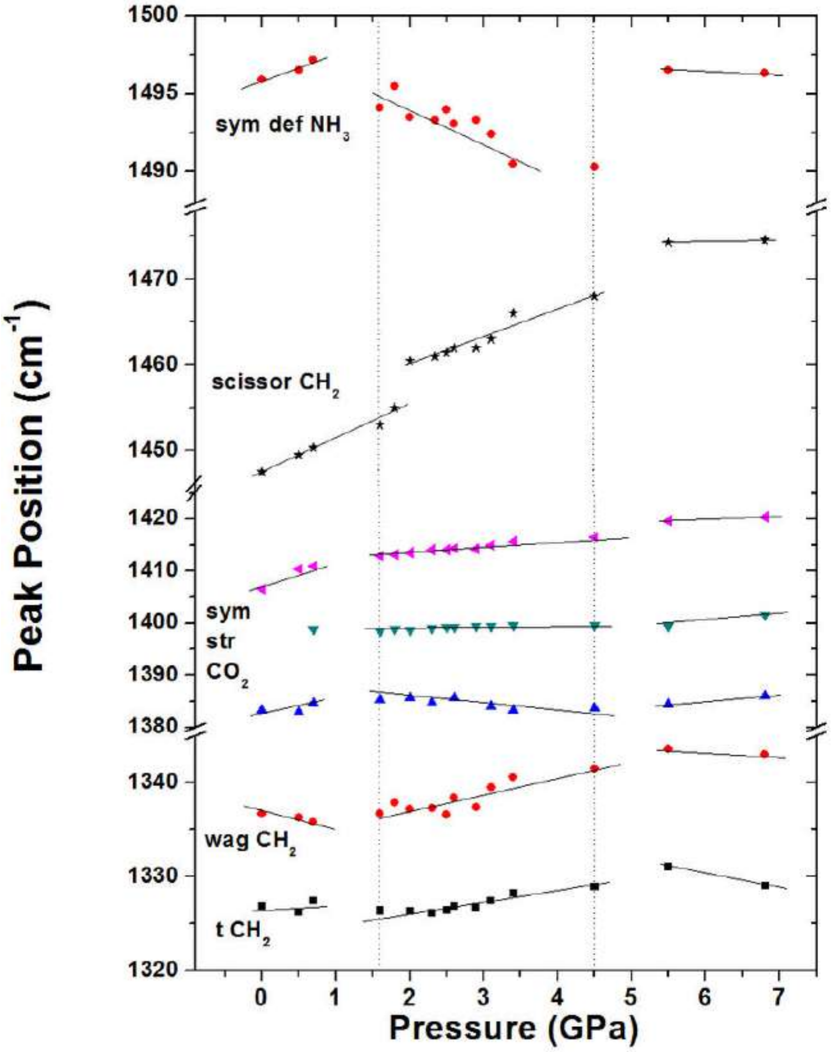

**Figure 5.6:** Pressure induced variation of IR active modes in the 1300-1500 cm$^{-1}$ spectral region.

phase transformation across 1.6 GPa in Bis(glycinium) oxalate. Many IR modes, which could be resolved up to 7 GPa, also show discontinuous changes across 4.5 GPa indicating another phase transition across this pressure. These results are consistent with the changes observed in the high pressure Raman spectra [138]. The most significant feature is that the new modes and features observed in the infrared spectra across the phase transition at 1.6 GPa are found to correspond to the Raman modes of glycine. The observed peak positions of C-C stretch modes of both cationic glycine molecules in the new phase are very close to that reported for triglycine sulphate which also has two cationic glycine molecules [54, 183]. Further, the new C-C mode which appeared in the infrared spectrum is found to show same high pressure behaviour as that of the corresponding C-C stretch Raman active mode of glycine.

Thus, from the corroboration of infrared and Raman spectra at high pressures, it is evident that the two glycine molecules have become non-equivalent above the transition pressure which implies that the centre of symmetry is lost and as there is no mutual exclusion rule, these modes have become both Raman and infrared active. These results are also supported by the high pressure X-ray diffraction studies where the possible space group for the higher pressure monoclinic phase was predicted as $P2_1$, which belongs to a non-centrosymmetric crystal structure [138].

## 5.4 High pressure behavior of strong hydrogen bonds in BGO

The structural arrangement of Bis(glycinium) oxalate is such that two glycine molecules are connected to one oxalate by hydrogen bonds and the overall network is also held together by other hydrogen bonds. There is a very short and strong hydrogen bond (O-H = 1.165 Å, H---O=1.3 Å, O---O=2.461 Å) between the carboxylic groups of oxalate and glycine molecules and this bond is close to symmetrization limit [64]. Before discussing the high pressure behavior of this very strong hydrogen bond, we first discuss the moderately strong N-H---O hydrogen bonds (Table 5.1) in BGO which construct the framework for the three dimensional structure.

### 5.4.1 The three dimensional network of N-H---O hydrogen bonds

Figure 5.7 shows the high pressure IR spectra in the region 2800 - 3400 cm$^{-1}$. This spectral region is quite complex due to the presence of many fundamentals as well as overtones and combinations. The present data indicate that the N-H stretching modes show initial softening which is followed by a discontinuous shift to a higher value at 1.6 GPa and small stiffening thereafter. The high pressure Raman data (for example see Figure 5.8), in addition to depicting various changes in internal modes signifying the phase transformation across 1.6 GPa, present relatively simpler spectra above 3000 cm$^{-1}$ with two clear modes corresponding to symmetric and asymmetric stretching $CH_2$ modes and a band characteristic of the N-H stretching modes near 3200 cm$^{-1}$ [138]. The N-H stretching Raman modes clearly depict a discontinuous blue shift across 1.6 GPa, which shows a good consistency with the infrared spectral features in this region. The pressure induced variations in the IR and Raman modes for N-H stretching vibrations have been plotted in Figure 5.9. These observations indicate that the N-H---O hydrogen bonds are broken and reformed across the phase transformation.

### 5.4.2 Short O-H---O hydrogen bonds

The behavior of strong O-H---O hydrogen bond which forms between two different molecules having different proton affinity, is quite interesting and at variance with what was encountered in the previous two cases of OAD (oxalic acid dihydrate -chapter 3 of this thesis) and GO (glycinium oxalate - chapter 4 of this thesis). This can be inferred from the reported bond energy, estimated using Lippincott & Schroeder (1955) semi-empirical potential function [64, 187]. The detailed analysis shows that while this bond has partial covalent nature, there is no disorder in the hydrogen bond. The O-H stretching frequency corresponding to this short hydrogen bond in BGO at ambient conditions has been estimated

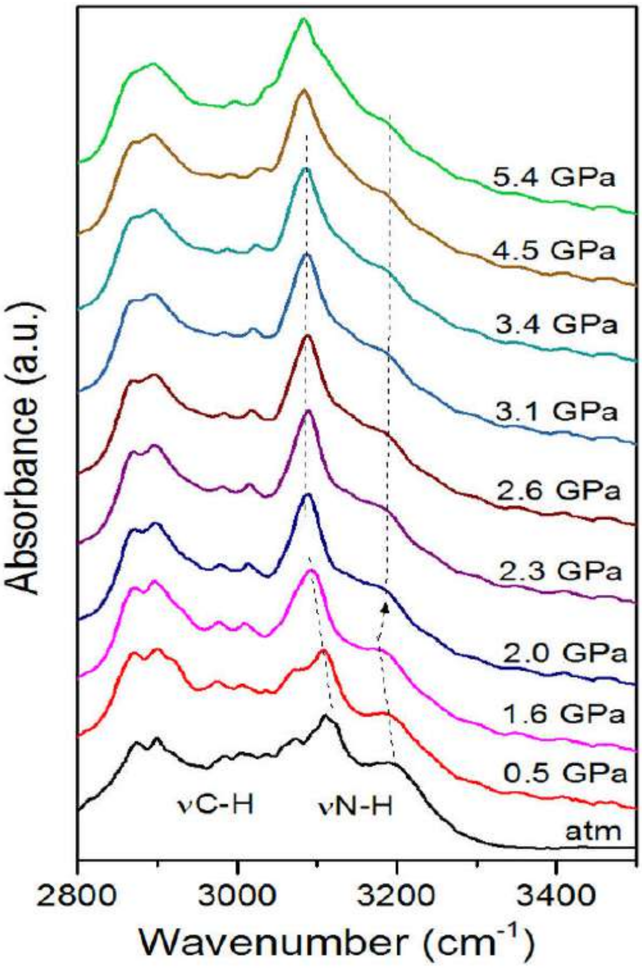

**Figure 5.7:** Infrared spectra of Bis(glycinium) oxalate in the spectral region 2800-3400 cm$^{-1}$ at various pressure, dashed lines and arrow are guide to the eye to follow the N−H stretching modes; $\nu$ - stretching.

to be around ∼1745 cm$^{-1}$ [64]. This is substantially lower than the value for a free O−H stretching vibration at ∼3700 cm$^{-1}$, as the O−H stretching vibrational frequency in an O−H---O hydrogen bond is found to reduce with the reduction of H---O distance. Corresponding to the O---O distance 2.461 Å in Bis(glycinium) oxalate, the assignment of the mode observed at 1745 cm$^{-1}$ to the OH stretching mode is also consistent with the empirical correlation curve between experimental values of O−H---O distance and O−H stretching frequency for various compounds given in references [12, 13, 162, 188]. While carrying out

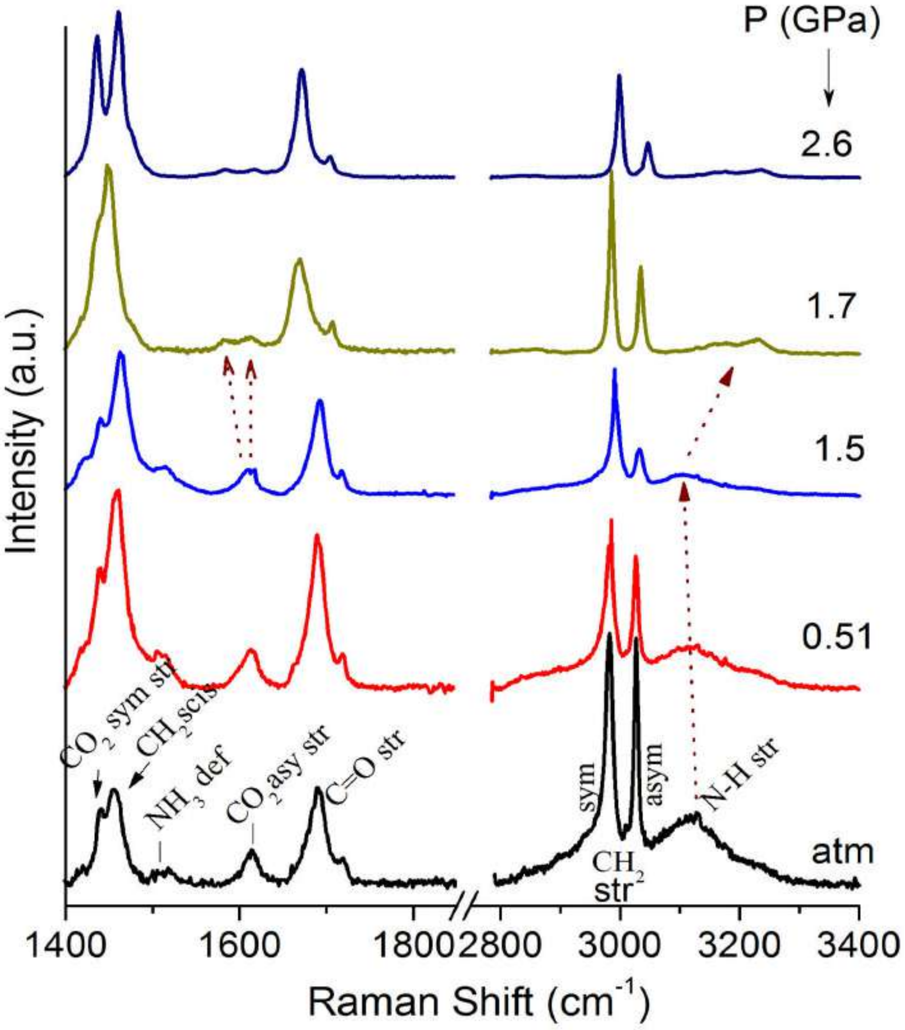

**Figure 5.8:** High pressure Raman spectra of Bis(glycinium) oxalate showing the behavior of various Raman active modes with pressure.

the ambient characterization of BGO in an earlier work, a broad band in the infrared spectrum around 1700 - 1755 cm$^{-1}$ was assigned to the O-H stretching mode [64]. But strong C=O vibrations are also expected in this region. We could observe all the modes present in this region on increasing the resolution in our infrared spectra, as shown in Figure 5.10(left). The O-H stretching vibrational peak corresponding to the O-H---O hydrogen bond is present as a shoulder of the strong C=O peak (1717 cm$^{-1}$) at ambient conditions.

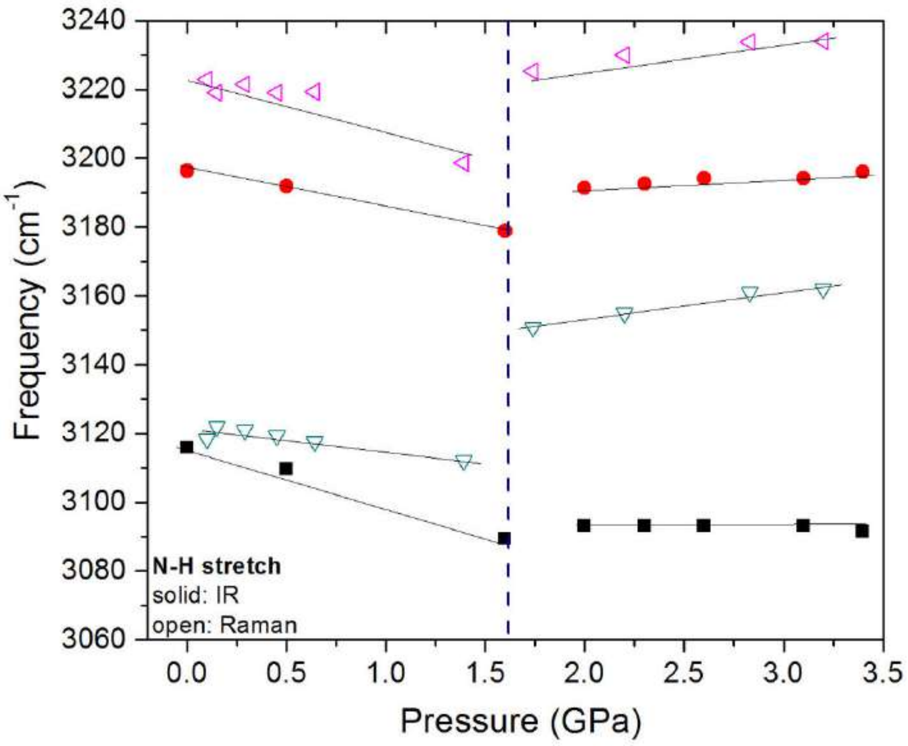

**Figure 5.9:** High pressure behavior of IR (solid) and Raman (open) N–H stretching modes in BGO.

Figure 5.10(right) shows the variation in frequencies of C=O and O–H stretching modes in this region as a function of pressure. The mode corresponding to the C=O group exhibits a pressure induced stiffening, but with different rates in the ambient pressure phase and the high pressure phases beyond 1.6 and 4.5 GPa. The O–H stretching mode (1745 cm$^{-1}$) initially softens with pressure. However, above 1.6 GPa, this mode discontinuously shifts to a higher value. This shift is about 10 cm$^{-1}$ from the value at ambient conditions. Beyond this pressure, the frequency of this mode remains nearly same up to 4.5 GPa which suggests that there are negligible changes in the O–H---O bonds in this pressure range. The softening of the O–H stretching mode up to 1.6 GPa indicates strengthening of the O–H---O hydrogen bond and stiffening above this pressure, in general, implies weakening of this hydrogen bond.

It is important to mention here that at ambient conditions this short O–H---O

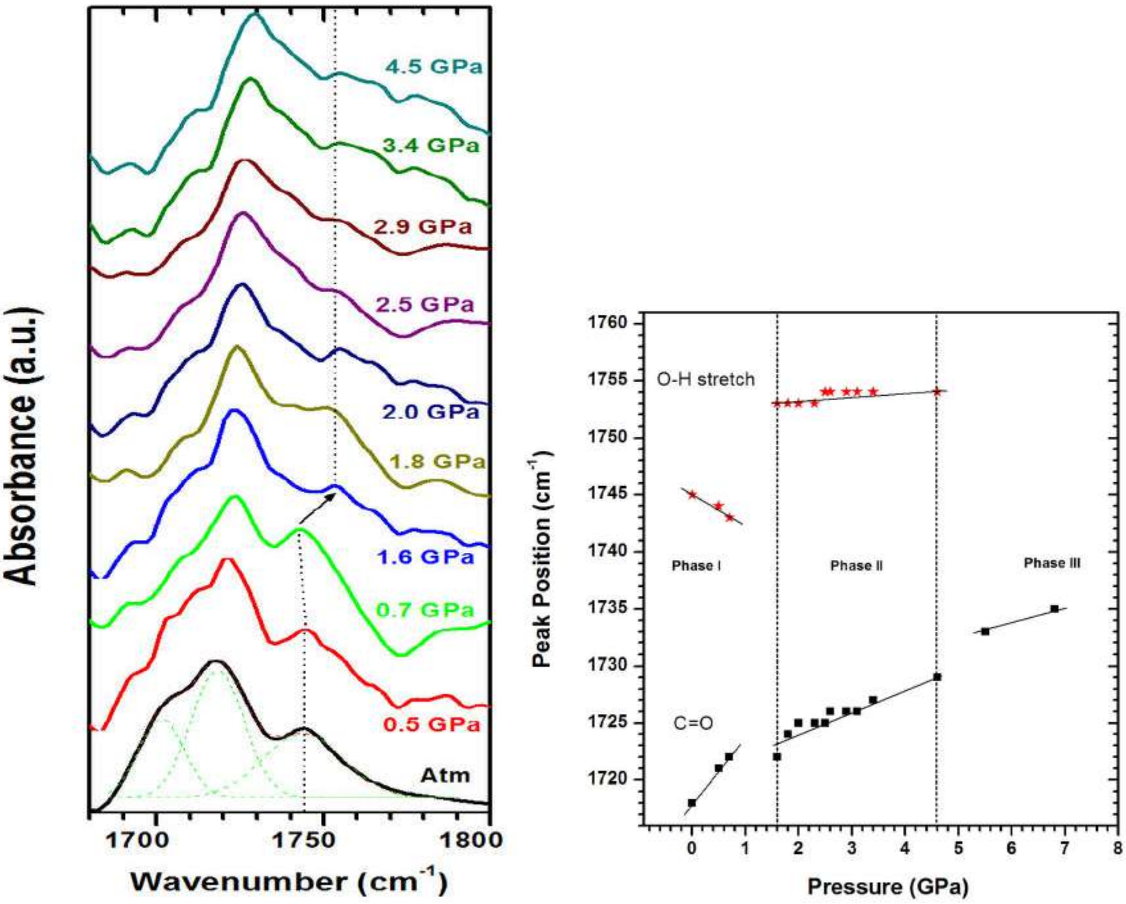

**Figure 5.10:** (left) High pressure infrared spectra of Bis(glycinium) oxalate in the 1700 $\mathrm{cm}^{-1}$ region and (right) Behaviour of carbonyl and OH stretching vibrational modes with pressure.

bond is very close to the symmetrization limit and hence under pressure one can expect possible symmetrization. However, for symmetrization to occur the slope of the variations in the OH frequency is expected to be rather steep and negative, for the soft mode. In our study, the reduction in the value up to 1.6 GPa is $\sim 5$ $\mathrm{cm}^{-1}$. As the correlation of OH frequency vs O-H---O bond distance for very strong hydrogen bonds [20] is found to have a large scatter, without the knowledge on the hydrogen bond parameters it is not possible to comment on this aspect. However, the discontinuous changes in the OH stretching mode at

$\sim$ 1.6 GPa suggests that O-H---O hydrogen bonds are re-formed across the transformation.

Therefore, it can be concluded that the reorientation of the glycine molecules under pressure results in breaking and re-formation of O-H---O as well as N-H---O hydrogen bonds in Bis(glycinium) oxalate. However, the increase in OH stretching mode (10 cm$^{-1}$) above the transition pressure means that the OH stretching frequency in the new phase is $\sim$1755 cm$^{-1}$ compared to the value at ambient condition 1745 cm$^{-1}$. This new value is still far too small compared to the free OH stretching frequency $\sim$3700 cm$^{-1}$, which indicates that O-H---O bond in the new phase, is still strong and closer to the symmetrization limit. Single crystal diffraction study would be required to determine the new phase with refined hydrogen atom positions and hence the hydrogen bond parameters.

## 5.5 High pressure dielectric properties of BGO

The spectroscopic studies have indicated a phase transition in BGO at 1.6 GPa and in the daughter phase, the principle of mutual exclusion of Raman and IR activity becomes inapplicable. In the high pressure phase, identified to be a non-centrosymmetric structure, the lattice parameters, in particular, the shorter axis and the $\beta$-angle change drastically [138]. With the motivation from these results, we have further carried out dielectric measurements on BGO at high pressures, as the low frequency dielectric constant may provide a direct correlation with the structural modifications.

The dielectric constant was determined by measuring capacitance at each pressure with the experimental arrangement as shown in Figure 5.11. The powdered sample was made into a pellet of 3 mm diameter with 230 $\mu$m thickness, using a specially designed stainless steel piston cylinder pelletizer. A parallel plate capacitor was formed using two fine polished copper foils of diameter 2.25 mm and thickness 20 $\mu$m. The sample disc was sandwiched between the two copper plates

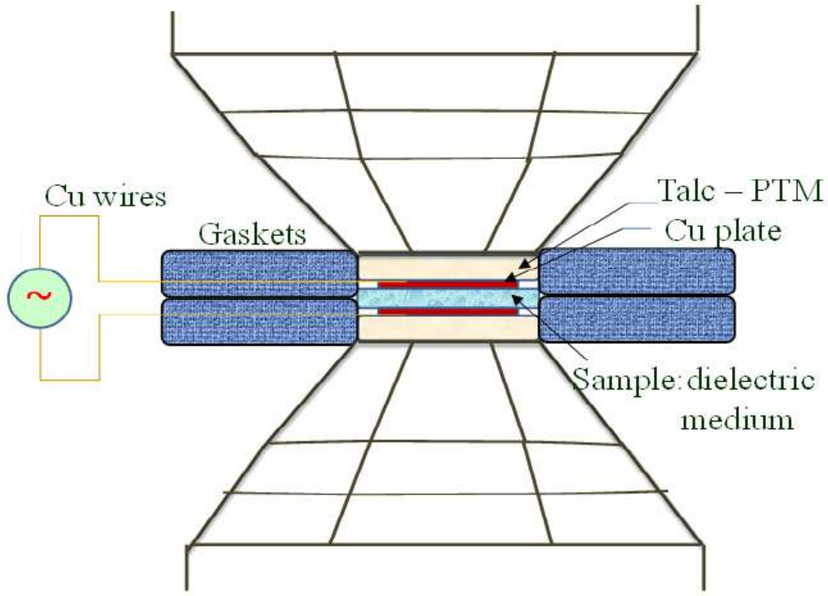

**Figure 5.11:** High pressure sample chamber for capacitance measurements used with a Bridgman Anvil apparatus.

and served as the dielectric medium in the parallel plate capacitor. The capacitor was placed in the sample chamber made using two pyrophyllite gaskets of 12.5 mm OD, 3 mm ID and 0.22 mm thickness. One talc-epoxy disc of 3 mm diameter was placed below the capacitor and the other on the top, which worked as the pressure transmitting medium. The two gaskets contained flattened copper leads, which extended to the inside of the sample chamber and inserted between the talc disc and copper plates. High pressure dielectric measurements were carried out using a Bridgman anvil (BA) apparatus of 12.7 mm face diameter. The capacitance and other bridge parameters were measured as a function of pressure using a Keysight E4980A Precision LCR Meter at different frequencies. The pressure was determined by calibration of the load applied to the anvils against fixed points of known compounds.

At any given pressure, the capacitance, $C$, is defined as,

$$C(P) \propto \epsilon(P)\frac{A(P)}{d(P)} \tag{5.1}$$

where, $\epsilon = \kappa\epsilon_0$, $\kappa$ is dielectric constant and $\epsilon_0$ = Permittivity of free space = 8.85 × $10^{-12}$ Farad/meter, $A$ = Area of the copper plate = $\pi r^2$, r = 1.125 mm, $d$ = Thickness of dielectric = 230 $\mu$m.

From equation 5.1, the dielectric constant can be calculated by measuring capacitance at any given pressure. The change in sample dimension induced by compression was accounted from the pressure dependent bulk modulus values obtained from an earlier high pressure X-ray diffraction measurement [138]. Figure 5.12(a) shows the changes observed in the dielectric constant of Bis(glycinium) oxalate with increasing pressure. A clear peak is noted in the dielectric behaviour of the sample under pressure across 1.6 GPa, with values remaining almost constant above 2 GPa. This peak seems to be somewhat broad and less sharp as compared to the conventionally observed sharp rise in temperature induced dielectric constant of many ferroelectric materials, which may be due to several factors including the complexity in the high pressure experiments, deviations from pure hydrostatic compression inducing non-homogeneous distribution of stresses, pressure intervals which depend upon the external applied load or the material properties itself etc. Nonetheless, this behaviour was perfectly repeatable in three independent measurements and gives a good qualitative trend of the high pressure dielectric behaviour of BGO showing the anomaly across 1.6 GPa which is attributed to the pressure induced phase transition in this compound (Figure 5.12b) [138]. These results are consistent with the structural as well as spectroscopic investigations on BGO and hence the combined IR, Raman, XRD and capacitance studies at high pressures in Bis(glycinium) oxalate are indicative of a pressure induced structural transformation to a ferroelectric phase above 1.6 GPa.

The high pressure phase transformation in BGO seems to be governed by breaking and re-formation of the strong as well as moderately strong hydrogen bonds which result in reorientation of the three dimensional framework of the crystal structure, rather than being a drastic transition in crystal structure. This is also evident

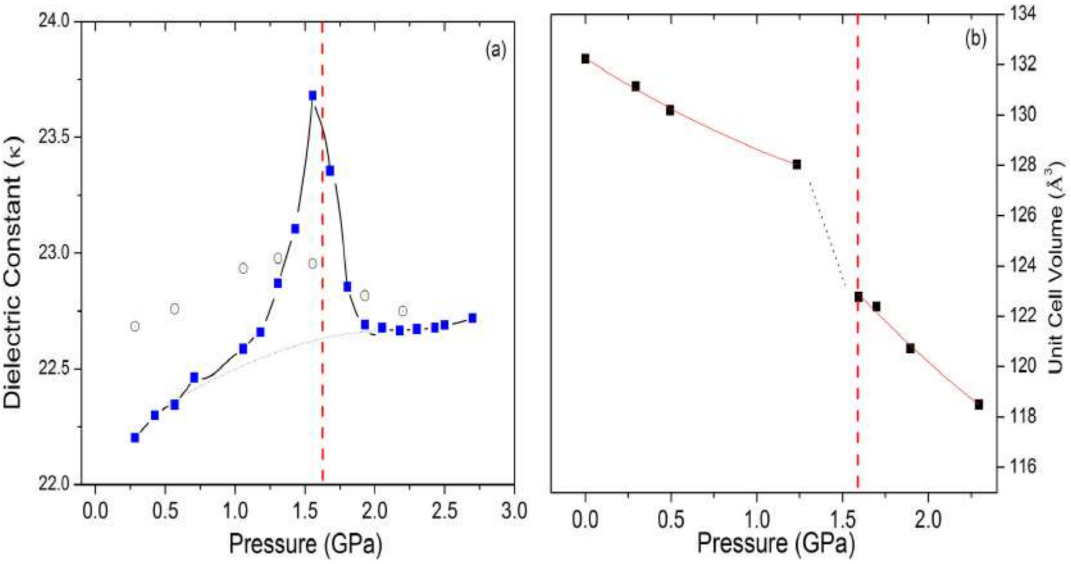

**Figure 5.12:** (a) Pressure dependent dielectric constant of BGO; filled and open symbols represent data recorded during compression and decompression respectively; (b) Change in unit cell volume with pressure showing phase transition across 1.6 GPa.

**Table 5.2:** Lattice parameters of BGO in parent and daughter phase; $a$, $b$, $c$ are in Å units [138].

| | ambient phase | 1.7 GPa |
|---|---|---|
| $a$ | 4.9 | 10.6 |
| $b$ | 9.9 | 9.6 |
| $c$ | 10.9 | 11.2 |
| $\beta$ | 97.4° | 154.7° |

from the fact that the crystal symmetry remains monoclinic across the transition and only the lattice parameters $a$ and $\beta$ show major distortion across 1.6 GPa (see Table 5.2) [138]. This reorientation induces a net dipole moment and hence a net polarization in the structure. The knowledge of atomic coordinates, in particular hydrogen bond parameters at higher pressures would be very useful in probing this effect in further detail.

## 5.6 Variable temperature studies of BGO

Pressure and temperature generally follow an inverse rule, i.e. increase in pressure has similar effects as lowering the temperature, though temperature lowering is not as effective as increasing pressure (in gigapascals range) towards the tuning of interatomic separations. Moreover, in many ferroelectric materials, it has been observed that pressurizing the system lowers the transition temperature. Further, the independent high pressure and low temperature studies on a room temperature ferroelectric material Tri glycine sulphate revealed that although both pressure and temperature bring about the ferro-paraelectric transition, the mechanism is completely different, latter being an order-disorder type and the former a displacive type transition [55]. However, both, temperature and pressure studies confirmed reorientation of a glycine molecule to a planar configuration resulting in the transformation.

Thus, we have carried out a temperature dependent study of Bis(glycinium) oxalate to shed light on the phase transitions observed. Noticeably, variable temperature experiments can be much more controlled and simpler than high pressure experiments in terms of homogenously imparting the change in thermodynamic condition, large sample concentration and adequately large spot size of the probing beam etc. Thus, in addition to the spectroscopic experiments, single crystal X-ray diffraction experiments are also easier to perform at low temperatures which can provide valuable details about the atomic and hydrogen bond coordinates.

### 5.6.1 Experimental details

In-situ infrared absorption studies on BGO (polycrystalline sample dispersed in CsI matrix) were carried out in the temperature range 350 - 77 K. Note that the compound showed melting at temperatures slightly above 400 K in differential scanning calorimetry experiments [64]. The measurements were carried out in the newly developed IR beamline facility at Indus-1, RRCAT, Indore using a

LHe Oxford Optisat CF cryostat mounted in the sample compartment of Bruker Vertex 80V FTIR, employing the thermal IR source. Entire mid infrared spectral range 400 - 6000 cm$^{-1}$ was measured at each temperature using a liquid nitrogen cooled MCT detector and KBr beamsplitter. The temperature variation was carefully controlled using a PID controller. Flow of the cryogen was controlled using a well calibrated gas flow controller and exhaust gas valve in the transfer line. Liquid nitrogen was used as the cryogen in the present case. The vacuum near the cold finger and in the spectrometer was controlled independently. All the data were collected in the transmission mode. A total of 100 scans at a resolution of 4 cm$^{-1}$ were coadded in each case. To support the spectroscopic observations on hydrogen bonding interactions in BGO, low temperature single crystal X-ray diffraction experiments were performed using a Bruker Smart CCD area detector diffractometer using Mo K$_\alpha$ radiation. The details of data collection and methodology for refinement can be found in reference [189].

### 5.6.2 Infrared spectra in the fingerprint region

Figure 5.13 shows the infrared absorption spectra of BGO in the spectral region 400 - 1600 cm$^{-1}$ at various temperatures. The characteristic skeletal stretching modes and internal bending vibrations of alkyl, carboxylic acid and amino groups are observed in this region. It can be seen that the peaks are relatively sharper at low temperatures in comparison to the ambient, following the general trend of temperature lowering. However, the decrease in line widths becomes more pronounced only below 250 K, due to which the peaks are well resolved at lower temperatures. The skeletal modes, $\nu$C-C ($\sim$ 912 cm$^{-1}$) and $\nu$C-N ($\sim$ 1025 cm$^{-1}$) of oxalate and glycine respectively, show stiffening up to the lowest temperature. The $\nu$C-C glycine mode ($\sim$ 860 cm$^{-1}$) depicts an increase in relative intensity at low temperatures. However, the appearance of any new mode is not distinctively revealed in the complete temperature range. Moreover, the frequency versus temperature variation of almost all the modes are monotonous except for some small fluctuations near 250 K. Similarly, the peak widths and shape does not show significant changes on increasing the temperature from room temperature up to 350 K.

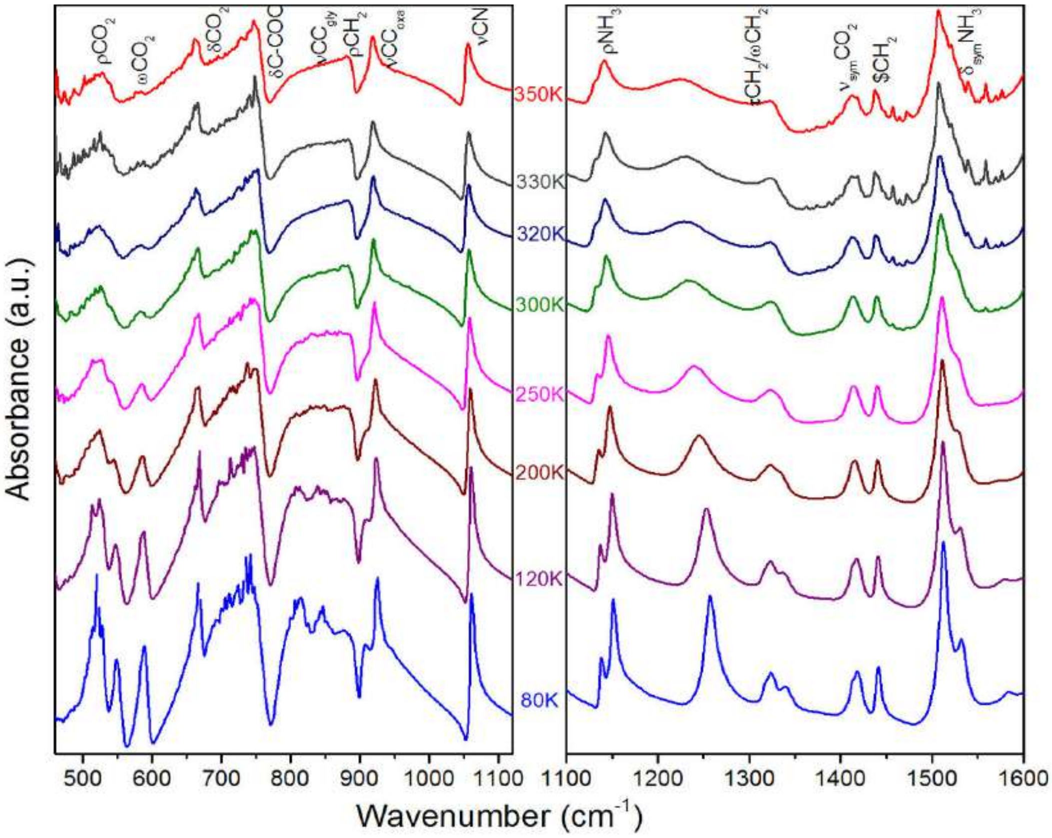

**Figure 5.13:** IR spectra of BGO in the spectral range 400 - 1600 cm$^{-1}$ at various temperatures in the range 350 - 80 K.

Therefore, in the measured temperature range (350 - 77 K), the spectroscopic observations indicate that the local molecular structure remains almost fully invariant. This is in striking dissimilarity to the high pressure behavior of BGO, where the vibrational structure showed drastic changes.

**Table 5.3:** Hydrogen bond parameters in Bis(glycinium) oxalate at 100 K.

| X-H---Y | X-H (Å) | H---Y (Å) | X---Y (Å) | ∠XHY (°) |
|---|---|---|---|---|
| N2-H1---O1 | 0.92 (2) | 2.01 (2) | 2.883 (2) | 159 (2) |
| N1-H2---O1 | 0.93 (2) | 1.90 (2) | 2.830 (2) | 175 (1) |
| N1-H3---O4 | 0.92 (2) | 1.95 (2) | 2.857 (2) | 166 (2) |
| O3-H6---O2 | 1.09 (3) | 1.37 (3) | 2.451 (2) | 174 (2) |
| C3-H4---O2 | 0.94 (2) | 2.65 (2) | 3.415 (2) | 139 (1) |
| C3-H5---O2 | 0.96 (2) | 2.45 (2) | 3.100 (2) | 126 (1) |

### 5.6.3 Hydrogen bonds at low temperature

A first hand information on the hydrogen bonding interactions can be determined by following the trend of O−H and N−H stretching vibrational modes. Figures 5.14 (a) and (b) shows the high pressure infrared spectra in the 1700 cm$^{-1}$ and 3200 cm$^{-1}$ region respectively. The spectrum in the O−H stretching region depicts a complex profile due to the superposition of carbonyl mode with the OH stretching vibrations. In the measured temperature range, the spectra do not show any unexpected changes in profiles and large discontinuous shifts in the band positions.

### 5.6.4 Single crystal X-ray diffraction studies

From the single crystal X-ray diffraction studies also, a comparison of the cell parameter of BGO at room temperature and at 100 K shows that the shrinkage in the unit cell parameters and unit cell volume is up to the extent of 1-2%. The overlap of crystal structure at room temperature (RT) and at 100 K (LT) has been shown in Figure 5.15. The variation in the bond parameters including the hydrogen bond parameters between the structures at RT and LT are also within the standard deviation. For comparison with those at room temperature, the hydrogen bonding parameters for the structure at low temperature are given in Table 5.3.

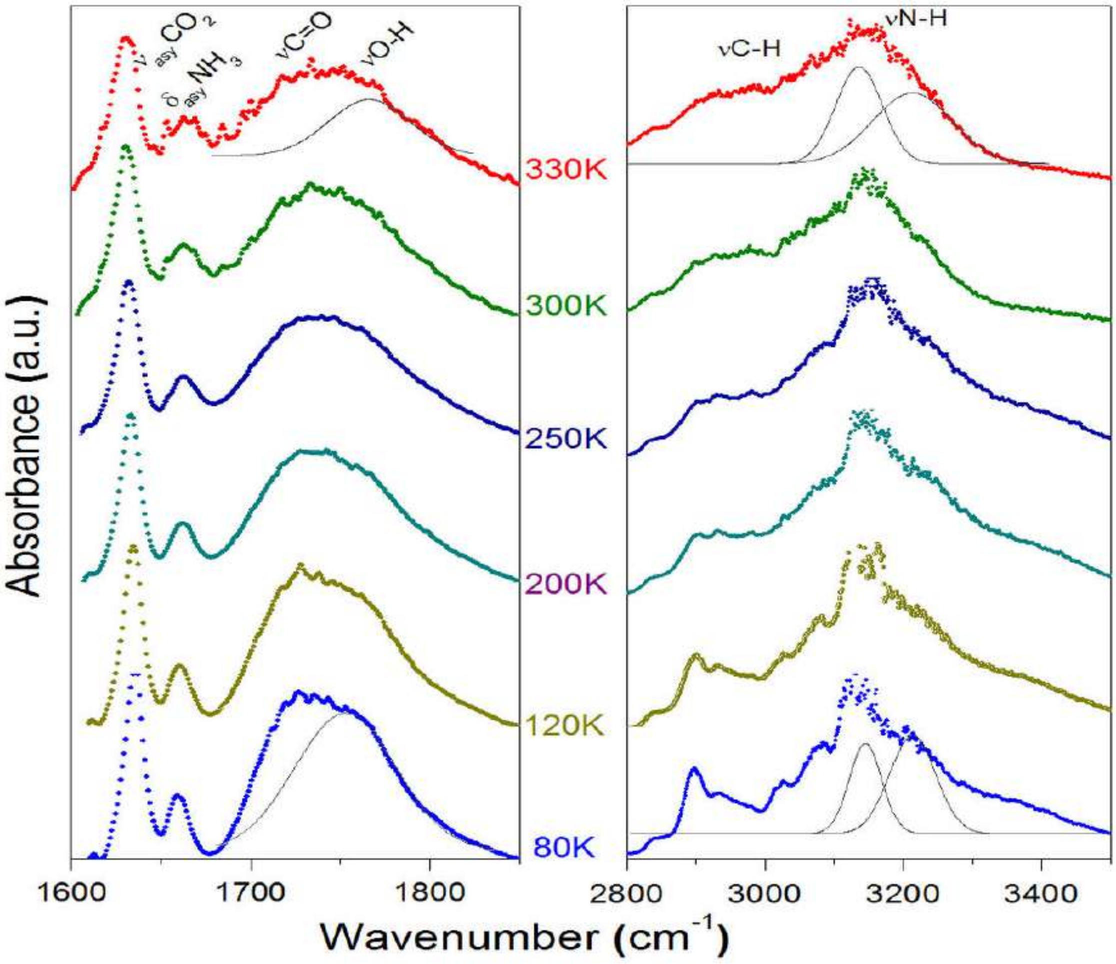

**Figure 5.14:** IR spectra of BGO in the (a) OH and (b) NH stretching regions at some representative temperatures in the range 350 - 80 K.

### 5.6.5 Comparison of low temperature and high pressure behaviour

For closer inspection of the low temperature behaviour, the position of the IR stretching bands of O−H and N−H vibrational modes were estimated using Gaussian fits. Figure 5.16 shows the variation of $\nu$O−H band position with decreasing temperature. The band centre initially showed signatures of softening up to 250 K. Across this temperature, the slope of the frequency versus temperature plot changes and it starts stiffening thereafter up to 100 K. This observation was re-

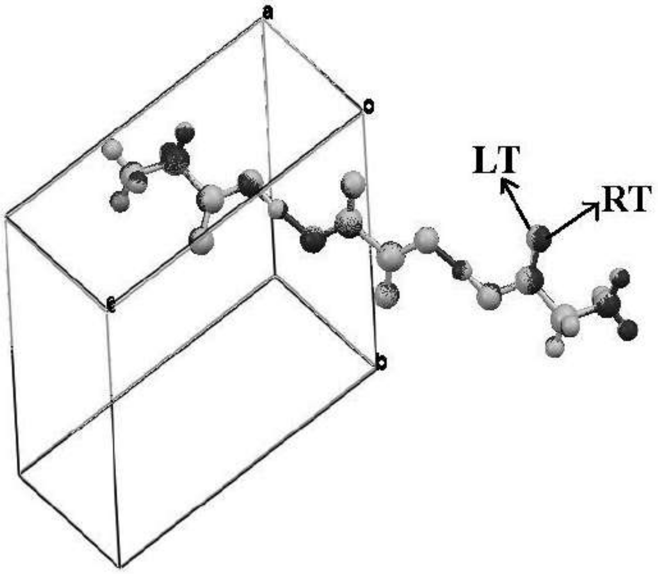

**Figure 5.15:** An overlap of structures of BGO at room temperature (RT - black circles) and at 100 K (LT - grey circles).

producible in the increasing as well as decreasing temperature cycle. However, the frequency variation is not more than 8 $cm^{-1}$ in the entire temperature range. Thus, apart from the above subtle changes around 250 K, the strong hydrogen bonding network remains nearly unperturbed due to temperature induced contraction. Similar behavior, as indicated by the $\nu$N–H mode variations with temperature, has been observed for the moderately strong N–H---O hydrogen bonds. For comparison, the corresponding high pressure behavior of these modes has also been plotted alongside in Figure 5.16.

All these observations indicate that the local and overall structure of BGO remains stable in the entire temperature range of 77 K to 350 K and there is no phase transition occurring at low temperature unlike that observed in the high-pressure studies of the same complex. Note that the pressure induced phase transition in BGO seems to have direct correlation with initial hydrogen bond strengthening between glycine and oxalate molecules. This implies that the steric limits are reached much faster due to pressure tuning compared to temperature,

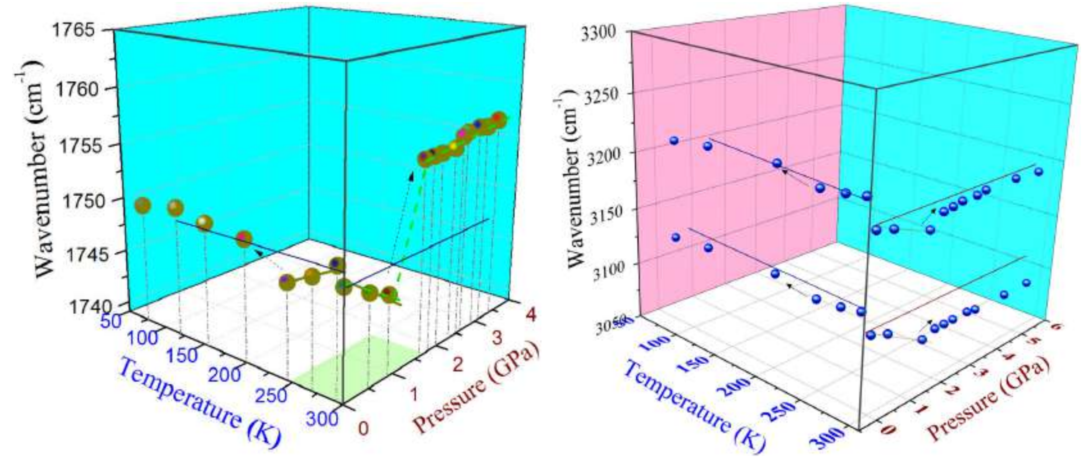

**Figure 5.16:** Variation of (left) $\nu$O–H and (right) $\nu$N–H mode positions under low temperture and high pressure conditions in BGO.

thus inducing reorientations in the N-H---O and O-H---O hydrogen bonds resulting in a completely new structure at high pressures. Interestingly, the low temperature studies also, though relatively marginal, indicate an incipient softening of the O–H stretching mode up to 250 K. These observations can be used to study the thermodynamics and phase diagram of this compound in the vicinity of ambient conditions. It is possible that in-situ cooling of BGO at slightly elevated pressures can trigger the phase transition at temperature-pressure parameters much more close to the ambient conditions. Note that the detailed studies of glycine complexes in environments slightly deviating from ambient pressure and temperature are of importance in life sciences, astrobiology, infrared detectors, ferroelectric properties and geophysical research and thus these results may direct more such studies under varying thermodynamic parameters in glycine and other amino acid complexes.

## 5.7 Conclusions

Our high pressure infrared absorption studies of Bis(glycinium) oxalate carried out up to 7 GPa, indicate structural transformations across 1.6 and 4.5 GPa.

The appearance of Raman active modes in the infrared spectra above 1.6 GPa confirms that glycine molecules have become non equivalent leading to loss of centre of symmetry and hence a non centrosymmetric high pressure phase. The sudden shifts in N–H stretching mode variations with pressure suggest reorientation of N–H---O hydrogen bonds across the phase transition. The softening of the O–H stretching mode up to 1.6 GPa suggests strengthening of the short O–H---O hydrogen bond in this pressure range. The discontinuous jump of OH stretching mode to a slightly higher value across the phase transition indicates that in the high pressure phase above 1.6 GPa, though relatively weaker compared to that in the parent phase, yet strong O–H---O bonds exist. These observations suggest that the reorientation of the glycine molecules during the transition influences the O–H---O hydrogen bonds also. The phase transition to a non-centrosymmetric structure was further investigation by studying the high pressure behaviour of dielectric constant which showed a peak at pressure value corresponding to the structural phase transition. The combined low temperature infrared and X-ray diffraction studies confirmed that the compound remains stable and depicts similar molecular structure at room temperature and low temperatures. Low temperature induces closer packing of the molecules and general shrinkage of the unit cell, sharp and well resolved spectral features and shortening of the hydrogen bonds by about 2%. There is no phase transition occurring at low temperatures.

# 6

# Capability demonstration and first results from the IRBL facility developed

As described in chapter 2, total three experimental facilities have been developed during the course of this thesis, viz. a condensed matter infrared spectroscopy lab at Indus-1 synchrotron source at RRCAT, India, a high resolution fourier transform spectroscopy lab and a FT-Raman facility at BARC, India. The present thesis is aimed at solid state infrared spectroscopy of materials and development of a synchrotron IR beamline and hence the focus of this chapter is to present the first results obtained at various stages of the development of the IR beamline facility at Indus-1.

## 6.1 Commissioning of the experimental station

The heart of the experimental station at IR beamline is the fourier transform spectrometer which has been coupled to an IR microscope. In addition, there are various accessories to carry out investigations like ATR, DRIFT, specular reflection, polarization dependent studies, micro-ATR, variable temperature studies in a continuous flow liquid helium cryostat, near IR studies of overtones and combinations etc. using various detectors like $LN_2$ cooled MCT and InSb, room temperature DTGS and Si-diode, LHe cooled bolometer; sources like Hg lamp, globar, tungstem lamp and synchrotron radiation; beamsplitters such as Mylar, KBr and $CaF_2$ etc. The experiments can be done in absorption and reflection modes, both providing some specific information of the specimen. For first absorption studies after the commissioning of the spectrometer, we chose an inorganic sample having simple, clear and well established spectral features. These features were also helpful, later, for comparison of sources subsequent to the coupling of the synchrotron beamline with the spectrometer. The first high pressure absorption studies were carried out on various molecular solids, sesquioxides and other organic systems (some of which have been presented in previous chapters), whereas the high pressure reflection studies for optical properties determination were carried out on a cuprate material Ru1212 which shows superconducting as well as magnetic transitions at low temperatures. In the following two subsections, we present the first studies carried out in absorption and reflection modes.

### 6.1.1 Microscopic structure determination from absorption studies - Effects of calcination on SOFC interconnect: doped nano-crystalline $LaCrO_3$

In recent past, a lot of studies [190–194] have been devoted to Solid Oxide Fuel Cells (SOFC), a potential candidate for distributed generation, due to its capability of power production at high efficiencies, fuel flexibility and long term stability. But, still there are concerns over the issues related to the physico-chemical properties of its components at high temperatures, as SOFC is generally operated at temperatures ranging around 850°C to 1000°C. The three basic components of a SOFC are the ionic electrolyte, two porous electrodes and interconnect that sits between each individual cells to provide an electrical pathway from anode of one cell to cathode of the adjacent cell. There are various requirements for making the interconnects viz. the material should have good chemical stability in oxidizing as well as in reducing atmospheres, high electrical conductivity, compatibility of thermal expansion behaviour with other components of the cell, high density to avoid material deposition at high temperatures and good mechanical strength at high temperatures. Stoichiometric lanthanum chromite perovskites, $LaCrO_3$, are known to show excellent chemical stability under oxidizing or reducing atmospheres at high temperature, but exhibit poor sintering in air and low electrical conductivity at SOFC operating temperatures [194–197]. This is due to the fact that chromium vapor component starts evaporating at temperatures beyond 1000°C [198, 199], thus disturbing the densification of lanthanum chromite particles by vaporization-condensation transport mechanism. Doping of alkaline earth metals like Sr and Ca in $LaCrO_3$ has shown to improve the sintering properties, apart from retaining all the stringent requirements of a SOFC interconnect [194, 200]. Nearly 20 mol % of Sr doping and 30 mol % of Ca doping have been explored extensively as they provide reasonably optimum properties considering all the rigorous requirements of the interconnect [192, 197, 200–207]. Further, better sintering properties can be obtained by using nano-phase material [208, 209] and also calcination of the ceramics at higher temperatures is an effective method to achieve sintered material. However, during calcination of doped lanthanum chromites, the microscopic as well as mesoscopic structure and dynamics get modified with temperatures. In a recent study on underdoped and overdoped $La_{0.7}Ca_xCrO_3$, it was noticed that a transient liquid phase formed between 850°C and 1000°C causing a partial densification [200]. Similar studies on $(La_{0.7}Sr_{0.3})_xCrO_3$ have also been carried out [210]. However, the issues related to achievement of highly sintered material at lower temperatures, which fulfills the requirements, still require attention and fundamental knowledge of the microscopic details of the mechanism of sintering at elevated temperatures. Consequently, the mesoscopic structure, governing the sintering and microscopic structure, governing the physical and chemical properties of the system must be investigated.

We have carried out detailed microstructural investigations and showed the evolution of transient phases upon calcination of gel-combustion synthesized nanocrystalline $La_{0.7}Ca_{0.3}CrO_3$ (LCC) and $La_{0.8}Sr_{0.2}CrO_3$ (LSC) using infrared (IR) spectroscopy and the results have been well supported by X-ray diffraction (XRD). The remarkable influence of these modifications on the evolution of the mesoscopic structure governed by liquid state assisted sintering, have been observed using small angle neutron scattering (SANS) as well as scanning electron microscopy (SEM) studies.

#### 6.1.1.1 Experimental methods

The details of sample preparation and IR instrumentation have been discussed in chapter 2. The far-IR spectra have been measured in the range 150 - 700 $cm^{-1}$ using, 3$\mu$m Mylar beamsplitter, Hg lamp source and DTGS detector. XRD patterns of the powders were recorded using a rotating anode X-ray generator equipped with Mo source. Data were collected using a Mar345 imaging plate and the images were converted into 1D diffraction patterns using FIT2D software. GSAS software was used for structural refinement.

SANS experiments have been performed using a double crystal based medium resolution small angle neutron scattering instrument (MSANS) at Guide Tube Laboratory of the Dhruva reactor at Trombay, India [211]. The instrument consists of a non-dispersive (1, -1) setting of (111) reflections from silicon single crystals with specimen between two crystals. Scattered intensities have been recorded as a function of modulus of wave vector transfer $|q|[= 4\pi\sin(\theta)/\lambda$, where $2\theta$ is the scattering angle and the incident neutron wavelength was set at $\lambda = 0.312$ nm]. SANS profiles of specimens, recorded by the instrument, were corrected for smearing effect after transmission and background corrections, using the methods given in literatures [212,213]. Scanning Electron Microscopy (SEM) experiments have been performed to support the mesostructural observations.

#### 6.1.1.2 Microscopic structure of Ca- and Sr- doped $LaCrO_3$

The structure of the $ABO_3$ perovskite is such that they form two polyhedra $AO_{12}$ and $BO_6$, i.e. $LaO_{12}$ and $CrO_6$ in $LaCrO_3$ as shown in Figure 6.1. Vibrational spectroscopy is highly sensitive to any kind of volumetric changes in $ABO_3$ perovskite due to the deformation of these polyhedral via variation of their bond lengths ($d_{\text{La-O}}$ and $d_{\text{Cr-O}}$) and bond angles ($\theta_{\text{O-Cr-O}}$) [207]. Usually there are three kinds of vibrational modes in $LaCrO_3$ perovskites. La site external modes and internal $CrO_6$ octahedral distortions consisting of Cr−O−Cr bending modes and Cr−O stretching modes. Group theoretical calculations on perovskites with *Pnma* phase and the IR/ Raman active vibrational modes for $LaCrO_3$ have been extensively studied and available in literature [207,210,214,215]. Substitution of divalent cations $Sr^{2+}$ and $Ca^{2+}$ in place of trivalent $La^{3+}$ in the perovskite may be accompanied by a variation in the internal as well as external modes.

The IR spectra of LCC and LSC nano-crystalline samples, shown in Figure 6.2, depict three broad absorption bands in the frequency range: 670-570 $cm^{-1}$ (High frequency), 480-350 $cm^{-1}$ (mid frequency) and at 190 $cm^{-1}$ (low frequency). These IR modes have been found similar to those of the orthorhombic perovskite $LaCrO_3(D_{2h}^{16})$ with *Pnma* symmetry [214–216]. The irreducible representation of the optical modes [216], for $ABO_3$ structured compounds (A = rare earth element and B= Transition metal) with orthorhombic phase predicts 25 $(7B_{1u} + 9B_{2u} + 9B_{3u})$ IR active modes. The observed modes have been shown by dotted lines in the data. The lack of multiplicity, i.e. the observation of less number of modes compared to the predicted number of 25, can be due to the superposition of many modes very close to each other or small oscillator strengths of some of the modes. As discussed earlier, the dominant character of these IR modes is grouped into three types of vibrations, i.e. stretching, bending and external vibrations respectively, which is more like the higher symmetry Pm3m

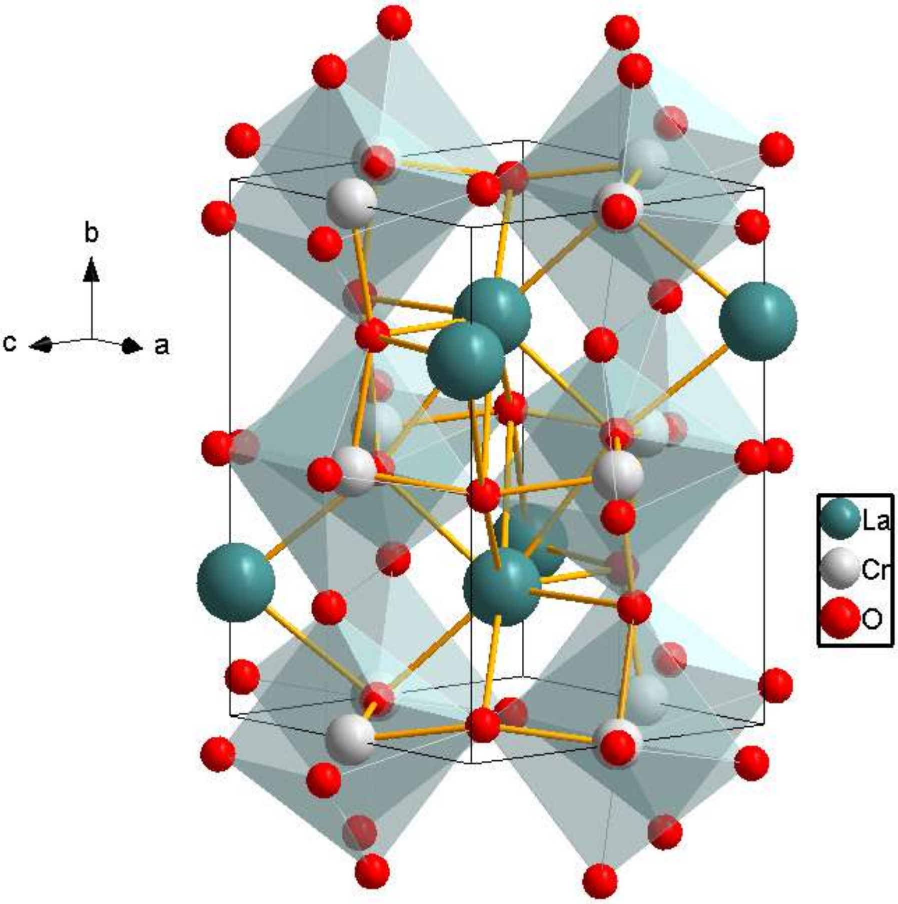

**Figure 6.1:** Crystal structure of the as prepared $LaCrO_3$ perovskite with 30% calcium doping, showing $CrO_6$ octahedra. $LaO_{12}$ polyhedra are not shown here.

cubic vibrations that have only three IR active phonon bands [217].

**A. High frequency band -the stretching vibrations**

This band (570 to 670 $cm^{-1}$) arises mainly due to Cr−O−Cr asymmetric stretching of $CrO_6$ octahedron [214]. It has been well established that the frequency of this mode is inversely proportional to bond length $d_{Cr-O}$ [207]. The unit cell volume is proportional to the third power of $d_{\text{Cr-O}}$ and cosine of the tilt angle [218]. Doping induced disorder due to the changed mass, charge and lattice parameters broadens the bands. A detailed study on variation of this high frequency band with change of B site dopant has shown that large octahedral field stabilization energies could lead to higher stretching frequencies [219]. The Cr−O stretching band appears

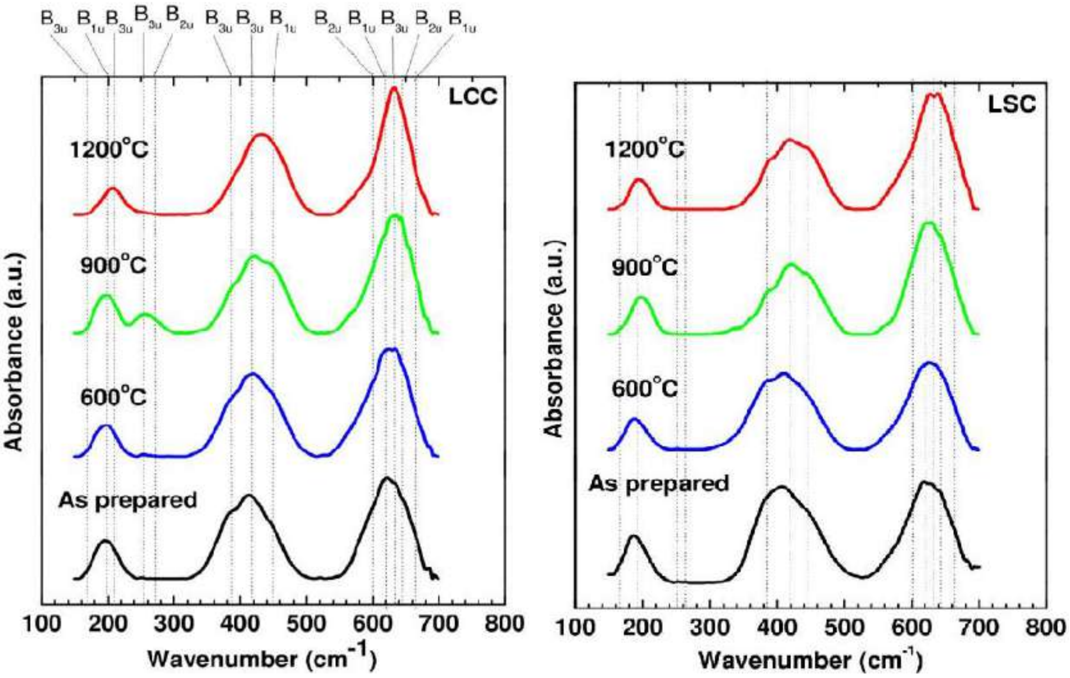

**Figure 6.2:** FTIR spectra of (left) LCC and (right) LSC specimens in the spectral range 150 - 700 cm$^{-1}$. Spectra have been offset along $y$-axis to avoid overlap and make the visualization clear.

at 630 cm$^{-1}$ for LaCrO$_3$ [214]. It has been observed from Figure 6.2 that the stretching vibrations shift towards lower frequencies upon Sr- or Ca- substitution. Shoulders in the spectra may imply the existence of several modes merged in the band. Apart from strong B$_{3u}$ (in-plane oxygen vibration; 630 cm$^{-1}$) and B$_{2u}$ (apical oxygen vibration; 640 cm$^{-1}$), shoulders at 602 cm$^{-1}$ (B$_{2u}$) and 621 cm$^{-1}$ (B$_{1u}$) have been observed. The shoulder in the spectra at nearly 665 cm$^{-1}$ can be assigned to a combination band (B$_{1u}$) of O–Cr–O bending vibrations which appears at 675 cm$^{-1}$ for LaCrO$_3$ [214]. For LSC specimens, the Cr–O stretching band shifts towards higher frequency with increasing calcination temperature, as shown in Figure 6.3, which implies a reduction in Cr–O bond length. B$_{3u}$ (630 cm$^{-1}$) is prominent in all the samples, but B$_{2u}$ (640 cm$^{-1}$) is split in high temperature calcined samples. For LCC specimens, the stretching band, although shows a similar blue shift as the calcination temperature is increased, the rate of increase is considerably higher from 600°C to 900°C. This indicates that there is a difference in the behaviour of microscopic structure at different temperatures for Sr- and Ca- doped samples, and that the temperature range across 900°C is crucial for comparison of these two doped nanoceramics. At 600°C, the band position of LCC ($\sim$ 623.5 cm$^{-1}$) is slightly lower than LSC ($\sim$ 625 cm$^{-1}$), but as the temperature is increased to 900°C, the position of LCC reaches nearly 631.5 cm$^{-1}$, whereas for LSC it is nearly 627.5 cm$^{-1}$, thus a larger reduction of Cr−O bond for LCC than LSC at the same higher temperatures of calcination. Though the reduction in Cr−O bond length may suggest a decrease in the unit cell volume, but the XRD data show that the unit cell volume increases with increasing calcination temperature (Table 6.1). This may be due to the reduction in the tilt angle with temperature and would thus compensate for the reduction in the bond length. Implications of Table 6.1 will be discussed in a later section.

**B. Mid frequency band - the bending vibrations**

The moderately strong mid frequency band is again a superposition of many modes and is spread from 350 to 480 cm$^{-1}$. These modes arise due to the deformations of $CrO_6$ octahedron. For $LaCrO_3$, various O-Cr-O bending modes which are responsible for this broad band have been reported [215]. Apart from weak shoulders, three strong features are visible in the spectra shown in Figure 6.2, which have been identified as $B_{1u}$ (apical oxygen vibration; at 445 cm$^{-1}$), $B_{3u}$ (in plane oxygen vibration; at 410 cm$^{-1}$) and $B_{3u}$ (at 380 cm$^{-1}$) by comparison with the previously reported band positions for $LaCrO_3$ [207, 215]. It is interesting to mention that for the doped perovskite compounds, the bending vibrations are proportional to and are predominantly governed by the bond length $d_{\mathrm{La-O}}$ [220]. Moreover, the position of this mode is also inversely proportional to the La(Sr/Ca) site cation radius. The two $B_{3u}$ modes correspond to bands at 425 cm$^{-1}$ and 380 cm$^{-1}$ for $LaCrO_3$ [215]. The LSC frequencies for these internal bending vibrations are at lower values compared to LCC, as depicted in Figure 6.3, which confirms the dependence of the bending mode on the dopant ionic

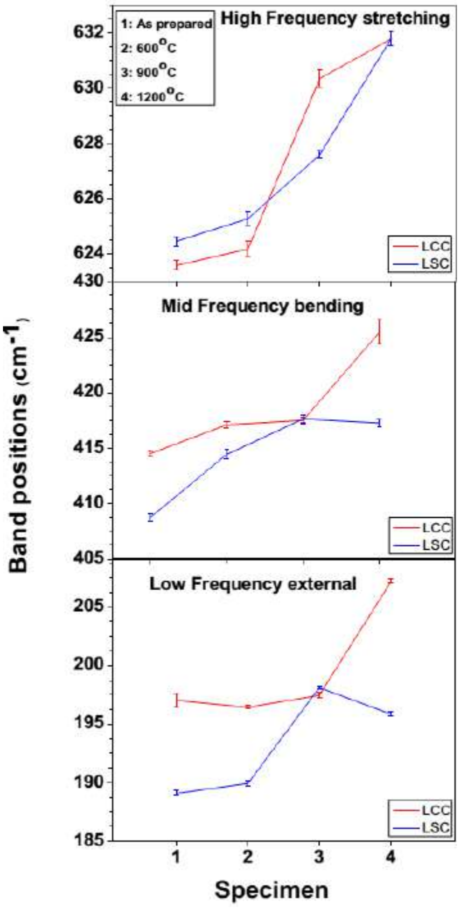

**Figure 6.3:** Evolution of vibrational bands of LCC and LSC with calcination temperature.

radius (larger for Sr than Ca). For LSC specimens, frequencies gradually increase from as prepared sample to 900°C calcined sample and show a small decrease at 1200°C. These observed trends imply that the La-O bond length increases as the calcination temperature increases up to 900°C. For LCC samples, the band positions and hence La-O bond length increases from as prepared to 600°C calcined sample. The frequency remains nearly constant up to 900°C and increases further from 900°C to 1200°C calcined sample. Interestingly, the frequencies for the two doped systems are very close at 900°C, where the intermediate phases show prominent presence, discussed in the next section. Noticeably, the low frequency bending modes $B_{2u}$ (265 $cm^{-1}$) and $B_{3u}$ (240 $cm^{-1}$) are either very weak or not at all present in most of the samples except for the 900°C calcined LCC sample, where $B_{3u}$ (257 $cm^{-1}$) has emerged very strongly. There exists a weak shoulder at around 517 $cm^{-1}$ for as prepared and 600°C calcined samples only of LCC, which can be explained as a defect band due to distortions of $CrO_6$ octahedron by the high valence cations. This weak band completely vanishes at higher calcination temperatures, implying a decrease in the structural disorder at higher calcination temperatures.

**C. Low frequency band - the external vibrations** External modes arising from the La vibrations are expected to be present in the low frequency regions of IR spectra, owing to higher mass of lanthanum. These modes occur due to a relative motion of the $CrO_6$ octahedra against the surrounding La(Sr/Ca) atoms. Five IR-active modes are expected to be present in the far infrared region from 100 to 200 $cm^{-1}$ [216]. In the present infrared spectra, Figure 6.2, from 150 $cm^{-1}$ to 200 $cm^{-1}$, a sharp band is observed peaked at around 200 $cm^{-1}$ ($B_{1u}$) with a weak shoulder at nearly 165 $cm^{-1}$ ($B_{3u}$) at ambient conditions. At higher temperatures, the frequency of the external mode is blue shifted, as shown in Figure 6.3, which can be attributed to the increased force constants and higher bond strengths for higher calcination temperatures. As for the bending modes, the frequencies are again closer at 900°C for the two systems.

#### 6.1.1.3 Evolution of transient phases with temperature

The ambient spectra of the as prepared samples of both Ca- and Sr- doped samples resemble that of pure $LaCrO_3$. But as the calcination temperature is increased, intermediate phases start appearing as shown in Figure 6.4. The signatures of intermediate phases in the IR spectra have been identified by the stretching modes of $CaCrO_4$ in LCC and $SrCrO_4$ in LSC. Alhough the bending vibrations of these compounds, near 350 to 400 $cm^{-1}$, are overlapped by the La(Sr/Ca)$CrO_3$ internal bending modes, the stretching vibrations (850 to 950 $cm^{-1}$) are well away from the overlap and clearly visible for the samples for which the respective phase has appeared. The interesting observation from the present IR study is not only the evolution and disappearance of transient phases but also the absorption intensity of these phases, especially for LCC, becomes comparable to the native perovskite intensities. For LCC specimens, calcined at intermediate temperatures, the stretching modes of $CaCrO_4$ have been observed near 840 $cm^{-1}$, 880 $cm^{-1}$, 903 $cm^{-1}$, 920 $cm^{-1}$ and 938 $cm^{-1}$ (Figure 6.4), which are in reasonable agreement with the reported values of pure compound (at 924 $cm^{-1}$, 912 $cm^{-1}$, 902 $cm^{-1}$, 870 $cm^{-1}$ and 850 $cm^{-1}$ [221]). Their emergence can be seen as a broad band for 600°C calcined sample and at 900°C it develops into a very strong and sharp band, peaked at 903 $cm^{-1}$ with shoulders on either side, whereas no such signature has been observed for the 1200°C calcined sample. $SrCrO_4$ also has its stretching and bending vibrational modes present at similar frequencies. The stretching IR modes have been reported at 925 $cm^{-1}$, 912 $cm^{-1}$, 890 $cm^{-1}$, 875 $cm^{-1}$ and 843 $cm^{-1}$ [221]. It is interesting to note that the IR spectrum of LSC specimen, Figure 6.4, calcined at 900°C shows nearly all of these frequencies with clear and distinct peaks at 850 $cm^{-1}$, 880 $cm^{-1}$, 912 $cm^{-1}$ and 950 $cm^{-1}$ and others as shoulders. In LSC also, there were no impurity phase features present in the as prepared sample.

#### 6.1.1.4 X-ray diffraction studies

The XRD patterns of LCC and LSC nanoparticles have been shown in Figure 6.5. It can be seen that the patterns for both the as prepared powders are almost identical. This leads to iso-structural crystalline phase of both LCC and LSC. The evolution of diffraction patterns with calcinations temperature confirms the formation of transient species. Structural refinement, carried out using the XRD data, also gives the weight percentage of the intermediate phases and volume of the unit cell which are reported in Table 6.1. The weight percent of the dopant chromate phases have been fitted using a quadratic function as shown in Figure 6.5.

$CaCrO_4(D_{2h}^{11})$ crystallizes in the *Pbcm* Space group and the analysis of the XRD

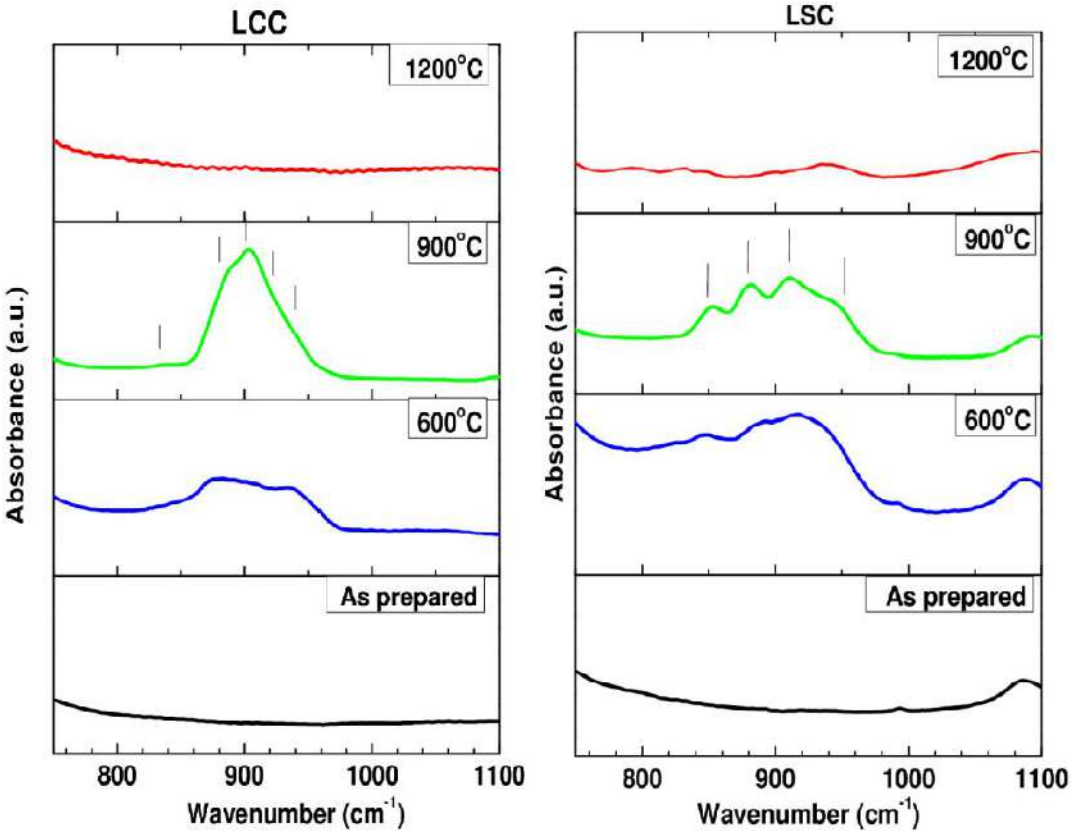

**Figure 6.4:** IR spectra of (a) LCC and (b) LSC specimens in 700 - 1100 cm$^{-1}$ spectral range showing $CaCrO_4$ modes appearing after the high frequency stretching modes.

data showed maximum $CaCrO_4$ phase formation at around 864°C (Figure 6.6), whereas 1200°C calcined sample contains very small amount of $CaCrO_4$. On the other hand, the maximum phase formation of $SrCrO_4$ ($C^5_{2h}$) with $P2_1/n$ space group, as obtained from the fitted XRD data of LSC, takes place at around 644°C (Figure 6.6). These observations provide insight into the sintering mechanisms in LCC and LSC. From the combined IR and XRD data, it can be concluded that the intermediate phase formation starts at relatively lower temperature below 600°C for LSC than LCC. Completely stabilized phase of $CaCrO_4$ is formed at some intermediate temperature close to 900°C after which it starts dissolving, whereas $SrCrO_4$ begins to dissolve back at relatively lower temperatures in the range 600°C to 900°C. Up to 1200°C, while $SrCrO_4$ vanishes almost completely,

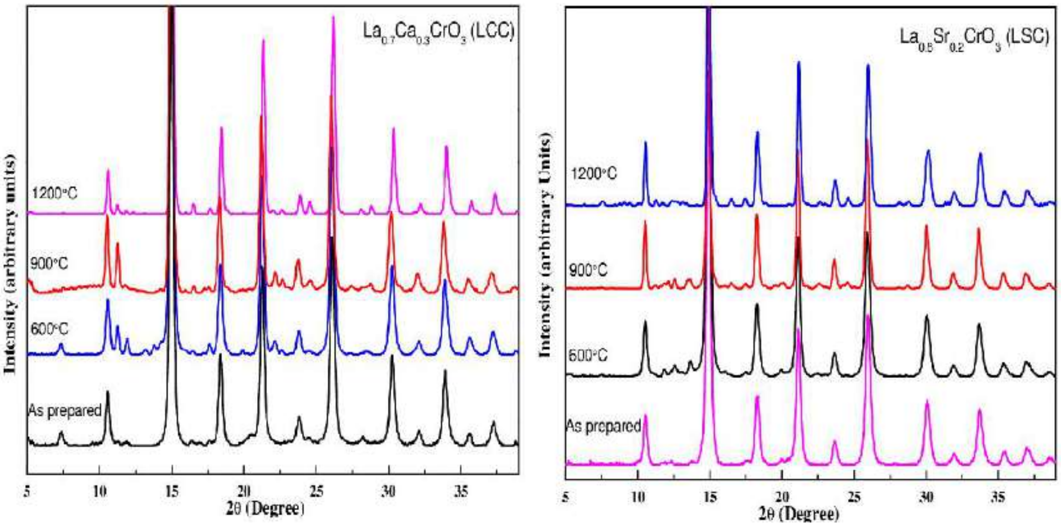

**Figure 6.5:** X-ray diffraction patterns of (a) LCC and (b) LSC calcined at various temperatures.

**Table 6.1:** Extracted parameters from fitting of XRD data of LCC and LSC.

| Calcination Temperature | Wt% of $CaCrO_4$ | Wt% of $SrCrO_4$ | Unit cell vol. of $La_{0.7}Ca_{0.3}CrO_3$ (Å$^3$) | Unit cell vol. of $La_{0.8}Sr_{0.2}CrO_3$ (Å$^3$) |
|---|---|---|---|---|
| As prepared | 0% | 0% | 228.767 | 232.609 |
| 600°C | 10.4% | 12.5% | 229.138 | 233.153 |
| 900°C | 13.8% | 10.1% | 230.629 | 233.584 |
| 1200°C | 4% | 0.04% | 226.514 | 231.527 |

$CaCrO_4$ may be completely dissolved at temperatures higher than 1200°C.

Having confirmed the transient phase formation, one can now comment on the mechanism of microstructural modifications in these nano-crystalline systems. From Figure 6.3, it can be noticed that vibrations involving the cation La(Sr/Ca), i.e. the internal bending modes and the external modes, show similar trends on increasing the calcination temperature. These LSC and LCC frequencies are very close to each other at 900°C, where the intermediate phase has completely formed. It implies that the La-($CrO_6$) structural units are similar to each other at around 900°C for both LCC and LSC, and the structure of the left out system, after the exsolution of some of the dopants as chromates, should be more like the pure $LaCrO_3$ system. From 900°C to 1200°C, when the intermediate phase

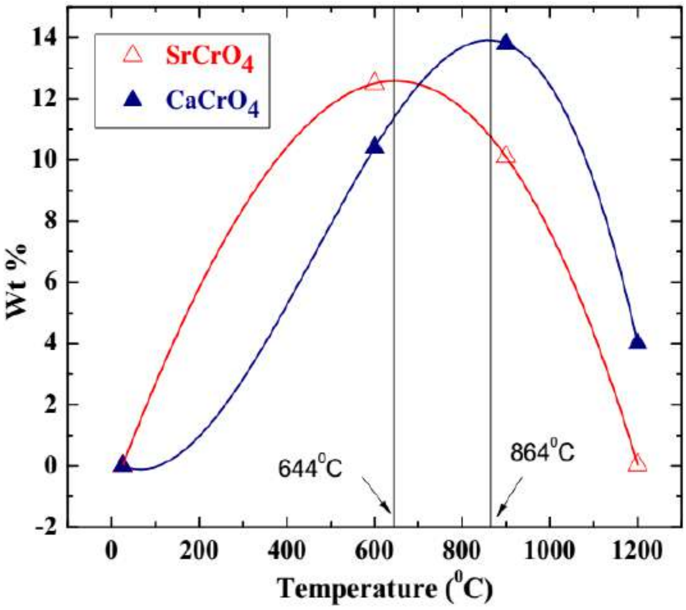

**Figure 6.6:** Variation of weight percentage of transient phases with calcination temperature, obtained by fitting the XRD data. Solid vertical lines mark the position of maximum wt %.

dissolves back into the perovskite, the original structure is regained with LCC frequencies higher than LSC frequencies, but with sufficiently higher values than the as prepared powders. This difference in the frequencies was not noticeable at lower calcination temperature, i.e. between as prepared to 600°C calcined samples. These observations suggest that the microscopic structure gets significantly modified during the process of "formation and dissolution" of the intermediate phases. This is further supported by the trend of internal stretching modes involving only pure $CrO_6$ cages, for which the frequencies depict relatively faster rise in the regime of intermediate phase formation. Hence, the temperature range across 900°C emerges as the crucial point and for 1200°C calcination temperature, the structures are similar to the as prepared samples, i.e. with practically no dopant phases, but the frequencies have been enhanced showing stronger bond strengths. Another striking feature is that at 900°C, for LCC, more number of splitted modes are observed, which more like a pure orthorhombic character is. The effects of intermediate phase formation on the microscopic structure of LSC is smaller as compared to that of LCC which may be attributed to the lower extent of doping, as the relative intensity of the IR peaks of $CaCrO_4$ are more than $SrCrO_4$ implying lesser formation of the $SrCrO_4$, or lower buckling of octahedra along the *b*-axis for LSC than LCC, as the *Pnma* unit cell can be obtained from the cubic one by a combined rotation of the octahedra along the (100) and (110) direction resulting in a buckling of the octahedra along the *b*-axis [222].

#### 6.1.1.5 Transient phases modifying the Mesoscopic structure

**A. Small angle neutron scattering**

In general, synthesis of nano-ceramics by gel-combustion method results into agglomerates of nano-particles and the sintering of agglomerates are accompanied by a modification in the mesoscopic structure [208, 209, 223, 224]. Agglomerates in nano-ceramics may be represented in various situations by fractals and SANS is a well established nondestructive technique to study fractal morphology in various materials in mesoscopic length scale [225, 226]. It can probe both open and close pores in solids. The mathematical relation characterizing a fractal aggregate of radius R and mass M is given by $\mathrm{M}\ (\mathrm{R}) \propto \mathrm{R}^{\mathrm{D_f}}$, here $\mathrm{D_f}$ is the fractal dimensionality of the system [227], different from its normal Euclidean dimension. In reality, fractal nature of the aggregate is valid within some limited length scales, namely lower and upper cutoff. The scattered intensity I(q), at high enough wave-vector transfer q region varies as $\mathrm{q}^{-\mathrm{D}}$ for mass or volume fractal objects within its cutoff lengths. The fractal dimension is also a quantitative measurement of the compactness of agglomerates. For compact and dense agglomerates, D is close to its Euclidean dimension. Scattering contributions from nano-phase structures are concentrated at small scattering angles. Scattering of neutrons in small-angle regime occurs if coherent scattering length density of the inhomogeneities is different from that of the medium. In case of porous solids, pores can be thought of as inhomogeneities and small-angle scattering of neutrons arises due to scattering contrast between the pores and the surrounding solid matrix [228–230].

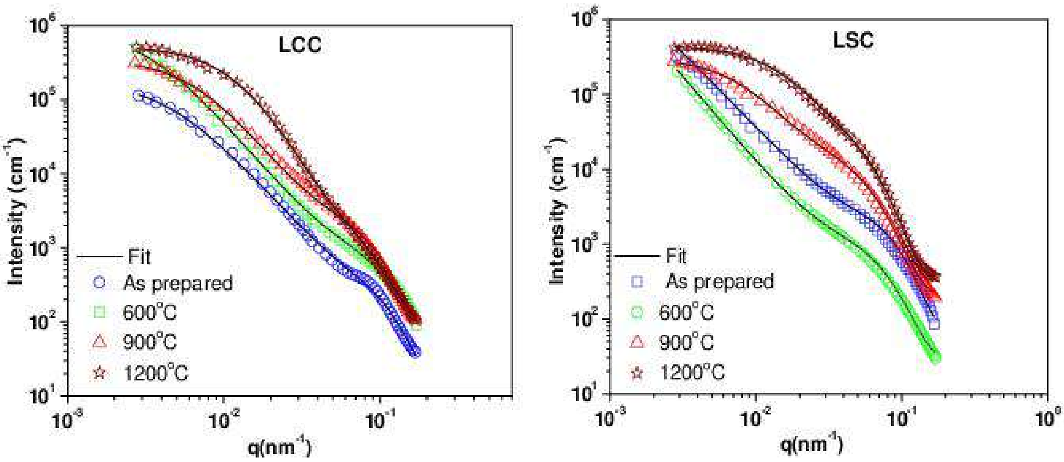

**Figure 6.7:** SANS profiles at different calcination temperatures for (left) LCC and (right) LSC samples.

The SANS data for the LCC and LSC samples have been plotted in absolute scale in Figure 6.7. SANS profiles for LCC specimens, show power law behaviour in certain q-range, indicating a fractal type correlation of the aggregates. Fractal correlation gets modified with increasing calcination temperature. It is also evident from the profiles that a hump like structure appears at high q (q∼ 0.09 nm$^{-1}$), which is pronounced at lower calcination temperatures. This is attributed to the hard sphere type correlation of the primary particles. Power law behaviour in SANS profiles has also been observed for LSC samples (Figure 6.7). It has been observed that SANS profiles for both LCC and LSC powders are best described by accounting the fractal and hard sphere type correlation of the primary particles of the aggregate,

$$\frac{d\sum}{d\Omega}(q) = c1\left[\int_0^\infty v_p^2(r)P(q,r)D(r)S_{HS}(q,r,\eta)dr + c2\int_0^\infty v_p^2(r)P(q,r)D(r)S_{Fractal}(q,r,\xi)dr\right] \tag{6.1}$$

where, $c1$ and $c2$ are the $q$ independent scale factors, $V_p(r)$ is volume of primary particle with radius $r$, $P(q,r)$ is form factor of the particle. In the present case spherical form factor has been adopted for data analysis as it could best fit our

**Table 6.2:** Extracted parameters from model fitting to the LCC data obtained by SANS.

| Calcination temperature | Fractal dimension ($D_f$) | Mean radius (nm) | Polydispersity index (b) | Upper cutoff $\xi$ (nm) |
|---|---|---|---|---|
| As prepared | 2.2 | 15.8 | 0.3 | 221 |
| 600°C | 2.3 | 16.0 | 0.3 | 294 |
| 900°C | 2.5 | 17.7 | 0.3 | 144 |
| 1200°C | 2.9 | 16.8 | 0.3 | 73 |

data and is given as,

$$P(q) = 9\left[\frac{sin(qR) - qRcos(qR)}{(qR)^3}\right]^2 \tag{6.2}$$

$S_{HS}$ $(q,r,\eta)$ is hard sphere structure factor [231] to account high $q$ correlation ($q\sim0.09$ nm$^{-1}$) of the primary particles in the present $q$ window, where $\eta$ is the volume fraction of the primary particles. $S_{Fractal}$ $(q,\ r,\xi)$ is structure factor to account the mass fractal correlation [225, 226] at lower q range. $\xi$ is the upper cutoff length of the fractal aggregate and represents the length scale up to which fractal correlation exists. $D(r)$ is particle size distribution. In the present case log-normal distribution has been taken as

$$D(r, a, b) = \frac{1}{\sqrt{2\pi b^2 r^2}} exp\left(\frac{-[ln(r/a)]^2}{2b^2}\right) \tag{6.3}$$

where $a$ and $b$ are the parameters representing the median and polydispersity index of the distribution. The size distributions of the primary particles for both LCC and LSC have been depicted in Figure 6.8. It is evident that the primary particle size increases with increasing calcination temperature indicating the coalescence of smaller particles to form bigger particles. Important parameters, extracted from fitting to the scattering data for LCC and LSC samples, are shown in Tables 6.2 and 6.3, respectively.

From Figure 6.8(left) and Table 6.2, it is clear that agglomerates in as prepared LCC powder possess a mass fractal like morphology with a mass fractal dimension ($D_f$) of 2.2 and upper cutoff length 221 nm. These fractal agglomerates consist

**Table 6.3:** Extracted parameters from model fitting to the LSC data obtained by SANS

| Calcination temperature | Fractal dimension ($D_f$) | Mean radius (nm) | Polydispersity index (b) | Upper cutoff $\xi$ (nm) |
|---|---|---|---|---|
| As formed | 2.0 | 18.9 | 0.31 | - |
| 600°C | 2.3 | 19.3 | 0.33 | - |
| 900°C | 2.5 | 22.6 | 0.35 | 118 |
| 1200°C | 2.9 | 26.0 | 0.30 | 52 |

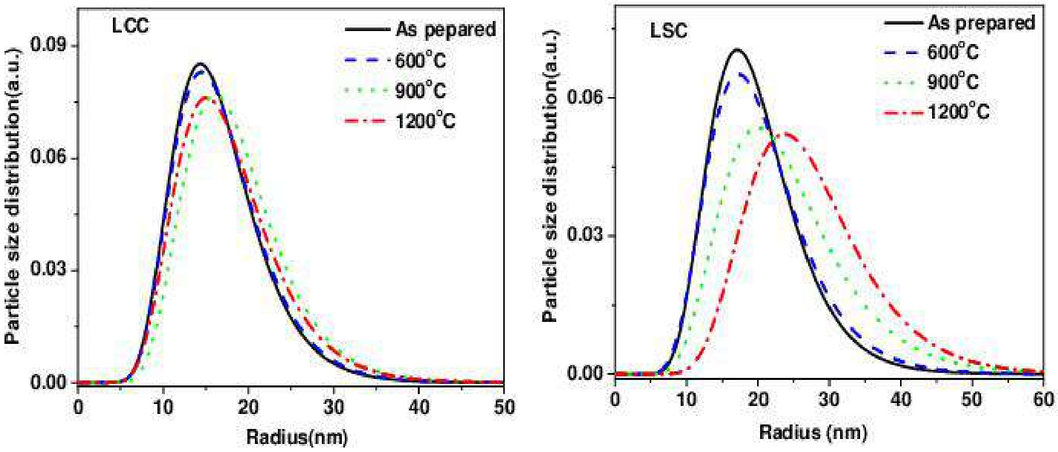

**Figure 6.8:** Primary particle size distributions of (left) LCC and (right) LSC aggregate with temperature.

of primary particles with an average radius 15.8 nm. This indicates that the fractal agglomerates of initial precursor powder are very loose. Fractal dimension ($D_f$) of agglomerates increases towards ∼2.9 with increasing calcination temperature. Further, the upper cutoff of the fractal decreases significantly at higher temperatures. These modifications below calcinations temperature of 900°C may be attributed to the compaction of the fractal aggregates via diffusion during sintering process at lower calcination temperature. However, it is interesting to note that fractal dimension increases considerably, to 2.9, when calcination temperature is increased beyond 900°C. This shows that the agglomerates, which are loose in nature at lower temperature, start getting compacted at higher calcination temperatures. It is interesting to note that the diffusion mechanisms at lower calcination temperatures may be grain boundary diffusion. However, around and beyond 900°C, due to the formation of intermediate phases by the melting of dopant chromates, as revealed by IR spectroscopy, the diffusion is dominated by viscous flow of the material that leads to faster densification and thus compaction of aggregate.

Similar observations have been realized for the LSC specimens except for some quantitative differences. From Figure 6.8(right) and Table 6.3, it is clear that the structure of the agglomerate in as prepared LSC powder also possesses a mass fractal morphology but with a mass fractal dimension of 2.0 and an upper cutoff length more than 1000 nm that was beyond the SANS instrumental resolution. The size of the primary particles was found to be approximately 19 nm. It is clear that upper cutoff is significantly larger for as prepared powder of LSC in comparison to that of LCC. Furthermore, the average size of the primary particles for LSC is somewhat larger than that for LCC powders. In addition, the position of the hump in the scattering profile due to the presence of inter particle interference differs in virgin LSC and LCC powders. These comparisons also indicate that agglomerates in initial virgin powder of LSC possess relatively loose structure and is also larger as compared to that of LCC. Further, from the difference in agglomeration nature of LCC and LSC, it appears that the sintering of LCC virgin powder is relatively easier as compared to that of LSC inspite of their iso-structural phase.

### B. Scanning Electron Microscopy (SEM)

To verify the mesostructural modifications during calcination of the specimens, obtained by scattering data, Scanning Electron Microscopy (SEM) has also been carried out. It is noteworthy to mention here that microscopy is a direct method to observe the mesoscopic length scale; however it is local probe of the matter. Scattering is an indirect method to see the mesoscopic length scale and is a bulk sensitive technique. The information extracted by scattering is statistically averaged over bulk of the specimen. In general, microscopy and scattering methods are used as complimentary techniques to probe the mesoscopic length scale. To

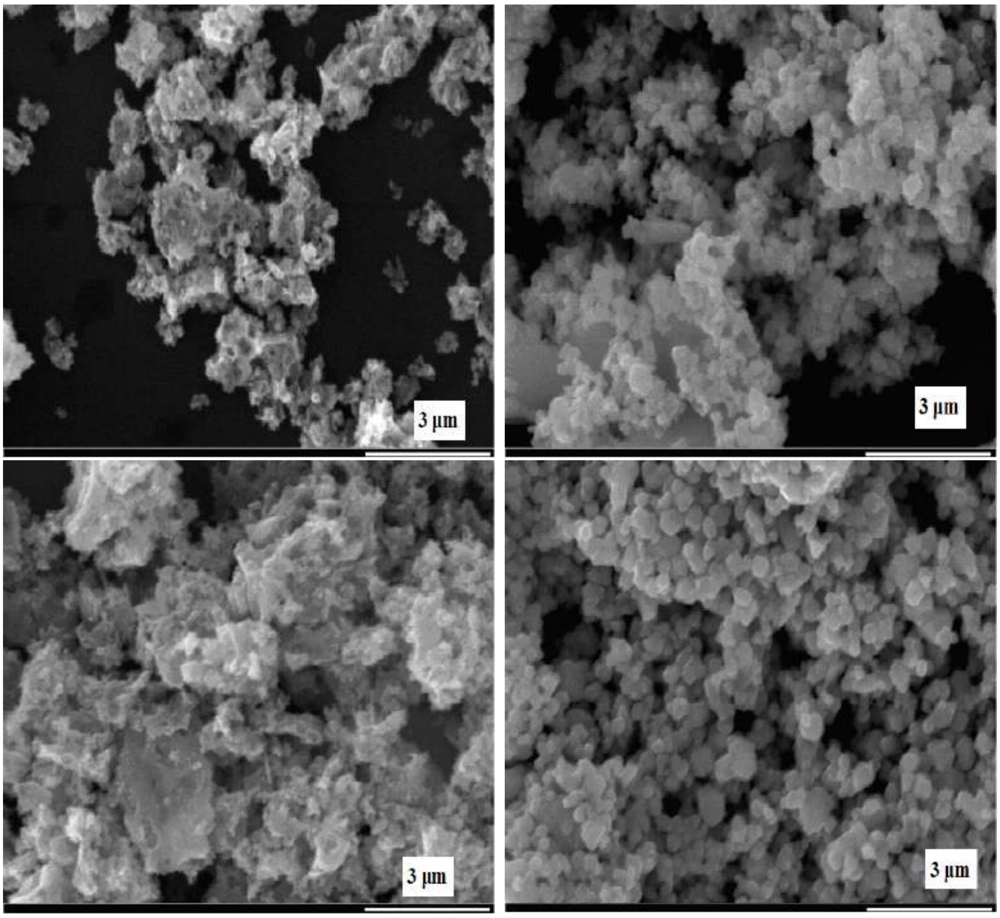

**Figure 6.9:** SEM images of the (left) as prepared and (right) 1200°C calcined specimens of (top) LSC and (bottom) LCC.

observe the modifications in the agglomerates during calcination, SEM micrographs of the as prepared and calcined specimens of both LSC and LCC have been shown in Figure 6.9. As predicted, the agglomerates of the as prepared specimens are very loose. It is also evident from the images that the overall agglomerate size decreases and the agglomerates get compacted with increasing calcination temperature. These observations corroborate with SANS results, as fractal dimension of the agglomerates increases towards the Euclidean dimension ($D_f = 3$) and also the fractal upper cutoff length decreases with increasing calcination temperature (Tables 6.2 and 6.3).

#### 6.1.1.6 Conclusions

Calcination behaviour of nano-crystalline lanthanum chromites doped with Calcium and Strontium has been probed by Fourier Transform IR spectroscopy, X-ray diffraction and small- angle neutron scattering as a function of temperature. For LCC and LSC, IR active vibrations are mostly confined in three broad absorption bands. Evolution of intermediate phases ($CaCrO_4$ for LCC and $SrCrO_4$ for LSC) takes place as the calcination temperature is increased. The evolution and disappearance of transient phases takes place at lower calcination temperatures for Sr doped chromites. During calcination at intermediate temperatures, the decrease in Cr−O stretch, increase in La-O bond length and decrease in tilt angle results in increase in the unit cell volume. Thus, the microscopic structure of the systems get modified with calcination temperature in the regime of intermediate phase formation, which is regained at higher temperatures where the dopant chromates get redissolved into the original structure, but with sufficiently higher bond strengths. The influence of these microstructural changes on the sintering properties of the composites have been investigated by neutron scattering and SEM studies which enlighten the mesoscopic nature. The bridge between the two studies is the possibility of the occurrence of the phenomenon of liquid state assisted sintering through the melting of intermediate phases. It has been noticed that not only the microscopic, but the mesoscopic structure of the nanoceramics also gets significantly modified with calcination temperature. Fractal dimension and cutoff lengths of the agglomerates get altered at higher temperature leading to compaction of the agglomerates. The temperature regime across 900°C emerges as crucial range for the comparison of the two doped nanocrystalline perovskites as well as for the sintering mechanisms in the two systems.

### 6.1.2 Determination of optical properties from IR reflectivity measurements on Ru1212 under high pressure

$RuSr_2GdCu_2O_8$ (Ru1212) system has drawn attention due its remarkable property of coexistence of superconductivity ($T_c \sim 45$ K) as well as magnetism ($T_m \sim 130$ K) [232,233]. Moreover, the incipient superconductivity does not result in the loss of magnetism. The structure of this compound is similar to the well known high Tc superconductor $YBa_2Cu_3O_{7-\delta}$ (YBCO) [233]. While in YBCO, CuO ribbons connect the superconducting $CuO_2$ planes, in the tetragonal structure in Ru1212, $RuO_2$ planes connect the alternate $CuO_2$ planes as shown in Figure 6.10. The magnetic ordering in this compound owes to the ruthenate layers and superconductivity arises due to $CuO_2$ planes. For pure Ru1212, optical conductivity studies at low temperature have shown the evidence of electron-phonon coupling, in particular the broadening of the Cu-O bending mode near 300 $cm^{-1}$ across $T_c$, shift in the broad mid IR polaron band and suppression of spectral weight at low frequencies [234]. Copper doping for Ru has shown to raise the Tc at the expense of magnetism and a Tc value of as high as 72 K was reported for ∼40% dilution of ruthenium sublattice with copper ions [235]. However, the magnetic ordering above the superconducting transition temperature could be preserved only for 10% and 20% of copper for ruthenium [235]. On the other hand, Ru1212, when subjected to high pressure, shows no or very little variations in Tc ($dT_c/dP = 1.9$ $KGPa^{-1}$) [236, 237]. However, the magnetic ordering has shown strong pressure dependence ($dT_m/dP = 5.7$ $KGPa^{-1}$) and an increase in transition temperature is noticed with pressure up to 1.6 GPa. Beyond this pressure, the increase was saturated [236]. The present work is aimed at understanding the underlying effects of pressure, which selectively influences the magnetic ordering in Ru1212, with 10% copper doping for ruthenium.

**A. Experiments and modeling**

High pressure infrared reflectivity measurements up to 8 GPa were carried out

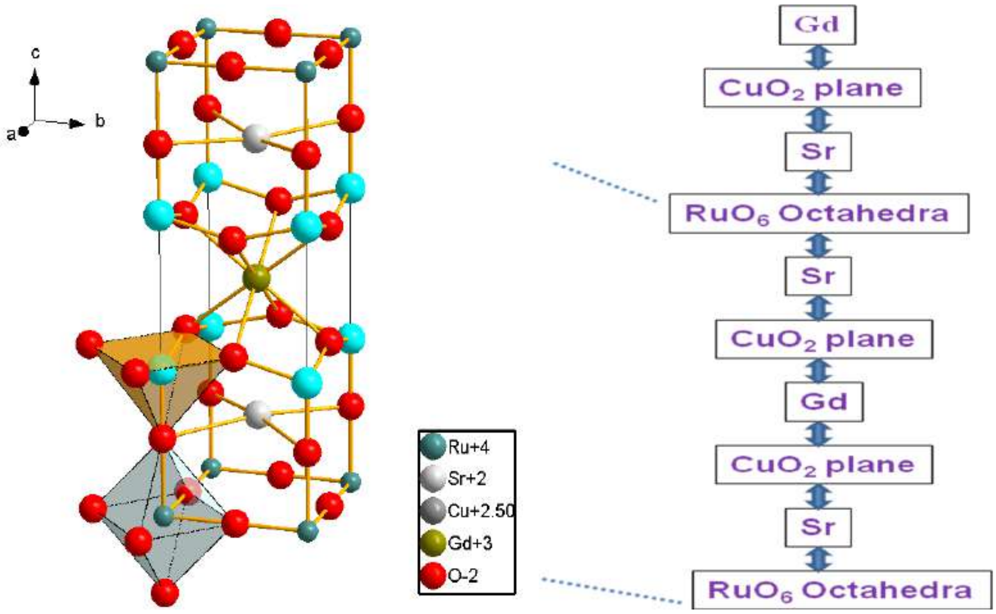

**Figure 6.10:** Various layers in the crystal structure of Ru1212. Also shown are the tetrahedra and octahedra around Cu and Ru atoms respectively connected by the apical oxygen along the *c*-axis.

at room temperature using Diamond Anvil Cell and Bruker FTIR instrument coupled with the Hyperion microscope. The mid-IR data (600 - 10000 cm$^{-1}$) were recorded at our facility at Indus-1 and repeat measurements at some pressures were performed at the Elettra synchrotron, which was primarily used for far infrared characterization (150 - 600 cm$^{-1}$) using the bolometer detector, with the diffraction limited spot size of $\sim$ 100 $\mu$m. CsI was used as the pressure transmitting medium and all the reflectivity data were normalized for background and diamond contribution (see Figure 6.11) using the following method,

$$r_0 = \frac{r_{s-d}}{r_{ud}}, r_1 = \frac{r_{ld}}{r_{ud}}; R_{sd} = \frac{r_0}{r1} \times \frac{1-n^2}{1+n^2} \tag{6.4}$$

where $r_{s-d}$ = measured reflectivity from sample diamond interface, $r_{ud}$ and $r_{ld}$ = reflection from upper and lower diamond surface respectively, n = refractive index of diamond and $R_{sd}$ is the true reflectivity from the sample diamond interface. The optical constants can be obtained by exploiting the refractive index depen-

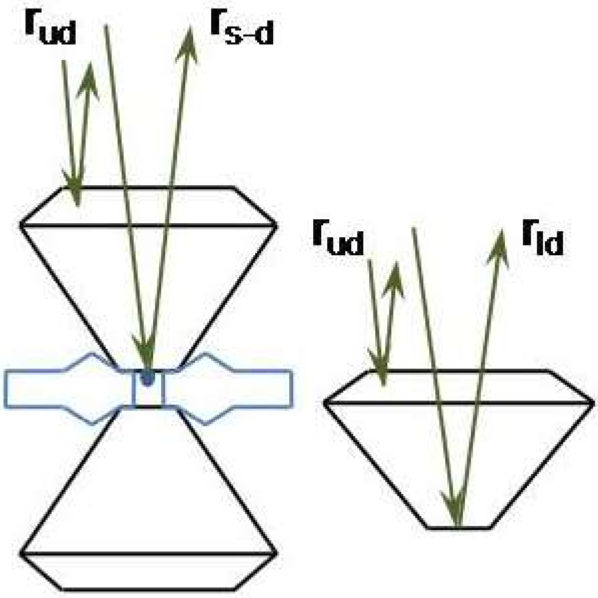

**Figure 6.11:** Schematic showing background correction during high pressure IR reflectivity measurements.

dence on reflectivity through Kramer-Kronig transformations. We employ Drude-Lorentz formalism to extract the parameters by fitting the reflectivity data [71]. However, this method requires the experimentally observed data to be measured in a wide spectral range (0 to $\infty$ in theory) which is not possible in practice. Hence, we measure the data in the widest possible spectral range beyond which it is extrapolated to far enough frequencies. For example, the lower frequency extrapolation is taken up to $R = 1$ for $\omega = 0$ in the case of metallic samples. For Ru1212, a continuous low frequency extrapolation of the reflectivity data was carried out according to the Hagen-Rubens extrapolation for normal state up to $\omega = 0$ as,

$$R(\omega) = 1 - (a \times \omega^s) \tag{6.5}$$

where $a$ = constant, $\omega$ = frequency and $s$ is a parameter = 0.5 for normal state and 2 for the superconducting state. For higher frequencies, over and above the measured spectral range, it was assumed that there still is some contribution due to inter/intra band transitions and the extrapolation was carried out as:

$$R(\omega) = R_H \times \left(\frac{\omega_H}{\omega}\right)^s \tag{6.6}$$

where $\omega_H$ and $\mathrm{R_H}$ are the highest measured frequency and the reflectivity value at this frequency respectively. $s$ is a parameter which is generally taken as 2 and 4 at high and very high (i.e. asymptotic limit) frequencies. The reflectivity data obtained from measurements at various pressures can be utilized to find the optical conductivity and dielectric constant from the following relations:

$$\tilde{n} = n + ik \quad ; \quad \tilde{\epsilon} = \epsilon_1 + i\epsilon_2 \tag{6.7}$$

$$R(\omega) = \frac{(1 - n(\omega)^2) + k(\omega)^2}{(1 + n(\omega)^2) + k(\omega)^2} \tag{6.8}$$

$$\epsilon_1(\omega) = n(\omega)^2 - k(\omega)^2 \;\; ; \quad \epsilon_2(\omega) = 2.n(\omega).k(\omega) \tag{6.9}$$

$$R = \frac{\sqrt{(\epsilon_1^2 + \epsilon_2^2)} + 1 - \sqrt{(2(\sqrt{(\epsilon_1^2 + \epsilon_2^2)}) + \epsilon_1)}}{\sqrt{(\epsilon_1^2 + \epsilon_2^2)} + 1 + \sqrt{(2(\sqrt{(\epsilon_1^2 + \epsilon_2^2)}) + \epsilon_1)}} \tag{6.10}$$

$$\sigma_1(\omega) = \frac{1}{4\pi}\omega.\epsilon_2(\omega) \tag{6.11}$$

where $n$, $k$ and $\epsilon_1$, $\epsilon_2$ are real and imaginary parts of the complex refractive index and dielectric constant respectively. $R$ is measured reflectivity and $\sigma_1$ is the real part of optical conductivity.

The Drude model is based on the free electron gas model which assumes that electrons in metals can be treated as randomly moving free particles. This contributes to a maximum reflectance, i.e. $R = 1$ for $\omega = 0$ in the case of metals. For $\omega > 0$, the reflectivity profile may depend on various transitions involving phonons, interband transitions etc. which are described by the Lorentz oscillators. The final expressions as obtained from the electromagnetic theory of waves in matter, are as follows:

$$\epsilon(\omega) = \epsilon_\infty - \left(\frac{\omega_p^2}{\omega^2 + i\omega\Gamma}\right) - \sum_j \left(\frac{s_j\omega_j^2}{(\omega^2 - \omega_j^2) + i\omega\Gamma_j}\right) \tag{6.12}$$

$$\epsilon_1(\omega) = \epsilon_\infty + \left(\frac{\Gamma_p}{\omega^2 + \Gamma_p^2}\right) + \sum_j \left(\frac{s_j(\omega - \omega_j^2)}{(\omega^2 - \omega_j^2)^2 + \Gamma_j^2\omega^2}\right) \tag{6.13}$$

$$\epsilon_2(\omega) = \sum_j \left(\frac{s_j\Gamma_j\omega}{(\omega^2 - \omega_j^2)^2 + \Gamma_j^2\omega^2}\right) \tag{6.14}$$

$$\sigma_1(\omega) = \frac{\omega_p^2}{4\pi}\left(\frac{\Gamma_p}{\omega^2 + \Gamma_p^2}\right) + \frac{1}{4\pi}\sum_j \left(\frac{s_j^2\Gamma_j\omega^2}{(\omega^2 - \omega_j^2)^2 + \Gamma_j^2\omega^2}\right) \tag{6.15}$$

here $\omega_j$, $s_j$ and $\Gamma_j$ are oscillator frequency, oscillator strength and dampening parameter respectively corresponding to the $j^{th}$ harmonic oscillator, $\omega_p$ is plasma frequency and $\epsilon_\infty$ is dielectric constant at high frequencies. The first term in the $\sigma_1$ (real part of optical conductivity) corresponds to the Drude behaviour and the second term takes care of various transitions.

### B. Optical conductivity of Cu doped Ru1212 at high pressures

The ambient characterization of the samples was carried out using infrared spectroscopy and X-ray diffraction to ascertain the phase formation. Figure 6.12(left) shows the far-IR absorption spectra of pure Ru1212 and 10% Cu doped (for Ru) sample, henceforth known as Ru1 and Ru0.9 respectively. The patterns for the two samples are almost identical and match with the reported data [238]. Further, the magnetic transition temperature, as shown in Figure 6.12(right) for Ru0.9, is also found close to 130 K in accordance with the reported values for this class of materials [239].

The reflectivity spectra of $Ru_{0.9}Sr_2GdCu_{2.1}O_8$ at different pressures have been plotted in Figure 6.13 in the mid and far-infrared regions (300 - 9000 cm$^{-1}$). The

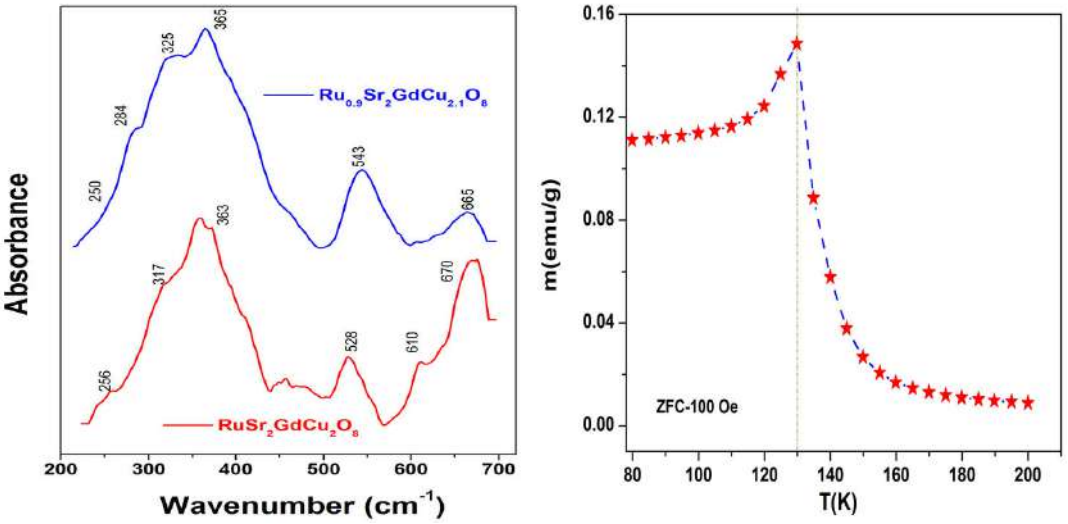

**Figure 6.12:** (left) IR absorption spectra (y-offset) of Ru1 and Ru0.9 samples. (right) Magnetization measurement data of Ru0.9, the transition temperature was clearly identified in both field cooled (FC) and zero field cooled (ZFC) measurements.

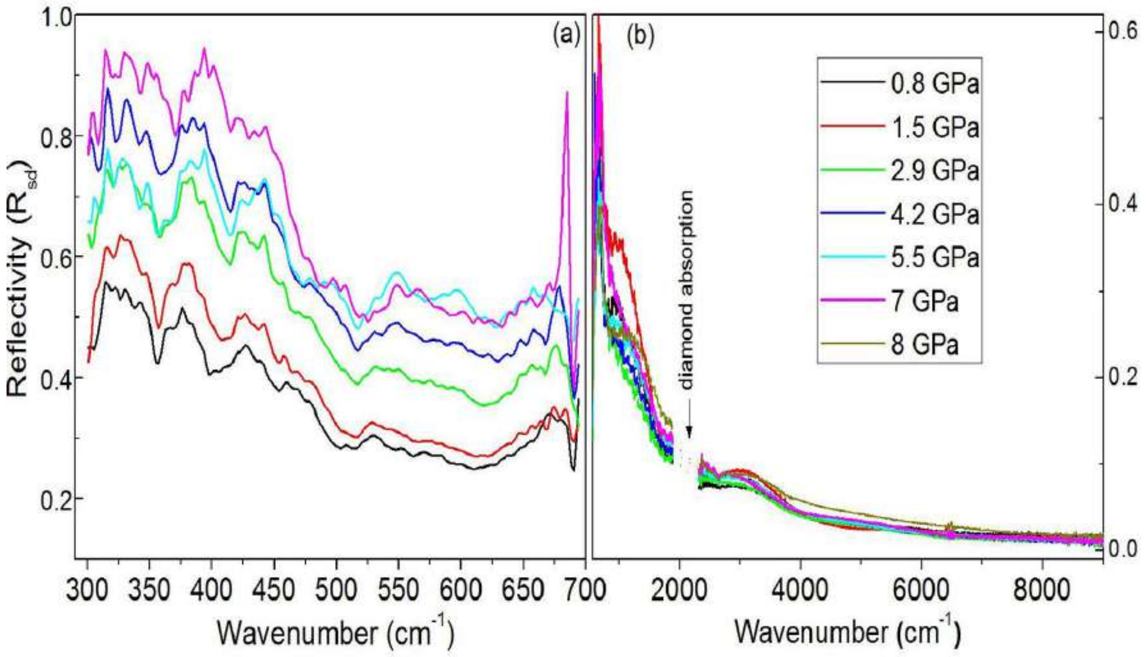

**Figure 6.13:** Reflectivity spectra of Ru0.9 in (a) far and (b) mid infrared regions at various pressures.

blocked range near 2300 cm$^{-1}$ is the region of strong absorption due to diamond. The reflectivity data at all the pressures show a sharp fall with frequency up to ~2000 cm$^{-1}$ which is similar to the undoped compound [234]. This indicates a metallic type low frequency response, whereas a relatively much slower fall in reflectivity is observed at higher frequencies. The optical conductivity was determined from the parameters obtained by fitting of these spectra using Drude-Lorentz formalism. Typical fitting results for a few representative pressures have been shown in Figure 6.14.

From the reflectivity spectra (Figure 6.13), it was observed that the reflectance of the Ru0.9 sample initially shows very small changes upon compression. However, across 1.5 GPa, we observe a transfer in spectral weight from higher frequencies to lower frequencies as shown in Figure 6.15. These observations indicate that this compound shows a tendency towards enhanced free electron type metallic behaviour upon further compression. This is verified from the far-IR reflectivity patterns (Figure 6.13) which clearly show a pressure induced rise in reflectivity, particularly above 1.5 GPa. The broad mid IR band seen in the 3000 - 4000 cm$^{-1}$ range in Figure 6.15 is typical of small polaron absorption, which is discussed in subsequent sections. We also notice that an electronic background of $\sigma_1 \sim 100$ $\Omega^{-1}$ cm$^{-1}$ has been obtained which is in agreement with the dc conductivity value at room temperature.

In Ru1212, the apical oxygen, surrounded by Sr in plane atoms, connects $CuO_2$ plane on one side and the $RuO_6$ octahedra on the other side. The phonon modes related to apical oxygen vibrations (~650 cm$^{-1}$), $CuO_2$ bending mode (~300 cm$^{-1}$) and $RuO_6$ octahedral vibrations (~190 cm$^{-1}$) have shown marked changes in the optical conductivity spectra across magnetic and superconducting transitions in Ru1212 [234]. Although, the $RuO_6$ vibrations could not be checked in the current investigations, due to diffraction limitations at high pressure, we could probe the apical oxygen vibration (*c*-axis phonon mode due to Cu-O bond) and $CuO_2$ bending mode. It can be seen in Figure 6.16(left), the peak intensity of

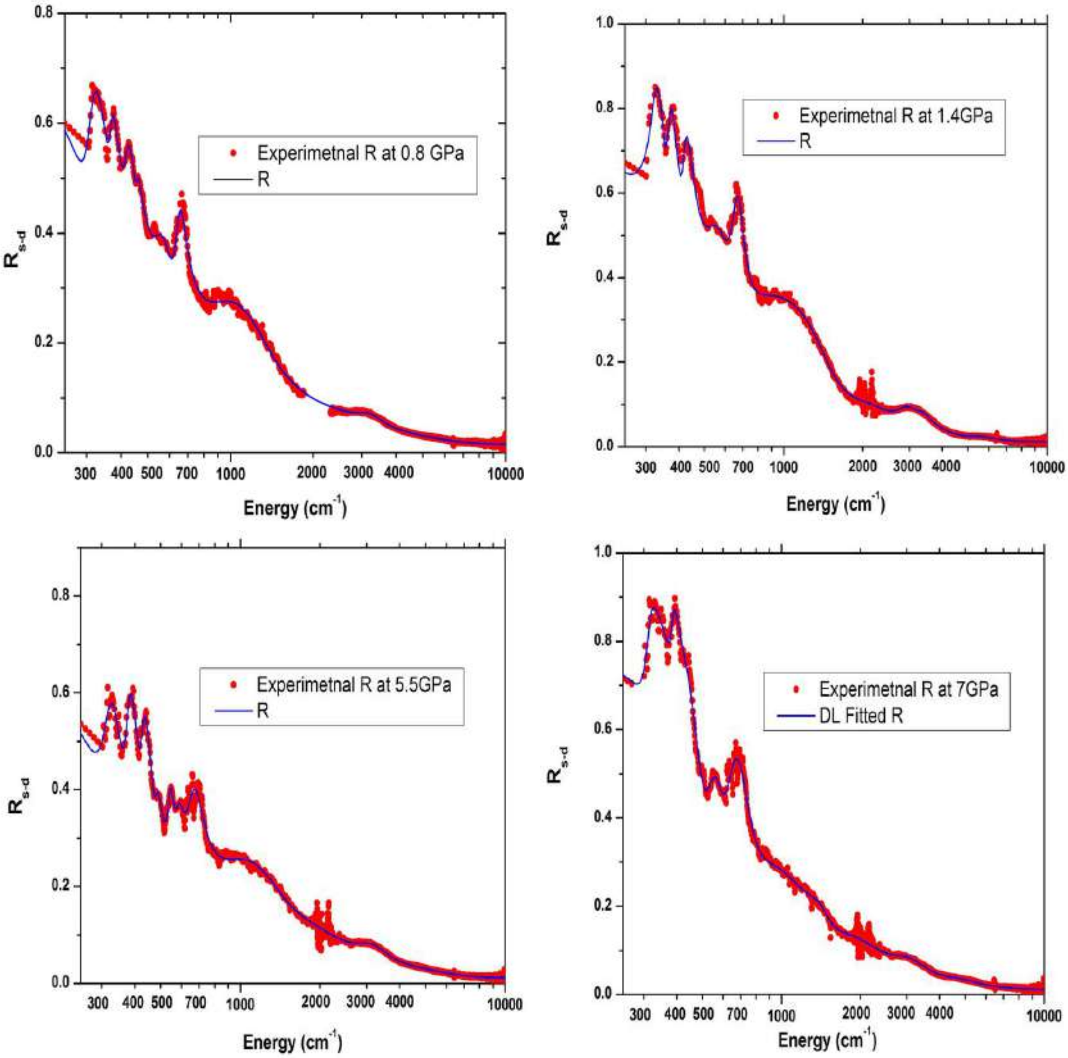

**Figure 6.14:** Measured (red filled circles) and simulated using Drude Lorentz formalism (blue solid lines) reflectivity spectra of Ru0.9 in IR spectral range 250 - 10000 $cm^{-1}$ at some pressures. Fluctuations near 2000 $cm^{-1}$ are due to diamond absorption and have not been included in fitting.

the $CuO_2$ bending mode near 300 $cm^{-1}$ in the optical conductivity spectrum at 0.8 GPa is comparable to the peak intensity of the apical oxygen mode near 650 $cm^{-1}$. As the material is compressed beyond 2 GPa, the spectral contribution of the bending mode increases, whereas that of the apical oxygen mode decreases. Interestingly, this is also accompanied with a discontinuous red shift in the position of the bending mode across 1.5 GPa. Softening as well as gain in intensity

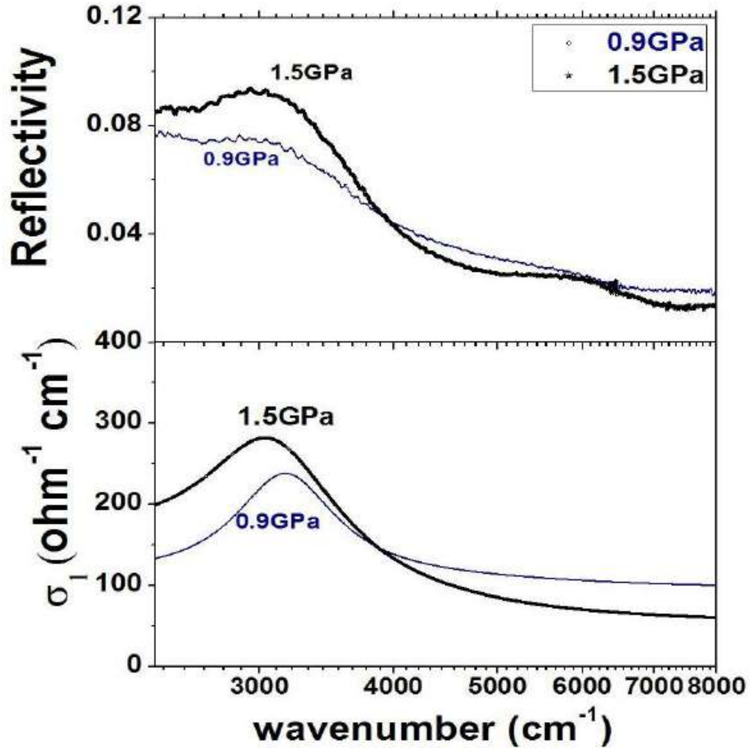

**Figure 6.15:** Reflectivity spectra and corresponding real parts of optical conductivity of $Ru_{0.9}Sr_2GdCu_{2.1}O_8$ at 0.9 and 1.5 GPa.

with pressure of this mode over and above a distinctive rise in the peak width indicates an increase in anharmonicity and interactions with the surrounding system. Further compression has very little effect on this mode. In the MIR region, we also observe a red shift in the polaronic band position near 3000 - 4000 cm$^{-1}$ region up to 1.5 GPa beyond which it shifts slightly to a higher frequency and does not vary much at higher pressures.

The Cu-Cu distance defining the thickness of $CuO_2$ double layers, and the buckling angle of $CuO_2$ planes are the structural parameters primarily affected by the magnetic ordering at lower temperatures [233]. Our results indicate that pressure has strong effects on the $CuO_2$ bending mode and the overall structure up to nearly 1.5 GPa, thus influencing the magnetic properties in this compound. The magnetic ordering in this compound has similar origin as that in the well known ruthenate $SrRuO_3$, where Ru ion is in 4d$^{4+}$ state with configuration $t_{2g}^4$

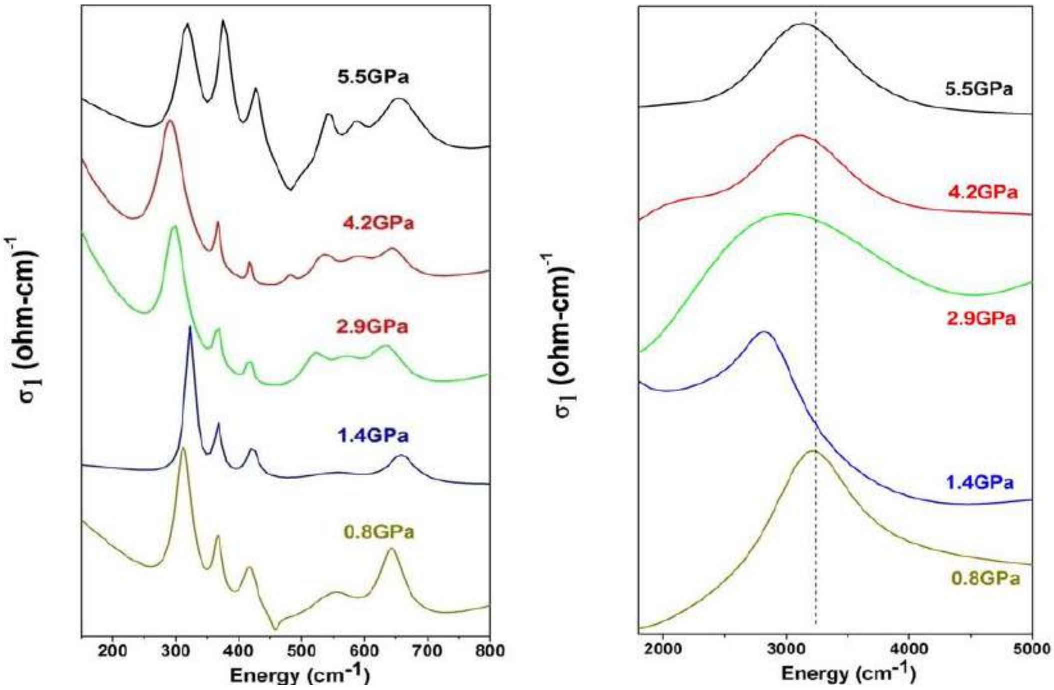

**Figure 6.16:** Optical conductivity of Ru0.9 calculated from the fitted parameters of reflectivity in (left) 200 - 800 $cm^{-1}$ and (right) 1800 - 5000 $cm^{-1}$ spectral regions.

$e_g^0$ [240]. The total spin is S = 1 ($t_{2g}^3 \uparrow$ $t_{2g}^1 \downarrow$ $e_g^0$) as shown in Figure 6.17. The ferromagnetic coupling between Ru ions is transmitted via the itinerant electrons of the minority $t_{2g}$ band [234].

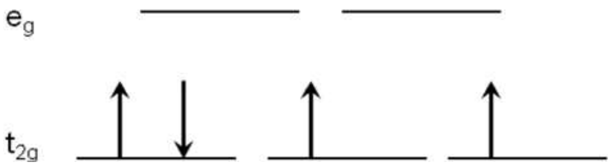

**Figure 6.17:** Electronic spin in $t_{2g}$ orbital in a ruthenate perovskite $SrRuO_3$.

The basic difference between $SrRuO_3$ and Ru1212 is that the $t_{2g}$ minority orbital in Ru1212 is partially occupied due to hole doping of $CuO_2$ biplanes. The mid-IR band is associated with the hopping conductivity of minority $t_{2g}$ electrons and thus the small variation in the polaronic band position of Ru0.9 ($\sim$ 3500 $cm^{-1}$) compared to the undoped compound Ru1 ($\sim$ 4000 $cm^{-1}$) [234,238] can be due to greater overlap because of Cu dilution. In the low temperature studies of Ru1, an increase in spectral weight and red shift of the polaronic band in the ferromagnetic state ($T < T_m$) was correlated with increase in kinetic energy of charge carriers resulting in a reduced effective electron- phonon coupling. Upon pressurizing Ru0.9, we observe that this mode has shown a red shift of nearly 400 $cm^{-1}$ up to 1.5 GPa. Therefore, if an analogy is drawn from the temperature dependent studies of Ru1, which must however be verified with further studies and theory, it is possible that compression would enhance the extent of overlap in Ru0.9 which may further reduce the electron- phonon coupling making the charge carriers more energetic. The argument is consistent with the noted enhancement in free electron metallic behaviour at pressures above 1.5 GPa. Further, emergence of new peaks are also noted in the 400 - 600 $cm^{-1}$ region above 1.5 GPa, which are similar to the *c*-axis modes related to the tilting of octahedra [234]. The above mentioned changes in the observed spectral data across 1.5 GPa are well supported by the crystal structure variations studied by X-ray diffraction at high pressures.

Figure 6.18 shows the high pressure X-ray diffraction patterns of the Ru0.9 sample at various pressures up to 25 GPa recorded using a membrane DAC at the Elettra synchrotron. The corresponding lattice parameters and unit cell volume obtained by structural refinement have been plotted in Figure 6.19. The data show that Ru0.9 does not depict any structural phase transition in the measured pressure range and the unit cell volume follows a monotonous reduction under pressure. However, the *c*-axis lattice parameter shows a deviation from the trend of variation of *a*-axis parameter across 1.5 GPa and subsequently follows a different slope, confirming the subtle structural variations noticed across this pressure value. The larger compressibility observed along the *c*-axis (Figure 6.19) may be responsible for the decrease in Cu-Cu distance and octahedral distortion leading to the emergence of new modes in IR spectra. It would be interesting to study the changes in electronic density of states at high pressures which can provide further insight on the hopping conductivity in this compound.

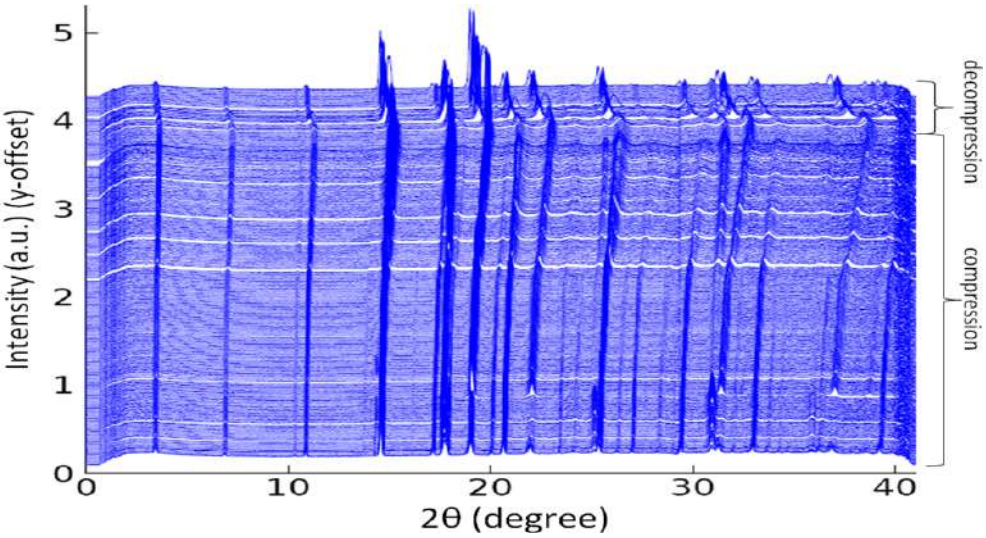

**Figure 6.18:** High pressure X-ray diffraction patterns (y-offset for clarity) of Ru0.9 at various pressures from ambient to 25 GPa showing a monotonous trend upon compression.

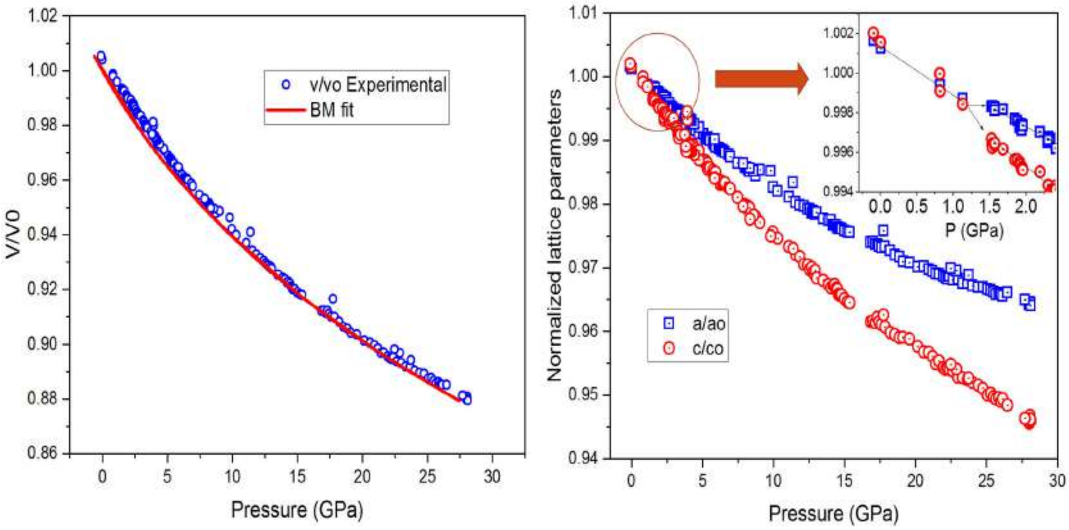

**Figure 6.19:** Variation of (left) unit cell volume and (right) a and c lattice parameters with pressure; inset shows detailed variations in the low pressure regions.

## C. Conclusions

$Ru_{0.9}Sr_2GdCu_{2.1}O_8$ shows a low frequency free electron metallic response, as indicated by the infrared spectra, which is enhanced upon compression beyond 1.5 GPa. The rise in kinetic energy of charge carriers is attributed to the reduction of electron- phonon coupling. Pressure also tunes the $CuO_2$ structure across 1.5

GPa and a red shift in the bending mode has been observed at this pressure. Also an increase in effective spectral weight of this mode is indicated at the expense of apical oxygen mode strength. The above modifications are no longer as effective at further higher pressures as in the lower pressure regime. Structural data have indicated that although there are subtle variaitons across 1.5 GPa, the compound does not undergo any pressure induced phase transition upto 27 GPa. In addition, *c*-axis compressibility shows a steeper variation under pressure above 1.5 GPa as compared to the *a*-axis . These results can be useful to address the reported pressure dependence of magnetic transition temperature in this compound.

## 6.2 Commissioning of the beamline

The infrared beamline at Indus-1 synchrotron source was commissioned and integrated with the experimental station in the year 2015. Because of the restrictions imposed by the dipole chamber; it is currently designed for mid-IR microspectroscopy. The primary areas which benefit the most and having a large user base, are 1) high pressure material investigations in a DAC with samples dimensions of the order of few tens of microns and 2) microscopy/ imaging studies of surfaces and biological systems with dimensions of the order of 5 - 100 $\mu$m. The first performance results and synchrotron based high pressure investigations on a molecular crystal are presented in this section.

### 6.2.1 First performance results

The beamline installation and details of optical components have been discussed in chapter 2. The final integration of the beamline with the spectrometer has been carried out using a pair of paraboloidal and plane mirrors. The focused spot size using the paraboloidal mirrors was less than 350 $\mu$m . Note that the synchrotron emission is directional as compared to the isotropic emission from a thermal source which results in the focusing capabilities of the SR source to such small sizes. This has several advantages compared to the lab source, particularly in the microscopy experiments where the beam is focused to small spot sizes (to even less than 50 $\mu$m) using schwarzchild objectives. With the lab based sources, which radiate isotropically, an aperture is used in the spectrometer to select the radiation in one direction which is treated as an approximate point source. The additional field stops used in the microscope, block most of the beam in order to achieve a small spot size (typically 5 - 100 $\mu$m) and only a fraction of the total source power reaches the sample and detector. On the contrary, the synchrotron radiation source overcomes this limitation, especially for very small spot size applications.

Figure 6.20(upper) shows the total flux from Indus-1 as a function of energy of the emitted radiation and the first signal measured (inset) at the IR beamline using a microscopic aperture of 60 $\mu$m. In Figure 6.20(lower), similar comparision has been shown while measuring the known single channel spectra of Sr-doped $LaCrO_3$ pellet in transmission mode keeping the microscopic aperture at $\sim$ 60 $\mu$m which indicates significantly higher signal to noise ratio with SR source as compared to the thermal source. Further, an analysis of the 100% gold reflection lines shows that for synchrotron source, the signal to noise ratio (SNR) depicts relatively much smaller decline as compared to the thermal source, upon reducing the microscopic aperture (Figure 6.21,right). For example, even at 20 $\mu$m illuminated area, reasonably high signal to noise ratio (more than an order of magnitude) could be achieved using the SR source in the full range (600 - 10000 cm$^{-1}$) because of the brilliance advantage offered by the "directional" point source. Note that, for specimens smaller than 20 - 30 $\mu$m, the thermal source practically becomes unusable unless the sample has very strong absorption bands. Figure 6.21(right) shows the measured RMS noise and SNR (inset) in the 950 - 1050 cm$^{-1}$ range for thermal source as well as SR source, which validate the above observations. The values shown get much improved for smaller apertures and higher frequencies [241]. Note that the actual values can still be better than these considering the spatial fluctuations in the source which might play a role at small spot sizes. Also shown in Figure 6.21(right) are the parameters measured at an extremely bright source at ALS (Advance Light Source, USA with fixed beam current of ~ 500 mA and electron energy ~ 2 GeV leading to much higher signal/flux than the present case), where noise correction systems employing a feedback mechanism system have also been installed which considerably improves the noise contributions into the signal [242]. Note that the signal levels are predominantly determined by the electron current and a high current is a necessity for microscopy studies. Thus, the first observations indicate that the synchrotron source at Indus-1, though with low electron energy and current, is also a good and very useful source for mid IR microscopy and also encourage us to further improve upon the performance within the design limitations, as discussed below. It is noteworthy that the net flux reaching the spectrometer and hence the maximum signal to noise ratio achievable also depends upon the transmittance of the windows used in the beamline. While diamond windows are ideal for use in the infrared beamlines, it is difficult to obtain very large high quality diamond windows. Due to the design and site restrictions in the present set up, it was necessary to use broad, i.e. large diameter vacuum isolation windows. KBr windows, though transmit more than 90% of light in the mid infrared region, deteriorates on the exposure to UV light (on the front end) and are extremely hygroscopic (to be used at the other end with atmospheric contact) and hence cant be used with the present setup. ZnSe windows are comparatively non-hygroscopic and non-reactive to UV irradiation. But, their transmittance is limited to 70% in the complete range. The use of three windows in the whole set up, thus considerably reduces the signal. At present, we have used a pair of 63 mm laser grade ZnSe windows (AR coated to enhance the transmittance), just above the first mirror (M1) chamber, to isolate the storage ring UHV and the rough vacuum in the rest of the beamline. Also, ZnSe transmits in a much wider spectral range in the mid and near IR regions than KBr, which is advantageous in experiments like

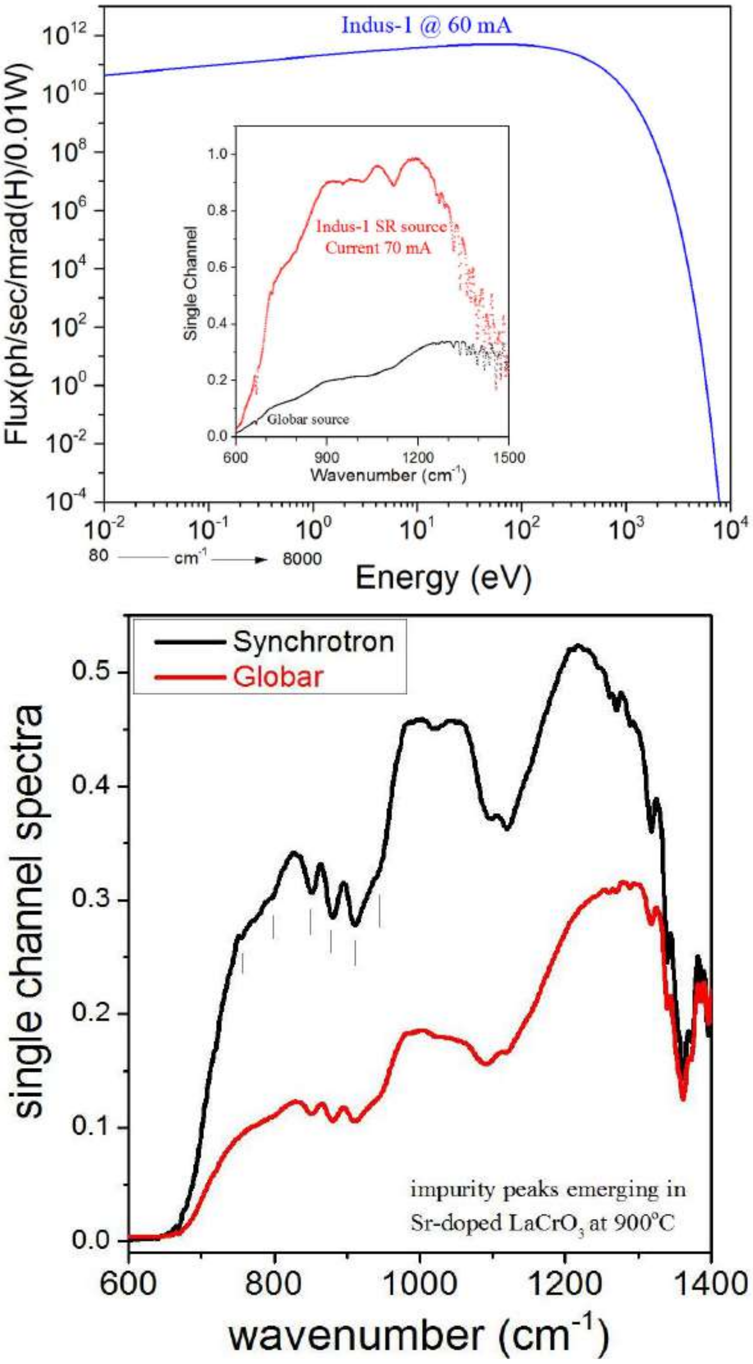

**Figure 6.20:** (upper) Indus-1 synhchrotron radiation flux as a function of photon energy. Inset: the first signal recorded from the beamline: single channel transmittance spectra in the "fingerprint" region measured using a CsI pellet, with Globar source and SR source (@ 70mA) at the microscope aperture of 60 $\mu$m. All the conditions and spectrometer parameters were kept identical during the two measurements. (lower) Single channel spectra recorded using a Sr- doped $LaCrO_3$ (calcined at 900°C) disc (prepared in CsI) at similar conditions, however the electron beam current had dropped to 60 mA during these measurements.

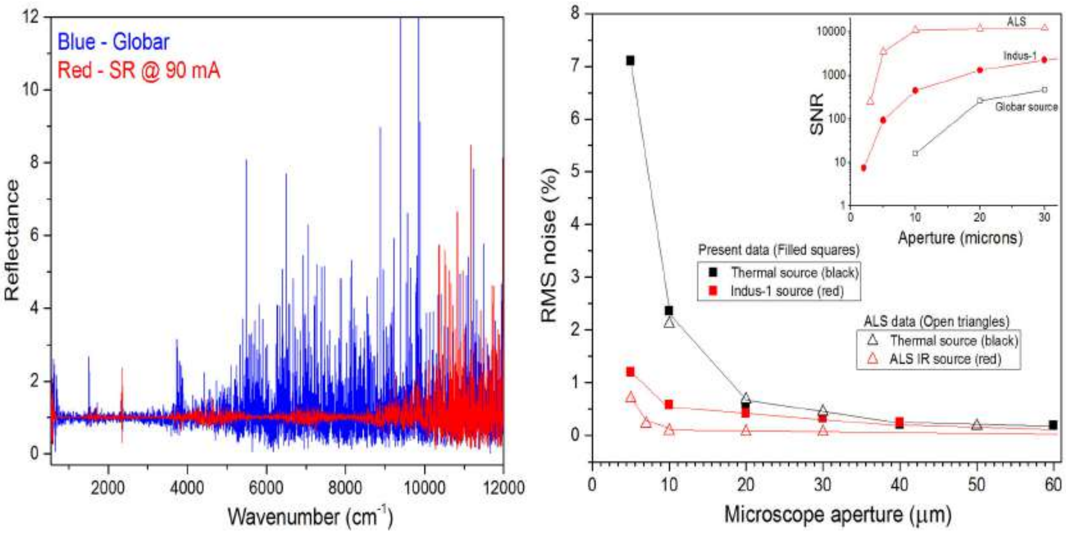

**Figure 6.21:** (left) 100% reflection lines measured using the SR source (red) as well as thermal source (blue) from a 20 m illuminated spot of a polished gold mirror. The spikes near 1500 and 2300 cm$^{-1}$ are due to atmosphere and the fluctuations with the SR source near 1800 - 2500, 4000 - 5000 and 6700 - 7400 cm$^{-1}$ are due to small transmission dips in the vacuum isolation windows. (right) Root mean square noise as a function of illuminated size of gold mirror for thermal and SR source (filled squares) at Indus-1; 0.45 GeV, 90 - 50 mA (in 950 - 1050 cm$^{-1}$), also shown are the reported values at Advanced Light Source at Berkeley; 2 GeV, 500 mA (in 2450 - 2500 cm$^{-1}$). Inset: corresponding signal to noise ratio.

metallic reflectivity measurements in broad spectral regions in order to estimate the optical properties and charge carrier density. In the mid infrared range, 600 - 4000 cm$^{-1}$, the use of these windows however results in a signal drop in the spectral profile which starts from ∼ 1800 and extends up to 2600 cm$^{-1}$ which is due to the interference from coating. In view of these effects, installation of new ZnSe windows with appropriate broad band coating so as to have a high signal in the complete infrared region is being considered, which may also require a re-alignment of the optics in successive operation and shut down periods.

In the final stage of coupling the beamline with spectrometer, a nearly collimated beam with reduced size, is directed along the path of the thermal FTIR source where further focusing and collimation takes place along various axes inside the instrument. The alignment is found to be critically dependent upon the incident angle of the beam at the interferometer entrance, as the SR beam has different focusing conditions along the two axes. The possible temporal fluctuations in the synchrotron beam and small spatial instability issues with varying electron beam current from high ($\sim$ 100 mA) to a low value ($\sim$ 30 mA) impose further constraints on the final alignment. Noise issues, infact, are inherent to the IR beamlines and have to be compensated after detailed performance assessment based on the corresponding ring parameters and appropriate considerations of the electronic noise from various nearby sources [243]. However, for utilizing the brilliance advantage of the synchrotron light, it is preferred to use the beamline at the highest current. Top-up mode operation of the storage ring can also be considered for maintaining a high and relatively constant signal to noise ratio.

At present, the major usage of the beamline has been aimed at mid IR microscopy, high pressure and low temperature studies, which can be extended to other areas based on user requirements. The 15X objective is best suited for high pressure experiments as it facilitates larger working distance (compared to 36X) required for mounting and aligning the Diamond Anvil cells (DAC) in the sample stage. The 15X objective, having lower numerical aperture than the 36X, also matches with the initial beamline collimating assembly of a pair of off-axis spherical mirrors (chapter 2), which compensates for aberrations in a similar way as in the Schwarzchild objectives with source located at a large focal length [244]. In the following subsection, we present the first in-situ high pressure results using DAC on an organic molecular solid, Acrylamide carried out using IR Synchrotron Radiation at Indus-1.

### 6.2.2 First Synchrotron based high pressure studies on the molecular soild Acrylamide

High pressure infrared (IR) studies of molecular crystals have gained tremendous interest because of its capability to provide unique information on proton dynamics and hydrogen bonding interactions. While many reports on various aspects of proton dynamics of O-H---O hydrogen bonds have been reported in recent times, inter and intra-molecular N-H---O hydrogen bonds are relatively less studied. These interactions are mostly displayed in amino acids and structures with amide bonds. Amide structures are best known for their hydrogen bonding abilities in protein structures. Acrylamide ($H_2C = CHCONH_2$), a well known pharmaceutical agent and a carcinogen in food products, is among the simple amides which is extensively used in industries (in making synthetic rubber, plastics and reagents) and biological procedures in both monomeric and polymeric forms. Thus, the polymerization of acrylamide has been a subject of interest and investigation using various techniques like X-ray irradiation, shear deformation, shock waves and chemical routes in the past [245–254]. Recently, the use of hydrostatic pressure to synthesize the polymeric form has gained particular attention as this methods enables to obtain a phase pure polymer just by tuning of chemical bonds, as no initiator or solvent is required. Note that pressure induced polymerization of Acrylamide is irreversible in nature [255].

#### 6.2.2.1 Pressure induced polymerization

At ambient conditions, solid Acrylamide forms N-H---O hydrogen bonded dimers in contrast to the dominant "trans" gaseous form. The strengths of the inter-dimer (N---O $\sim$ 2.84 $\AA$ and H---O $\sim$ 1.92 $\AA$) and intra-dimer (N---O $\sim$ 2.94 $\AA$ and H---O $\sim$ 1.98 $\AA$) hydrogen bonds are almost equal making it a nearly uniform three dimensional hydrogen bonded structure, as shown in the inset of Figure 6.22(right) [255]. The preliminary high pressure infrared studies up to 5 GPa showed that the monomeric form of acrylamide is polymerized after successive compression-decompression cycles [249]. More recently, Raman spectroscopic studies demonstrated the mechanism of pressure induced polymerization of Acrylamide which starts at 4 GPa and gets completed at 17 GPa. The systematic transformation towards a solid linear polymeric chain was inferred from the appearance of various new Raman modes in the deformation region, i.e. 300 -

1200 cm$^{-1}$ between 2.8 to 4 Ga [255]. But, the weak and broad $\nu_s$NH$_2$ (symmetric bond stretching) mode near 3200 cm$^{-1}$, which can give information on `N-H---O` hydrogen bonds, was found to soften up to 2.2 GPa and merges with the intense $\nu$CH$_2$ modes at this pressure. This was followed by the appearance of a weak mode at 3260 cm$^{-1}$ at 2.6 GPa which showed a blue shift at 2.8 GPa, beyond which it was not discernible.

Thus, the nature of `N-H---O` hydrogen bonds which stabilize the three dimensional structure of Acrylamide could not be probed across the transition at 4 GPa and in the polymerized state. This is because, unlike the C-H bond stretching vibrations, in general the relative intensity of O-H and N-H stretching Raman modes is very small in many amino acid crystals. However, relatively much stronger infrared absorption cross sections of $\nu$O-H and $\nu$N-H vibrational modes have led to some of the benchmark findings in molecular solids, for example hydrogen bond symmetrization, proton transfer in bio-geological systems and low barrier hydrogen bond formation in ammonia etc.

#### 6.2.2.2 High pressure IR investigations of Acrylamide

The high pressure infrared absorption spectra of Acrylamide are shown in Figure 6.22. The strong $\nu_s$NH$_2$ and $\nu_{as}$NH$_2$ (asymmetric stretch) IR modes, which are among the most prominent features to characterize this compound, can be distinctly noted near 3187 cm$^{-1}$ and 3352 cm$^{-1}$ respectively as recorded using IRSR at IR beamline in Indus-1, shown in Figure 6.22(right). The spectra were recorded at 4 cm$^{-1}$ resolution and a total of 60 scans were co-added in each case. The observed modes in the background corrected spectra were fitted using a Gaussian profile and the peak positions of the observed modes at ambient pressure are listed in Table 6.4, which are in excellent agreement with the earlier reported experimental and theoretical values [256]. Further, the high pressure beahviour of various modes was also compared with the corresponding Raman modes [255] to ascertain the mode assignments.

**Table 6.4:** Mode assignments of the observed IR active modes of Acrylamide. $\nu$- stretching, $\delta$- bending, $\rho$- rocking, $\omega$- wagging, sym- symmetric, asym- asymmetric, sci- scissoring.

| Frequency ($cm^{-1}$) | Assignment | Frequency ($cm^{-1}$) | Assignment |
|---|---|---|---|
| 3352 | $\nu_{asym}NH_2$ | 1282 | $\rho NH_2$ |
| 3187 | $\nu_{sym}NH_2$ | 1053 | $\rho CH_2$ |
| 2800-3150 | $\nu CH + \nu CH_2$ | 991 | $\omega NH_2$ |
| 1675 | $\nu C = O$ | 963 | $\omega CH_2$ |
| 1650 | $\nu C = C$ | 839 | $\delta CH$ |
| 1611 | $\nu CC$ | 816 | $\omega CH$ |
| 1582 | $\delta_{sci}NH_2$ | 708 | $tNH_2$ |
| 1430 | $\nu CN + \delta_{sci}CH_2$ | 660 | $tCH_2$ |
| 1359 | $\delta CH$ | 626 | $\rho CC$ |

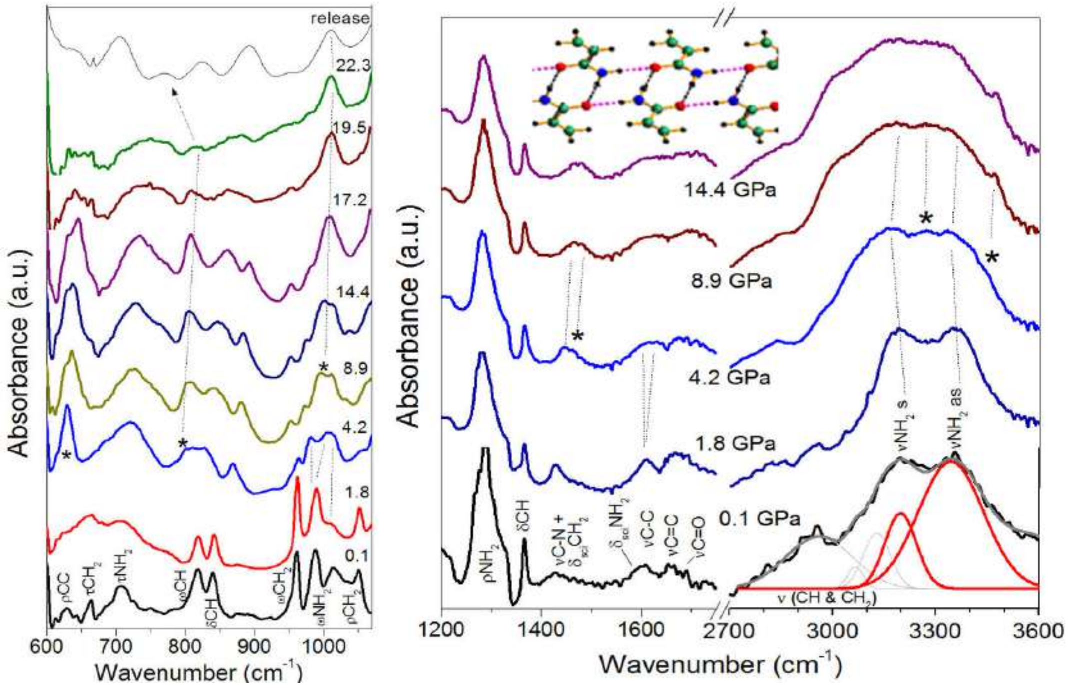

**Figure 6.22:** High Pressure infrared spectra of Acrylamide in the region (left) 600 - 1100 $cm^{-1}$; (right) 1200 - 1750 $cm^{-1}$ and 2700 - 3600 $cm^{-1}$. The mode assignments for various peaks have been reported in Table 6.4.

The high pressure IR spectra of Acrylamide in the deformation region 600 - 1700 $cm^{-1}$, shown in Figure 6.22(left), depict the appearance of various new peaks which correspond to the modes observed in poly-acrylamide [256], thus confirming the monomer to polymer transition under pressure. For example, the mode near 1430 $cm^{-1}$ splits into two modes near 1440 $cm^{-1}$ and 1468 $cm^{-1}$ above 4 GPa which correspond to the $\nu$C-N and $\delta$CH2 (deformation) modes of polyacrylamide (whose reported values are 1436 and 1465 $cm^{-1}$ respectively at ambient conditions). It is noted that in the case of polyacrylamide, the C-$NH_2$ wagging mode near 975 $cm^{-1}$, which is well split from the $NH_2$ wagging mode (991 $cm^{-1}$), is a characteristic feature which remains unchanged in all the polymeric forms like in solid polymers, aqueous solution or cross linked gel form. We observe a systematic transformation of the IR spectral profile in 950 - 1050 $cm^{-1}$ range to a dominant band which remains preserved even after the complete release of pressure. Infact, the infrared spectra on pressure release showed nearly all the spectral modifications observed in the high pressure phase suggesting an irreversible phase transformation in Acrylamide.

In addition, we could also probe the high pressure behavior of the N-O---O interactions in this compound by studying the vibrational features of N-H bonds. Figure 6.23 shows the pressure induced variations of the N-H stretching modes of Acrylamide. As seen in Figures 6.22(right) and Figures 6.23, both $\nu_s NH_2$ and $\nu_{as} NH_2$, initially show softening on compression, which is consistent with the earlier Raman studies [255]. With pressure, two new modes appear which could be distinctly identified at 3260 and 3385 $cm^{-1}$ near 4 GP. Above this pressure, a general trend of small stiffening is observed for all the modes except for the pressure region 9 - 17 GPa where peak positions are not much changed. These observations can be corroborated with the reported observations of pressure induced modifications in the structure with onset at 4 GPa accompanied with subtle changes across 8 GPa. The increase in broadening of $\nu NH_2$ modes to form a broad envelope at higher pressures, as observed from Figure 6.22(right) is also

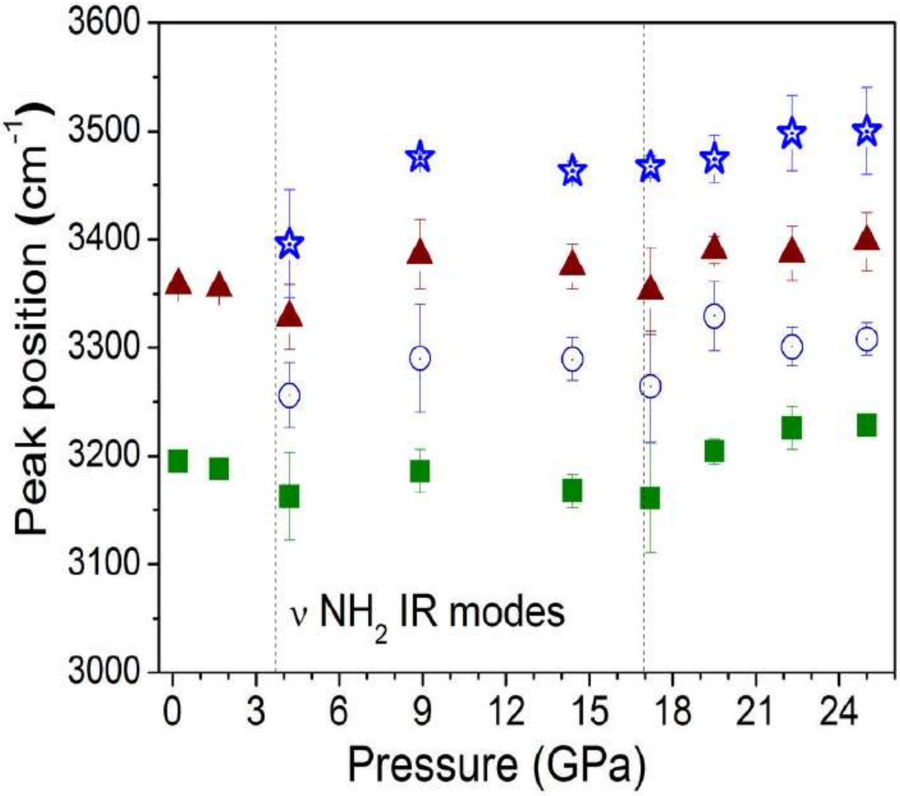

**Figure 6.23:** Frequency versus pressure plots of $NH_2$ stretching infrared modes Acrylamide.

consistent with the transformation to the polymeric form.

Thus, the changes observed in the present high pressure IR spectra of Acrylamide corroborate well with the reported Raman observations of pressure induced polymerization and reveal the mechanism of microstructural modifications accompanied with this phenomenon. The N-O---O hydrogen bonding interactions which bind the structure of this compound at ambient conditions were predicted to be broken and reformed during the transition as the weak $\nu$N-H Raman mode merged into other modes near 2.2 GPa and subsequently a weak mode appeared at a higher frequency. With a clear monitoring of $\nu$N-H modes, we now conclude that a subtle reorientation of N-O---O hydrogen bonds takes place across 4 GPa, but the two types of interactions, i.e. inter and intra dimeric linkages become diverse resulting in the emergence of new $\nu$N-H modes above 4 GPa, which continue to stiffen in the polymeric phase above 17 GPa.

These results are very useful to establish the role of external mechanical tunings (hydrostatic pressure) to synthesize novel polymeric materials without any chemical modification. It would be interesting to further probe the time evolution of IR and Raman spectral changes combined with simultaneous structural studies to monitor the dynamics of polymeric form in the high pressure phase and in the retrieved samples.

# 7

# Summary and Future Scope

To summarize, the present thesis has been aimed at understanding proton dynamics of strong hydrogen bonds under pressure, which are close to the symmetrization limit, in molecular solids of relevance to basic physics, materials chemistry and biology using infrared spectroscopy; and setting up of various state-of-the-art national experimental facilities for IR spectroscopic studies covering a wide scientific domain.

## 7.1 Proton dynamics of strong hydrogen bonds under pressure

The studies of strong hydrogen bonded molecular systems are important in the larger context of understanding proton dynamics in water, organic acids, minerals and biological systems in earth's interior as well as other celestial bodies where intermolecular interactions are governed by diverse chemical and thermodynamic environments. Hydrogen bonds play a decisive role in the structural stabilization of these materials. However, strong hydrogen bonds, close to the symmetrization limit, are particularly intriguing due to diverse proton dynamics across the potential barrier under compression. Because of this barrier, (1) symmetric hydrogen bonds with the proton localized at bond-centre and (2) proton transfer through the barrier are rare events, as Chandler says "dynamical bottlenecks". In the symmetrization limit ($d_{\mathrm{O{-}{-}{-}O}} < 2.4$ Å) of the O–H---O hydrogen bonds, many exotic phenomena of fundamental interest may occur, such as a unimodal symmetric well at bond centre, polymerization15 and structural distortion affecting spin cross-over.16 Crossing the potential barrier, i.e. proton transfer along the hydrogen bond is fundamental to a myriad of bio-geo-chemical processes in nature like enzymatic catalysis, signal transduction, acid-base reactions in water gossamers etc. In the third possibility of (3) hydrogen bond reorientation/ breaking and reformation under pressure, one would expect phase transition to different structures which may otherwise not be accessible under ambient conditions.

From the present studies, it is revealed that the complexes of glycine (the simplest amino acid) and oxalic acid (the simplest dicarboxylic acid) can serve as model systems for understanding hydrogen bonding networks; under pressure, this family of molecular systems has shown all the three possibilities mentioned above.

*Proton migration.* In oxalic acid dihydrate (OAD), we have demonstrated the proton transfer under pressure aiding a series of phase transformations, thus solving a century old problem. A systematic transition from neutral to doubly ionized oxalic acid and the formation of hydronium ion, which becomes a donor to three hydrogen bonds in the subsequent phases above 2 GPa, has been confirmed. As a result, there is a loss in the cooperativity of hydrogen bonds leading to another phase transition across 9 GPa. It is observed that, subsequent to transfer, the proton again moves in the reverse direction, strengthening the new hydrogen bond between the dominant $CO_2$ and $H_3O$ groups. These observations on proton dynamics are interesting from the view-point of two important fundamental problems. First the "transport mechanism of hydrated proton", crucial for molecular theories of ionic systems and interstellar research, and second, understanding "proton transfer pathways in protein environments", important to study protein-protein interactions and enzymatic catalysis. Indeed, the high pressure behaviour of hydronium ion, the simplest oxonium ion is of immense relevance in acid-base reactions and mineralogy. Investigations of the phenomenon of co-operative networks in molecular chains are important in the context of various biological specimens like polypeptide $\beta$-sheets and events like protein folding.

*Hydrogen bond symmetrization.* The evidences of pressure induced hydrogen bond symmetrization have been reported for the first time in a multi-component molecular solid, glycinium oxalate, at moderate pressures of 8 GPa. The signatures of the strongly damped soft mode have been traced well up to the far infrared regions in addition to the distinctive signatures of dynamical proton sharing between semioxalate units brought about by hopping across the barrier. This results in covalent like infinite oxalate chains forming rigid poles along the crystal $b$-axis. At pressures above 12 GPa, planar glycine sheets in the $ac$-plane are tied to two different oxalate poles through other moderately strong hydrogen bonds on both ends, forming a supramolecular assembly, like hammocks systematically distributed in the three dimensional continuum. Though hydrogen bond symmetrization under pressure has been investigated in molecular systems, in particular, binary systems, extensive knowledge on the proton dynamics is available only for the simplest system ice. The present results observed in glycinium oxalate, suggest that these oxalate complexes may serve as simple prototypes to study proton dynamics in a broader context of organic systems. Our reports of supramolecular structures formed through tuning of hydrogen bonds under pressure are also of relevance to organic linkages at extreme conditions and dynamic polymers with non covalent interactions in crystal engineering.

*Hydrogen bond reorientation.* In contrast to the above systems, the third complex of this family, i.e. Bis(glycinium)oxalate, undergoes a pressure induced structural phase transition across 1.6 GPa, triggered by a breaking and reformation of `O-H---O` and `N-H---O` hydrogen bonds. More importantly, upon phase transition at 1.6 GPa, the compound loses its centre of inversion symmetry, as confirmed by the emergence of Raman active modes in IR spectra and vice versa. Consequently, the high pressure dielectric studies, showing sharp peak at ∼1.6 GPa, have opened up the possibilities of finding a new ferroelectric material.

***Future Scope:*** One of the immediate projects which have been undertaken from the results obtained in this thesis is extensive investigations of the phase diagram of oxalic acid dihydrate to very high pressures in megabars and low temperatures up to 4.2 K in order to probe the possible strong linkage between the dominant $CO_2$ and $H_2O$ groups, which may be extremely useful to shed light on the assembly of simple molecules under extreme conditions.

Since ages, various anomalies in water ice have remained as the most mysterious and challenging problems to scientific community; ice melting and freezing under compression and decompression, hydrogen bond symmetrization under pressure being a few examples. An accurate description of force fields describing various interactions is still an open problem. Experimentally, while observing a perfectly sharp-unimodal symmetric state of hydrogen bond under pressure still remains a far-fetched proposition, the possibility of dynamically symmetric-hydrogen bond assisted supramolecular assembly through non-covalent interactions and ferroelectricity have opened up new avenues to look into glycine-oxalate complexes as potential candidates for technological applications.

While many amino acid and organic complexes possess strong hydrogen bonds, the high pressure investigations of these compounds are still limited. The simplest of these, glycine polymorphs and complexes, have shown varied high pressure response in different chemical environments, from subtle structural reorientations to drastic phase transitions. Systematic structural and spectroscopic studies of these compounds under varying thermodynamic conditions would be very useful to look for any systematic trend which can be exploited for predicting their structure and physico-chemical properties of large bio-molecules under varying environments.

## 7.2 Development of experimental facilities; an Infrared beamline at the Indian synchrotron

*Facilities.* During the course of this thesis, two comprehensive infrared laboratories have been developed. A Fourier transform Infrared microspectroscopy setup (primarily for condensed phase studies) has been commissioned at Indus-1, RRCAT, Indore, India. An infrared beamline (600 - 10000 cm$^{-1}$) has been designed, fabricated and installed at Indus-1 synchrotron (0.45 GeV) which is coupled to the above spectrometer. In addition, a lab based high resolution (0.0012 cm$^{-1}$) FTS system for Far-IR to UV range (10 - 45000 cm$^{-1}$) and a FT-Raman spectrometer (with 1064 nm Nd:YAG laser excitation for 60 - 3800 cm$^{-1}$) have been commissioned at BARC, Mumbai, India. Many auxillary developments required for various studies have also been carried out in both these labs. Various kinds of gas absorption cells for rotationally resolved vibrational spectroscopy in different spectral ranges and temperature conditions, which also includes an indigenously developed long optical path length cell (max. 60 m), optical setup for atomic emission studies from highly excited states of isotopes and radicals, which includes the studies of hyperfine structure, have been developed. For condensed phase studies, in addition to the conventional facilities, in-situ high pressure and in-situ low temperature (500 - 4.2 K) techniques have been successfully setup and studies have been initiated. Various national users have already started submitting proposals to use these facilities and many experiments have been conducted.

*Synchrotron IR beamline.* In the present thesis, in particular, complete details of development of the infrared beamline facility, which also includes detailed beam propagation simulations, have been presented. In chapter 6, we have presented various studies on different systems to demonstrate the capabilities, which however are not exhaustive, that were carried out during successive installation stages of the beamline. The usage of the facility can be broadly classified in three modes which are absorption studies to probe vibrational structure and phonons giving information about the microscopic structure, reflectivity studies to investigate optical properties in the infrared regions and microscopy studies for chemical imaging and spectroscopy of specimens with dimensions of the order of a few microns for example in high pressure studies. The first absorption studies, carried out on Sr- and Ca- doped nanocrystalline $LaCrO_3$ SOFC interconnect materials, which have simple and clearly distinct vibrational spectra to study stretching/ bending/ external modes, showed a novel mechanism, i.e. liquid state assisted sintering, of rearrangement in microscopic structure when calcined to high temperatures up to 1200°C. The reflectivity studies on a cuprate superconductor, $Ru_{0.9}Sr_2GdCu_{2.1}O_8$ indicate that the charge carriers may become more energetic upon compression up to a pressure of 1.5 GPa, as revealed by the red shift of the polaronic band and increase in low frequency reflectivity. The first performance results of the beamline along with synchrotron high pressure studies on pressure induced polymerization of Acrylamide, a model amide system, have also been presented and comparison of the source with other international facilities has been elucidated.

***Future Scope:*** The infrared beamline developed at Indus-1 synchrotron source, primarily for microspectroscopy, is the first IR beamline in the Indian subcontinent. While various efforts have been initiated to further improve the performance like signal to noise ratio, beam stability etc., it has been planned to extend the capabilities to far infrared regions and exploit the possibilities of time resolved measurements in pump-probe experiments. This development is well complemented by the setting up of a high resolution (0.0012 $cm^{-1}$) FTS lab from far-IR to UV, which can be used to study rotationally resolved vibrational spectra of various environmentally important molecules, atomic emission lines of various isotopes, transient species and radicals etc.

The availability of the above facilities opens up several opportunities in the front-line fields of condensed matter physics, viz. multiferroics, superconductivity, magnetism, semiconductors, topological insulators, metal to insulator transition etc. While it would be interesting, though extremely challenging, to study the novel high pressure behaviours like metallicity, superconductivity, quantum liquid state etc. in simple Vander waals molecular solids like hydrogen, studies on hydrogen rich compounds like silanes would be useful in predicting the properties of the celebrated metallic phase of solid hydrogen. Systematic microstructural studies of potential ferroelectric materials with perovskite, $ABO_2$ and $ABO_4$ structures and also organic molecular solids would be useful to establish a general rule for the role of pressure or temperature in inducing a spontaneous polarization in such systems. A thrust area in geophysics is the studies of hydrogen bonds in hydrous minerals and silicates in earths crust (pressure increases up to 360 GPa from surface to the centre of the earth), which are known for water transportation from surface into the deep mantle and are the major source of water in subducting slabs. The hydrogen bond strength in these hydroxyl materials range from weak to very strong and the possible existence of a symmetric hydrogen bond at high pressures is a debated issue in some of these oxyhydroxide minerals.

While it is envisaged to cater various experimental requirements in condensed matter physics, a key area of research which can now be initiated at our facility, given the scientific and technological infrastructure resulted from this thesis, is the microscopic studies on intermolecular interactions in biological systems and the study of proton transfer pathways and associated structural reorientations in biological reactions like enzymatic catalysis, protein folding, DNA recombination, photosynthesis of plants or in water gossamers, i.e. the subject of proton dynamics which is of paramount importance for the living world.

Since science research took off millions of generations ago with thrust on water, air and organic systems (food), we channelized knowledge, gained from information, into different science streams. Albert Einstein, on the subject of interdisciplinary science and human relationships once quoted "How on earth are you ever going to explain in terms of chemistry and physics so important a biological phenomenon as first love?" Now, we stand on a day where the boundaries between the physics, chemistry, biology, geology, astronomy and mathematics are again diminishing and channelized information is required from each other to solve the yet unanswered quests. The study of proton dynamics of bio-geological systems under varying thermodynamic and chemical conditions; and the use of large scale modern day facilities like synchrotrons might be the examples of the way forward.

# Appendix A

# Vibrational mode couplings and intensity

## A.1 Fermi resonance

Fermi had proposed a resonance effect to explain the doublet structure of $CO_2$ stretching vibration near 1300 $cm^{-1}$, stating that the complex vibrational structure may arise due to the mixing of wavefunctions of different vibrations, which are coupled via the anharmonic coupling strength W.
When a fundamental vibrational frequency is close to some other transition frequency for example that of an overtone or a combination band, they interact by the anharmonic part of the Hamiltonian by Fermi resonance. Important requirements for this effect are:

1. The frequencies must be close (typically within 30 $cm^{-1}$).
2. The two vibrations must have the same symmetry (as obtained from group theory).
3. There must be some mechnism (spatially) for the interaction. For example the vibrations can not be located in different parts of the molecule.

# APPENDIX A. VIBRATIONAL MODE COUPLINGS AND INTENSITY

In $CO_2$, a linear molecule with 3 non-degenerate vibrational modes, during the bending vibrational motion the oxygen atoms are pushed a little apart everytime the carbon atom passes through the equilibrium. This is twice for each bending cycle. Twice the bending frequency is close to the symmetric stretching frequency and therefore the overtone of bending and the fundamental of symmetric stretching mode interact through Fermi resonance.
The implications of Fermi resonance in spectra are [257]:

1. Frequency shifts through borrowing of intensity by one mode at the expense of other and mixing of wavefunctions with corresponding changes in IR and Raman activities. The higher frequency may show a blue shift and lower frequency a red shift.

2. Overtones may be unexpectedly intense and two strong bands may be observed when only one is expected.

3. Even a small change in the separation of zero-order frequencies results in large effect on the mixing. The separation may be altered by:

    (a) changing the physical state of solvents

    (b) deuteration

    (c) applying thermodynamic variables

The frequencies of perturbed vibrations, from first-order perturbation theory are given by,

$$\omega_{\pm} = \frac{1}{2}(\omega_1 + \omega_2) \pm \frac{1}{2}\sqrt{(\omega_1 - \omega_2)^2 + 4W^2} \tag{A.1}$$

where $\omega_1$ and $\omega_2$ are unperturbed fundamentals. W = coupling constant $\sim \frac{1}{2}KQ_1Q_2^2$ , $Q_1$ and $Q_2$ are normal coordinates of the vibrations. K is the anharmonicity constant and contains both intramolecular and intermolecular contributions.

If $\omega_1$ is a fundamental, most often $\omega_2$ is an overtone of another fundamental or a combination band. However, interactions due to different mechanisms is also possible between two fundamentals themselves in condensed phase systems. There have also been instances of couplings through anharmonic interactions between optical phonon modes with acoustic phonons [258,259], coupled plasmon-phonon modes [260, 261], polaritons [262] and dielectric phonon modes [263–265] in semiconductors etc.

For these coupled modes, the frequencies are squared in equation A.1. If the corresponding fundamentals are of Bose character, i.e. operators in the calculations can be expressed in terms of Bose creation and annihilation operators which follow commutation relations [266],

$$\omega_{\pm}^2 = \frac{1}{2}(\omega_1^2 + \omega_2^2) \pm \frac{1}{2}\sqrt{(\omega_1 - \omega_2)^2 + 4b^2} \tag{A.2}$$

where $b= \frac{k}{\sqrt{2\omega_2}}$ , or, $2W\sqrt{2\omega_1\omega_2}$, i.e. $b$ is a function of anharmonicity and treated as an empirical parameter.

These equations can be used to get information on the actual anharmonicity constant k. The anharmonic coupling constant contains both inter- and intra-molecular contributions, where inter-molecular part is generally smaller and neglected.

Further, it has been shown that for weak Fermi resonance, the anaharmonic coupling strength changes only the shape of two phonon continuum, whereas for strong Fermi resonance, bound states $\nu^+$ and $\nu^-$ may even split out of the two phonon continuum. The inter-molecular interactions pose significant contributions under the application of high pressure which modifies various parameters and coordinates, severely affecting the vibrational spectra [10, 131, 267, 268].

## A.2 Intensity of overtones/combination modes

Bohr- Sommerfeld- Einstein- Keller quantum condition (bound state semiclassical method) for coupled harmonic polyatomic (including non-linear molecules) systems is,

$$\oint_{C_i} \sum \vec{p}.d\vec{q} = (n_i + \delta_i)h \qquad (i = 1, ...., M) \tag{A.3}$$

$\vec{p}$ and $\vec{q}$ are 2M conjugate momenta and coordinates.

$n_i$ = quantum no.

$C_i$ = M topologically independent paths

$\delta_i$ = known constants

Classical spectral intensity, I, given by the fourier transform of autocorrelation function:

$$I = \frac{1}{2\pi} \int_{-\infty}^{\infty} < \mu(0), \mu(t) > e^{iwt} dt \tag{A.4}$$

or,

$$I = \sum_m | < m|\mu|n > |^2 \delta(\omega - \omega_{mn}) \tag{A.5}$$

Quntaum mechanically, the Hamiltonian for Morse oscillator is given by,

$$H = \frac{P^2}{2\mu} + D(1 - e^{-a(r-r_c)})^2 \tag{A.6}$$

The solutions are given by,

$$\psi_n(x) = N_n e^{-z/2} z^{b/2} L_n^b(z) \tag{A.7}$$

where, $N_n = [\frac{abn!}{\Gamma(k-n)}]^{1/2}$ ; $z = ke^{-a(r-r_e)}$; $b = k - 2n - 1$; $L_n$ are Laguerre polynomial.

$$k = 1/\chi_e = \frac{2\mu\omega_e}{\hbar a^2} \tag{A.8}$$

$$\omega_e = a\left(\frac{2D}{\mu}\right)^{1/2} \tag{A.9}$$

$\omega_e$ = angular frequency ; $\omega_e\chi_e$ = anharmonicity constant

Let

$$b' = k - 2m - 1 \tag{A.10}$$

for m $\neq$ n, $\mu_{mn} =< m|\mu|n > \; =< m|(r - r_e)|n >$ (if $\mu$ is constant plus $(r - r_e)$),

$$\mu_{mn} = \frac{N_m N_n}{a}\int_0^{ke^{ar_e}} e^{-z} z^{(\frac{b}{2}+\frac{b'}{2}-1)} a^{-1} ln(k/z) L_m^{b'}(z) L_n^{b}(z) dz \tag{A.11}$$

After solving one can obtain (for $m > n$),

$$\mu_{mn} = \frac{(-1)^{m-n+1}}{a(m-n)(k-m-n-1)}\left(\frac{m!}{n!}\;\frac{\Gamma(k-m)}{\Gamma(k-n)}bb'\right)^{1/2} \tag{A.12}$$

This can be put in equation A.5. In principle the problem reduces to calculating $|\mu_{mn}|^2$, i.e. square of dipole moment function. The problem can be approached through various routes of quantum mechanical, classical or semi-classical methods to compare the calculated intensities with the observed ones. Calculations have shown that the theoretical $|\mu_{mn}|^2$ are, particularly for overtones, sensitive to the assumed dipole moment function and to the assumed anharmonic potential.

Estimation of intensities of overtones is simpler in the one dimensional problem, but difficult otherwise and a high accuracy of wavefunction is required for computing matrix elements. For example, the application of equation A.12 to find the intensities of spectral lines in HF molecule shows that:

for D = 5.716 eV, $r_e = 1.75a_0$ and a = $1.22a_0^{-1}$, where $a_0$ is Bohr radius, calculated by a Morse fit to an *ab*-intio calculation [269] with $\omega_e$ and $\omega_e\chi_e$ determined within 1% accuracy with experimental values, the quantum intensity for various transitions is given by,

| Transition m→ n | Quantum Intensity $\|\mu_{mn}\|^2$ |
|---|---|
| 0→ 1 | $5.4 \times 10^{-2}$ |
| 0→ 2 | $6.1 \times 10^{-4}$ |
| 0→ 3 | $1.7 \times 10^{-5}$ |
| 0→ 4 | $8.6 \times 10^{-7}$ |

Similarly, the intensity of overtones of non-rotating OCS molecule, a well studied model system in spectroscopy for which all fundamentals, overtones and combination bands are IR active, as calculated by semi classical approach yielded the results [270] presented in the following table:

| Mode | Transition m→ n | Quantum Intensity $\|\mu_{mn}\|^2$ | $\bar{\nu}$ cm$^{-1}$ |
|---|---|---|---|
| $\nu_1$ | 0→ 1 | 1.0 | 861.4 |
| Symmetric | 0→ 2 | $9.4 \times 10^{-2}$ | 1715.4 |
| stretching | 0→ 3 | $2.0 \times 10^{-3}$ | 2561.4 |
| | 0→ 4 | $1.1 \times 10^{-4}$ | 3400.2 |
| | 0→ 5 | $3.1 \times 10^{-6}$ | 4231.6 |
| $\nu_3$ | 0→ 1 | 1.0 | 2064.0 |
| Asymmetric | 0→ 2 | $5.7 \times 10^{-4}$ | 4104.7 |
| stretching | 0→ 3 | $2.8 \times 10^{-6}$ | 6126.5 |
| | 0→ 4 | $7.6 \times 10^{-8}$ | 8124.6 |
| $\nu_1 + \nu_3$ | 0→ 1 | 1.0 | 2922.6 |
| Combination | 0→ 2 | $2.3 \times 10^{-4}$ | 5769.9 |

Here, intensities are normalised with respect to the 0→1 transition. 0→1 intensities for $\nu_1$ and $\nu_1 + \nu_3$ bands are 0.034 and 0.010 times $\nu_3$ band respectively. The absolute value of $|\mu_{mn}|^2$ for 0→1 transition of $\nu_1$ band is $4.0 \times 10^{-3}$ D$^2$.

# References

[1] M. Choukroun and O. Grasset. “Thermodynamic model for water and high-pressure ices up to 2.2 GPa and down to the metastable domain”. *Journal of Chemical Physics*, **127**(12), 124506–124506 (2007).

[2] A. N. Dunaeva, D. V. Antsyshkin, and O. L. Kuskov. “Phase diagram of $H_2O$: Thermodynamic functions of the phase transitions of high-pressure ices”. *Solar System Research*, **44**, 202–222 (2010).

[3] M. Cogoni, B. D’Aguanno, L. N. Kuleshova, et al. “A powerful computational crystallography method to study ice polymorphism”. *Journal of Chemical Physics*, **134**(20), 204506–204506 (2011).

[4] A. F. Goncharov, M. R. Manaa, J. M. Zaug, et al. “Polymerization of Formic Acid under High Pressure”. *Physical Review Letters*, **94**(6), 065505 (2005).

[5] N. Casati, P. Macchi, and A. Sironi. “Hydrogen migration in oxalic acid dihydrate at high pressure?” *Chem. Commun.*, pp. 2679–2681 (2009).

[6] J. Teixeira. “High-pressure physics - The double identity of ice”. *Nature*, **392**, 232–233 (1998).

[7] Y. Huang, X. Zhang, Z. Maa, et al. “Hydrogen-bond relaxation dynamics: Resolving mysteries of water ice”. *Coordination Chemistry Reviews*, **285**, 109 – 165 (2015).

[8] G. Jeffrey. “An Introduction to Hydrogen Bonding.” *New York: Oxford University Press* (1997).

[9] M. Benoit, D. Marx, and M. Parrinello. “Tunnelling and zero-point motion in high-pressure ice”. *Nature*, **392**, 258–261 (1998).

[10] V. V. Struzhkin, A. F. Goncharov, R. J. Hemley, et al. “Cascading Fermi Resonances and the Soft Mode in Dense Ice”. *Physical Review Letters*, **78**, 4446–4449 (1997).

[11] S. K. Grabowski. *Hydrogen BondingNew Insights* (Springer, Springer (The Netherlands), 2006).

[12] S. K. Sikka and S. M. Sharma. “The hydrogen bond under pressure”. *Phase Transitions*, **81**(10), 907–934 (2008).

[13] K. Nakamoto, M. Margoshes, and R. E. Rundle. “Stretching Frequencies as a Function of Distances in Hydrogen Bonds”. *Journal of the American Chemical Society*, **77**(24), 6480–6486 (1955).

[14] L. Sobczyk. “Quasi-Symmetric O-H–N Hydrogen Bonds in Solid State”. *Mol. Phys. Rep*, **14**, 19–31 (1996).

[15] E. Wigner and H. B. Huntington. “On the Possibility of a Metallic Modification of Hydrogen”. *Journal of Chemical Physics*, **3**, 764–770 (1935).

[16] N. W. Ashcroft. "Metallic Hydrogen: A High-Temperature Superconductor?" *Physical Review Letters*, **21**, 1748–1749 (1968).

[17] L. F. Lundegaard, G. Weck, M. I. McMahon, et al. "Observation of an $O_8$ molecular lattice in the $\epsilon$ phase of solid oxygen". *Nature*, **443**, 201–204 (2006).

[18] B. Militzer and R. J. Hemley. "Crystallography: Solid oxygen takes shape". *Nature*, **443**, 150–151 (2006).

[19] H. Katzke and P. Tolédano. "Theory of the mechanisms of pressure-induced phase transitions in oxygen". *Physical Review B*, **79**(14), 140101 (2009).

[20] S. Desgreniers, S. K. Vohra, and A. L. Ruoff. "Optical response of very high density solid oxygen to 132 GPa". *The Journal of Physical Chemistry*, **94**(3), 1117–1122 (1990).

[21] K. Shimizu, K. Suhara, M. Ikumo, et al. "Superconductivity in oxygen". *Nature*, **393**, 767–769 (1998).

[22] L. Craco, M. S. Laad, and S. Leoni. "Microscopic description of insulator-metal transition in high-pressure oxygen". *ArXiv e-prints* (2016).

[23] Y. Ma, A. R. Oganov, Z. Li, et al. "Novel High Pressure Structures of Polymeric Nitrogen". *Phys. Rev. Lett.*, **102**, 065501 (2009).

[24] M. I. Eremets, A. G. Gavriliuk, I. A. Trojan, et al. "Single-bonded cubic form of nitrogen". *Nature Materials*, **3**, 558–563 (2004).

[25] M. I. Eremets, A. G. Gavriliuk, and I. A. Trojan. "Single-crystalline polymeric nitrogen". *Applied Physics Letters*, **90**(17), 171904 (2007).

[26] I. Errea, M. Calandra, C. J. Pickard, et al. "Quantum hydrogen-bond symmetrization in the superconducting hydrogen sulfide system". *Nature*, **532**, 81–84 (2016).

[27] P. V. Hobbs. *Ice physics* (Oxford: Clarendon Press, 1974, 1974).

[28] R. J. Nelmes, J. S. Loveday, R. M. Wilson, et al. "Neutron diffraction study of the structure of deuterated ice VIII to 10 GPa". *Physical Review Letters*, **71**, 1192–1195 (1993).

[29] W. B. Holzapfel. "On the Symmetry of the Hydrogen Bonds in Ice VII". *Journal of Chemical Physics*, **56**, 712–715 (1972).

[30] M. Bernasconi, P. L. Silvestrelli, and M. Parrinello. "Ab Initio Infrared Absorption Study of the Hydrogen-Bond Symmetrization in Ice". *Physical Review Letters*, **81**, 1235–1238 (1998).

[31] C. Q. Sun, X. Zhang, and W. Zheng. "The hidden force opposing ice compression". *Chem. Sci.*, **3**, 1455–1460 (2012).

[32] J. Ellder, P. Friberg, A. Hjalmarson, et al. "On methyl formate, methane, and deuterated ammonia in Orion A". *Astrophysical Journal*, **242**, L93–L97 (1980).

[33] W. M. Irvine, P. Friberg, N. Kaifu, et al. "Observations of some oxygen-containing and sulfur-containing organic molecules in cold dark clouds". *Astrophysical Journal*, **342**, 871–875 (1989).

[34] D. R. Allan and S. J. Clark. "Impeded Dimer Formation in the High-Pressure Crystal Structure of Formic Acid". *Physical Review Letters*, **82**, 3464–3467 (1999).

[35] V. Mohaček-Grošev, J. Grdadolnik, J. Stare, et al. “Identification of hydrogen bond modes in polarized Raman spectra of single crystals of $\alpha$-oxalic acid dihydrate”. *Journal of Raman Spectroscopy*, **40**(11), 1605–1614 (2009).

[36] M. R. Manaa, N. Goldman, and L. E. Fried. “New phases of hydrogen-bonded systems at extreme conditions”. *Phase Transitions*, **80**(10-12), 1073–1084 (2007).

[37] A. Aubrey, H. J. Cleaves, J. H. Chalmers, et al. “Sulfate Minerals and Organic Compounds on Mars”. *Geology*, **34(5)**, 357–360 (2006).

[38] M. P. Bernstein, J. P. Dworkin, S. A. Sandford, et al. “Racemic amino acids from the ultraviolet photolysis of interstellar ice analogues”. *Nature*, **416**, 401–403 (2002).

[39] A. Brack and T. C. Pillinger. “Life on Mars: chemical arguments and clues from Martian meteorites”. *Extremophiles*, **2**(3), 313–319 (1998).

[40] P. A. Gerakines and R. L. Hudson. “Glycine’s Radiolytic Destruction in Ices: Firstin situLaboratory Measurements for Mars”. *Astrobiology*, **13**, 647–655 (2013).

[41] A. Sharma, J. H. Scott, G. D. Cody, et al. “Microbial Activity at Gigapascal Pressures”. *Science*, **295**, 1514–1517 (2002).

[42] T. Otake, T. Taniguchi, Y. Furukawa, et al. “Stability of Amino Acids and Their Oligomerization Under High-Pressure Conditions: Implications for Prebiotic Chemistry”. *Astrobiology*, **11**, 799–813 (2011).

[43] A. Witze. “Vibrant Pluto stuns scientists”. *Nature*, **523**, 389–390 (2015).

[44] B. Maté, Y. Rodriguez-Lazcano, Ó. Gálvez, et al. “An infrared study of solid glycine in environments of astrophysical relevance”. *Physical Chemistry Chemical Physics (Incorporating Faraday Transactions)*, **13**, 12268 (2011).

[45] G. M. Muñoz Caro, U. J. Meierhenrich, W. A. Schutte, et al. “Amino acids from ultraviolet irradiation of interstellar ice analogues”. *Nature*, **416**, 403–406 (2002).

[46] Y.-J. Kuan, S. B. Charnley, H.-C. Huang, et al. “Interstellar Glycine”. *Astrophysical Journal*, **593**, 848–867 (2003).

[47] R. E. Marsh. “A refinement of the crystal structure of glycine”. *Acta Crystallographica*, **11**(9), 654–663 (1958).

[48] Y. Iitaka. “The crystal structure of $\beta$-glycine”. *Acta Crystallographica*, **13**(1), 35–45 (1960).

[49] Y. Iitaka. “The crystal structure of $\gamma$-glycine”. *Acta Crystallographica*, **11**(3), 225–226 (1958).

[50] C. Murli, S. M. Sharma, S. Karmakar, et al. “$\alpha$-Glycine under high pressures: a Raman scattering study”. *Physica B Condensed Matter*, **339**, 23–30 (2003).

[51] S. V. Goryainov, E. V. Boldyreva, and E. N. Kolesnik. “Raman observation of a new ($\zeta$) polymorph of glycine?” *Chemical Physics Letters*, **419**, 496–500 (2006).

[52] S. V. Goryainov, E. N. Kolesnik, and E. V. Boldyreva. “A reversible pressure-induced phase transition in $\beta$-glycine at 0.76 GPa”. *Physica B Condensed Matter*, **357**, 340–347 (2005).

[53] V. Winterfeldt, G. Schaack, and A. Kloopperpieper. “Temperature behaviour of optical phonons near Tc in triglycine sulphate and triglycine selenate”. *Ferroelectrics*, **15**(1), 21–34 (1977).

[54] L. Santra, A. L. Verma, P. K. Bajpai, et al. "Raman spectroscopic study of alanine doped triglycine sulphate ferroelectric single crystals". *Journal of Physics and Chemistry of Solids*, **55**(5), 405 – 411 (1994).

[55] R. R. Choudhury, H. K. Poswal, R. Chitra, et al. "Pressure induced structural phase transition in triglycine sulfate and triglycine selenate". *Journal of Chemical Physics*, **127**(15), 154712–154712 (2007).

[56] A. K. Mishra, C. Murli, A. K. Verma, et al. "Conformation and Hydrogen-Bond-Assisted Polymerization in Glycine Lithium Sulfate at High Pressures". *The Journal of Physical Chemistry A*, **117**(28), 5734–5741 (2013).

[57] J. K. M. Rao and M. A. Viswamitra. "Crystal structure of glycine silver(I) nitrate". *Acta Crystallographica Section B*, **28**(5), 1484–1496 (1972).

[58] A. V. R. Warrier and P. S. Narayanan. "Infrared absorption spectra of single crystals of glycine silver nitrate and monoglycine nitrate". *Proceedings of the Indian Academy of Sciences - Section A*, **66**(1), 46–54 (1967).

[59] K. R. K. Easwaran. "Proton Magnetic Resonance Study of Glycine-$AgNO_3$". *Journal of the Physical Society of Japan*, **21**, 1614 (1966).

[60] R. R. Choudhury, L. Panicker, R. Chitra, et al. "Structural phase transition in ferroelectric glycine silver nitrate". *Solid State Communications*, **145**, 407–412 (2008).

[61] R. Chitra, R. R. Choudhury, F. Capet, et al. "Effect of deuteration: A new isotopic polymorph of glycine silver nitrate". *Journal of Molecular Structure*, **1049**, 27–35 (2013).

[62] E. A. Losev, M. A. Mikhailenko, A. F. Achkasov, et al. "The effect of carboxylic acids on glycine polymorphism, salt and co-crystal formation. A comparison of different crystallisation techniques". *New J. Chem.*, **37**, 1973–1981 (2013).

[63] N. A. Tumanov, E. V. Boldyreva, and N. E. Shikina. "Two new structures in the glycine–oxalic acid system". *Acta Crystallographica Section C*, **66**(6), o279–o283 (2010).

[64] R. Chitra and R. R. Choudhury. "Investigation of hydrogen-bond network in bis(glycinium) oxalate using single-crystal neutron diffraction and spectroscopic studies". *Acta Crystallographica Section B*, **63**(3), 497–504 (2007).

[65] M. S. Nandhini, R. V. Krishnakumar, and S. Natarajan. "dl-Alanine". *Acta Crystallographica Section C*, **57**(5), 614–615 (2001).

[66] D. Sajan, J. Binoy, B. Pradeep, et al. "NIR-FT Raman and infrared spectra and ab initio computations of glycinium oxalate". *Spectrochimica Acta Part A: Molecular Spectroscopy*, **60**, 173–180 (2004).

[67] G. Herzberg. *Molecular spectra and molecular structure. Vol.2: Infrared and Raman spectra of polyatomic molecules* (D. Van Nostrand Company; 16th Printing edition,, 1945).

[68] J. M. Chalmers and P. R. e. Griffiths. *Handbook of Vibrational Spectroscopy, ISBN: 978-0-471-98847-2* (Wiley, 2002).

[69] H. Poulet and J. P. Mathieu. *Vibration Spectra and Symmetry of Crystals, ISBN 0 67730180 4* (Gordon and Breach, Science Publishers Inc., New York, 1976).

[70] G. Turrell. *Infrared and Raman Spectra of Crystals, ISBN 0-12-705050-7* (Academic Press Inc. (London) Ltd., 1972).

[71] F. Wooten. *Optical Properties of Solids, ISBN 978-1483207339* (Academic Press, 1972).

[72] W. D. Duncan and G. P. Williams. “Infrared synchrotron radiation from electron storage rings”. *Applied Optics*, **22**, 2914–2923 (1983).

[73] G. Margaritondo. *Introduction to Synchrotron Radiation, ISBN 978-0195045246* (Oxford University Press, 1988).

[74] P. Duke. *Synchrotron Radiation: Production and Properties, ISBN 978-0199559091* (Oxford University Press, 2009).

[75] S. S. Ramamurthi and G. Singh. “Status of the INDUS-1 SR source”. *Nuclear Instruments and Methods in Physics Research A*, **359**, 15–20 (1995).

[76] D. D. Bhawalkar. “Indias first synchrotron radiation source Indus-1:A historical perspective”. *Current Science*, **82(3)**, 279–282 (2002).

[77] D. Angal-Kalinin, A. Banerji, P. R. Hannurkar, et al. “Synchrotron radiation source Indus-1”. *Current Science*, **82(3)**, 283–290 (2002).

[78] O. Chubar and P. Elleaume. “ Accurate and efficient computation of synchrotron radiation in the near field region ”. p. 1177 (1998).

[79] F. A. Polack, R. Mercier, L. Nahon, et al. “Optical design and performance of the IR microscope beamline at SUPERACO-France”. vol. 3775 of *Proc. SPIE*, pp. 13–21 (1999).

[80] H. Vora, S. Nakhe, K. Sarangpani, et al. “PROMISE, a software package for PROfile Measurement of image Size & Edge enhancement”. Tech. Rep. CAT Report, CAT/95-10, RRCAT, Indore, India (1996).

[81] P. R. Griffiths and J. A. de Haseth. *Fourier Transform Infrared Spectrometry, Second Edition* (John Wiley & amp, 2007).

[82] R. J. Bell. *Introductory Fourier transform spectroscopy* (London: Academic Press, 1972, 1972).

[83] J. W. Cooley and J. W. Tukey. “An Algorithm for the Machine Calculation of Complex Fourier Series”. *Mathematics of Computation*, **19**(90), 297–301 (1965).

[84] J. D. Barnett, S. Block, and G. J. Piermarini. “An Optical Fluorescence System for Quantitative Pressure Measurement in the Diamond-Anvil Cell” (1972).

[85] G. J. Piermarini and S. Block. “Ultrahigh pressure diamond-anvil cell and several semiconductor phase transition pressures in relation to the fixed point pressure scale”. *Review of Scientific Instruments*, **46**, 973–979 (1975).

[86] D. L. Decker. “High-Pressure Equation of State for NaCl, KCl, and CsCl”. *Journal of Applied Physics*, **42**, 3239–3244 (1971).

[87] S. J. Duclos, Y. K. Vohra, and A. L. Ruoff. “Pressure dependence of the $^4T_2$ and $^4T_1$ absorption bands of ruby to 35 GPa”. *Physical Review B*, **41**, 5372–5381 (1990).

[88] H. K. Mao, J. Xu, and P. M. Bell. “Calibration of the ruby pressure gauge to 800 kbar under quasi-hydrostatic conditions”. *J. Geophys. Research: Solid Earth*, **91**, 4673–4676 (1986).

[89] S. M. Sharma and Y. M. Gupta. “Theoretical analysis of R-line shifts of ruby subjected to different deformation conditions”. *Physical Review B*, **43**, 879–893 (1991).

[90] G. J. Piermarini, S. Block, J. D. Barnett, et al. “Calibration of the pressure dependence of the $R_1$ ruby fluorescence line to 195 kbar”. *Journal of Applied Physics*, **46**, 2774–2780 (1975).

[91] A. Dewaele, P. Loubeyre, and M. Mezouar. "Equations of state of six metals above 94 GPa". *Physical Review B*, **70**(9), 094112 (2004).

[92] J. Stare and D. Hadži. "Cooperativity Assisted Shortening of Hydrogen Bonds in Crystalline Oxalic Acid Dihydrate: DFT and NBO Model Studies". *J Chem Theory Comput.*, **10**(4), 1817–1823 (2014).

[93] R. Brill, C. Hermann, and C. Peters. "Röntgenographische Fouriersynthese von Oxalsäure-Dihydrat". *Annalen der Physik*, **434**, 357–377 (1943).

[94] J. D. Dunitz and J. M. Robertson. "36. The crystal and molecular structure of certain dicarboxylic acids. Part I. Oxalic acid dihydrate". *J. Chem. Soc.*, pp. 142–148 (1947).

[95] J. M. Robertson and A. R. Ubbelohde. "Structure and Thermal Properties Associated with Some Hydrogen Bonds in Crystals. I. The Isotope Effect". *Proc. R. Soc. London, Ser. A*, **170** (1939).

[96] J. M. Robertson and I. Woodward. "404. The structure of the carboxyl group. A quantitative investigation of oxalic acid dihydrate by Fourier synthesis from the X-ray crystal data". *J. Chem. Soc.*, pp. 1817–1824 (1936).

[97] F. R. Ahmed and D. W. J. Cruickshank. "A refinement of the crystal structure analyses of oxalic acid dihydrate". *Acta Crystallographica*, **6**(5), 385–392 (1953).

[98] P. Coppens and T. M. Sabine. "Neutron diffraction study of hydrogen bonding and thermal motion in deuterated $\alpha$ and $\beta$ oxalic acid dihydrate". *Acta Crystallographica Section B*, **25**(12), 2442–2451 (1969).

[99] A. Lehmann, P. Luger, C. W. Lehmann, et al. "Oxalic acid dihydrate – an accurate low-temperature structural study using high-resolution neutron powder diffraction". *Acta Crystallographica Section B*, **50**(3), 344–348 (1994).

[100] T. M. Sabine, G. W. Cox, and B. M. Craven. "A neutron diffraction study of $\alpha$-oxalic acid dihydrate". *Acta Crystallographica Section B*, **25**(12), 2437–2441 (1969).

[101] T. Steiner. "The Hydrogen Bond in the Solid State". *Angewandte Chemie International Edition*, **41**(1), 48–76 (2002).

[102] R. G. Delaplane and J. A. Ibers. "Direct Determination of the Effect of Isotopic Substitution on Bond Lengths in Solid Oxalic Acid Dihydrate". *The Journal of Chemical Physics*, **45**(9) (1966).

[103] P. Coppens, T. M. Sabine, G. Delaplane, et al. "An experimental determination of the asphericity of the atomic charge distribution in oxalic acid dihydrate". *Acta Crystallographica Section B*, **25**(12), 2451–2458 (1969).

[104] E. D. Stevens and P. Coppens. "Experimental electron density distributions of hydrogen bonds. High-resolution study of $\alpha$-oxalic acid dihydrate at 100 K". *Acta Crystallographica Section B*, **36**(8), 1864–1876 (1980).

[105] E. D. Stevens, P. Coppens, R. Feld, et al. "Electron density in the water molecule in $\alpha$-oxalic and dihydrate and the nature of short hydrogen bonds". *Chemical Physics Letters*, **67**, 541–543 (1979).

[106] D. Feil. "The electron density distribution in the hydrogen bond. A quantum chemical and crystallographic study". *Journal of Molecular Structure*, **237**, 33–46 (1990).

[107] M. P. C. M. Krijn and D. Feil. "Electron density distributions in hydrogen bonds: A local density-functional study of $\alpha$-oxalic acid dihydrate and comparison with experiment". *The Journal of Chemical Physics*, **89**, 4199–4208 (1988).

[108] M. P. C. M. Krijn, H. Graafsma, and D. Feil. “The influence of intermolecular interactions on the electron-density distribution. A comparison of experimental and theoretical results for $\alpha$-oxalic acid dihydrate”. *Acta Crystallographica Section B*, **44**(6), 609–616 (1988).

[109] E. V. Bartashevich, D. K. Nikulov, M. V. Vener, et al. “QTAIMC study of the X-H/H---O bond order indices (X = O, N, C) in molecular systems ”. *Computational and Theoretical Chemistry*, **973**(1-3), 33 – 39 (2011).

[110] B. C. Chakoumakos, H. Cao, F. Ye, et al. “Four-circle single-crystal neutron diffractometer at the High Flux Isotope Reactor”. *Journal of Applied Crystallography*, **44**(3), 655–658 (2011).

[111] P. Vishweshwar, N. Jagadeesh Babu, A. Nangia, et al. “Variable Temperature Neutron Diffraction Analysis of a Very Short O-H---O Hydrogen Bond in 2,3,5,6-Pyrazinetetracarboxylic Acid Dihydrate: Synthon-Assisted Short Oacid-H---Owater Hydrogen Bonds in a Multicenter Array”. *The Journal of Physical Chemistry A*, **108**(43), 9406–9416 (2004).

[112] P. Vishweshwar, A. Nangia, and V. M. Lynch. “Cooperative assistance in a very short O-H---O hydrogen bond. Low-temperature X-ray crystal structures of 2,3,5,6-pyrazinetetracarboxylic and related acids”. *Chem. Commun.*, pp. 179–180 (2001).

[113] T. Steiner, B. Lutz, J. van der Maas, et al. “Spectroscopic evidence for cooperativity effects involving C-H---O hydrogen bonds: crystalline mestranol”. *Chem. Commun.*, pp. 191–192 (1997).

[114] G. A. Jeffrey and W. Saenger. *Hydrogen bonding in biological structures* (Berlin ; New York : Springer-Verlag, 1994), study ed edn. Includes bibliographical references (p. [511]-546) and index.

[115] T. Steiner. “C-H---O Hydrogen Bond in Crystals”. *Crystallogr. Rev.*, **6** (1996).

[116] B. F. King, T. C. Farrar, and F. Weinhold. “Quadrupole coupling constants in linear $(HCN)_n$ clusters: Theoretical and experimental evidence for cooperativity effects in C-H---N hydrogen bonding”. *The Journal of Chemical Physics*, **103**, 348–352 (1995).

[117] B. F. King and F. Weinhold. “Structure and spectroscopy of $(HCN)_n$ clusters: Cooperative and electronic delocalization effects in C-H---N hydrogen bonding”. *The Journal of Chemical Physics*, **103**, 333–347 (1995).

[118] V. S. Znamenskiy, , and M. E. Green. “Quantum Calculations on Hydrogen Bonds in Certain Water Clusters Show Cooperative Effects”. *Journal of Chemical Theory and Computation*, **3**(1), 103–114 (2007).

[119] G. Rossetti, A. Magistrato, A. Pastore, et al. “Hydrogen Bonding Cooperativity in polyQ $\beta$-Sheets from First Principle Calculations”. *J Chem Theory Comput.*, **6**(6), 1777–82 (2010).

[120] A. D. Booth. “The Accuracy of Atomic Co-Ordinates Derived from Fourier Series in X-Ray Structure Analysis. IV. The Two-Dimensional Projection of Oxalic Acid”. *Proceedings of the Royal Society of London Series A*, **190**, 490–496 (1947).

[121] J. Dam, S. Harkema, and D. Feil. “The electron density of $\alpha$-oxalic acid dihydrate at 100 K by X-ray diffraction: a contribution to the IUCr Commission on Charge, Spin and Momentum Densities project on the accurate determination of electron densities”. *Acta Crystallographica Section B*, **39**(6), 760–768 (1983).

[122] A. Levstik, C. Filipič, V. Bobnar, et al. "Polaron conductivity mechanism in oxalic acid dihydrate: ac conductivity experiment". *Physical Review B*, **74**(15), 153104 (2006).

[123] A. Martin and A. A. Pinkerton. "Charge Density Studies Using CCD Detectors: Oxalic Acid at 100 K Revisited". *Acta Crystallographica Section B*, **54**(4), 471–477 (1998).

[124] Y. Wang, C. J. Tsai, W. L. Liu, et al. "Temperature-dependence studies of $\alpha$-oxalic acid dihydrate". *Acta Crystallographica Section B*, **41**(2), 131–135 (1985).

[125] D. Zobel, P. Luger, W. Dreissig, et al. "Charge density studies on small organic molecules around 20 K: oxalic acid dihydrate at 15 K and acetamide at 23 K". *Acta Crystallographica Section B*, **48**(6), 837–848 (1992).

[126] M.-L. Putkonen, R. Feld, C. Vettier, et al. "Powder neutron diffraction analysis of the hydrogen bonding in deutero-oxalic acid dihydrate at high pressures". *Acta Crystallographica Section B*, **41**(1), 77–79 (1985).

[127] N. M. W. G. S. A. Macchi, P.; Casati. "The $\alpha$ and $\beta$ Forms of Oxalic Acid Di-Hydrate at High Pressure: a Theoretical Simulation and a Neutron Diffraction Study." *CrystEngComm*, **12**(9), 2596–2603 (2010).

[128] Y. Ebisuzaki and S. M. Angel. "Raman study of hydrogen bonding in $\alpha$ and $\beta$-oxalic acid dihydrate". *Journal of Raman Spectroscopy*, **11**, 306–311 (1981).

[129] J. de Villepin, A. Novak, and de F. Romain. "Spectres de vibration des acides oxaliques. I.–Spectres infrarouge et Raman de la phase $\beta$ des acides H $_2$C $_2$O $_4$, D $_2$C $_2$O $_4$, H $_2$C $_2{}^{18}$O $_4$ et D $_2$C $_2{}^{18}$O $_4$". *Spectrochimica Acta Part A: Molecular Spectroscopy*, **34**(10), 1009–1017 (1978).

[130] J. De Villepin, A. Novak, and D. Bougeard. "$\alpha$- And $\beta$ Pahases of oxalic acid, H $_2$C $_2$O $_4$: Vibrational spectra, normal-coordinate calculations, and intermolecular forces". *Chemical Physics*, **73**, 291–312 (1982).

[131] H. Bhatt, C. Murli, A. K. Mishra, et al. "Hydrogen Bond Symmetrization in Glycinium Oxalate under Pressure". *The Journal of Physical Chemistry B*, **120**(4), 851–859 (2016).

[132] H. Bhatt, C. Murli, N. Garg, et al. "High pressure phase transformations in Bis(glycinium)oxalate - An infrared absorption study". *Chemical Physics Letters*, **532**, 57–62 (2012).

[133] J. de Villepin and A. Novak. "Vibrational Spectra of and Isotope Effect in Hydrogen Bonded Potassium Hydrogen Oxalate". *Spectroscopy Letters*, **4**(1-2), 1–8 (1971).

[134] J. de Villepin, A. Novak, and F. R. e. G. S. avec la Collaboration technique de N. Arnal. "Liaison hydrogène O-H-O symétrique. II. Spectres de vibration des oxalates acides de lithium hydratés et anhydres". *Journal of Molecular Structure*, **30**(2), 255–269 (1976).

[135] D. Hadži and B. Orel. "The "OH stretching" band of acid salts of carboxylic acids and the symmetry of the hydrogen bond". *Journal of Molecular Structure*, **18**(2), 227–239 (1973).

[136] Y. M. C. Jung. "Characterization of pH-Dependent IR Spectra of Oxalic Acid: Comparison of Self-Modeling Curve Resolution Analysis with Calculation of IR Frequencies." *Bull. Korean Chem. Soc.*, **24**(9), 1410–1412 (2003).

[137] A. K. Mishra, C. Murli, H. Bhatt, et al. “Hydrogen bonds in $\alpha$-oxalic acid dihydrate-A Raman spectroscopic study”. In “American Institute of Physics Conference Series”, vol. 1591 of *American Institute of Physics Conference Series*, pp. 136–138 (2014).

[138] A. K. Mishra, C. Murli, N. Garg, et al. “Pressure-Induced Structural Transformations in Bis(glycinium)oxalate”. *The Journal of Physical Chemistry B*, **114**(51), 17084–17091 (2010).

[139] D. E. Bethell and N. Sheppard. “The Infrared Spectrum of the $H_3O^+$ Ion in Acid Hydrates”. *Journal of Chemical Physics*, **21**, 1421–1421 (1953).

[140] C. C. Ferriso and D. F. Horning. “THE INFRARED SPECTRUM OF THE OXONIUM ION”. *Journal of the American Chemical Society*, **75**(16), 4113–4114 (1953).

[141] P. A. Giguére and S. Turrell. “H3O+ ions in aqueous acid solutions. The infrared spectra revisited”. *Canadian Journal of Chemistry*, **54**(21), 3477–3482 (1976).

[142] N. N. Haese and T. Oka. “Observation of the v(2) (1(-) - 0(+)) inversion mode band in H3O(+) by high resolution infrared spectroscopy”. *Journal of Chemical Physics*, **80**, 572 (1984).

[143] R. W. T. Wilkins, A. Mateen, and G. W. West. “The spectroscopic study of oxonium ions in minerals”. *Am. Mineral*, **59**, 811–819 (1974).

[144] G. V. Yukhnevich. “Advances in the Use of Infrared Spectroscopy for the Characterisation of OH Bonds”. *Russian Chemical Reviews*, **32**, 619–633 (1963).

[145] S. K. Sikka. “On some hydrogen bond correlations at high pressures”. *High Pressure Research*, **27**(3), 313–319 (2007).

[146] P. E. Blöchl. “Projector augmented-wave method”. *Physical Review B*, **50**(24), 17953–17979 (1994).

[147] G. Kresse and J. Hafner. “Efficiency of ab-initio Total Energy Calculations for Metals and Semiconductors Using a Plane-Wave Basis ”. *Comput. Mater. Sci.*, **6**(1), 15–50 (1996).

[148] G. Kresse and J. Hafner. “Norm-conserving and ultrasoft pseudopotentials for first-row and transition elements”. *Journal of Physics Condensed Matter*, **6**(40), 8245–8257 (1994).

[149] G. Kresse and D. Joubert. “From ultrasoft pseudopotentials to the projector augmented-wave method”. *Physical Review B*, **59**(3), 1758–1775 (1999).

[150] R. G. Delaplane and J. A. Ibers. “An X-ray study of $\alpha$-oxalic acid dihydrate $(COOH)_2.2H_2O$ and of its deuterium analogue, $(COOD)_2.2D_2O$: isotope effect in hydrogen bonding and anisotropic extinction effects”. *Acta Crystallographica Section B*, **25**(12), 2423–2437 (1969).

[151] J. P. Perdew, K. Burke, and M. Ernzerhof. “Generalized Gradient Approximation Made Simple”. *Physical Review Letters*, **77**(18), 3865–3868 (1996).

[152] H. J. Monkhorst and J. D. Pack. “Special points for Brillouin-zone integrations”. *Physical Review B*, **13**(12), 5188–5192 (1976).

[153] N. Huse, K. Heyne, J. Dreyer, et al. “Vibrational Multilevel Quantum Coherence due to Anharmonic Couplings in Intermolecular Hydrogen Bonds”. *Physical Review Letters*, **91**(19), 197401 (2003).

[154] J. STARE, J. PANEK, J. ECKERT, ET AL. "Proton Dynamics in the Strong Chelate Hydrogen Bond of Crystalline Picolinic Acid N-Oxide. A New Computational Approach and Infrared, Raman and INS Study". *The Journal of Physical Chemistry A*, **112**(7), 1576–1586 (2008).

[155] R. JANOSCHEK, E. G. WEIDEMANN, H. PFEIFFER, ET AL. "Extremely high polarizability of hydrogen bonds". *Journal of the American Chemical Society*, **94**(7), 2387–2396 (1972).

[156] R. JANOSCHEK, E. G. WEIDEMANN, AND G. ZUNDEL. "Calculated frequencies and intensities associated with coupling of the proton motion with the hydrogen bond stretching vibration in a double minimum potential surface". *J. Chem. Soc., Faraday Trans. 2*, **69**, 505–520 (1973).

[157] T. LANKAU AND C.-H. YU. "A quantum description of the proton movement in an idealized NHN+ bridge". *Phys. Chem. Chem. Phys.*, **13**, 12758–12769 (2011).

[158] G. ZUNDEL. "Hydrogen bonds with large proton polarizability in crystals". *Journal of Molecular Structure*, **552**(1-3), 81–86 (2000).

[159] P. A. KOLLMAN AND C. F. BENDER. "The structure of the H $^3$O $^+$ (hydronium) ion". *Chemical Physics Letters*, **21**, 271–274 (1973).

[160] K. J. ARUN AND S. G. JAYALEKSHMI. "Growth and Characterization of Glycinium Oxalate Crystals for Nonlinear Optical Applications." *Optoelect. Adv. Mater.*, **2**(11), 701–706 (2008).

[161] I. A. TUMANOV, A. F. ACHKASOV, E. V. BOLDYREVA, ET AL. "Following the products of mechanochemical synthesis step by step". *CrystEngComm*, **13**, 2213–2216 (2011).

[162] B. A. ZAKHAROV AND E. V. BOLDYREVA. "L-Alaninium Semi-Oxalate Monohydrate. Acta Crystallogr." *Acta Crystallogr., Sect. C: Cryst. Struct. Commun.*, **67**(2), o47–o51 (2011).

[163] B. A. ZAKHAROV AND E. V. BOLDYREVA. "A high-pressure single-crystal to single-crystal phase transition in DL-alaninium semi-oxalate monohydrate with switching-over hydrogen bonds". *Acta Crystallographica Section B*, **69**(3), 271–280 (2013).

[164] D. HADŽI. "Infrared Spectra of Strongly Hydrogen-Bonded Systems." *Pure Appl. Chem.*, **11**(3-4) (1965).

[165] D. HADŽI, B. OREL, AND A. NOVAK. "Infrared and Raman spectra of some acid salts containing crystallographically symmetric hydrogen bonds". *Spectrochimica Acta Part A: Molecular Spectroscopy*, **29**(9), 1745–1753 (1973).

[166] D. HADŽI, I. PETROV, AND M. ZITKO. "Mangini, A., Ed.;". In "In Advances in Molecular Spectroscopy", p. 794 (Elsevier: Amsterdam, 1962).

[167] A. LAUTIÉ AND Y. BELABBES. "Vibrational spectra and structure of some oxalic acid/substituted pyridine (methyl-, amino-, and dihalogeno-) complexes: Hydrogen bond features". *Spectrochimica Acta Part A: Molecular Spectroscopy*, **52**(14), 1903–1914 (1996).

[168] J. LINDGREN, J. DE VILLEPIN, AND A. NOVAK. "Isotope effect and hydrogen bonding in crystalline hydrazinium hydrogen oxalate, N $_2$H $_5$HC $_2$O $_4$". *Chemical Physics Letters*, **3**(2), 84–86 (1969).

[169] P. GIANNOZZI, S. BARONI, N. BONINI, ET AL. "QUANTUM ESPRESSO: a modular and open-source software project for quantum simulations of materials". *Journal of Physics Condensed Matter*, **21**(39), 395502 (2009).

[170] J. P. Perdew and A. Zunger. "Self-interaction correction to density-functional approximations for many-electron systems". *Physical Review B*, **23**(10), 5048–5079 (1981).

[171] A. P. Hammersley, S. O. Svensson, M. Hanfland, et al. "Two-dimensional detector software: From real detector to idealised image or two-theta scan". *High Pressure Research*, **14**(4-6), 235–248 (1996).

[172] A. C. Larson and V. Dreele. "GSAS: General Structure Analysis System". Tech. Rep. Los Alamos National Laboratory Report LAUR, NM2000; p 86, Los Alamos National Laboratory: Los Alamos, (1994).

[173] J. De Villepin, A. Novak, and J. Tomkinson. "Neutron inelastic scattering spectra of strongly hydrogen bonded acid oxalates NaHC $_2$O $_4$, KHC $_2$O $_4$ and LiHC $_2$O $_4$". *Chemical Physics*, **48**(1), 113–119 (1980).

[174] J. C. Evans. "Narrow transmission regions within broad infrared absorption bands in solids". *Spectrochimica Acta*, **18**(4), 507–512 (1962).

[175] L. Leiserowitz and F. Nader. "syn-Planar Conformation of Oxalic Acid: Crystal Structure of the Oxalic Acid-Acetamide Complex". *Angewandte Chemie International Edition in English*, **11**(6), 514–515 (1972).

[176] S. V. Bykov, N. S. Myshakina, and S. A. Asher. "Dependence of Glycine CH2 Stretching Frequencies on Conformation, Ionization State, and Hydrogen Bonding". *The Journal of Physical Chemistry B*, **112**(18), 5803–5812 (2008).

[177] R. Pepinsky, Y. Okaya, D. P. Eastman, et al. "Ferroelectricity in Glycine Silver Nitrate". *Physical Review*, **107**, 1538–1539 (1957).

[178] R. Pepinsky, K. Vedam, S. Hoshino, et al. "Ferroelectricity in Di-Glycine Nitrate $(NH_2CH_2COOH)_2.HNO_3$". *Physical Review*, **111**, 430–432 (1958).

[179] F. Shikanai, M. Komukae, Z. Czapla, et al. "Crystal Structure of $NH_3CH_2COOHH_2PO_3$ in the Ferroelectric Phase". *Journal of the Physical Society of Japan*, **71**, 498 (2002).

[180] S. Launer, M. L. Maire, G. Schaack, et al. "Pressure-temperature phase diagrams of betaine-arsenate, -phosphate, and -phosphite". *Ferroelectrics*, **135**(1), 257–270 (1992).

[181] F. Jona and G. Shirane. *Ferroelectric Crystals* (Pergamon Press, Oxford, London (1962)(chapter 2), Pergamon Press, Oxford, London (1962), 1962).

[182] S. Horiuchi and Y. Tokura. "Organic ferroelectrics". *Nature Materials*, **7**, 357–366 (2008).

[183] R. K. Khanna, M. Horak, and E. R. Lippincott. "Infrared studies on some ferroelectric compounds of glycine". *Spectrochimica Acta*, **22**, 1801–1811 (1966).

[184] H. Stenback. "On the Raman spectra of solid natural -glycine and solid 15N-substituted -glycine". *Journal of Raman Spectroscopy*, **5**(1), 49–55 (1976).

[185] J.-J. Max, M. Trudel, and C. Chapados. "Infrared titration of aqueous glycine". *Applied Spectroscopy*, **52**, 226–233 (1998).

[186] C. Murli, S. M. Sharma, S. K. Kulshreshtha, et al. "High-pressure behavior of $\beta$-Ni (OH) $_2$-A Raman scattering study". *Physica B Condensed Matter*, **307**, 111–116 (2001).

[187] E. R. Lippincott and R. Schroeder. "One-Dimensional Model of the Hydrogen Bond". *The Journal of Chemical Physics*, **23**(6) (1955).

[188] A. Novak. *Hydrogen bonding in solids correlation of spectroscopic and crystallographic data*, pp. 177–216 (Springer Berlin Heidelberg, Berlin, Heidelberg, 1974).

[189] R. Chitra, P. Roussel, and R. R. Choudhury. “53rd DAE Solid State Physics Symposium ”. p. 1177 (2008).

[190] B. C. H. Steele and A. Heinzel. “Materials for fuel-cell technologies”. *Nature*, **414**, 345–352 (2001).

[191] M. Gasik. *Materials for Fuel Cells* (Woodhead Publishing, 2008).

[192] M. Mori, T. Yamamoto, H. Itoh, et al. “Compatibility of alkaline earth metal (Mg, Ca, Sr)-doped lanthanum chromites as separators in planar-type high-temperature solid oxide fuel cells”. *Journal of Materials Science*, **32**(9), 2423–2431 (1997).

[193] X. J. Chen, Q. L. Liu, N. P. Brandon, et al. “High- performance cathode-supported SOFC with perovskite anode operating in weakly humidified hydrogen and methane”. *Fuel Cells Bull.*, **2007**(6), 12–16 (2007).

[194] L. L. Zhang. “Review, MSE 04053/CISM/11z,” (2004).

[195] T. Nakamura, G. Petzow, and L. Gauckler. “Stability of the perovskite phase LaBO3 (B = V, Cr, Mn, Fe, Co, Ni) in reducing atmosphere I. Experimental results”. *Materials Research Bulletin*, **14**(5), 649–659 (1979).

[196] O. Yamamoto. “Solid oxide fuel cells: Fundamental aspects and prospects”. *Electrochimica Acta*, **45**(15-16), 2423–2435 (2000).

[197] B. K. Flandermeyer, M. M. Nasrallah, D. M. Sparlin, et al. “High Temperature Stability of Magnesium Doped Lanthanum Chromite”. *High Temp. Sci.*, **20**, 259 (1985).

[198] H. C. Graham and H. H. Davis. “Oxidation/Vaporization Kinetics of Cr2O3”. *Journal of the American Ceramic Society*, **54**(2), 89–93 (1971).

[199] H. Yokokawa, N. Sakai, T. Kawada, et al. “Chemical Thermodynamic Considerations in Sintering of LaCrO3-Based Perovskites”. *Journal of the Electrochemical Society*, **138**(4), 1018–1027 (1991).

[200] L. Chick, J. Liu, J. Stevenson, et al. “Phase transitions and transient liquid-phase sintering in calcium-substituted lanthanum chromite”. *Journal of the American Ceramic Society*, **80**(8), 2109–2120 (1997).

[201] T. Armstrong, J. Stevenson, L. Pederson, et al. “Dimensional instability of doped lanthanum chromite”. *Journal of the Electrochemical Society*, **143**(9), 2919–2925 (1996).

[202] L. A. Chick, J. L. Bates, and G. D. Maupin. “Air-sintering mechanisms of chromites”. In “Presented at the 2nd International Symposium on Solid Oxide Fuel Cells, Athens, Greece, 2-5 Jul. 1991”, (1991).

[203] S. Simner, J. Hardy, J. Stevenson, et al. “Sintering mechanisms in strontium doped lanthanum chromite”. *Journal of Materials Science*, **34**(23), 5721–5732 (1999).

[204] N. Sammes, R. Ratnaraj, and M. Fee. “The effect of sintering on the mechanical properties of SOFC ceramic interconnect materials”. *Journal of Materials Science*, **29**(16), 4319–4324 (1994).

[205] D. B. Meadowcroft. “Some properties of strontium-doped lanthanum chromite”. *Journal of Physics D: Applied Physics*, **2**(9), 1225 (1969).

[206] M. Mori, Y. Hiei, and N. Sammes. "Sintering behavior and mechanism of Sr-doped lanthanum chromites with A site excess composition in air". *Solid State Ionics*, **123**(1), 103–111 (1999).

[207] R. Gupta and C. Whang. "Effects of anion and synthesis route on the structure of $(La_{0.9}Sr_{0.1})$ $(Cr_{0.85}Fe_{0.05}Co_{0.05}Ni_{0.05})O_3 - \delta$ perovskite and removal of impurity phases". *Solid State Ionics*, **178**(29-30), 1617–1626 (2007).

[208] J. Bahadur, D. Sen, S. Mazumder, et al. "Non-Debye to Debye transition of ac dielectric response in $YCrO_3$ nanoceramic under sintering: effect of pore structure". *Journal of Physics Condensed Matter*, **20**, 345201 (2008).

[209] D. Sen, J. Bahadur, S. Mazumder, et al. "Smoothening of the non-Euclidean surface of $Nd_2O_3$ doped $CeO_2$ nanoceramic grains under sintering: an ultra-small angle x-ray scattering investigation and a computer simulation study". *Journal of Physics Condensed Matter*, **20**(3), 035103 (2008).

[210] I. Smirnova. "Normal modes of the LaMnO3 Pnma phase: Comparison with La2CuO4 Cmca phase". *Physica B: Condensed Matter*, **262**(3-4), 247–261 (1999).

[211] S. Mazumder, D. Sen, T. Saravanan, et al. "Performance and calibration of the newly installed medium resolution double crystal based small-angle neutron scattering instrument at Trombay". *Journal of Neutron Research*, **9**(1), 39–57 (2001).

[212] P. W. Schmidt and R. Hight, Jnr. "Slit height corrections in small angle X-ray scattering". *Acta Crystallographica*, **13**(6), 480–483 (1960).

[213] J. A. Lake. "An iterative method of slit-correcting small angle X-ray data". *Acta Crystallographica*, **23**(2), 191–194 (1967).

[214] G. V. S. Rao, C. N. R. Rao, and J. R. Ferraro. "Infrared and Electronic Spectra of Rare Earth Perovskites: Ortho-Chromites, -Manganites and -Ferrites". *Applied Spectroscopy*, **24**, 436–445 (1970).

[215] G. Tompsett and N. Sammes. "Characterisation of the SOFC material, LaCrO3, using vibrational spectroscopy". *Journal of Power Sources*, **130**(1-2), 1–7 (2004).

[216] M. Daturi, G. Busca, and R. Willey. "Surface and structure characterization of some perovskite-type powders to be used as combustion catalysts". *Chemistry of Materials*, **7**(11), 2115–2126 (1995).

[217] F. Mayr, C. Hartinger, and A. Loidl. "Structural aspects of the phonon spectra of $La_{1-x}Sr_xMnO_3$". *Phys. Rev. B*, **72**, 024425 (2005).

[218] P. Radaelli, G. Iannone, M. Marezio, et al. "Structural effects on the magnetic and transport properties of perovskite $A_{1-x}A'_xMnO_3$ (x = 0.25, 0.30)". *Physical Review B - Condensed Matter and Materials Physics*, **56**(13), 8265–8276 (1997).

[219] P. Ganguly and N. Vasanthacharya. "Infrared and Mössbauer spectroscopic study of the metal-insulator transition in some oxides of perovskite structure". *Journal of Solid State Chemistry*, **61**(2), 164–170 (1986).

[220] L. Martín-Carrón, A. de Andrés, M. J. Martínez-Lope, et al. "Raman phonons as a probe of disorder, fluctuations, and local structure in doped and undoped orthorhombic and rhombohedral manganites". *Phys. Rev. B*, **66**, 174303 (2002).

[221] D. Stoilova, M. Georgiev, and D. Marinova. "Infrared study of the vibrational behavior of SO42- guest ions matrix-isolated in metal (II) chromates (Me = Ca, Sr, Ba)". *Vibrational Spectroscopy*, **39**(1), 46–49 (2005).

[222] A. K. Bogush, V. I. Pavlov, and L. V. Balyko. “Structural phase transitions in the LaMnO3+ system”. *Crystal Research and Technology*, **18**(5), 589–598 (1983).

[223] A. Patra, J. Bahadur, S. Mazumder, et al. “Small-angle neutron scattering investigations on sintering behavior of combustion synthesized la 0.8Sr 0.2CrO 3”. *Journal of Nanoscience and Nanotechnology*, **8**(4), 2157–2162 (2008).

[224] J. Bahadur, D. Sen, S. Mazumder, et al. “Effect of heat treatment on pore structure in nano-crystalline NiO: A small angle neutron scattering study”. *Journal of Solid State Chemistry*, **181**(5), 1227–1235 (2008).

[225] J. Teixeira. “Small-angle scattering by fractal systems”. *Journal of Applied Crystallography*, **21**(6), 781–785 (1988).

[226] T. Freltoft, J. Kjems, and S. Sinha. “Power-law correlations and finite-size effects in silica particle aggregates studied by small-angle neutron scattering”. *Physical Review B*, **33**(1), 269–275 (1986).

[227] B. B. Mandelbrot. *The fractal geometry of nature* (New York, W.H. Freeman and Co., 1983).

[228] A. Guinier and G. Fournet. *Small-angle Scattering of X-rays* (John Wiley and Sons, Inc, New York, 1955).

[229] L. Feigin and D. Svergun. *Structure analysis by small-angle X-ray and neutron scattering* (Plenum Press. New York., 1987).

[230] G. Kostorz. *Treatise ou Materials Science and Technology*, vol. 15 (Academic Press, New York, 1979).

[231] R. J. Baxter. “Percus-Yevick Equation for Hard Spheres with Surface Adhesion”. *The Journal of Chemical Physics*, **49**(6), 2770–2774 (1968).

[232] I. Felner, U. Asaf, Y. Levi, et al. “Coexistence of magnetism and superconductivity in $R_{1.4}$ $Ce_{0.6}$ $RuSr_2$ $Cu_2$ $O_{10-\delta}$s(R=Eu and Gd)”. *Phys. Rev. B*, **55**, R3374–R3377 (1997).

[233] O. Chmaissem, J. D. Jorgensen, H. Shaked, et al. “Crystal and magnetic structure of ferromagnetic superconducting $RuSr_2GdCu_2O_8$”. *Phys. Rev. B*, **61**, 6401–6407 (2000).

[234] A. V. Boris, P. Mandal, C. Bernhard, et al. “Phonon anomalies and electron-phonon interaction in the $RuSr_2GdCu_2O_8$ ferromagnetic superconductor: Evidence from infrared conductivity”. *Phys. Rev. B*, **63**, 184505 (2001).

[235] P. W. Klamut, B. Dabrowski, S. Kolesnik, et al. “Superconductivity in $Ru_{1-x}Sr_2GdCu_{2+x}O_{8-y}$ compounds”. *Phys. Rev. B*, **63**, 224512 (2001).

[236] Y. Yamada, Y. Fujimoto, S. Hatanaka, et al. “Pressure effects on the superconductivity and magnetization in RuSr 2 GdCu 2 O 8”. *Journal of Physics: Condensed Matter*, **14**(44), 10763 (2002).

[237] G. Oomi, F. Honda, T. Eto, et al. “The effect of pressure on the superconductivity and magnetism of $RuSr_2GdCu_2O_8$”. *Journal of Physics: Condensed Matter*, **14**(44), 10747 (2002).

[238] T. N. Sairam, M. Premila, J. Janaki, et al. “Temperature and composition dependence of phonon modes in $GdSr_2Ru_{1-x}Cu_{2+x}O_8$”. *Journal of Physics: Condensed Matter*, **16**(46), 8311 (2004).

[239] I. Felner, I. Nowik, M. I. Tsindlickt, et al. "Magnetic behavior of superconducting and nonsuperconducting $RuSr_2Y_{2-x}Ce_xCu_2O_{10}$ (x=0.5,1.0)". *Physical Review B*, **76**(14), 144514 (2007).

[240] I. I. Mazin and S. D. J. "Electronic structure and magnetism in Ru-based perovskites". *Physical Review B*, **56**, 2556–2571 (1997).

[241] Y. C. Lo, C. I. Chen, and C. H. Chang. "Mid-Infrared beamline, Beamline Development". *NSRRC Activity Report 2002/2003* (2002-2003).

[242] M. C. Martin, H.-Y. Holman, and W. R. McKinney. "First Performance Results for the New Continuum$^{TM}$ IR Microscope". *Report, Advanced Light Source, Lawrence Berkeley National Laboratory*.

[243] P. Lerch, P. Dumas, T. Schilcher, et al. "Assessing noise sources at synchrotron infrared ports". *Journal of Synchrotron Radiation*, **19**(1), 1–9 (2012).

[244] F. A. Polack, R. Mercier, L. Nahon, et al. "Optical design and performance of the IR microscope beamline at SUPERACO-France". vol. 13 (American Physical Society, 1999).

[245] N. G. Golubeva and A. O. Velikanov. "Raman spectroscopy study of the process of polymerization of polyacrylamide gel". *Journal of Applied Spectroscopy*, **53**, 1290–1292 (1990).

[246] M. K. Gupta and R. Bansil. "Laser Raman spectroscopy of polyacrylamide". *Journal of Polymer Science, Polymer Physics Edition*, **19**(2), 353–360 (1981).

[247] T. L. Rapp, W. K. Kowalchyk, K. L. Davis, et al. "Acrylamide polymerization kinetics in gel electrophoresis capillaries. A Raman microprobe study". *Analytical Chemistry*, **64**(20), 2434–2437 (1992).

[248] A. Usanmaz. "Crystal structure effect in radiation-induced solid-state polymerization of acrylamide". *Turkish Journal Of Chemistry*, **21**(4), 304–312 (1997).

[249] M. G. Bradbury, S. D. Hamann, and M. Linton. "Solid-phase polymerizations at high pressures". *Australian Journal of Chemistry*, **23**(3), 511–523 (1970).

[250] A. A. Zharov. "The Polymerisation of Solid Monomers Under Conditions of Deformation at a High Pressure". *Russian Chemical Reviews*, **53**, 140–149 (1984).

[251] L. V. Babare. *Chernogolovka, Fiz. Goreniya Vzryva*, **17**, 133 (1981).

[252] T. A. Fadner and H. Morawetz. "Polymerization in the crystalline state. I. Acrylamide". *Journal of Polymer Science*, **45**(146), 475–501 (1960).

[253] B. W. Dodson and C. Arnold Jr. "Shock-induced activation of acrylamide polymerization". *The Journal of Physical Chemistry*, **87**(16), 3023–3024 (1983).

[254] N. P. Chistotina and A. A. Zharov. *Bull. Russ. Acad. Sci.*, **41**, 994 (1992).

[255] B. B. Sharma, C. Murli, and S. M. Sharma. "Hydrogen bonds and polymerization in acrylamide under pressure". *Journal of Raman Spectroscopy*, **44**(5), 785–790 (2013).

[256] R. Murugan, S. Mohan, and A. Bigotto. "FTIR and Polarised Raman Spectra of Acrylamide and Polyacrylamide". *Journal of the Korean Physical Society*, **32**, 505–512 (1998).

[257] D. W. Mayo, F. A. Miller, and R. W. e. Hannah. *Course Notes on the Interpretation of Infrared and Raman Spectra* (John Wiley & Sons, Inc, 2004).

[258] M. Lax. “Quantum relaxation, the shape of lattice absorption and inelastic neutron scattering lines”. *Journal of Physics and Chemistry of Solids*, **25**, 487–503 (1964).

[259] S. J. F. “Proc. 2nd Int. Conf. on Light Scattering in Solids ed. M Balkanski (Paris: Flammarion)”. pp. 387–392 (1971).

[260] A. Mooradian and G. B. Wright. “Observation of the Interaction of Plasmons with Longitudinal Optical Phonons in GaAs”. *Physical Review Letters*, **16**, 999–1001 (1966).

[261] G. Irmer, J. Monecke, and W. Siegel. “Raman scattering study of dopant homogeneity in GaP and GaAs single crystals”. *Crystal Research and Technology*, **20**(8), 1125–1131 (1985).

[262] M. Born and K. Huang. *Dynamical Theory of Crystal Lattices* (Clarendon Press, Oxford University Press, 1954).

[263] B. H. Bairamov, V. V. Toporov, G. Irmer, et al. “Observation of raman scattering by localized optical phonons bound to neutral donors in GaP:Si”. *Solid State Communications*, **55**, 487–490 (1985).

[264] P. J. Dean, D. D. Manchon, and J. J. Hopfield. “Observation of Optical Phonons Bound to Neutral Donors”. *Physical Review Letters*, **25**, 1027–1030 (1970).

[265] S. M. Kogan and R. A. Suris. “Resonance Interaction of an Impurity-center Electron with Lattice Oscillations”. *Soviet Journal of Experimental and Theoretical Physics*, **23**, 850 (1966).

[266] J. Monecke. “Theory of Fermi resonances in Raman and infrared spectra”. *Journal of Raman Spectroscopy*, **18**, 477–479 (1987).

[267] H. Olijnyk and A. P. Jephcoat. “Effect of pressure on Fermi resonance in orthorhombic high-pressure phase-III and of isotopic species of CO $_2$”. *Physica B Condensed Matter*, **265**, 54–59 (1999).

[268] H. Bhatt, A. K. Mishra, C. Murli, et al. “Proton transfer aiding phase transitions in oxalic acid dihydrate under pressure”. *Physical Chemistry Chemical Physics*, **18**, 8065–8074 (2016).

[269] J. R. Stine and D. W. Noid. “Classical treatment of the dissociation of hydrogen fluoride with one and two infrared lasers”. *Optics Communications*, **31**, 161–164 (1979).

[270] M. L. Koszykowski, D. W. Noid, and R. A. Marcus. “Semiclassical theory of intensities of vibrational fundamentals, overtones, and combination bands”. *The Journal of Physical Chemistry*, **86**(12), 2113–2117 (1982).